MONASH University

# Synthesis and Applications of Fe- and Mg-based Nanomaterials from Victorian Brown Coal Fly Ash

**Binbin Qian**

A thesis submitted for the degree of

**Doctor of Philosophy**

Department of Chemical Engineering
MONASH University

2021

## Copyright notice

© Binbin Qian, 2021. Except as provided in the Copyright Act 1968, this thesis may not be reproduced in any form without the written permission of the author.

I certify that I have made all reasonable efforts to secure copyright permissions for third-party content included in this thesis and have not knowingly added copyright content to my work without the owner's permission.

# Table of Contents

## Abstract

Coal is one of the biggest commercial fuel all over the world. Fly ash, a coal combustion by-product, is consequently produced and the production of fly ash worldwide is estimated to be 750 million tons annually while the rate of utilization is only about 50%. Here in Australia, approximately 10 million tons fly ash are generated from coal-combustion industry every year and most of them are directly transported into ash pond, resulting in the environmental issues such as the pollutions of air, soil and groundwater. In Victoria, Mg and Fe are abundant in the brown coal fly ash and considering the value-added utilization of this industrial waste, it is thus hypothesized to be a promising feedstock to synthesize Fe- and Mg- based nanomaterials.

Previous works have investigated various leaching methods and leaching agents to extract Mg and Fe out of various fly ash. However, either harsh conditions with high extraction yields or moderate conditions with low extraction yields were obtained. To address this special brown coal fly ash, synergistic leaching agents (HCl and $NH_4Cl$) were used to make the leaching conditions comparatively moderate. However, the maximum leaching yields of Mg and Fe were only 65% and 29%, respectively. The main challenge is how to cleave the strong affinity between Mg and Fe within the inverse-spinel structure of $MgFe_2O_4$ matrix, which cannot be easily broken by the weak leaching agents or single step leaching method. As for Fe- and Mg-based nanomaterials including $\alpha$-$Fe_2O_3$, $Mg(OH)_2$ and MgO, they are usually synthesized from pure reagent grade chemicals. Synthesis of these nanomaterials from industrial wastes is rarely reported, which will not only convert those industrial wastes into value-added products, but also accelerate the development of low-cost production of these nanomaterials. Moreover, atomic understandings of natural impurity doped $\alpha$-$Fe_2O_3$ as well as growth process for $Mg(OH)_2$ are still blank, which determines their nanostructures and the influences the subsequent applications including water remediation and catalysis.

In this study, (1) a high-efficient extraction strategy of two-step leaching method was employed

for cleaving the inverse-spinel structure of $MgFe_2O_4$ and thus a high extraction yield for Fe (45 *wt%*) and Mg (25 *wt%*) was obtained. The resultant leachate then worked as a Mg-source and Fe-source for the synthesis of nanosized α-$Fe_2O_3$, $Mg(OH)_2$ and MgO. (2) As for the synthesized α-$Fe_2O_3$, a unique $Fe_{1.72}Al_{0.28}O_3$ (FAO) nanoflake has been successfully synthesized. the $Al^{3+}$ dopant distorted the original atomic structure of standard α-$Fe_2O_3$, resulting in reduced lattice parameters (a=5.005(43) Å, c=13.727 (44) Å), a smaller first shell (Fe-O bond distance of 1.95(0.21) Å) and a reduced periodic symmetry (Fe coordination number of 4.5(0.3)). Compared with the standard nanosized α-$Fe_2O_3$ and even those reported in the literature, the as-synthesized FAO nanoflakes exhibit higher efficiency and enhanced adsorption performance with a maximum adsorption capacity of 68.3, 80.6, 61.1 and 213.8 mg $g^{-1}$ of Cr(VI), As(V), As(III) and Congo red, respectively. These values are around 3-5 times larger than the standard α-$Fe_2O_3$ nanoparticles that is free in $Al^{3+}$. (3) In terms of the nano-$Mg(OH)_2$, a facile synthesis of a facet-engineered MgO(111)-Fe(III) nanosheet from BCFA waste as a HT-WGSR catalyst was demonstrated. During the HT-WGSR, the reduced ethanol-mediated MgO(111)-Fe(III) catalyst is beneficial in promoting the formation and decomposition of surface formates owing to the enhanced CO and $H_2O$ adsorption as well as the reduction of $Fe^{3+}$ on the oxygen vacancy of the (111) facet, leading to increased CO conversion by a factor of two in comparison to the commercial $Mg(OH)_2$ loaded with the same amount of $Fe^{3+}$, and by nearly seven time compared to the nano-sized hematite reference. (4) Finally, magnetite-based, surrounded catalysts with a core-shell structure were successfully synthesized from the coal fly ash. The nanosheet-like $Fe^{3+}$ hydroxide precursor broke into smaller particles with a core in form of magnetite and a diameter of ~20 nm, whereas the impurity elements were activated to migrate to the outer surface forming a shell with a thickness of a few nanometres. Due to the protection of shell on the sintering, the two catalysts derived from fly ash exhibited improved activity, thermal stability and long-term durability for

HT-WGSR at 400ºC and 450ºC compared to pure hematite. In particular, the catalyst synthesized with a thicker shell slightly more impurities exhibited the highest activity at a temperature. Compared to the pure hematite, the best activity increased the CO conversion by nearly four times and decreased the magnitude of the deactivation rate constant by three times.

The completion of this project is expected to address the global environmental challenge facing the industrial solid waste: how to utilize the coal fly ash waste in a value-added strategy. The low-rank coal is the main local fuel for the power generation plant or industry boiler, which will produce large amount of coal fly ash after the combustion. The disposal of this coal fly ash will cause land occupation, financial burden and environmental risk. This project is therefore crucial for the power generation plants and industrial boilers burning low-rank coal that are suffering from the accumulation caused by coal fly ash. Additionally, this research on the synthesis of Fe- and Mg-based nanomaterials will be essential for the development of low-coat production of these nanomaterials, which is a pivotal trend in sustainable development.

## Declaration

This thesis contains no material which has been accepted for the award of any other degree or diploma at any university or equivalent institution and that, to the best of my knowledge and belief, this thesis contains no material previously published or written by another person, except where due reference is made in the text of the thesis.

Signature: ……

Print Name: ……..……

Date: ……..……

## Publications during Enrolment

***Peer-reviewed journal papers***

**Binbin Qian**, Jianghao Zhang, Song Zhou, Jun Lu, Yue Liu, Cheng Liu, Yong Wang, Huanting Wang, Lian Zhang*, Synthesis of (111) Facet-Engineered MgO Nanosheet from Coal Fly Ash and Its Superior Catalytic Performance for High-Temperature Water Gas Shift Reaction, *Applied Catalysis A: General*, 2021, 618, 118132.

**Binbin Qian**, Cheng Liu, Jun Lu, Meipeng Jian, Xiaoyi Hu, Song Zhou, Tara Hosseini, Barbara Etschmann, Xiwang Zhang, Huanting Wang, Lian Zhang*, Synthesis of *in-situ* $Al^{3+}$-defected iron oxide nanoflakes from coal ash: A detailed study on the structure, evolution mechanism and application to water remediation, *Journal of Hazardous Materials*, 2020, 395, 122696.

**Binbin Qian**, Tahereh Hosseini, Xiwang Zhang, Yue Liu, Huanting Wang and Lian Zhang*, Coal Waste to Two-Dimensional Materials: Fabrication of α-$Fe_2O_3$ Nanosheets and MgO Nanosheets from Brown Coal Fly Ash, *ACS Sustainable Chemistry & Engineering*, 2018, 6, 15982-15987.

Song Zhou, **Binbin Qian**, Tahereh Hosseini, Anthony De Girolamo, and Lian Zhang*, Pyrohydrolysis of $CaCl_2$ Waste for the Recovery of HCl Acid upon the Synergistic Effects from $MgCl_2$ and Silica, *ACS Sustainable Chemistry & Engineering*, 2019, 7, 3349-3355.

Song Zhou, Barbara Etschmann, **Binbin Qian**, Cheng Liu, Lian Zhang*, Synchrotron X-ray absorption spectroscopy study of the evolution of chlorine during the pyro-hydrolysis of calcium and magnesium chloride waste, *Waste Management*, 2020, 120, 608-615.

Song Zhou, Xue Yan, Cheng Liu, **Binbin Qian**, Lian Zhang*, Can $CO_2$ and Steam React in the Absence of Electrolysis at High Temperatures? *ChemSusChem*, 2020, 13, 6660-6667.

***Conference papers***

**Binbin Qian**, Tahereh Hosseinni, Xiwang Zhang and Lian Zhang*, Synthesis of high-purity MgO Nano-sheets from Victorian brown coal fly ash, 1st International Conference on Bioinspired Materials and Membranes and 1st International Conference on Energy-efficient Separation, 23-27 January 2017, Melbourne.

## Thesis including published works declaration

I hereby declare that this thesis contains no material which has been accepted for the award of any other degree or diploma at any university or equivalent institution and that, to the best of my knowledge and belief, this thesis contains no material previously published or written by another person, except where due reference is made in the text of the thesis.

This thesis includes three original papers published in peer reviewed journals and one submitted journal paper. The core theme of the thesis is: synthesis and applications of Fe- and Mg-based nanomaterials from Victorian brown coal fly ash. The ideas, development and writing up of all the papers in the thesis were the principal responsibility of myself, the student, working within the Department of Chemical Engineering under the supervision of Lian Zhang.

The inclusion of co-authors reflects the fact that the work came from active collaboration between researchers and acknowledges input into team-based research.

In the case of chapters 3, 4 and 5, my contribution to the work involved the following:

| Thesis Chapter | Publication title | Status | Nature and % of student contribution | Co-author name(s) Nature and % of Co-author's contribution* | Co-author(s), Monash student |
|---|---|---|---|---|---|
| 3 | Coal Waste to Two-Dimensional Materials: Fabrication of $\alpha$−$Fe_2O_3$ Nanosheets and MgO Nanosheets from Brown Coal Fly Ash | Published | 88% Concept, experimental work and writing | 1) Tahereh Hosseini, Experimental setup, 2%<br>2) Xiwang Zhang, Suggestions, 2%<br>3) Yue Liu, Suggestions, 2%<br>4) Huanting Wang, Suggestions, 1%<br>5) Lian Zhang, Suggestions 5% | No<br>No<br>No<br>No<br>No |
| 4 | Synthesis of *in-situ* $Al^{3+}$-defected iron oxide nanoflakes from coal ash: A detailed study on the structure, evolution mechanism and application to water remediation | Published | 83% Concept, experimental work and writing | 1) Cheng Liu, Experimental setup, 2%<br>2) Jun Lu, Suggestions, 2%<br>3) Meipeng Jian, Suggestions, 1%<br>4) Xiaoyi Hu, Suggestions, 1%<br>5) Song Zhou, Suggestions 1%<br>6) Tahereh Hosseini, Suggestions 1%<br>7) Barbara Etschmann, Suggestions, 2%<br>8) Xiwang Zhang, Suggestions, 1%<br>9) Huanting Wang, | Yes<br>No<br>No<br>Yes<br>No<br>No<br>No<br>No<br>No |

| | | | | | |
|---|---|---|---|---|---|
| | | | | Suggestions, 1%<br>10) Lian Zhang,<br>Suggestions 5% | No |
| 5 | Synthesis of (111) Facet-Engineered MgO Nanosheet from Coal Fly Ash and Its Superior Catalytic Performance for High-Temperature Water Gas Shift Reaction | Published | 85% Concept, experimental work and writing | 1) Jianghao Zhang, Experimental setup, 2%<br>2) Song Zhou, Suggestions, 1%<br>3) Qianqian Wang, Suggestions, 2%<br>4) Jun Lu, 1%<br>5) Yue Liu, 1%<br>6) Cheng Liu, 1%<br>7) Yong Wang, 1%<br>8) Huanting Wang, 1%<br>9) Lian Zhang,<br>Suggestions 5% | No<br>No<br>No<br>No<br>No<br>Yes<br>No<br>No |

I have renumbered sections of submitted or published papers in order to generate a consistent presentation within the thesis.

**Student signature**: **Date**:

The undersigned hereby certify that the above declaration correctly reflects the nature and extent of the student's and co-authors' contributions to this work.

**Main Supervisor signature**: **Date**:

## Acknowledgements

It has been almost 3 years and a half since I started my PhD. Time is really so fast. I still remember the first day I came to Australia and I was so lucky to get the chance to conduct my PhD project in Monash. Right now, I will finish this wonderful journey and it's important for me to express my sincere gratitude to the following people.

First of all, I would like to thank my main supervisor Prof. Lian Zhang for his support, patience, encouragement and guide. Without him, I will not complete my PhD successfully and this period will become a precious treasure in my life. Also, I want to thank Prof. Huanting Wang (my co-supervisor) and Prof. Xiwang Zhang for their suggestions and comments.

Secondly, the China Scholarship Council (CSC)-Monash PhD Scholarship and Monash top-up scholarship are acknowledged for the financial supports.

I want to thank many good friends in Monash and we enjoyed this happy time together. Tahereh, Baiqian, Song, Cheng, Tanvir, Vincent, Ali, Lei, Anthony, Qiaoqiao, Sasha and Yu, I was so lucky to meet and work with you in the same group. You will be my best friends forever. I also would like to acknowledge many colleagues from other groups, including Jun, Xiaoyi, Jian, Yue and Meipeng, thanks for your support and suggestions. Meanwhile, I want to thank all the staff in Chemical Engineering, especially Tracy Groves, Lilyanne Price, Kim Phu, Harry Bouwmeester, Gus Austin, and Ross Ellingham.

Finally, and most importantly, thanks to my dear wife-Huiling Liu for her love, understanding and support. Although we were separate these years, thanks God, love still makes us together. Also, I want to thank the staff and students in SINANO during my final year of overseas research due to the influence of COVID-19.

## List of Figures

### Chapter 1



### Chapter 2



### Chapter 3

## Chapter 4

orientations (inset: SAED of (a)), (b) High magnification TEM from (a), (c) The corresponding intensity profiles of the red box from (b), (d-i) and (d-ii) are two crystallized cases of single FAO nanoflake, (e-i) and (e-ii) are SAED of (d-i) and (d-ii), respectively, (f) From top to bottom: HAADF-STEM image of region characterization from (d), element mapping of Fe (green) and Al (red)

**Figure 4-4** XRD and XAS analysis of as-synthesized α-$Fe_2O_3$ products synthesized from BCFA. (a) A selected range of XRD patterns of $Fe_2O_3$ at the hydrothermal treatment duration of 8 h, 10 h, 20 h and 50 h (FAO nanoflakes), (b) Lattice parameters of a value, c value and cell volume of $Fe_2O_3$ calculated based on the Rietveld refinement method, (c) Fe K-edge XANES spectra of FAO nanoflakes and α-$Fe_2O_3$ reference, (d) The measured (solid line) and corresponding fitting curve (dashed line) of $k^3$-weighted EXAFS spectra of α-$Fe_2O_3$ products compared with α-$Fe_2O_3$ standard, (e) Schematic illustration of crystal defects formation process

**Figure 4-5** Adsorption properties of the fresh as-synthesized FAO nanoflakes. (a) Langmuir adsorption isotherms of Cr(VI), As(V), As(III), (b) Adsorption rate curves of Cr(VI), As(V), As(III), (c) Langmuir adsorption isotherm of Congo red, (d) Adsorption rate curves of Congo red. (In all the four figures, solid lines are for the FAO nanoflakes and dashed lines are for the standard α-$Fe_2O_3$ nanoparticles. In (c) and (d), inset is the molecule structure for Congo red with C (grey), H (white), N (blue), O (red) and S (yellow))

**Figure S4-1** Block flow diagram of the two-stage cross flow leaching of water-washed brown coal fly ash

**Figure S4-2** Concentrations of major cations from initial leachate

**Figure S4-3** (a) adsorption-desorption isotherm of as-synthesized FAO nanoflakes and pure α-$Fe_2O_3$ nanoparticles. (b) pore size distribution of as-synthesized FAO nanoflakes

**Figure S4-4** SEM images of hydrothermal products from brown coal fly ash at different

## Chapter 5

## Chapter 6

## List of Tables

## Chapter 2



## Chapter 3



## Chapter 4

## Chapter 5



## Chapter 6

## Abbreviations and Nomenclature

**Al** Aluminium

**As** Arsenic

**C** Carbon

**Ca** Calcium

**Cl** Chlorine

**Co** Cobalt

**CO** Carbon monoxide

**Cr** Chromium

**CR** Congo red

**Cu** Copper

**DRIFTS** Diffuse reflectance infrared Fourier transform spectroscopy

**EXAFS** Extended X-ray absorption fine structure spectroscopy

**Fe** iron

**H** Hydrogen

**He** Helium

**HCl** Hydrochloric

**ICP-OES** Inductively coupled plasma optical emission spectrometry

**MB** Methylene blue

**Mg** Magnesium

**Mn** Manganese

**MO** Methyl orange

**N** Nitrogen

**Na** Sodium

**O** Oxygen

**Pb** Lead

**S** Sulfur

**SAED** Selected area electron diffraction

**Si** Silica

**SEM** Scanning electron microscopy

**STEM** Scanning transmission electron microscopy

**TEM** Transmission Electron Microscopy

**TEY** Total electron yield

**Ti** Titanium

**TPR** Temperature programmed reduction

**WGSR** Water gas shift reaction

**XPS** X-ray photoelectron spectroscopy

**XRD** X-ray diffraction

**XRF** X-ray fluorescence

**XAS** X-ray absorption spectroscopy

**XANES** X-ray absorption near-edge spectroscopy

# Chapter 1 Introduction

## 1.1 Overview

Low-rank coal is more commonly referred to brown coal or sub-bituminous coal, which accounts for more than 50% of the world's coal reserves [1]. It is abundant in many countries such as USA, China, Australia, and Germany and hence offers an economically energy alternative to high-rank black coal (i.e. bituminous coal and anthracite) for electricity generation [2,3]. The use of low-rank coal is becoming significantly critical with the continuous depletion of high-rank bituminous coal. However, after the combustion of low-rank coal, large amount of coal fly ash is produced, most of which is however simply dumped into ash ponds. This hazardous ash waste poses potential threats to the air, soil, and even underground water while little is being used.

Conventionally, coal fly ash is used as a low-value additive into the cement or concrete [4], geotechnology, road [5] and agriculture [6]. However, these traditional applications are usually limited to high-rank fly ash, which is abundant in Al and Si. For the ash derived from a low-rank coal such as brown coal, it is implausible to utilize it in these applications, due to the shortage of these two elements in the respective ashes. For example, brown coal fly ash in the state of Victoria in Australia contains relatively high concentrations of metallic cations, particularly $Fe^{3+}$ and $Mg^{2+}$ [7]. One promising methodology is to extract these valuable elements out of fly ash and use them as raw feedstock to synthesize value-added products.

Through a hydrometallurgical leaching process, previous works have extracted Fe or Mg from fly ash while with low extraction yields [8-10]. Based on this special brown coal fly ash, it is found that there is a need for further research to develop an efficient extraction process which breaks the structure of the magnesium ferrite inverse-spinels to release $Fe^{3+}$ and $Mg^{2+}$. The main challenge is that $NH_4Cl$ is too weak to cleave the strong affinity between Mg and Fe

within the $MgFe_2O_4$ matrix, which would otherwise still remain in the final residue and has to be returned as a waste to the fly ash pond. In light of this, a more efficient leaching method including the improvement of both leaching agents and steps is necessary.

For the extracted $Mg^{2+}$, it can be used for the synthesis for widely used nano-$Mg(OH)_2$ or MgO. Previously, Mg-bearing nanomaterials usually synthesized from pure chemicals such as $Mg(NO_3)_2 \cdot 6H_2O$ [11], $MgCl_2$ [12] and $MgSO_4$ [11], which seriously increases the production cost and thus limits the wider use of these materials. Another thing is that the directional growth of $Mg(OH)_2$ or MgO is always complex and energy-intensive, it is still challenging to develop a facile growth method for the synthesis of a well-defined facet-dominant MgO/$Mg(OH)_2$. For the extracted $Fe^{3+}$, it can also be used for the fabrication for nano-α-$Fe_2O_3$, γ-$Fe_2O_3$, $Fe_3O_4$ and FeOOH. Similarly, these nanomaterials are commonly synthesized from pure chemicals such as $FeCl_3 \cdot 6H_2O$ [13], and $Fe_2(SO_4)_3 \cdot 7H_2O$ [14], which will also increase the cost of production process and subsequent applications.

In this PhD project, a high-efficient extraction strategy of two-step leaching method was employed for cleaving the inverse-spinel structure of $MgFe_2O_4$ to further increase the extraction yields of Fe and Mg out of brown coal fly ash. The resultant leachate then worked as a Mg-source and Fe-source for the synthesis of nanosized α-$Fe_2O_3$, $Mg(OH)_2$ and MgO. As for the synthesized α-$Fe_2O_3$, the effect of $Al^{3+}$ on its growth process, crystal structure, atomic environment and adsorption performance (towards $As^{3+}$, $As^{5+}$, $Cr^{6+}$ and Congo red) were investigated. In addition, various nanostructured α-$Fe_2O_3$ materials were synthesized from coal fly ash and were used as catalysts for WGSR. In terms of the nano-$Mg(OH)_2$, to gain an atomic insight into the growth mechanism under hydrothermal conditions, density functional theory calculations were conducted and the resultant MgO-$Fe^{3+}$ nanosheet with different exposed facet

were employed as high-performance catalysts in the WGSR.

To achieve the project aims, a number of advanced experimental, analytical and modelling techniques have been used. First of all, experiments were conducted first to extract the Fe and Mg from brown coal fly ash. To obtain high extraction yields, first step 60 °C- second step 60 °C leaching method was used. In parallel, first step (20, 40 and 60 °C)-second step 60 °C were also conducted to optimize the leaching conditions. Then multistep precipitation process was conducted to remove impurities including $Al^{3+}$ and $Ca^{2+}$ to achieve high-purity $Fe_2O_3$/$Mg(OH)_2$/MgO nanomaterials. In the second part of this project, the evolution of morphologies, lattice parameters, crystal structures and atomic environments were investigated during the hydrothermal synthesis of $Al^{3+}$-contained α-$Fe_2O_3$ nanomaterials. In addition, adsorption tests have been conducted extensively for some typical heavy metal ions and inorganic dyes in waste water, including Cr(VI), As(V), As(III) and Congo red. In the third part of this project, the synthesis of (001) facet rich $Mg(OH)_2$ nanosheets was achieved and the two-dimensional $Mg(OH)_2$ was then loaded with $Fe^{3+}$ to catalyze the industrial water gas shift reaction to produce hydrogen. In the fourth part of this project, various nanostructured iron oxides were synthesized and the catalysis performance of WGSR was evaluated, the impurity enhanced mechanism was proposed to elucidate the boosted hydrogen production.

The expected outcomes from this project include the determination of the synthesis conditions of Fe- and Mg-based nanomaterials from brown coal fly ash. The high-efficiency and moderate-operation leaching methods which can extract Fe and Mg out of the Victorian brown coal fly ash and the multi-step precipitation process will also be important to industry to obtain high quantity and high purity products. The completion of this project is expected to address the global environmental challenge facing the industrial solid waste: how to utilize the coal fly

ash waste in a value-added strategy. The low-rank coal is the main local fuel for the power generation plant or industry boiler, which will produce large amount of coal fly ash after the combustion. The disposal of this coal fly ash will cause land occupation, financial burden and environmental risk. This project is therefore crucial for the power generation plants and industrial boilers burning low-rank coal that are suffering from the accumulation caused by coal fly ash. Additionally, this research on the synthesis of Fe- and Mg-based nanomaterials will be essential for the development of low-coat production of these nanomaterials, which is a pivotal trend in sustainable development.

## 1.2 Research aims

This PhD project aims to develop an efficient, cost-effective and environmentally friendly process which can efficiently extract Mg and Fe out of fly ash. After that, the growth mechanisms of as-synthesized nanomaterials will be clarified and their applications to water treatment and WGSR will be conducted. Through experimental investigations and micro characterizations, this PhD project is planned to cover the following specific research targets with the main chapters outline shown in **Figure 1-1**:

1. To conduct experimental investigations on further optimization of the conditions for cleaving the stable crystal inverse-spinel structure $MgFe_2O_4$ to increase extraction yields of Mg and Fe;
2. To determine the optimum conditions for the removal of impurities ($Al^{3+}$ and $Ca^{2+}$) in the precipitation processes to obtain high-purity nanosized $Fe_2O_3$/$Mg(OH)_2$/MgO;
3. To investigate the effect of $Al^{3+}$ on α-$Fe_2O_3$ nanomaterials in terms of morphologies, lattice parameters, crystal structures and atomic environments;

4. To investigate the synthetic conditions of (001) facet rich $Mg(OH)_2$ under hydrothermal conditions;
5. To test the adsorption performance towards $As^{3+}$, $As^{5+}$, $Cr^{6+}$ and Congo red of the $Al^{3+}$ doped α-$Fe_2O_3$ nanomaterials.
6. To test the catalytic performance towards the water gas shift reaction of the nanosized $Mg(OH)_2$ loading with $Fe^{3+}$.

## 1.3 Thesis outline

**Chapter 1** gives an overview of the research area and highlights the specific research aims.

**Chapter 2** is a review of the literature, specifically focusing on the leaching methods of coal fly ash as well as the synthesis and applications of Mg- and Fe-bearing nanomaterials. This review ultimately led to the clarification of research gaps that established the fundament of this PhD project.

**Chapter 3** gives a detailed study on the extraction and fabrication of high-purity two-dimensional α-$Fe_2O_3$ nanosheets and MgO nanosheets from the Victorian brown coal fly ash. This chapter aimed to identify the most efficient leaching process to extract $Fe^{3+}$ and $Mg^{2+}$ out of fly ash and use them as feedstocks to synthesize the two-dimensional α-$Fe_2O_3$ nanosheets and MgO nanosheets. To achieve this, A two-stage counter-current solid−liquid extraction method was first employed under the mild conditions of 25−60 °C and atmospheric pressure to selectively extract $Fe^{3+}$ and $Mg^{2+}$, which were then precipitated out separately upon gradual addition of NaOH and subsequent hydrothermal treatment. Finally, 2-D nanosized α-$Fe_2O_3$ nanosheet was obtained with a lamellar morphology, while the synthesized $Mg(OH)_2$ precursor undertook an extra multistep calcination to convert into the respective 2-D MgO nanosheet.

This chapter has been published as a journal article: **Binbin Qian**, Tahereh Hosseini, Xiwang Zhang, Yue Liu, Huanting Wang and Lian Zhang*, Coal Waste to Two-Dimensional Materials: Fabrication of α-$Fe_2O_3$ Nanosheets and MgO Nanosheets from Brown Coal Fly Ash, ACS Sustainable Chemistry & Engineering, 2018, 6(12), 15982-15987.

**Chapter 4** explores the effect of $Al^{3+}$-defect on the structure and performance of α-$Fe_2O_3$. This chapter found that $Fe_{1.72}Al_{0.28}O_3$ nanoflakes were successfully synthesized from the Victorian brown coal fly ash. The obtained nanoflakes possess a round-shape morphology with a diameter of around 300 nm and 50 nm in thickness. $Al^{3+}$ serves as the disordered defects on the hematite surface, leading to decreased crystal parameters for hematite, the formation of a compact first shell and a reduced periodical symmetry for the central cation $Fe^{3+}$. The defects were also found to significantly improve the adsorption capacity of the resultant nanoflake for Cr(VI), As(V), As(III) and Congo red in waste water.

Part of this chapter has been published as a journal article: **Binbin Qian**, Cheng Liu, Jun Lu, Meipeng Jian, Xiaoyi Hu, Song Zhou, Barbara Etschmann, Xiwang Zhang, Huanting Wang, Lian Zhang*, Synthesis of in-situ $Al^{3+}$-defected iron oxide nanoflakes from coal ash: A detailed study on the structure, evolution mechanism and application to water remediation, Journal of Hazardous Materials, 2020, 395, 122696.

**Chapter 5** studies the growth of nanosized $Mg(OH)_2$ and application in the HT-WGSR. This chapter concluded that a well-defined (111)-facet-dominant MgO, and its superior catalytic performance upon the loading of $Fe^{3+}$ for hydrogen production from HT-WGSR can be achieved, the (001)-facet-rich $Mg(OH)_2$ nanosheet can be firstly synthesized from fly ash by leaching, precipitation and ethanol-mediated hydrothermal process in sequence, followed by subsequent loading of 30 *wt%* $Fe^{3+}$ via incipient wetness impregnation and in-situ

transformation to MgO(111) during the HT-WGSR. The resultant nanosheet from fly ash bears a specific surface area of around 100 $m^2/g$, and an averaged aspect ratio of 11.8, as opposed to only 1.5 for the commercial $Mg(OH)_2$ and the one synthesized without the mediation of ethanol during hydrothermal processing. The fly ash derived $Mg(OH)_2$ nanosheet was subsequently loaded with 30 *wt%* $Fe^{3+}$ (as $Fe_2O_3$) via incipient wetness impregnation and calcined into a (111) facet-rich MgO, which was proved for a superior catalysis performance for high-temperature water gas shift reaction (HT-WGSR). At the reaction temperatures of 400-450 °C, the CO conversion was increased by a factor of two compared to a reference catalyst consisting of identical Fe loading on a $Mg(OH)_2$ support synthesized without ethanol, and by a factor of seven compared to a nano-sized hematite catalyst synthesized from same hydrothermal process without ethanol addition. This is mainly due to the abundant oxygen vacancy on the (111) facet of the MgO nanosheet support, which improved the reducibility of $Fe^{3+}$ as well as facilitated the formation of intermediate formates that in turn promoted the forward reaction.

This chapter has been under review in a journal article: **Binbin Qian**, Jianghao Zhang, Song Zhou, Jun Lu, Yue Liu, Cheng Liu, Yong Wang, Huanting Wang, Lian Zhang*, Synthesis of (111) Facet-Engineered MgO Nanosheet from Coal Fly Ash and Its Superior Catalytic Performance for High-Temperature Water Gas Shift Reaction, Applied Catalysis A: General, under review.

**Chapter 6** reveals the synthesis of two nanostructured iron oxides with various morphologies from the Victorian brown coal fly ash and the formation of defective metal oxides ($MgO_x$, $AlO_x$) /$Fe_3O_4$ catalyst during the HT-WGSR. This chapter confirmed that nanosized α-$Fe_2O_3$ with two morphologies including irregular nanosheet and round nanoflake were synthesized with some inherent impurities in them. They were also used as HT-WGSR catalysts and the irregular α-$Fe_2O_3$ nanosheet exhibited the most hydrogen production. During the HT-WGSR, impurities

including Al and Mg that remained in the iron oxides will migrate out of active $Fe_3O_4$, forming a thin layer of Mg-Al-$O_x$. The formed nanolayer will spatially encapsulate and isolate the active $Fe_3O_4$ nanoparticles from sintering. In addition, this thin layer is 2-3 nm and 5-6 nm for the irregular nanoflake and round nanoflake, respectively. However, for the pure hematite, those active $Fe_3O_4$ nanoparticles are fully exposed, causing its sintering during HT-WGSR.

This chapter has been in draft: **Binbin Qian**, Jianghao Zhang, Song Zhou, Cheng Liu, Yong Wang, Huanting Wang, Lian Zhang*, Synthesis of Magnetite with a Surrounded Core-Shell Structure from Fly Ash Waste and Its Superior Catalysis Performance for High-Temperature Water-Gas Shift Reaction.

**Chapter 7** gives the conclusions for this PhD project and recommendations for future work related to the methods for low-rank coal fly ash leaching and large-scale applications for the Mg- and Fe-bearing nanomaterials.

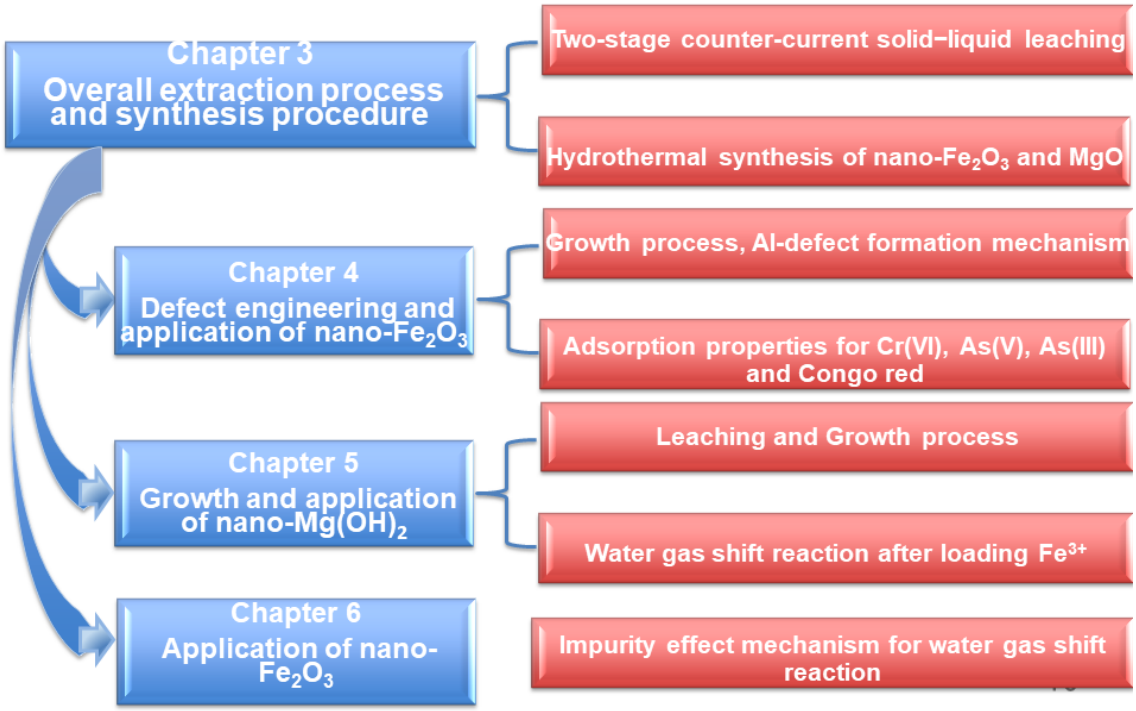


**Figure 1-1** Thesis outline summary

## Reference

[1] Zhou, S.; Hosseini, T.; Zhang, X.; Haque, N.; Zhang, L. Selective removal of sodium and calcium from low-rank coal–Process integration, simulation and techno-economic evaluation. *Fuel Processing Technology* **2018**, 172, 13-28.

[2] Low, F.; De Girolamo, A.; Wu, X.; Dai, B.; Zhang, L. Inhibition of lignite ash slagging and fouling upon the use of a silica-based additive in an industrial pulverised coal-fired boiler: Part 3–Partitioning of trace elements. *Fuel* **2015**, 139, 746-756.

[3] Wu, X.; Zhang, X.; Yan, K.; Chen, N.; Zhang, J.; Xu, X.; Dai, B.; Zhang, J.; Zhang, L. Ash deposition and slagging behavior of Chinese Xinjiang high-alkali coal in 3 MWth pilot-scale combustion test. *Fuel* **2016**, 181, 1191-1202.

[4] Palomo, A.; Grutzeck, M. W.; Blanco, M. T. Alkali-activated fly ashes: A cement for the future. *Cement and Concrete Research* **1999**, 29, 1323-1329.

[5] Rogbeck, J.; Hartlén, J. Ash gravel -A material for recycling. *Waste Management* **1996**, 16, 109-112.

[6] Pandey, V. C.; Singh, N. Impact of fly ash incorporation in soil systems. *Agriculture Ecosystems & Environment* **2010**, 136, 16-27.

[7] Choo, T. K.; Song, Y.; Zhang L.; Selomulya C.; Zhang L. Mechanisms Underpinning the Mobilization of Iron and Magnesium Cations from Victorian Brown Coal Fly Ash. *Energy & Fuels* **2014**, 28, 4051-4061.

[8] Sahoo, P. K.; Kim, K.; Powell, M. A.; Equeenuddin, S. M. Recovery of metals and other beneficial products from coal fly ash: a sustainable approach for fly ash management. *International Journal of Coal Science and Technology* **2016**, 3, 267−283.

[9] Valeev, D.; Mikhailova, A.; Atmadzhidi, A. Kinetics of Iron Extraction from Coal Fly Ash by Hydrochloric Acid Leaching. *Metals* **2018**, 8 (7), 533.

[10] Hosseini, T.; Selomulya, C.; Haque, N.; Zhang, L. Indirect carbonation of Victorian brown

coal fly ash for $CO_2$ sequestration: multiple-cycle leaching-carbonation and magnesium leaching kinetic modelling. *Energy Fuels* **2014**, 28, 6481−6493.

[11] Ding, Y.; Zhang, G.; Wu, H.; Hai, B.; Wang, L.; Qian, Y. Nanoscale Magnesium Hydroxide and Magnesium Oxide Powders: Control over Size, Shape, and Structure via Hydrothermal Synthesis. *Chemistry of Materials* **2001**, 13, 435−440.

[12] Henrist, C.; Mathieu, J. P.; Vogels, C.; Rulmont, A.; Cloots, R. Morphological study of magnesium hydroxide nanoparticles precipitated in dilute aqueous solution. *Journal of Crystal Growth* **2003**, 249, 321− 330.

[13] Hao, H.; Sun, D.; Xu, Y.; Liu, P.; Zhang, G.; Sun, Y.; Gao, D. Hematite nanoplates: Controllable synthesis, gas sensing, photocatalytic and magnetic properties. *Journal of Colloid and Interface Science* **2016**, 462, 315−324.

[14] Tadic, M.; Panjan, M.; Damnjanovic, V.; Milosevic, I. Magnetic properties of hematite (α-$Fe_2O_3$) nanoparticles prepared by hydrothermal synthesis method. *Applied Surface Science* **2014**, 320, 183−187.

# Chapter 2 Literature Review

## Scope of literature review

This literature review covers the motivation for this work on the coal fly ash. The importance of leaching methods is presented first, followed by the current synthesis for nanosized α-$Fe_2O_3$, $Mg(OH)_2$ and MgO. Next, related applications for the above nanomaterials are addressed, especially the water treatment and WGSR are well reviewed.

## 2.1 Fly Ash: An Industry Byproduct

Since 1920s, coal combustion for power generation has become predominant worldwide and million tonnes of ash have been produced. Currently, the total production of coal ash all over the world is around 750 million tonnes annually, in which fly ash occupies 75-80% of the total [1]. With the rapid development of the society, the demand of energy is much higher than it was in the previous days. Therefore, the amount of released fly ash has been increasing these years throughout the world. How to properly deal with this tremendous amount of fly ash an urgent issue.

Fly ash is constituted by fine particles and powders, and most of the shape is sphere, either solid or hollow. The chemical properties of fly ash are influenced by many factors such as the coals being combusted and the conditions used for handling and storage while the principal components of fly ash are silica, alumina, iron oxide, calcium oxide and magnesium oxide with unburnt carbon. **Table 2-1** shows the normal range of chemical composition for three kinds of fly ash, bituminous, sub-bituminous and lignite [1]. It is clear that sub-bituminous and lignite coal fly ash have more CaO and sulphate compounds content and less LOI compared with bituminous coal fly ash. Based on oxides content in fly ash, American Society for Testing

Materials (ASTM) has defined that class F fly ash contains more than 70 *wt%* $SiO_2$+$Al_2O_3$+$Fe_2O_3$ and low amount of CaO while class C fly ash has 50-70 *wt%* of $SiO_2$+$Al_2O_3$+$Fe_2O_3$ with high CaO. The difference of CaO content basically derives from the coal. The Class C fly ash with high content calcium is usually produced from the combustion of low-rank coals such as sub-bituminous and lignite. As for the low content calcium Class F fly ash, it is normally produced from the burning of high-rank coal such as bituminous. **Table 2-1** shows the major elements of fly ash. It is clear that the most abundant elements in fly ash are usually Si, Al, Fe, Ca and Mg. In addition, there are still some trace elements such as As, B, Ba, Be, Cr, Mn, Cu, Co and others [2]. If not properly dealt with, these elements will have great influence on the environment [3, 4].

In summary, fly ash will definitely raise environmental concerns on our social lives and due to limited utilization and application, around half of the worldwide produced fly ash will be simply dumped by landfilling. These hazardous pollutants will contaminate the underground water sources and soil due to uncontrolled leaching process, which is an important environmental problem nowadays.

**Table 2-1** Chemical components of three kinds of fly ash [1]

| Component (*wt%*) | Bituminous | Sub-bituminous | Lignite |
|---|---|---|---|
| $SiO_2$ | 20-60 | 40-60 | 15-45 |
| $Al_2O_3$ | 5-35 | 20-30 | 10-25 |
| $Fe_2O_3$ | 10-40 | 4-10 | 4-15 |
| CaO | 1-12 | 5-30 | 15-40 |
| MgO | 0-5 | 1-6 | 3-10 |

| | | | |
|---|---|---|---|
| $SO_3$ | 0-4 | 0-2 | 0-10 |
| $Na_2O$ | 0-4 | 0-2 | 0-6 |
| $K_2O$ | 0-3 | 0-4 | 0-4 |
| LOI | 0-15 | 0-3 | 0-5 |

## 2.2 Fly Ash Utilization

The reason for increasing the amount of fly ash to get further utilization is that it is really a kind of industrial waste. Another is that fly ash is also a kind of potential resource. **Figure 2-1** illustrates the modes of application for fly ash in the regions of China, India and Europe.

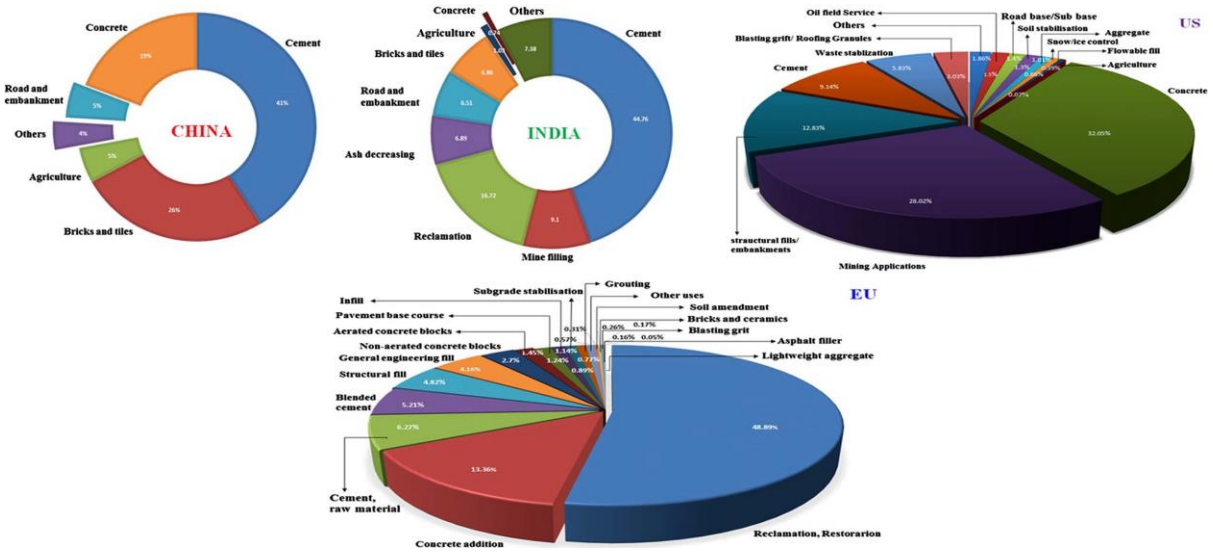


**Figure 2-1** Modes of fly ash applications in China, India, US and EU [5].

### 2.2.1 Physical Method

Utilization of fly ash physically means that the fly ash is used directly in some areas without or with little further treatment. A traditional application of this method is fly ash used in construction materials such as cement clinker [6], concrete [7], roadway or pavement, highway base and embankment [8]. Adsorbent is another large area that fly ash can be directly used

because it contains high specific surface area materials such as unburnt carbon. In the field of flue gas cleaning, fly ash can be used for the removal of $SO_x$ [9], $NO_x$ [10], mercury [4] and gaseous organics [11]. In the area of wastewater treatment, fly ash can be a simple and effective resource for the removal of heavy metals such as $Zn^{2+}$, $Cd^{2+}$, $Pb^{2+}$, $Cu^{2+}$, $Ni^{2+}$, $Cr^{3+}$ , $Cr^{6+}$, $Hg^{2+}$, $As^{3+}$, and $As^{5+}$ [1]; for the inorganic components such as phosphate [12], fluoride [13] and boron [14]; for the organic compounds such as phenolic, pesticides and some others [15]; for the dyes such as azo, thiazine, xanthene, arylmethane, and others [16]. In addition to above wide applications, fly ash can also be used in agriculture [17], mine back fill [18], glass-ceramic sintered raw material [19] and catalyst [20].

### 2.2.2 Chemical Method

In addition to the above applications, elemental recovery is another area for fly ash application. As discussed in section **2.1**, fly ash is traditionally rich is Al, Si, Fe, Mg and Ca. To extract these elements from fly ash, there are some technologies that can recover metals from fly ash: pyrometallurgy, hydrometallurgy, and bio-hydrometallurgy. Among them, hydrometallurgy is a methodology in which chemical reactions are carried out in an organic leaching agent or organic solution for the recovery of elements. During the hydrometallurgy, leaching process is the most important part of the whole recovery and different leaching methods aimed at various fly ashes will be introduced.

Alkaline Leaching:

The alkaline (base) leaching is commonly used for the recovery of the metals including Ga [21], V [21], Si [22], Pb [23] and Zn [24] out of fly ash. Font [21] recovered Ga via NaOH-based extraction method from gasification fly ash and concluded that, when optimal conditions were fixed at 25 °C, NaOH 0.7-1 M, NaOH/FA ratio of 5 L/Kg and reaction time of 6 h, the Ga

yields were 60-86%. Some nanosized materials can also be synthesized from fly ash. For example, Yan [22] prepared nanosilica from coal fly ash (as shown in **Figure 2-2**) under the conditions of 30 min at 110 °C in 25 *wt %* NaOH solution, and the L/S ratio of 1.5. The extraction yield of silica could reach up to 46.62% and nanosilica has a purity of 99.35%, surface area of 1157 $m^2/g$ and pore volume 0.95 $cm^3/g$. In summary, alkaline leaching method can extract some elements from fly ash while this method is not applicable to most metal elements.

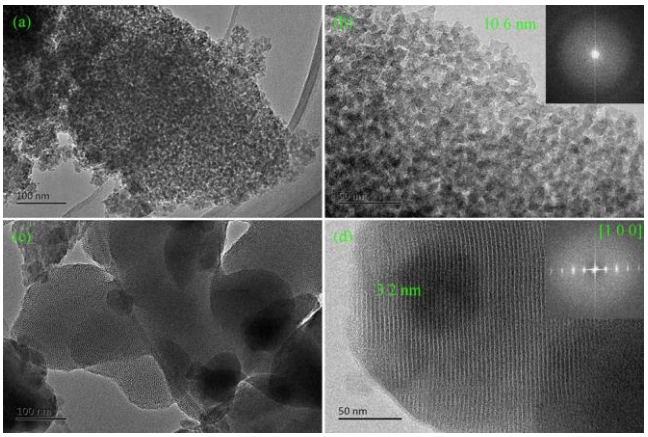


**Figure 2-2** TEM images of nano silica [22]

Acid Leaching:

The acid leaching method is widely used in the elemental recovery from fly ash. A lot of metal oxides/hydroxide/carbonate can dissolve in acid solutions, and hence extracting metals from fly ash through acid leaching is well developed. Elements that can be extracted include Mg [25, 26, 28, 34-39], Al [27, 36], Fe [25, 26, 28, 34-39], even heavy elements [29-31] and rare earth elements [32,33]. Particularly, Mg and Fe extractions have attracted much attention because the two elements are fundamental raw materials in industry. **Table 2-2** summaries the leaching methods for Mg and Fe recovery through acid leaching with various conditions. It is clear that for these leaching methods, strong acids such as HCl, $H_2SO_4$ or $HNO_3$ are usually used as leaching agents. Leaching temperature is a very important factor to accelerate the leaching rate and extraction yield for both Mg and Fe and normally it is in the range of 25-80 °C. However,

if a super-high extraction yield is obtained, harsh conditions are necessary. For example, L/S ratio: 20 ml/g, temperature: 106 °C and time 120 min for an extraction yield almost 100% of Fe; L/S ratio: 10 ml/g and leaching time 14 d for an extraction yield 94.8% of Mg. A two-stage leaching method was used and the extraction yields for Mg and Fe were 63% and 71%, respectively. Although more Fe and Mg have been extracted out, there is still considerable amount of Fe- or Mg-bearing minerals remained in the final residual [25]. However, without those harsh conditions and if single step and moderate leaching conditions are employed, the extraction yields for Fe and Mg are only 9-51% and 6-69%, respectively.

**Table 2-2** Leaching method for Mg and Fe extraction

| Type of fly ash | Leaching agent | Conditions | Yield/% | Reference | Supplement |
|---|---|---|---|---|---|
| Brown Coal Fly Ash | Hydrochloric acid (HCl) | Single stage, L/S ratio: 6.67 ml/g, stirring speed: 350 rpm, temperature: 20, 70 and 100 °C, HCl concentration: 2 M, time: 1-60 min | Maximum Fe%= 42% and maximum Mg%= 53% | [25] | L/S is Liquid/Solid |
| | | Single stage, L/S ratio: 6.67 ml/g, stirring speed: 350 rpm, temperature: 20-200 °C, HCl concentration: 2 M, time: 5 min | Maximum Fe%= 36% and maximum Mg%= 50% | | |
| | | Single stage, L/S ratio: 4-10 ml/g, stirring speed: 350 rpm, temperature: 20 °C, HCl concentration: 2 M, time: 1 min | Maximum Fe%= 18% and maximum Mg%= 39% | | |

| | | | | | |
|---|---|---|---|---|---|
| | | Single stage, L/S ratio: 6.67 ml/g, stirring speed: 350 rpm, temperature: 20 °C, HCl concentration: 2-6 M, time: 1 min | Maximum Fe%= 20% and maximum Mg%= 35% | | |
| | | Two stage: First stage, L/S ratio: 6.67 ml/g, stirring speed: 350 rpm, temperature: 20 °C, HCl concentration: 2 M, time: 60 min. Second stage, L/S ratio: 6.67 ml/g, stirring speed: 350 rpm, temperature: 20, 100 and 200 °C, HCl concentration: 2 M, time: 1-35 min. | First stage: Fe%= 11% and maximum Mg%= 6%. Second stage: Maximum Fe%= 52% and maximum Mg%= 50%. Overall: Maximum Fe%= 63% and maximum Mg%= 71%. | | |

| | | | | | |
|---|---|---|---|---|---|
| | | Single stage, L/S ratio: 6 ml/g, stirring speed: 350 rpm, temperature: 25 °C, HCl concentration: 1 M, time: 30 min | Maximum Fe%= 18% and maximum Mg%= 41% | [26] | |
| | HCl and ammonia chloride ($NH_4Cl$) | Single stage, L/S ratio: 6 ml/g, stirring speed: 350 rpm, temperature: 80 °C, HCl concentration: 1 M, $NH_4Cl$: 4 M and time: 30 min, pH<4.5 | Fe%= 9% and maximum Mg%= 49%. | | |
| Weathered brown coal fly ash | HCl | Single stage, L/S ratio: 6 ml/g, stirring speed: 350 rpm, temperature: 25 °C, HCl concentration: 1 M, time: 30 min | Fe%= 21% and maximum Mg%= 42%. | | |
| | | Single stage, L/S ratio: 6 ml/g, stirring speed: 350 rpm, temperature: 25-80 °C, HCl | Maximum Fe%= 26% and maximum Mg%= | | |

| | | | | | |
|---|---|---|---|---|---|
| | | concentration: 1 M, time: 30 min | 45% | | |
| | HCl and $NH_4Cl$ | Single stage, L/S ratio: 6 ml/g, stirring speed: 350 rpm, temperature: 80 °C, HCl concentration: 1 M, $NH_4Cl$: 4 M and time: 30-60 min, pH<4.5 | Maximum Fe%= 29% and maximum Mg%= 65% | | |
| | | Single stage, L/S ratio: 6 ml/g, stirring speed: 350 rpm, temperature: 25-80 °C, HCl concentration: 1 M, $NH_4Cl$: 4 M and time: 40 min, pH<4.5 | Maximum Fe%= 21% and maximum Mg%= 69% | | |
| | HCl | Single stage, L/S ratio: 6 ml/g, stirring speed: 350 rpm, temperature: 25-80 °C, HCl concentration: 1 M, $NH_4Cl$: 4 | Maximum Fe%= 28% and maximum Mg%= 45% | | |

| | | | | | |
|---|---|---|---|---|---|
| | | M and time: 30 min | | | |
| Municipal Solid Waste Incineration fly ash | Nitric acid ($HNO_3$), sulphuric acid ($H_2SO_4$), citric acid ($C_6H_8O_7$), oxalic acid ($C_2H_2O_4$) and gluconic acid ($C_6H_{12}O_7$) | Single stage, W/V ratio: 1%, stirring speed: 120 rpm, temperature: 30 °C, acid concentration: 0.1 and 0.5 M, time: 48 h | Fe%= 30%, 23%, 26%, 51%, 18% | [34] | Acid concentration: 0.1 M, W/V: Weight/Volume |
| | | | Fe%= 31%, 30%, 20%, 52%, 30% | | Acid concentration: 0.15 M |
| | $H_2SO_4$ | Single stage, stirring speed: 320 rpm, airflow rate: 1 l/min, temperature: 25 °C, $H_2SO_4$ concentration: 4 M, and time: 30 min | Fe%= 91% and maximum Mg%= 99% | [35] | Raw FA contains 1.70% MgO and 0.79% $Fe_2O_3$. The FA (10% v/v) and distilled water |

| | | | | | |
|---|---|---|---|---|---|
| | | | | | (90% v/v) were treated with $H_2SO_4$, final pH: 1 |
| | HCl, $HNO_3$, $H_2SO_4$ | Single stage, temperature: 25 °C, and time: 24 h | Fe%=63%, 48% and 81%, Mg%= 64%, 58% and 82% | | 3 M HCl L/S ratio: 5 ml/g, 3 M $HNO_3$ L/S ratio: 5 ml/g and 1.5 $H_2SO_4$ M L/S ratio: 10 |
| Coal Fly Ash | HCl and $H_2SO_4$ | Two stage: First stage, stirring speed: 200 rpm, temperature: 25 °C, HCl concentration: 37%, time: 24 h. Second stage, stirring speed: 200 rpm, temperature: 25 °C, $H_2SO_4$ concentration: 2 M, time: 48 h and 12 d | Overall: Maximum Fe%= 19% | [36] | First step: Using 300 g FA and treated at pH 4, 3 and 2. The FA was dispersed in 2 L deionized water, and the pH adjustment was achieved by adding |

| | | | | | |
|---|---|---|---|---|---|
| | | | | | HCl. Second step, leaching with $H_2SO_4$ at fxed pH 1.5 |
| Coal Mining Waste | HCl | Single stage, L/S ratio: 20 ml/g, stirring speed: 500 rpm, temperature: 40-106 °C, HCl concentration: 3, 4, 5, 6, and 7 mol/L, and time: 1-120 min | Maximum Fe%= 100% | [37] | |
| Coal Fly Ash | $HNO_3$ | Single stage, L/S ratio: 16 ml/g, temperature: 25 °C, $HNO_3$ concentration: 0.5 mol/L, and time: 20 min | Fe%= 4.5% and Mg%= 75% | [38] | Ferromagnetic particles were separated from the bulk fly ash between the poles of a small electromagnet operating at a magnetic flux |

| | | | | | |
|---|---|---|---|---|---|
| | | | | | density of ~ 1.4 Tesla. |
| | $H_2SO_4$ | Single stage, L/S ratio: 10 ml/g, temperature: 25 °C, $H_2SO_4$ concentration: 1 M, time: 14 d | Maximum Fe%= 83.1% and maximum Mg%= 94.8% | [39] | 100 g of FA was mixed with 900 g of deionized water. The slurry was stirred and 1 M $H_2SO_4$ was added to bring the pH to 1.0. |

## 2.3 Synthesis of $Mg(OH)_2$ Nano-Particles

Magnesium hydroxide ($Mg(OH)_2$), also known as brucite in mineralogy, is conventionally used as an ecological and environment-friendly flame retardant by virtue of its high decomposition temperature and good thermal stability to undergo endothermic dehydration in fire conditions while with no evolution of hazardous by-products [40]. In addition, it has been found to exhibit promising $CO_2$ adsorption properties due to its mineral carbonation process [41], an important precursor of preparing MgO and water environment remediation [42]. Recently, as the rapid progress in nanotechnology, traditional materials have been brought into a new world pregnant with technological innovation and industry transformation. Identically, it broadens the applications of nanosized $Mg(OH)_2$ in many areas such as medicine [43], catalyst [44], conservation of cultural heritage [45], antibacterial agents [46] and composite nanomaterials due to the special morphology such as laminated form which can be incorporated into other materials. In the meantime, different shapes of nano-$Mg(OH)_2$ have been obtained via different approaches, including the precipitation method [47], sol-gel method [48], hydrothermal reaction/modification [49], solvothermal modification [50], and others [51]. Amongst these methods, the hydrothermal method is more usually employed in practice than others since it is easy-operated and economically acceptable. **Table 2-3** summaries some of the previous works of $Mg(OH)_2$ preparation through hydrothermal method. It is clear that through hydrothermal treatment: temperature 50-180 °C and time 1.5-48 h, $Mg(OH)_2$ nanoparticles with the size less than 200 nm and a regular hexagonal shape are obtained. Without hydrothermal conditions while nanosized $Mg(OH)_2$ was obtained, some special conditions (very slow injection rate) must be used [56]. In addition, with the doping of surfactant such as ethylene diamine or polyethyleneglycol, various morphologies of nanosized $Mg(OH)_2$ such as nanorod or nanoneedle [52] can be synthesized. For example, Li [51] synthesized $Mg(OH)_2$ nanorods using Mg powder as starting the material and ethylene diamine as the template, ethylene

diamine acted as a bidentate ligand to form the relatively stable $Mg^{2+}$ complex and arranged to the structure shown in **Figure 2-3**. During hydrothermal process, $OH^-$ coordinated to the $Mg^{2+}$ complex and caused a 1D $Mg(OH)_2$ nanorod, which then condensed along with the gradual loss of the bidentate ethylene diamine ligands. After the attacks of $OH^-$, the bonds between $Mg^{2+}$ and N became weaker while $Mg^{2+}$ and $O^{2-}$ became stronger, finally making $Mg^{2+}$ and N separate from each other and resulting a 1 D $Mg(OH)_2$ nanorod structure.

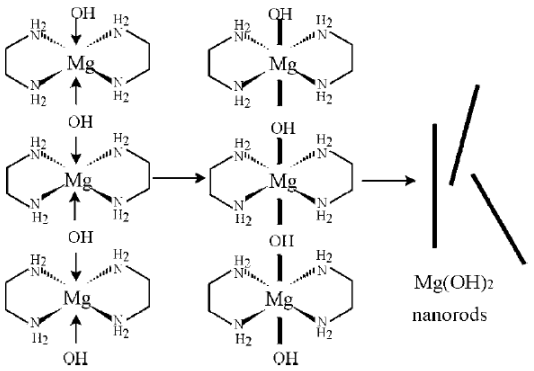


**Figure 2-3** Schematic diagram of the mechanism of formation of $Mg(OH)_2$ nanorods [51]

Wang [47] used $MgCl_2 \cdot 6H_2O$ and $NH_3 \cdot H_2O$ as the starting materials and polyethyleneglycol as the dispersant and template. As is shown in **Figure 2-4 (A)**, when the synthesis temperature was at 20 °C and 40 °C, the crystal faces that paralleled with c axis would absorb polyethyleneglycol, preventing the solute diffusion to the faces. Therefore, $Mg(OH)_2$ grew along one direction and finally formed nanoneedles. When it was at 60 °C and 80 °C, (0 0 1) crystal faces were more easily to absorb polyethyleneglycol, the crystal was confined to grow along the [0 0 1] direction. Thus, nanosheets of $Mg(OH)_2$ were synthesized, as shown in **Figure 2-4(B)**.

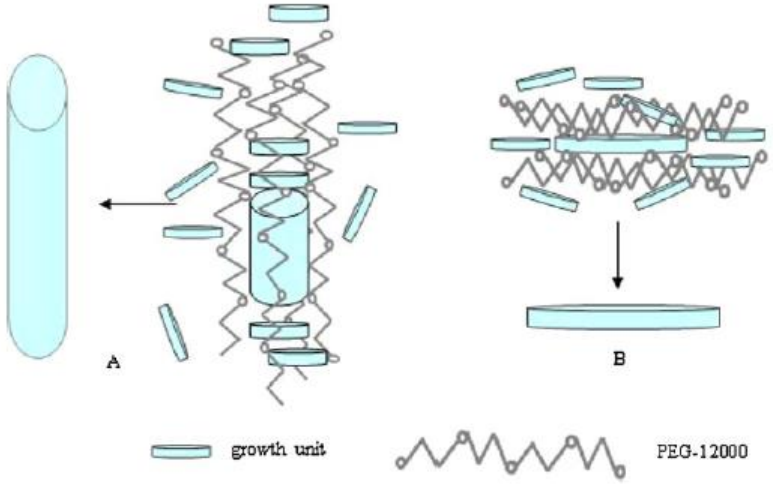


**Figure 2-4** Schematic diagram of growth modes influenced by temperature: (A) 20 °C and 40 °C and (B) 60 °C and 80 °C [47]

**Table 2-3** Summary of chemistry hydrothermal method for preparing nano-$Mg(OH)_2$ or nano-MgO

| Mg-source | Precipitator | Temperature (°C) | Time(h) | Stage 1:$Mg(OH)_2$ | | Stage 2:MgO | | | | Reference | Supplement |
|---|---|---|---|---|---|---|---|---|---|---|---|
| | | | | Morphology | Size(nm) | Experimental parameters | Surface area($m^2/g$) | Morphology | Size(nm) | | |
| Mg | en[a]-$H_2O$ (8:1)[b] | 180 | 20 | Nanorod | 20×200 | | | | | [52] | |
| | en-$H_2O$ (1:6) | | | Nanosheet | 50-100 | 280 °C-1h→250 °C-2h→450 °C-2h | 122.05 | Nanosheet | 50-100 | [52] | |
| | en-$H_2O$ (14:1) | | | Nanorod | (8-20)×(200-450) | | | | | [51] | Without stirring |
| | $NH_3 \cdot H_2O$(14:1) | | | Nanoplate | ~200 | | | | | [51] | |
| | $NH_3 \cdot H_2O$(pH=10) | | | Nano (sheet,tube) | 25-200, 40×600 | | | | | [52] | |
| | $H_2O$ | 160 | 24 | Nanoplate | ~900 | 450 °C-4h | | Nanoplate | ~700 | [40] | |

| | | | | | | | | | | | |
|---|---|---|---|---|---|---|---|---|---|---|---|
| $MgSO_4$ | en-$H_2O$ (4:1) | 180 | 20 | Nanoneedle | (10-20)×(50-100) | 280 °C-1h→250 °C-2h→450 °C-2h | 132.21 | Nanoneedle | (20-40)×(100-200) | [52] | |
| | en-$H_2O$ (1:1) | 180 | 20 | Nanosheet | 100-150 | 280 °C-1h→250 °C-2h→450 °C-2h | 161.49 | Nanosheet | 100-150 | [52] | |
| | $NH_3 \cdot H_2O$(pH=11) | 110 | 20 | Nanosheet | 150 | | | | | [52] | |
| | en-$H_2O$ (14:1) | 180 | | Nanorod | | | | | | [52] | |
| $MgNO_3 \cdot 6H_2O$ | en | | | Nanosheet | 80-100 | 280 °C-1h→250 °C-2h→450 °C-2h | 147.71 | Nanosheet | 50-100 | [52] | |
| | $NH_3 \cdot H_2O$(pH=10) | | | Nanosheet | 100-200 | | | | | [52] | |
| | NaOH(0.1 M) | 80 | 2 | Nanosheet | 50 | 280 °C-1h→250 °C-2h→450 °C- | 143.37 | Nanosheet | 20-40 | [52] | |

| | | | | | | | | | | | |
|---|---|---|---|---|---|---|---|---|---|---|---|
| | | | | | | 2h | | | | | |
| $MgNO_3$ (0.2M) | $NH_3 \cdot H_2O$ | | | Plate | | 480° C,730 °C and 1000 °C | | | 30-75 | [53] | |
| $MgCl_2 \cdot 6H_2O$ | $NH_3 \cdot H_2O$ | 50 | 1.5 | | | 450 °C-1.5h | | Nanoplate | ~100 | [54] | Polyethylene glycol and ethanol as solvent |
| $MgCl_2 \cdot 6H_2O$ (0.1 M) | $NH_3 \cdot H_2O$(pH=10.5) | 20 | 0 | | | 550 °C-2 | | Nanoplate | ~1μm | [55] | Dropwise with vigorous stirring, microwave |
| $MgCl_2 \cdot 6H_2O$ (2.5 M) | $NH_3 \cdot H_2O$ (5 *wt%*)+ NaOH (8 *wt%*) | 2,10,10 and 20 | Different inject time, stir 1h and react 1h | Nanoneedle, nanosheet, nanorod and nanosheet | 5×100,30×140,160×3000,20-100 and 100-200 | | | | | [56] | Dispersant, peristaltic pump and vigorous stirring |

| | | | | | | | | | | | |
|---|---|---|---|---|---|---|---|---|---|---|---|
| | $NH_3 \cdot H_2O$ (25 *wt%*)+ NaOH (8 *wt%*) | 2,10 and 20 | | Nanosheet | 50,150-200 and 300-350 | | | | | | |
| $MgCl_2 \cdot 6H_2O$ (0.75 M) | $NH_3 \cdot H_2O$(1.5M) | 60,47,25 and 10 | 24 | Plate | 302,218, 360 and 341 | | | | | [57] | Ultrasonicated bath, peristaltic pump and vigorous stirring |
| | NaOH(1.5 M) | 60 | 24 | Globular, large aggregates of spherical units | | | | | | | |
| $MgNO_3$ (0.75M) | $NH_3 \cdot H_2O$(1.5M) | 25 | 24 | Plate | 351 | | | | | | |
| $MgSO_4$(0.75M) | $NH_3 \cdot H_2O$(1.5M) | 25 | 24 | Agglomerated particles | | | | | | | |
| $Mg(CH_3COO)_2$ | eg[c] | | | nanoparticles | | | | | | [58] | Microwave |
| $MgCl_2$( 0.75 M) | NaOH(1.5 M), pH=12.5 | 60 | 1 | Thin plates, well | 47 | | | | | [59] | Metering pumps |

| | | | | | | | | | | | |
|---|---|---|---|---|---|---|---|---|---|---|---|
| | $NH_3 \cdot H_2O$(1.5M) pH=10.5 | | | developed hexagonal shape | 50 | | | | | | control addition rate:1.5ml/ min |
| | $NH_3 \cdot H_2O$(1.5M) pH=10 | | | Imperfect crystals and indented outlines | 183 | | | | | | |
| | $NH_3 \cdot H_2O$(1.5M) pH=9.5 | | | Well defined hexagonal perfect crystals | 147 | | | | | | |
| | $NH_3 \cdot H_2O$(1.5M) pH=9 | | | Poorer quality crystals, less well developed hexagonal plates | 112 | | | | | | |
| | $NH_3 \cdot H_2O$(1.5M) | | | Equiaxed | 303 | | | | | | |

| | | | | | | | | | | | |
|---|---|---|---|---|---|---|---|---|---|---|---|
| | pH=8.75 | | | particles, stacked-plate and apparent layers normal to c- axis | | | | | | | |
| $MgNO_3 \cdot 6H_2O$( 0.5M) | NaOH(5 M) | 180 | 24 | Micro disk | | | | | | [60] | Ultrasonicated bath, manual stirring |
| | | 180 | 48 | Polyhedron | | | | | | | |
| | | 200 | 3 | Micro disk | ~3μm | 250 °C-1h→350 °C-2h→450 °C-2h | | | | | |
| | | 200 | 12 | Nano disk | 35-150 | 250 °C-1h→350 °C-2h→450 °C-2h | | | | | |
| | | 200 | 24 | Polyhedron | | | | | | | |
| | | 200 | 48 | | 48μm | 250 °C-1h→350 °C- | | | | | |

| | | | | | | | | | | | |
|---|---|---|---|---|---|---|---|---|---|---|---|
| | | | | | | 2h→450 °C-2h | | | | | |
| | | 250 | 24 | | | | | | | | |
| | | 250 | 48 | | | | | | | | |
| $MgNO_3 \cdot 6H_2O$ | $N_2H_4 \cdot H_2O$ | 150 | 24 | Flakes with rounded edges | 127±34 | | | | | [49] | Mean longer side ~120±30 nm and thickness~15nm |
| | | 150 | 12 | | 75±55 | | | | | | A strong tendency to form agglomerate |
| | | 180 | 12 | | 163±45 | | | | | | Well defined hexagonal nanoplates |

| | | | | | | | | | | | |
|---|---|---|---|---|---|---|---|---|---|---|---|
| | | | | | | | | | | | with a uniform size of ~160±40nm and a thickness of 18 nm |
| | | 180 | 6 | | 456±53 | | | | | | Average sizes of around 450±50 nm and thicknesses of ~20 nm |

[a] en ethylene diamine

[b] in volume ratio

[c] eg ethylene glycol

## 2.4 Synthesis of $Fe_2O_3$ Nano Particles

Iron oxide ($Fe_2O_3$) nanoparticles with various polymorphs (α, β, γ and ε) have been the focus of numerous studies in the past decades owing to their excellent performance and wide applications [61]. Upon the development of nanotechnology, iron oxide nanoparticles are at the leading edge of rapid development of nanomaterials, resulting in several advanced applications in the fields such as biomedical, health care, environmental remediation, energy, aerospace and electronics [62-64]. $Fe_2O_3$ nanoparticles can be synthesized by three main methods, as shown in **Figure 2-5**. They are chemical methods, physical methods and biological methods [65]. A comparison of detailed preparation methods by previous studies is given in **Table 2-4** [65]. For physical methods, they are usually complex process which cannot control the particle size within nanometer [66]; for the chemical methods, they are usually simple and high efficient with stable morphology and particle size [70]; for biological methods, they usually take a long time to synthesize and both morphology and size are not homogenous [77]. Therefore, chemical methods are most widely employed because of low cost and high production yield. It is also easy to control morphology and make final size in the nanometer range.

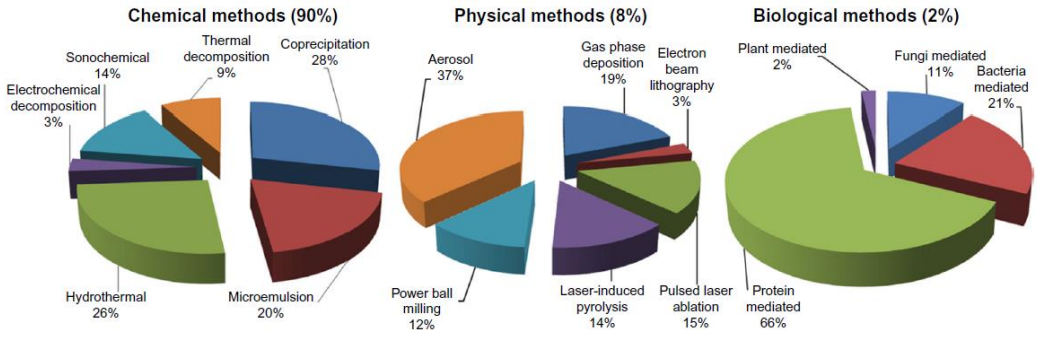


**Figure 2-5** $Fe_2O_3$ nanoparticles synthesized from three different routes [65].

**Table 2-4** Comparison for $Fe_2O_3$ nanoparticles synthesis: morphology, advantages and disadvantages [65].

| Methods | | Morphology | Advantages | Disadvantages | References |
|---|---|---|---|---|---|
| Physical | Deposition of gas phase | Spheres and irregular spheres | Easy to execute | Problematic in controlling the size of particle | [66] |
| | Electron beam lithography | Spheres and rods | Well-controlled interparticle spacing | Requires expensive and highly complex machines | [67] |
| Chemical | Sol–gel method | Spheres, irregular spheres, porous and nonporous spheres, or spindles | Aspect ratio, precisely controlled in size, and internal structure | High permeability, weak bonding, low wear resistance | [68] |
| | Oxidation | Irregular elongated and small spheres | Narrow size distribution and uniform size | Ferrite colloids of small size | [69] |
| | Chemical co-precipitation | Spheres | Simple and effective | Inappropriate for the synthesis of high untainted, precise stoichiometric | [70] |

| | | | | | |
|---|---|---|---|---|---|
| | | | | phase | |
| | Hydrothermal | Elongated, compact irregular spheres, and numerous shapes | Particle size and shapes are easily controllable | High pressure and reaction temperature | [71] |
| | Flow injection | Small rods, irregular spheres, sheets, or rhombic shapes | Homogeneity with high mixing with a accurate control of the procedure and good reproducibility | Under a laminar flow regime in a capillary reactor, it requires continuous or segmented mixing of reagents | [72] |
| | Electrochemical | Spherical NPs, nanorods, hexagonal nanocrystals, and facets | Controllable particle size | Inability to reproduce | [68] |
| | Aerosol/vapor phase | Mesoporous single crystals and small | Large-scale products | Requires very high temperatures | [73] |

| | | | | | |
|---|---|---|---|---|---|
| | | particles, octahedral cages | | | |
| | Sonochemical decomposition | Bipyramids, spheres, or truncated rods | Size distribution in narrow particle | Still, mechanism is not well understood | [74] |
| | Supercritical fluid method | Mesoporous single crystals, elongated irregular nanotubes | No organic solvents involved and efficient control of the particle size | No organic solvents involved and efficient control of the particle size | [75] |
| | Using nanoreactors | Spheres, hollow and spherical nanoparticles | Likelihood to specifically control the size of nanoparticles | Complicated conditions | [76] |
| Biological | Microbial incubation | Small platelets, spherical or rod-like spheres, irregular spheres | Good reproducibility and scalability, high yield, and low cost | Slow and laborious | [77] |

## 2.5 Applications of $Fe_2O_3$ Nano Particles

The α-$Fe_2O_3$-based nanomaterials display outstanding performance in many applications, mainly including (1) conventional thermal catalysts in WGSR, CO oxidation and steam/dry methane reforming; (2) distinguished photo- and electro- catalysts that provide substitutes for noble-metal nanomaterials in numerous energy conversion reactions; (3) remarkable energy storage capabilities; (4) acceptable operation cost for large-scale industrial production due to the high earth abundances of Fe; (4) long-term stability and sustainability due to their availability, low cost and continuous chemical reactivity. The superiorities of α-$Fe_2O_3$, including low cost, high availability, low toxicity, and high specific capacity, make it one of the promising materials with the greatest potential for environmental and energy applications.

### 2.5.1 Water treatment

Nowadays, the anthropogenic release of heavy metals and organic dyes into the natural environment is becoming a serious issue throughout the world [78]. Among the various water treatment technologies, adsorption is widely popular for removal of pollutants due to its low cost, high efficiency, and ease simplicity [79]. α-$Fe_2O_3$ has been widely used as an adsorbent for the removal of heavy metals and organic dyes [80]. For example, HERING [81] found that even the bulk iron oxide minerals, they can remove arsenic (V and III). Later, with the rapid development of nanotechnology, nanosized α-$Fe_2O_3$ has been synthesized and thus various morphologies and structures have been reported, which can remove multiple pollutants is waste water, as shown in Table 2-5. The adsorption mechanism is normally attributed to the electrostatic forces between the negatively charged adsorbent and positive metal ions or positively charged adsorbent and negative metal-oxygen ions.

**Table 2-5** Comparison of adsorption capacities of nanosized α-$Fe_2O_3$ adsorbents

| Morphology | Size (nm) | BET surface area ($m^2$ $g^{-1}$) | Maximum removal capacity (mg $g^{-1}$) | Reference |
|---|---|---|---|---|
| Round nanoflakes | ~400 nm in diameter and ~50 nm in thickness | 80.12 | 68.3 for Cr(VI)<br>80.6 for As(V)<br>61.1 for As(III)<br>213.8 for CR | [82] |
| Polyhedron nanoparticles | ~200 nm | 31.73 | 15.7 for Cr(VI)<br>22.7 for As(V)<br>10.6 for As(III)<br>65.9 for CR | |
| Hollow nestlike spheres | ~400 nm | 152.42 | 58.6 for Cr(VI)<br>75.3 for As(V)<br>160 for CR | [83] |
| Flowerlike nanostructures | 0.8−1 μm in diameter | 130 | 30 for Cr(VI)<br>51 for As(V) | [84] |
| Irregular spherical nanoparticles | ~50 nm | 164.1 | 17 for Cr(VI)<br>253.8 for CR | [85] |
| Nanorods | diameter of 100–200 nm and length of micrometers | 22.78 | 78.13 for CR | [86] |
| Nanowires deposited diatomite | 250-300 nm in length and 10-15 nm in diameter | 30 | 81.2 for As(V)<br>60.6 for As(III) | [87] |
| Uniform granular crystals | ~5 nm | 173 | 51.8 for As(III) | [88] |
| Mesoporous nanorods | ~235 nm in length and ~40 nm in diameter | 98 | 57.2 for CR | [89] |
| Hierarchical spherical nanoparticles | ~40 nm | 152.3 | 723.8 for CR<br>150.7 for MO<br>54.5 for MB | [90] |
| Porous microcubes | ~400 nm | 155 | 175.5 for Cr(VI)<br>97.8 for Pb(II)<br>66.2 for Cu(II)<br>60.4 for Co(II)<br>429.9 for MB | [91] |
| One-dimensional nanorods | ~250 nm in length and ~50 nm in diameter | 16.1 | 172.41 For Pb(II) | [92] |

| | | | | |
|---|---|---|---|---|
| Nanofibers | 23-62 nm in diameter | 7.2-59.2 | 10.2-90.9 for Cr(VI) | [93] |
| Bowknot-like hierarchical porous nanoparticles | - | 124.56 | 139.86 for CR | [94] |
| hierarchical nanostructures | ~600 nm | 69 | 66 for CR | [95] |
| Rice-shaped nanoparticles | 250 nm in length and 50 nm in width | 110.2 | 161 for CR | [96] |
| Cauliflower-like microstructures | 420–550 nm | 31.57 | 71.63 for CR<br>17.27 for Cr(VI)<br>32.54 for Pb(II) | [97] |
| Flowerlike nanoparticles | ~4 μm in diameter | 40 | 4.47 for Cr(VI)<br>5.31 for As(V) | [98] |

### 2.5.2 Catalysts of WGSR

The WGSR represents a significant industrial reaction for hydrogen production. Currently, more than 80% hydrogen is produced by steam methane reforming (SMR) followed by the WGS reaction [99]. As the world is making transitions towards a cleaner energy future by using hydrogen-based fuel-cell technology, the WGSR has attracted renewed research attention. Whilst there is also interest in renewable $H_2$ production by photocatalytic water splitting and biomass reforming, it is expected that the availability of methane and cost-competitive economics will continue to drive the SMR-WGS process as the dominant technology for hydrogen production in the foreseeable future.

The industrial importance of the WGS reaction is further enhanced by its application as an essential intermediate step to adjust the $H_2$ to CO ratio of syngas in major manufacturing processes, including Fischer-Tropsch synthesis of hydrocarbons, methanol synthesis, and ammonia production. Derived from the steam reforming of methane or liquid hydrocarbons and the gasification of coal/biomass/municipal waste [100], syngas comprises a mixture of mainly $H_2$ and appreciable amounts of CO. However, the presence of CO is problematic for

many downstream processes, such as poisoning of the iron-based catalyst used in ammonia production and the platinum electrode used in hydrogen fuel cells. In the latter case, deactivation of electrodes can be caused by CO concentrations as low as 10-50 ppm [101,102]. To satisfy downstream process requirements, the WGS reaction is used to adjust the syngas $H_2$/CO ratio by CO reduction and $H_2$ enrichment. Accordingly, the reaction is critical for its functions to preliminary CO clean-up and additional hydrogen generation.

$$CO_{(g)} + H_2O_{(g)} \rightleftharpoons CO_{2_{(g)}} + H_{2_{(g)}} \qquad \Delta H^{\circ}{}_{298} = -41.19\ kJ/mol$$

Due to its reversible and exothermic nature, the WGS reaction is thermodynamically favoured at lower temperatures and kinetically favoured at higher temperatures. Hence commercially, these processes are conducted in two adiabatic stages: a high-temperature water gas shift (HT-WGS) operated at 350-450$^{o}$ C, followed by a low-temperature water gas shift (LT-WGS) at 190-250$^{o}$ C [103]. At kinetically favorable conditions, the conventional high temperature shift (HTS) catalyst used in the first stage is an iron-chromium (Fe-Cr) oxide catalyst capable of lowering the CO concentration in syngas to 3 mol% [102]. In the second stage, the copper-zinc-oxide (Cu/ZnO) based low temperature shift (LTS) catalyst achieves CO outlet concentrations of 0.1-0.3 mol% at the more favorable equilibrium conditions [104].

Despite the high activity, durability, and relatively low manufacturing costs of iron-based catalysts, there still remain certain disadvantages that drive continual research. Notably, the slow kinetics of the WGSR necessitates use of the largest volume of any catalyst in a fuel-related process [105]. This is in direct contrast to techno-economic requirements of hydrogen fuel cells for catalyst beds with reduced volume and weight, thereby enforcing the need for a more active iron oxide catalyst. Moreover, the commercially-used iron-oxide catalyst is doped with around 8-14 *wt%* of toxic chromium promoter, of which the hexavalent $Cr^{6+}$ form is carcinogenic, water-soluble and poses serious environmental and health threats [102].

Practically, this leads to higher cost of disposal of spent catalyst and hazardous processes during manufacture. As such, the development of Cr-free iron catalysts is strongly desired, and extensive work has been conducted to investigate use of alterative promoters. That is, either textural promoters ($Al^{3+}$, $Th^{4+}$, $Mg^{2+}$) which stabilize surface area and prevent thermal sintering, or chemical/structural promoters ($Cu^{2+}$, $Rh^{2+}$) which provide catalytic active sites.

From a process sustainability perspective, synthesis of catalysts from low-value starting materials such as industrial waste is crucial.

Conversely, for HT-WGS catalysis application, the presence of $Fe_2O_3$ and other metallic impurities is desirable. In particular, $Al^{3+}$ has been recognized as a potential substitute to $Cr^{3+}$ in iron-oxide based catalysts [105]. This therein lies an opportunity to convert the industrial low-rank fly ash waste into a valuable, low-cost, non-toxic and environmentally friendly nanosized catalyst for the HT-WGS reaction.

### 2.5.3 Other applications

In addition to adsorbents and thermo catalysts, α-$Fe_2O_3$ can also be used to synthesize batteries [106], sensors [107], photo- and electro- catalysts for $CO_2$ reduction and $H_2O$ splitting [108] and supercapacitors [109].

## 2.6 Literature review summary and research gaps

This literature review has shown that the Victorian brown coal fly ash has abundant Mg and Fe, which results in the unsuitability of conventional utilization methods to deal with this solid waste while it is a promising feedstock of great potentials to synthesized nanosized Fe- and Mg-bearing materials. Previous researchers have developed various leaching methods to extract Mg and Fe out of various fly ash. However, either harsh conditions with high extraction yields or moderate conditions with low extraction yields were obtained. To address this special

brown coal fly ash, synergistic leaching agents (HCl and $NH_4Cl$) were used to make the leaching conditions comparatively moderate. Nevertheless, the maximum leaching yields of Mg and Fe were only 65% and 29%, respectively. In addition, as for Fe- and Mg-based nanomaterials including α-$Fe_2O_3$, $Mg(OH)_2$ and MgO, they are usually synthesized from pure reagent grade chemicals. Synthesis of these nanomaterials from industrial wastes is rarely reported, which will not only convert those industrial wastes into value-added products, but also accelerate the development of low-cost production of these nanomaterials. Moreover, atomic understandings of natural impurity doped α-$Fe_2O_3$ as well as growth process for $Mg(OH)_2$ are still blank, which determines their nanostructures and the influences the subsequent applications including water remediation and catalysis. Finally, even though various nanomaterials have been synthesized from fly ash, such as silicon nanorods, carbon nanofibers, geopolymer, mesoporous nanosilica, zeolite and ordered mesoporous molecular sieves. All these nanomaterials are limited to alumina and/or silica-based materials, which are abundant in the coal ashes produced from high-rank coals. For the ash produced from a low-rank coal such as the brown coal, it is implausible to synthesize these Al-/Si-based nanomaterials as they are generally lean in the low-rank coal ashes.

This chapter has offered an in-depth literature review of the current state of knowledge regarding the leaching technologies of coal ash, synthesis of MgO/$Mg(OH)_2$ and α-$Fe_2O_3$ and Fe-based catalysts for the WGSR. As a result, the research gaps of this PhD project are identified as follows:

(1) Fe and Mg are abundant in the Victorian brown coal fly ash in the crystal form of magnesioferrite ($MgFe_2O_4$), which has an inverse-spinel structure and is chemically stable. Previous leaching researches used complex experimental conditions (leaching agent, concentration, time and temperature) while the extraction yield is still low. To date few studies

have been reported on how to improve the leaching efficiency that can break the strong chemical bond of $MgFe_2O_4$.

(2) Synthesis of facet-engineered nano-$Mg(OH)_2$ from coal fly ash is still blank. This seriously restricts the wider applications of facet-engineered Mg-based nanomaterials.

(3) The influences of foreign impurities on the atomic environments, growth mechanisms, crystal structures and subsequent applications (such as water treatment and WGSR) of α-$Fe_2O_3$ are less reported. Especially, there is no study about the synthesis and mechanisms of impurity-enhanced α-$Fe_2O_3$ from coal fly ash as a high-efficient adsorbent. Furthermore, researches on the synthesis of α-$Fe_2O_3$ catalysts in WGSR are completely blank.

## Reference

[1] Ahmaruzzaman, M. A review on the utilization of fly ash. *Progress in Energy and Combustion Science* **2010**, 36 (3), 327-363.

[2] Izquierdo, M.; Querol X. Leaching behaviour of elements from coal combustion fly ash: An overview. *International Journal of Coal Geology* **2012**, 94, 54-66.

[3] Ferreira, C.; Ribeiro, A.; Ottosen L. Possible applications for municipal solid waste fly ash. *Journal of Hazardous Materials* **2003**, 96 (2), 201-216.

[4] Hower, J. C.; Senior, C. L.; Suuberg, E. M.; Hurt, R. H.; Wilcox, J. L.; Olson, E. S. Mercury capture by native fly ash carbons in coal-fired power plants. *Progress in Energy and Combustion Science* **2010** 36 (4), 510-529.

[5] Asl, S. M. H.; Ghadi, A.; Baei, M. S.; Javadian, H.; Maghsudi, M.; Kazemian, H. Porous catalysts fabricated from coal fly ash as cost-effective alternatives for industrial applications: A review. *Fuel* **2018**, 217, 320-342.

[6] Ma, B.; Li, X.; Shen, X.; Mao, Y.; Huang, H. Enhancing the addition of fly ash from thermal power plants in activated high belite sulfoaluminate cement. *Construction and Building Materials* **2014**, 52, 261-266.

[7] Mo, L.; Lv, L.; Deng, M.; Qian, J. Influence of fly ash and metakaolin on the microstructure and compressive strength of magnesium potassium phosphate cement paste. *Cement and Concrete Research* **2018**, 111, 116-129.

[8] Forteza, R.; Far, M.; Seguı, C.; Cerda, V. Characterization of bottom ash in municipal solid waste incinerators for its use in road base. *Waste Management* **2004**, 24 (9), 899-909.

[9] Al-Shawabkeh, A.; Maisuda, H.; Hasatani, M. Comparative reactivity of treated FBC- and PCC-Fly ash for $SO_2$ removal. *The Canadian Journal of Chemical Engineering* **1995**, 73 (5), 678-685.

[10] Lu, G. Q.; Do D. D. Adsorption properties of fly ash particles for $NO_x$ removal from flue

gases. *Fuel Processing Technology* **1991**, 27 (1), 95-107.

[11] Rothenberg, S. J.; Mettzler, G.; Poliner, J.; Bechtold, W. E.; Eidson, A. F.; Newton, G. J. Adsorption kinetics of vapor-phase m-xylene on coal fly ash. *Environmental Science & Technology* **1991**, 25 (5), 930-935.

[12] Kuziemska, I. Application of water extract of brown coal fly ash to phosphate precipitation from polluted waters. *Water Research* **1980**, 14 (9), 1289-1293.

[13] Chaturvedi, A. K.; Yadava, K. P.; Pathak, K. C.; Singh, V. N. Defluoridation of water by adsorption on fly ash. *Water, Air, and Soil Pollution* **1990** 49 (1) 51-61.

[14] Öztürk, N.; Kavak, D. Adsorption of boron from aqueous solutions using fly ash: Batch and column studies. *Journal of Hazardous Materials* **2005**, 127 (1), 81-88.

[15] Alemany, L. J.; Jimenez, M. C.; Larrubia, M. A.; Delgado, F.; Blasco, J. M. Removal of Phenol from Aqueous Solution by Adsorption on to Coal Fly Ash. *Adsorption Science & Technology* **1996**, 13 (6), 527-536.

[16] Acemioğlu, B. Adsorption of Congo red from aqueous solution onto calcium-rich fly ash. *Journal of Colloid and Interface Science* **2004**, 274 (2), 371-379.

[17] Pandey, V. C.; Singh, N. Impact of fly ash incorporation in soil systems. *Agriculture, Ecosystems & Environment* **2010**, 136 (1), 16-27.

[18] Magnuson, M.; Malenka, W. Utilization of fly ash for remote filling of mine voids. *United States Department of the Interior, Bureau of Mines Information Circular* **1970**, 8488.

[19] Erol, M.; Küçükbayrak, S.; Ersoy-Meriçboyu, A. Comparison of the properties of glass, glass–ceramic and ceramic materials produced from coal fly ash. *Journal of Hazardous Materials* **2008**, 153 (1), 418-425.

[20] Xuan, X.; Yue, C.; Li, S.; Yao, Q. Selective catalytic reduction of NO by ammonia with fly ash catalyst☆. *Fuel* **2003**, 82 (5), 575-579.

[21] Font, O.; Querol, X.; Juan, R.; Casado, R.; Ruiz, C. R.; López-Soler, Á.; Coca, P.; Peña,

F. G. Recovery of gallium and vanadium from gasification fly ash. *Journal of Hazardous Materials* **2007**, 139 (3), 413-423.

[22] Yan, F.; Jiang, J.; Tian, S.; Liu, Z.; Shi, J.; Li, K.; Chen, X. Xu, Y. A Green and Facile Synthesis of Ordered Mesoporous Nanosilica Using Coal Fly Ash. *ACS Sustainable Chemistry & Engineering* **2016**, 4 (9), 4654-4667.

[23] Nagib, S.; Inoue, K. Recovery of lead and zinc from fly ash generated from municipal incineration plants by means of acid and/or alkaline leaching. *Hydrometallurgy* **2000**, 56 (3), 269-292.

[24] Tang, J.; Steenari, B. M. Solvent extraction separation of copper and zinc from MSWI fly ash leachates. *Waste Management* **2015**, 44, 147-154.

[25] Choo, T. K.; Song, Y.; Zhang, L.; Selomulya, C.; Zhang, L. Mechanisms Underpinning the Mobilization of Iron and Magnesium Cations from Victorian Brown Coal Fly Ash. *Energy & Fuels* **2014**, 28 (6), 4051-4061.

[26] Hosseini, T.; Han, B.; Selomulya, C.; Haque, N.; Zhang, L. Chemical and morphological changes of weathered Victorian brown coal fly ash and its leaching characteristic upon the leaching in ammonia chloride and hydrochloric acid. *Hydrometallurgy* **2015**, 157, 22-32.

[27] Matjie, R. H.; Bunt, J. R.; Van Heerden, J. H. P. Extraction of alumina from coal fly ash generated from a selected low rank bituminous South African coal. *Minerals Engineering* **2005**, 18, 299-310.

[28] Choo, T. K.; Etschmann, B.; Selomulya, C.; Zhang, L. Behavior of $Fe^{2+/3+}$ Cation and Its Interference with the Precipitation of $Mg^{2+}$ Cation upon Mineral Carbonation of Yallourn Fly Ash Leachate under Ambient Conditions. *Energy & Fuels*, **2016**, 30 (4), 3269-3280.

[29] Jiao, F.; Zhang, L.; Dong, Z.; Namioka, T.; Yamada, N.; Ninomiya, Y. Study on the species of heavy metals in MSW incineration fly ash and their leaching behavior. *Fuel Processing Technology* **2016**, 152, 108-115.

[30] Huang, S. J.; Chang, C. Y.; Chang, F. C.; Lee, M. Y.; Wang, C. F. Sequential extraction for evaluating the leaching behavior of selected elements in municipal solid waste incineration fly ash. *Journal of Hazardous Materials* **2007**, 149, 180-188.

[31] Fedje, K. K.; Ekberg, C.; Skarnemark, G.; Steenari, B. M. Removal of hazardous metals from MSW fly ash—An evaluation of ash leaching methods. *Journal of Hazardous Materials*, **2010**, 173, 310-317.

[32] Blissett, R. S.; Smalley, N.; Rowson, N. A. An investigation into six coal fly ashes from the United Kingdom and Poland to evaluate rare earth element content. *Fuel* **2014**, 119, 236-239.

[33] Franus, W.; Wiatros-Motyka, M. M.; Wdowin, M. Coal fly ash as a resource for rare earth elements. *Environmental Science and Pollution Research* **2015**, 22 (12), 9464-9474.

[34] Wu, H. Y.; Ting, Y. P. Metal extraction from municipal solid waste (MSW) incinerator fly ash—Chemical leaching and fungal bioleaching. *Enzyme and microbial technology* **2006**, 38 (6), 839-847.

[35] Funari, V.; Mäkinen, J.; Salminen, J.; Braga, R.; Dinelli, E.; Revitzer, H. Metal removal from Municipal Solid Waste Incineration fly ash: A comparison between chemical leaching and bioleaching. *Waste Management* **2017**, 60, 397-406.

[36] Seidel, A.; Zimmels, Y. Mechanism and kinetics of aluminum and iron leaching from coal by ash by sulfuric acid. *Chemical Engineering Science* **1998**, 53 (22), 3835-3852.

[37] Cui, L.; Guo, Y.; Wang, X.; Du, Z.; Cheng, F. Dissolution kinetics of aluminum and iron from coal mining waste by hydrochloric acid. *Chinese Journal of Chemical Engineering* **2015**, 23 (3), 590-596.

[38] Warren, C. J.; Dudas, M. J. Leachability and partitioning of elements in ferromagnetic fly ash particles. *Science of the Total Environment* **1989**, 84, 223-236.

[39] Seferinoğlu, M.; Paul, M.; Sandström, Å.; Köker, A.; Toprak, S.; Paul, J. Acid leaching of

coal and coal-ashes. *Fuel* **2003**, 82 (14), 1721-1734.

[40] Yu, J. C.; Xu, A.; Zhang, L.; Song, R.; Wu, L. Synthesis and Characterization of Porous Magnesium Hydroxide and Oxide Nanoplates. *The Journal of Physical Chemistry B* **2004**, 108 (1), 64-70.

[41] Fricker, K. J.; Park, A. H. A. Effect of $H_2O$ on $Mg(OH)_2$ carbonation pathways for combined $CO_2$ capture and storage. *Chemical Engineering Science* **2013**, 100, 332-341.

[42] Li, C.; Zhuang, Z.; Huang, F.; Wu, Z.; Hong, Y.; Lin, Z. Recycling Rare Earth Elements from Industrial Wastewater with Flowerlike Nano-$Mg(OH)_2$. *ACS Applied Materials & Interfaces* **2013**, 5 (19), 9719-9725.

[43] Janning, C.; Willbold, E.; Vogt, C.; Nellesen, J.; Meyer-Lindenberg, A.; Windhagen, H.; Thorey, F.; Witte, F. Magnesium hydroxide temporarily enhancing osteoblast activity and decreasing the osteoclast number in peri-implant bone remodelling. *Acta Biomaterialia* **2010**, 6 (5), 1861-1868.

[44] Cunningham, D. A. H.; Vogel, W.; Haruta, M. Negative activation energies in CO oxidation over an icosahedral Au/$Mg(OH)_2$ catalyst. *Catalysis Letters* **1999**, 63 (1), 43-47.

[45] Giorgi, R.; Bozzi, C.; Dei, L.; Gabbiani, C.; Ninham, B. W.; Baglioni, P. Nanoparticles of $Mg(OH)_2$: Synthesis and Application to Paper Conservation. *Langmuir* **2005**, 21 (18), 8495-8501.

[46] Pan, X.; Wang, Y.; Chen, Z.; Pan, D.; Cheng, Y.; Liu, Z.; Guan, X. Investigation of Antibacterial Activity and Related Mechanism of a Series of Nano-$Mg(OH)_2$. *ACS Applied Materials & Interfaces* **2013**, 5 (3), 1137-1142.

[47] Wang, P.; Li, C.; Gong, H.; Wang, H.; Liu, J. Morphology control and growth mechanism of magnesium hydroxide nanoparticles via a simple wet precipitation method. *Ceramics International* **2011**, 37, 3365-3370.

[48] Minami, H.; Kinoshita, K.; Tsuji, T.; Yanagimoto, H. Preparation of Highly Crystalline Magnesium Oxide and Polystyrene/Magnesium Hydroxide Composite Particles by Sol–Gel Processes in an Ionic Liquid. *The Journal of Physical Chemistry C* **2012**, 116 (27), 14568-14574.

[49] Sierra-Fernández, A.; Gomez-Villalba, L. S.; Milosevic, O.; Fort, R.; Rabanal, M. E. Synthesis and morpho-structural characterization of nanostructured magnesium hydroxide obtained by a hydrothermal method. *Ceramics International* **2014**, 40, 12285-12292.

[50] Fan, W.; Sun, S.; You, L.; Cao, G.; Song, X.; Zhang, W.; Yu, H. Solvothermal synthesis of $Mg(OH)_2$ nanotubes using $Mg_{10}(OH)_{18}Cl_2 \cdot 5H_2O$ nanowires as precursors. *Journal of Materials Chemistry* **2003**, 13 (12), 3062-3065.

[51] Li, Y.; Sui, M.; Ding, Y.; Zhang, G.; Zhuang, J.; Wang, C. Preparation of $Mg(OH)_2$ Nanorods. *Advanced Materials* **2000**, 12 (11), 818-821.

[52] Ding, Y.; Zhang, G.; Wu, H.; Hai, B.; Wang, L.; Qian, Y. Nanoscale Magnesium Hydroxide and Magnesium Oxide Powders: Control over Size, Shape, and Structure via Hydrothermal Synthesis. *Chemistry of Materials* **2001**, 13 (2), 435-440.

[53] Fedorov, P. P.; Tkachenko, E. A.; Kuznetsov, S. V.; Voronov, V. V.; Lavrishchev, S. V. Preparation of MgO nanoparticles. *Inorganic Materials* **2007**, 43 (5), 502-504.

[54] Wang, W.; Qiao, X.; Chen, J.; Li, H. Facile synthesis of magnesium oxide nanoplates via chemical precipitation. *Materials Letters* **2007**, 61 (14), 3218-3220.

[55] Yang, M.; Wang, J.; Xiao, C.; Zhao, H. Microwave enhanced preparation of MgO nanoparticles. I*ntegrated Ferroelectrics* **2016**, 172 (1), 1-9.

[56] Lv, J.; Qiu, L.; Qu, B. Controlled growth of three morphological structures of magnesium hydroxide nanoparticles by wet precipitation method. *Journal of Crystal Growth* **2004**, 267 (3), 676-684.

[57] Henrist, C.; Mathieu, J. P.; Vogels, C.; Rulmont, A.; Cloots, R. Morphological study of magnesium hydroxide nanoparticles precipitated in dilute aqueous solution. *Journal of Crystal Growth* **2003**, 249 (1), 321-330.

[58] Makhluf, S.; Dror, R.; Nitzan, Y.; Abramovich, Y.; Jelinek, R.; Gedanken, A. Microwave-Assisted Synthesis of Nanocrystalline MgO and Its Use as a Bacteriocide. *Advanced Functional Materials* **2005**, 15 (10), 1708-1715.

[59] Phillips, V. A.; Kolbe, J. L.; Opperhauser, H. Effect of pH on the growth of $Mg(OH)_2$ crystals in an aqueous environment at 60°C. *Journal of Crystal Growth* **1977**, 41 (2), 228-234.

[60] Kumari, L.; Li, W. Z.; Vannoy, C. H.; Leblanc, R. M.; Wang, D. Z. Synthesis, characterization and optical properties of $Mg(OH)_2$ micro-/nanostructure and its conversion to MgO. *Ceramics International* **2009**, 35 (8), 3355-3364.

[61] Navale, S. T.; Bandgar, D. K.; Nalage, S. R.; Khuspe, G. D.; Chougule, M. A.; Kolekar, Y. D.; Patil, V. B. Synthesis of $Fe_2O_3$ nanoparticles for nitrogen dioxide gas sensing applications. *Ceramics International* **2013**, 39 (6), 6453-6460.

[62] Cao, K.; Jiao, L.; Liu, H.; Liu, Y.; Wang, Y.; Guo, Z.; Yuan, H. 3D Hierarchical Porous α-$Fe_2O_3$ Nanosheets for High-Performance Lithium-Ion Batteries. *Advanced Energy Materials* **2015**, 5 (4), 1401421.

[63] Nie, Z.; Petukhova, A.; Kumacheva, E. Properties and emerging applications of self-assembled structures made from inorganic nanoparticles. *Nature Nanotechnology* **2009**, 5, 15.

[64] Wang, H.; Xu, Z.; Yi, H.; Wei, H.; Guo, Z.; Wang, X. One-step preparation of single-crystalline $Fe_2O_3$ particles/graphene composite hydrogels as high performance anode materials for supercapacitors. *Nano Energy* **2014**, 7, 86-96.

[65] Ali, A.; Hira Zafar, M. Z.; ul Haq, I.; Phull, A. R.; Ali, J. S.; Hussain, A. Synthesis,

characterization, applications, and challenges of iron oxide nanoparticles. *Nanotechnology, Science and Applications* **2016**, 9, 49-67.

[66] Cuenya, B. R. Synthesis and catalytic properties of metal nanoparticles: Size, shape, support, composition, and oxidation state effects. *Thin Solid Films* **2010**, 518 (12), 3127-3150.

[67] Lin, X. M.; Samia, A. C. Synthesis, assembly and physical properties of magnetic nanoparticles. *Journal of Magnetism and Magnetic Materials* **2006**, 305 (1), 100-109.

[68] Laurent, S.; Forge, D.; Port, M.; Roch, A.; Robic, C.; Vander Elst, L.; Muller, R. N. Magnetic Iron Oxide Nanoparticles: Synthesis, Stabilization, Vectorization, Physicochemical Characterizations, and Biological Applications. *Chemical Reviews* **2008**, 108 (6), 2064-2110.

[69] Soenen, S. J.; Brisson, A. R.; M. Cuyper, De. Addressing the problem of cationic lipid-mediated toxicity: The magnetoliposome model. *Biomaterials* **2009**, 30 (22), 3691-3701.

[70] Wu, S.; Sun, A.; Zhai, F.; Wang, J.; Xu, W.; Zhang, Q.; Volinsky, A. A. $Fe_3O_4$ magnetic nanoparticles synthesis from tailings by ultrasonic chemical co-precipitation. *Materials Letters* **2011**, 65 (12), 1882-1884.

[71] Cha, H. G.; Kim, S. J.; Lee, K. J.; Jung, M. H.; Kang, Y. S. Single-Crystalline Porous Hematite Nanorods: Photocatalytic and Magnetic Properties. *The Journal of Physical Chemistry C* **2011**, 115 (39), 19129-19135.

[72] Salazar-Alvarez, G.; Muhammed, M.; Zagorodni, A. A. Novel flow injection synthesis of iron oxide nanoparticles with narrow size distribution. *Chemical Engineering Science* **2006**, 61 (14), 4625-4633.

[73] Ling, D.; Hyeon, T. Chemical Design of Biocompatible Iron Oxide Nanoparticles for Medical Applications. *Small* **2013**, 9 (9-10), 1450-1466.

[74] Unsoy, G.; Yalcin, S.; Khodadust, R.; Gunduz, G.; Gunduz, U. Synthesis optimization and

characterization of chitosan-coated iron oxide nanoparticles produced for biomedical applications. *Journal of Nanoparticle Research* **2012**, 14 (11), 964.

[75] Teja, A. S.; Koh, P. Y. Synthesis, properties, and applications of magnetic iron oxide nanoparticles. *Progress in Crystal Growth and Characterization of Materials* **2009**, 55 (1), 22-45.

[76] Thorek, D. L.; Chen, A. K.; Czupryna, J.; Tsourkas, A. Superparamagnetic Iron Oxide Nanoparticle Probes for Molecular Imaging. *Annals of Biomedical Engineering* **2006**, 34 (1), 23-38.

[77] Narayanan, K. B.; Sakthivel, N. Biological synthesis of metal nanoparticles by microbes. *Advances in Colloid and Interface Science* **2010**, 156 (1), 1-13.

[78] Nordstrom, D. K. Worldwide Occurrences of Arsenic in Ground Water. *Science* **2002**, 296, 2143-2145.

[79] Luo, J.; Sun, M.; Ritt, C. L.; Liu, X.; Pei, Y.; Crittenden, J. C.; Elimelech, M. Tuning Pb(II) Adsorption from Aqueous Solutions on Ultrathin Iron Oxychloride (FeOCl) Nanosheets. *Environmental Science & Technology* **2019**, 53, 2075-2085.

[80] Yuan, Q.; Li, P.; Liu, J.; Lin, Y.; Cai, Y.; Ye, Y.; Liang, C. Facet-Dependent Selective Adsorption of Mn-Doped α‑$Fe_2O_3$ Nanocrystals toward Heavy-Metal Ions. *Chemistry of Materials* **2017**, 29, 10198-10205.

[81] Dixit, S.; Hering, J. G. Comparison of Arsenic(V) and Arsenic(III) Sorption onto Iron Oxide Minerals: Implications for Arsenic Mobility. *Environmental Science & Technology* **2003**, 37, 4182-4189.

[82] Qian, B.; Liu, C.; Lu, J.; Jian, M.; Hu, X.; Zhou, S.; Zhang, L. Synthesis of in-situ $Al^{3+}$-defected iron oxide nanoflakes from coal ash: A detailed study on the structure, evolution mechanism and application to water remediation. *Journal of Hazardous Materials* **2020**, 395, 122696

[83] Wei, Z.; Xing, R.; Zhang, X.; Liu, S.; Yu, H.; Li, P. Facile Template-Free Fabrication of Hollow Nestlike α-$Fe_2O_3$ Nanostructures for Water Treatment. *ACS Applied Materials & Interfaces* **2013**, 5, 598-604.

[84] Cao, C. Y.; Qu, J.; Yan, W. S.; Zhu, J. F.; Wu, Z. Y.; Song, W. G. Low-Cost Synthesis of Flowerlike α-$Fe_2O_3$ Nanostructures for Heavy Metal Ion Removal: Adsorption Property and Mechanism. *Langmuir* **2012**, 28, 4573-4579.

[85] Hao, T.; Yang, C.; Rao, X.; Wang, J.; Niu, C.; Su, X. Facile additive-free synthesis of iron oxide nanoparticles for efficient adsorptive removal of Congo red and Cr(VI). *Applied Surface Science* **2014**, 292, 174-180.

[86] Dhal, J. P.; Mishra, B. G.; Hota, G. Ferrous oxalate, maghemite and hematite nanorods as efficient adsorbents for decontamination of Congo red dye from aqueous system. *International Journal of Environmental Science and Technology* **2015**, 12, 1845–1856.

[87] Du, Y.; Fan, H.; Wang, L.; Wang, J.; Wu, J.; Dai, H. α-$Fe_2O_3$ nanowires deposited diatomite: highly efficient absorbents for the removal of arsenic. *Journal of Materials Chemistry A* **2013**, 1 (26), 7729-7737.

[88] Qiu, G.; Huang, H.; Genuino, H.; Opembe, N.; Stafford, L.; Dharmarathna, S.; Suib, S. L. Microwave-Assisted Hydrothermal Synthesis of Nanosized α-$Fe_2O_3$ for Catalysts and Adsorbents. *The Journal of Physical Chemistry C* **2011**, 115 (40) 19626-19631.

[89] Maiti, D.; Mukhopadhyay, S.; Devi, P. S. Evaluation of Mechanism on Selective, Rapid, and Superior Adsorption of Congo Red by Reusable Mesoporous α-$Fe_2O_3$ Nanorods. *ACS Sustainable Chemistry & Engineering* **2017**, 5 (12), 11255-11267.

[90] Kang, D.; Hu, C.; Zhu, Q. Morphology controlled synthesis of hierarchical structured $Fe_2O_3$ from natural ilmenite and its high performance for dyes adsorption. *Applied Surface Science* **2018**, 459, 327-335.

[91] Li, X.; Liu, Y.; Zhang, C.; Wen, T.; Zhuang, L.; Wang, X.; Wang, X. Porous $Fe_2O_3$

microcubes derived from metal organic frameworks for efficient elimination of organic pollutants and heavy metal ions. *Chemical Engineering Journal* **2018**, 336, 241–252.

[92] Hoque, M. I. U.; Yamauchi, Y.; Naidu, R.; Holze, R.; Saidur, R.; Qu, Q.; Chowdhury, A. N. A Facile Synthesis of Hematite Nanorods from Rice Starch and Their Application to Pb(II) Ions Removal. *Chemisty Select* **2019**, 4(13), 3730-3736.

[93] Nalbandian, M. J.; Zhang, M.; Sanchez, J.; Choa, Y. H.; Nam, J.; Cwiertny, D. M.; Myung, N. V. Synthesis and optimization of $Fe_2O_3$ nanofibers for chromate adsorption from contaminated water sources. *Chemosphere* **2016**, 144, 975–981.

[94] Jia, Z.; Liu, J.; Wang, Q.; Li, S.; Qi, Q.; Zhu, R. Synthesis of 3D hierarchical porous iron oxides for adsorption of Congo red from dye wastewater. *Journal of Alloys and Compounds* **2015**, 622, 587-595.

[95] Fei, J.; Cui, Y.; Zhao, J.; Gao, L.; Yang, Y.; Li, J. Large-scale preparation of 3D self-assembled iron hydroxide and oxide hierarchical nanostructures and their applications for water treatment. *Journal of Materials Chemistry* **2011**, 21, 11742.

[96] Wang, J.; Xu, L.; Zhang, Z.; Sun, P.; Fang, M.; Liu, H. Shape-controlled synthesis of α-$Fe_2O_3$ nanocrystals for efficient adsorptive removal of Congo red. *RSC Advances* **2015**, 5, 49696-49702.

[97] Cheng, X. L.; Jiang, J. S.; Jin, C. Y.; Lin, C. C.; Zeng, Y.; Zhang, Q. H. Cauliflower-like α-$Fe_2O_3$ microstructures: Toluene–water interfaceassisted synthesis, characterization, and applications in wastewater treatment and visible-light photocatalysis. *Chemical Engineering Journal* **2014**, 236, 139–148.

[98] Zhong, L. S.; Hu, J. S.; Liang, H. P.; Cao, A. M.; Song, W. G.; Wan, L. J. Self-Assembled 3D Flowerlike Iron Oxide Nanostructures and Their Application in Water Treatment. *Advanced Materials* **2006**, 18, 2426–2431.

[99] Zhu, M.; Wachs, I. E. Iron-Based Catalysts for the High-Temperature Water−Gas Shift

(HT-WGS) Reaction: A Review. *ACS Catalysis* **2016**, 6 (2), 722-732.

[100] Gawade, P.; Mirkelamoglu, B.; Tan, B.; Ozkan, U. S. Cr-free Fe-based water-gas shift catalysts prepared through propylene oxide-assisted sol–gel technique. *Journal of Molecular Catalysis A: Chemical* **2010**, 321 (1-2), 61-70.

[101] Martos, C.; Dufour, J.; Ruiz, A. Synthesis of $Fe_3O_4$-based catalysts for the high-temperature water gas shift reaction. *International Journal of Hydrogen Energy* **2009**, 34 (10), 4475-4481.

[102] Pal, D. B.; Chand, R.; Upadhyay, S. N.; Mishra, P. K. Performance of water gas shift reaction catalysts: a review. *Renewable and Sustainable Energy Reviews* **2018**, 93, 549-565.

[103] Zhu , M.; Wachs, I. E. A perspective on chromium-Free iron oxide-based catalysts for high temperature water-gas shift reaction. *Catalysis Today* **2018**, 311, 2-7.

[104] Rodriguez, J. A.; Hanson, J. C.; Stacchiola, D.; Senanayake, S. D. *In situ/operando* studies for the production of hydrogen through the water-gas shift on metal oxidecatalysts. *Physical Chemistry Chemical Physics* **2013**, 15, 12004−12025.

[105] Natesakhawat, S.; Wang, X.; Zhang, L.; Ozkan, U. S. Development of chromium-free iron-based catalysts for high-temperature water-gas shift reaction. *Journal of Molecular Catalysis A: Chemical* **2006**, 260 (1-2), 82-94.

[106] Zhang, L.; Wu, H. B.; Madhavi, S.; Hng, H. H.; Lou, X. W. Formation of $Fe_2O_3$ Microboxes with Hierarchical Shell Structures from Metal−Organic Frameworks and Their Lithium Storage Properties. *Journal of the American Chemical Society* **2012**, 134 (42), 17388−17391.

[107] Nie, Z.; Petukhova, A.; Kumacheva, E. Properties and emerging applications of self-assembled structures made from inorganic nanoparticles. *Nature nanotechnology* **2010**, 5 (1), 15-25.

[108] Peerakiatkhajohn, P.; Yun, J. H.; Chen, H.; Lyu, M.; Butburee, T.; Wang, L. Stable hematite nanosheet photoanodes for enhanced photoelectrochemical water splitting. *Advanced Materials* **2016**, 28 (30), 6405-6410.

[109] Tian, W.; Wang, X.; Zhi, C.; Zhai, T.; Liu, D.; Zhang, C.; Bando, Y. Ni $(OH)_2$ nanosheet@$Fe_2O_3$ nanowire hybrid composite arrays for high-performance supercapacitor electrodes. *Nano energy* **2013**, 2 (5), 754-763.

# Chapter 3 Leaching and synthesis of Fe-and Mg-based nanomaterials from Victorian brown coal fly ash

The literature review in chapter 2 has shown that the current leaching methods are not suitable the Victorian coal fly ash. In addition, the synthesis of nanosized MgO/$Mg(OH)_2$ and α-$Fe_2O_3$ are mostly from the expensive chemical agents. Therefore, a two-stage countercurrent solid−liquid extraction method was employed to selectively extract Fe and Mg, which were then precipitated out separately upon gradual addition of NaOH. As a feedstock, the extracted Mg and Fe were used to synthesize nanosized α-$Fe_2O_3$ nanosheet and MgO nanosheet. This chapter has been partially published in ***ACS Sustainable Chemistry & Engineering***: **Binbin Qian**, Tahereh Hosseini, Xiwang Zhang, Yue Liu, Huanting Wang and Lian Zhang*, *Coal Waste to Two-Dimensional Materials: Fabrication of α-$Fe_2O_3$ Nanosheets and MgO Nanosheets from Brown Coal Fly Ash,* ***ACS Sustainable Chemistry & Engineering***, 2018, 6, 15982-15987.

## Abstract

High-purity 2-D α-$Fe_2O_3$ nanosheets and MgO nanosheets have been successfully fabricated with a high extraction yield of 45 and 25 *wt* %, respectively, from a brown coal fly ash, an otherwise valueless waste. A two-stage countercurrent solid−liquid extraction method was first employed under the mild conditions of 25−60 °C and atmospheric pressure to selectively extract $Fe^{3+}$ and $Mg^{2+}$, which were then precipitated out separately upon gradual addition of NaOH and subsequent hydrothermal treatment. Finally, 2-D nanosized α-$Fe_2O_3$ nanosheet was obtained with a lamellar morphology, while the synthesized $Mg(OH)_2$ precursor undertook an extra multistep calcination to convert into the respective 2-D MgO nanosheet.

Keywords: Brown coal fly ash, Waste utilization, Multistep acid leaching, Hydrothermal treatment, Nanosheet

## 3.1 Introduction

Since the synthesis of carbon tubes in 1991 [1], nanometric materials with varying morphologies such as nano-ribbons [2], nano-rods [3], nano-wires [4] nano-rings [5] and nano-sheets [6] have been attracting increased attention around the world, owing to their unique properties and potential applications. Among the nanostructured families, the nanosized MgO and $Fe_2O_3$, both as accessible and versatile metal oxide, have been used widely in a variety of applications, including adsorbent [7], catalyst [8], refractory materials [9], cancer therapy [10], antibacterial [11], superconductor [12], battery [13], gas sensing [14] and photoelectrochemical performance [15].

In the past couple of decades, a variety of synthesis methods have been developed and optimized for the manufacturing of nano-MgO and nano-$Fe_2O_3$, including wet precipitation

[16], CVD [17], sol-gel [14,18], solid state reaction [19], thermal treatment [20], hydrolysis [11,21], hydrothermal [22], anodization method [15] and solvothermal method [23]. Although the nano-MgO and nano-$Fe_2O_3$ have been successfully synthesized from these methods, the starting materials are mostly pure chemicals such as $Mg(NO_3)_2 \cdot 6H_2O$ [16], $MgCl_2$ [24], $MgSO_4$ [16], $FeCl_3 \cdot 6H_2O$ [23] and $Fe_2(SO_4)_3 \cdot 7H_2O$ [25], only limited studies have taken the feedstock into account [26,27]. In this sense, from the process sustainability perspective, the utilization of a low-cost feedstock such as Mg or Fe-rich industrial waste is critical. To this end, a brown coal fly ash collected from the brown coal-fired power generation station in the state of Victoria in Australia has been tested. To date, over one million tonnes of brown coal fly ash have been produced annually in the last thirty years in Victoria, most of which is however simply dumped into the ash ponds. This hazardous ash waste poses potential threats to the air, soil and even underground water while little is being used. Traditionally, fly ash is used widely as an additive into cement [28], concrete [29], and agricultural industries [30]. Some fly ashes are also used to synthesize nanomaterials such as nanosilica [31], zeolite [32,33] and CNT [34]. However, different from the bituminous coal fly ashes, the brown coal fly ash in Victoria contains relatively high concentrations of metallic cations, particularly $Fe^{3+}$ and $Mg^{2+}$. It is thus impractical to use the brown coal fly ash in the traditional ways mentioned above. Instead, we hypothesized that the (Fe, Mg)-rich Victorian Brown coal fly ash could be a good raw material for the synthesis of α-$Fe_2O_3$ nanosheets and MgO nanosheets.

Through a hydrometallurgical leaching process, previous works have extracted Fe or Mg from fly ash while with low extraction yields [35-37]. Based on this special brown coal fly ash, Hosseini et al. [37] found that there is a need for further research to develop an efficient extraction process which breaks the structure of the magnesium ferrite inverse-spinels to release the $Fe^{3+}$ and $Mg^{2+}$. The main challenge is that the $NH_4Cl$ is too weak to cleave the

strong affinity between Mg and Fe within the $MgFe_2O_4$ matrix, which would otherwise still remain in the final residue and has to be returned as a waste to the fly ash pond. This forms our hypothesis in this study for the use of a strong acid such as $H_2SO_4$ as an alternative leaching agent. Therefore, a novel two-step counter-current leaching method using $H_2SO_4$ as the leaching agent, as shown in **Figure 3-1**, is further employed to enforce the extraction of $Fe^{3+}$ and $Mg^{2+}$ out of the ferrite inverse-spinels in the brown coal fly ash. It is desirable that the process developed here and the results are applicable to the other brown coal ashes in the world rich in magnesium ferrite, such as the ash samples from the pulverized brown coal-fired power plants from Romania and Poland [38], the Mg-rich process tailings and waste rocks [39], and even the acid activation of Mg-abundant clay minerals [40].

In this section, we for the first time report the extraction results of the $Mg^{2+}$ and $Fe^{3+}$ out of the inverse-spinel ferrites rich brown coal fly ash via a two-stage counter-current solid-liquid leaching method through the use of sulphuric acid. Additionally, efforts were made to synthesize two-dimensional $\alpha$-$Fe_2O_3$ nanosheets and MgO nanosheets based on the resultant leachate. As far as the authors are aware, such an effort has yet to be reported for any fly ash sample across the world. The results achieved are thus expected to shed new insights on the value-added utilisation of low-rank coal fly ash samples.

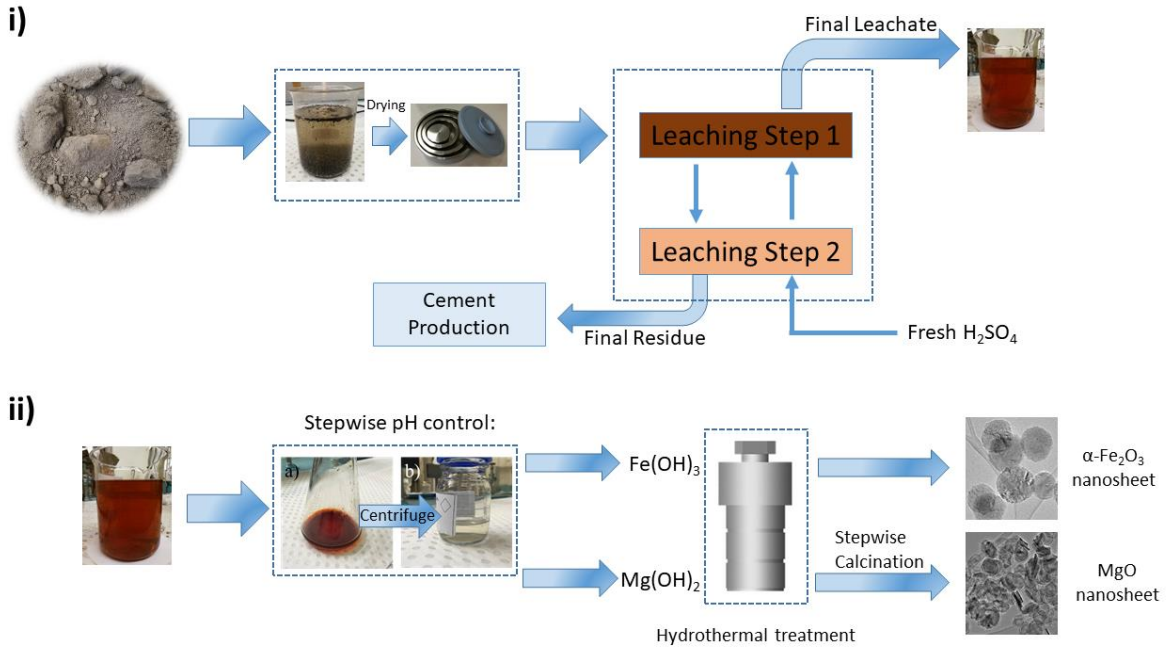


**Figure 3-1** Schematic illustration of (i) the two-step counter-current leaching method for Victorian brown coal fly ash and (ii) α-$Fe_2O_3$ nanosheets and MgO nanosheets synthesized from final leachate in (i)

## 3.2 Experimental section

### 3.2.1 Chemicals, experiment and instruments

The fly ash sample was collected as dry powders from the Energy Australia Yallourn power plant located in Latrobe Valley, Victoria, Australia. The as-received fly ash sample was initially washed with water with a liquid to solid (L/S) mass ratio of 10 to remove the unburnt carbon and water-soluble species such as sodium and potassium salt. Subsequently, the fly ash samples after water-washing were dried in an oven at 120 °C in 12 hours and were ground using a tungsten-carbide vibratory ring pulverizer, producing a particle size less than 90 μm prior to use. Pure NaOH was purchased from Sigma-Aldrich with a purity of 99.99% and pure $Na_2CO_3$ was also purchased from Sigma-Aldrich with a purity of 99.95%. Milli-Q water was used in throughout the experiments. X-ray Diffraction (XRD) data were collected from the XRPD

patterns recorded on a Rigaku SmartLab 3000A diffractometer with Cu Ka radiation (λ =0.15406 nm). The X-ray tube was operated at 40 kV and 15 mA. X-ray fluorescence spectroscopy (XRF) was used to determine the chemical compositions of raw fly ash and leaching residues, extraction yield of Fe, Mg and Ca was calculated based on **Equation 3-1**

$$Yield\ \% = \frac{M_{raw}X_{raw} - M_{residue}X_{residue}}{M_{raw}X_{raw}} \times 100\% \qquad \textbf{Equation 3-1}$$

Where Yield% refers to the extraction yield of Fe, Mg and Ca, M refers to the mass of either raw fly ash or its residue, X is the XRF-quantified concentration (*wt*%) of $Fe_2O_3$, MgO and CaO. The subscripts, raw and residue are for the raw fly ash and its residue, respectively.

Inductively coupled plasma optical emission spectroscopy (ICP-OES, Optima 7000 DV, PerkinElmer) was used to quantify the concentration of Al, Na, Fe, Mg and Ca cations in leachates. Scanning Electron Microscopy (SEM): The microstructures of MgO nanosheets were observed using scanning electron microscopy (SEM) (FEI Nova NanoSEM 450 FEGSEM) in the Monash Centre for the Electron Microscopy (MCEM). SEM sample of MgO nanosheet was prepared by placing a 1 cm-diameter drop of dilute MgO nanosheet ethanol suspension on a 1×1 cm section of silicon wafer and allowing solvent to evaporate. The wafer was then attached to an aluminium sample holder with conductive carbon tab. Finally, the sample was coated with gold to eliminate any possible charging effect. Transmission Electron Microscopy (TEM): Images of the nanostructured MgO details and SAED patterns were recorded using TEM (Model FEI Tecnai G2 T20 TWIN TEM) with an accelerating voltage of 200 kV at the Monash Centre for Electron Microscopy. The MgO nanosheets redispersed ultrasonically in ethanol prior to deposition on a TEM copper grids with thin carbon films. A droplet of the solution was allowed to sit on the TEM grid for 5-10 minutes until ethanol is completely evaporated. There was then no further treatment of samples prior to electron

microscopy analysis.

### 3.2.2 Leaching process

After pre-treatment of Yallourn fly ash, analytical grade hydrochloric acid (HCl, 32%) was used as the leaching agent. 10 g of above fly ash or first stage residue and 20 mL of HCl (Liquid/Solid ratio = 2 mL/g) were mixed in a closed 250 mL conical flask containing a magnetic stir bar on a thermostatically controlled water bath (T= room temperature (RT) or high temperature (HT, 40 °C or 60 °C)), stirring rate was set at 300 rpm throughout the experiment. The leachate was sampled over time, filtered and prepared for ICP-OES analysis. After the final setting time, the slurry was immediately filtered via a vacuum. Subsequently, the residual was washed and dried at 105 °C and the weight was measured for further analysis. **Figure 3-2** shows the whole process of multi-step leaching method.

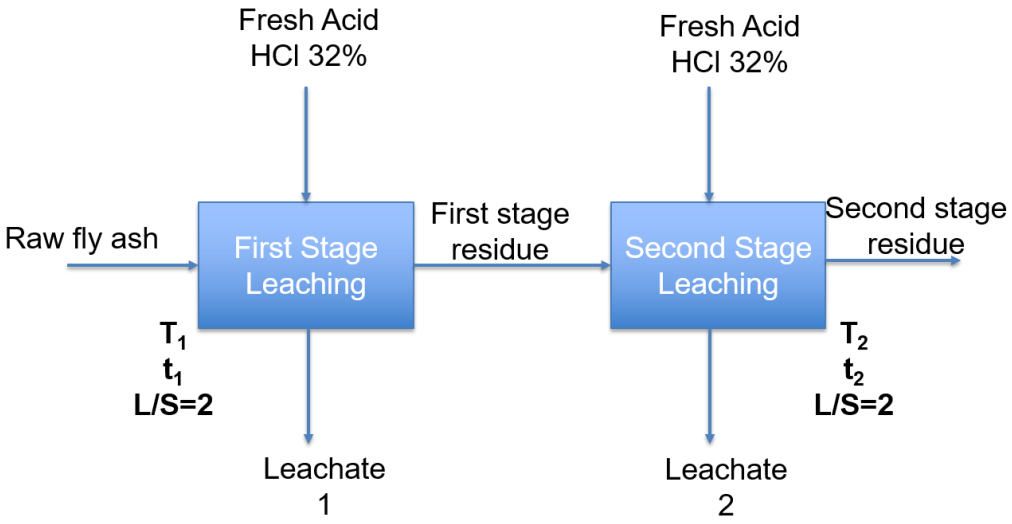


**Figure 3-2** Block flow diagram of the two-stage cross current leaching

### 3.2.3 Impurity Precipitation

After leaching experiment, the obtained leachate will contain $Fe^{3+}$, $Mg^{2+}$, $Al^{3+}$ and $Ca^{2+}$. Step

1, 1 M NaOH will be added dropwise to leachate and the final pH is set at 4.7-5.2. This step will precipitate most of the $Fe^{3+}$ and $Al^{3+}$ while trace amount of $Mg^{2+}$ will retain and through high speed centrifuge (8000-10000 rpm), $Fe^{3+}$-$Al^{3+}$ precipitation slurry and $Mg^{2+}$-$Ca^{2+}$ leachate were obtained. Step 2, for the precipitation slurry, water was added and magnetic stir was used to make them a homogeneous turbid liquid and add 1 M NaOH to set the final pH of 13. This step will remove the $Al^{3+}$ because of this reaction, as shown in **Equation 3-2**:

$$Al(OH)_3 + NaOH \rightarrow NaAlO_2 + 2H_2O \qquad \textbf{Equation 3-2}$$

Then the slurry will be centrifuged and use water wash to obtain the final neutral and high-purity $Fe(OH)_3$ precipitation. The $Fe(OH)_3$ will be used for hydrothermal synthesis. Step 3, for the $Mg^{2+}$-$Ca^{2+}$ leachate, 1M $Na_2SO_4$ will be added dropwise to remove the $Ca^{2+}$ because of this reaction, as shown in **Equation 3-3**:

$$CaCl_2 + Na_2SO_4 \rightarrow CaSO_4 \downarrow + 2NaCl \qquad \textbf{Equation 3-3}$$

Then the slurry will be centrifuged and use water wash to obtain the final neutral and high-purity $Mg(OH)_2$ precipitation. The $Mg(OH)_2$ will be used for hydrothermal synthesis.

### 3.2.4 Hydrothermal synthesis

The obtained $Fe(OH)_3$ or $Mg(OH)_2$ precipitation will be put in a beaker and added with water by vigorous stirring to make a homogeneous slurry. Subsequently, the slurry will be transferred into a Teflon-lined autoclave of 120 mL. Then the autoclave will be put in an oven at 180 °C for a duration of 12 h. After the hydrothermal synthesis, the autoclave will be cooled down to room temperature naturally. The obtained precipitates will be centrifuged, washed with Milli-Q water and ethanol sequentially to reduce the agglomeration, and later further dried at 80 °C for 2 h for later analysis.

## 3.3 Result and discussion

### 3.3.1 Fly Ash Properties

**Figure 3-3** shows the raw ash particle size analysis via sieving, from which it is concluded that the ash pond sample is a mixture of fly ash, water and bottom ash. Around half of the sample is in the large particle size bin of >500 μm. **Figure 3-4** shows the crystal phases in the ash sample by X-ray diffraction (XRD) pattern. It is clear that magnesioferrite ($MgFe_2O_4$) and quartz ($SiO_2$) are the most dominant crystal phases and each particle size range has similar crystal phases. **Table 3-1** shows the chemical compositions of the fly ash for each size distribution in terms of most stable oxides quantified by XRF. Iron is the most abundant element, followed by magnesium, silica and aluminum in a descending sequence.

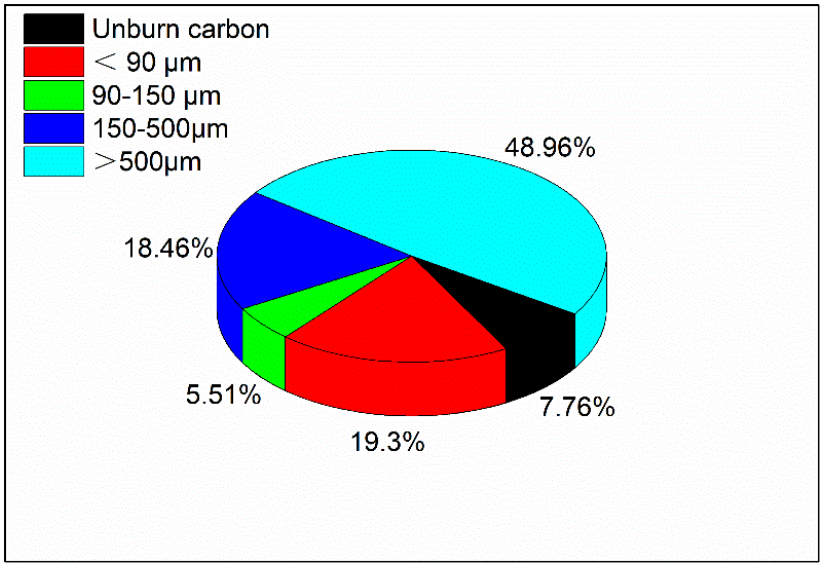


**Figure 3-3** Particle Size Distribution

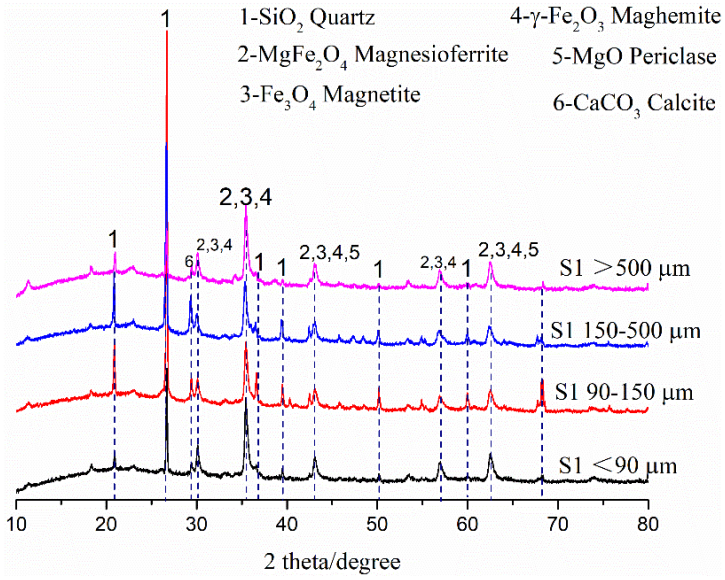


**Figure 3-4** XRD patterns of different particle size of ash pond sample

**Table 3-1** Elemental Compositions for ash pond sample, *wt%*

| | **S1 <90 μm** | **S1 90-150 μm** | **S1 150-500 μm** | **S1>500 μm** |
|---|---|---|---|---|
| $SiO_2$ | 16.13 | 28.94 | 21.2 | 10.98 |
| $Al_2O_3$ | 10.68 | 11.21 | 9.62 | 10.22 |
| $Fe_2O_3$ | 40.99 | 27.61 | 29.73 | 41.41 |
| CaO | 5.69 | 7.31 | 11.9 | 6.15 |
| MgO | 21.4 | 19.32 | 20.5 | 25.49 |
| $Na_2O$ | 0.19 | 0.43 | 0.92 | 0.36 |
| $SO_3$ | 2.53 | 3.13 | 4.3 | 3.12 |
| MnO | 0.55 | 0.36 | 0.39 | 0.59 |
| $TiO_2$ | 0.91 | 0.95 | 0.7 | 0.76 |

### 3.3.2 Pre-treatment

For the above ash sample, sulphur removal was done by testing two different methods: (1)

washing by $Na_2CO_3$ solution (M=0.24 mol/L) only and (2) washing by $Na_2CO_3$ solution with a continuous bubbling of $CO_2$ at 10 mL/min.

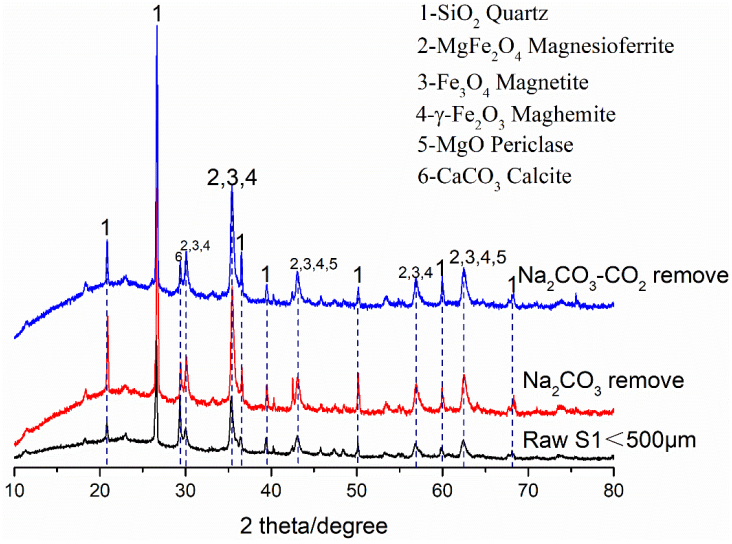


**Figure 3-5** XRD patterns of fly ash after sulfur removal

**Table 3-2** Elemental Compositions for sulfur removal stage, *wt%*

| | **Raw S1＜500 μm** | **$Na_2CO_3$ wash** | **$Na_2CO_3$-$CO_2$ wash** |
|---|---|---|---|
| $SiO_2$ | 12.05 | 12.34 | 12.56 |
| $Al_2O_3$ | 7.28 | 7.28 | 8.47 |
| $Fe_2O_3$ | 33.35 | 33.27 | 29.73 |
| CaO | 5.19 | 5.4 | 5.71 |
| MgO | 14.21 | 14.38 | 17.49 |
| $SO_3$ | 1.42 | 0.82 | 1.33 |
| LOI% | 24.33 | 23.63 | 22.43 |

**Figure 3-5** shows the XRD patterns before and after sulphur removal. It is obvious that the sulphur-removal residuals have similar crystal phases. Through the XRF analysis of samples before and after the sulphur removal stage in **Table 3-2**, it was found that the contents of $SO_3$

only decrease from 1.42% to 0.82% and 1.33% with $Na_2CO_3$ solution method and $Na_2CO_3$ solution with a continuous bubbling of $CO_2$ method, respectively. Since the sulphur removal is insignificant, this step was removed in later leaching experiments.

### 3.3.3 Leaching Process

**Two-Stage Cross-Flow Hydrochloric Acid Leaching at High Temperature (60° C)-High Temperature (60° C)**

In the first stage, raw fly ash was leached with 60 °C and L/S of 2 using 32%HCl. In the second stage, the leaching residual from the first stage underwent the same leaching conditions. The effect of different leaching time on extraction yields was investigated from both stages in order to optimize a best condition in this leaching method.

**First Stage Leaching**

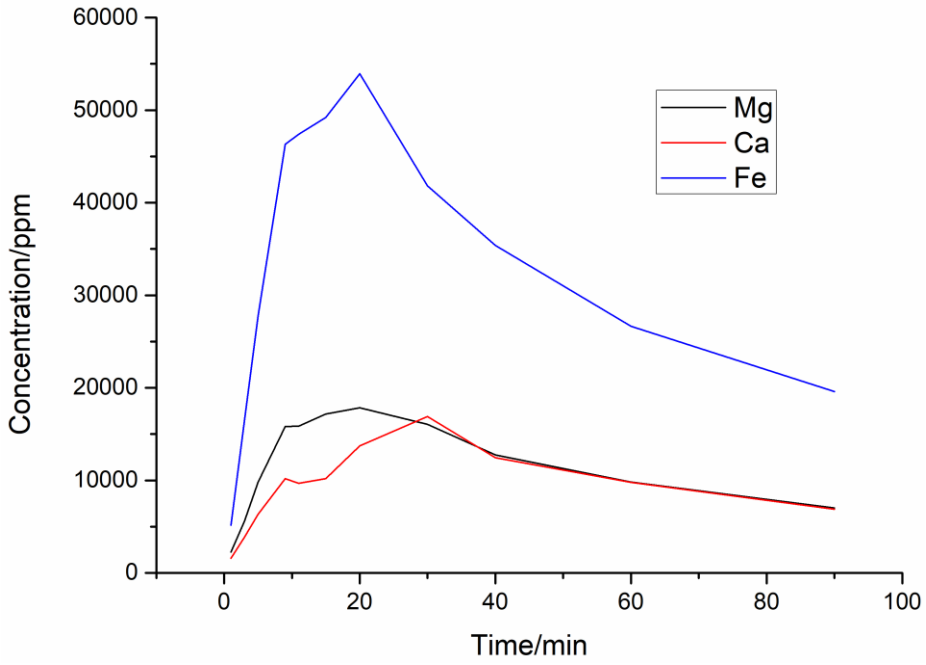


**Figure 3-6** Concentration profiles for dissolved $Ca^{2+}$, $Mg^{2+}$ and $Fe^{3+/2+}$ from the leaching of

raw fly ash

**Figure 3-6** is the ICP analysis of different cations in the leachates in this stage. Obviously, the overall trend for all the elements demonstrates a maximum peak at around 20 min. For $Mg^{2+}$ and $Fe^{3+}$, the concentrations increased rapidly in the first 20 min and reached their maximum values of 17,840 ppm and 51,940 ppm. However, they began to decrease afterwards. In terms of the $Ca^{2+}$ concentration, it slowly increased in the first 30 min to reach 13712 ppm, and then decreased after 30 min. Therefore, the duration of 20 min is the optimum time for the first stage leaching at 60 °C.

**Table 3-3** Composition of fly ash and water washed residue after leaching

| | **Composition (*wt%*)** | | **Extraction Yield (%)** |
|---|---|---|---|
| | S removed FA | First stage HCl leached | |
| $SiO_2$ | 12.34 | 30.44 | 19.29 |
| $Al_2O_3$ | 7.28 | 8.14 | 63.43 |
| $Fe_2O_3$ | 33.27 | 16.86 | 83.42 |
| CaO | 5.41 | 0.74 | 95.71 |
| MgO | 14.38 | 3.45 | 92.15 |
| $Na_2O$ | 0.82 | 0.08 | 96.93 |
| $SO_3$ | 0.81 | 2.43 | 2.45 |
| LOI | 23.63 | 33.54 | - |

**Table 3-3** shows the XRF analysis for the residue after first stage leaching at 60 °C as well as

the extraction yields for the major elements. It is clear that after this stage, the extraction yield for $Fe^{3+}$, $Mg^{2+}$ and $Ca^{2+}$ is 83.42%, 92.15% and 95.71%, respectively. Residual analysis shows that the remained $Fe_2O_3$, CaO and MgO are 16.86%, 0.7% and 3.45%, respectively.

**Second Stage Leaching**

**Figure 3-7** shows the final residue from leaching at 90 min. The reason why the residue is dark is because there are still some unburn carbon remained in the fly ash, which can be confirmed by the XRF analysis (LOI) in **Table 3-3**.

**Figure 3-7** Residue from the second stage leaching at 90 min

**Figure 3-8** shows the XRD patterns for different leaching residuals at 30, 60 and 90 min leaching time. It demonstrates that after second step leaching, quartz is the predominant phase in all the three residues and only a very little amount of magnesioferrite after this stage. Perhaps, it could be used as an additive into concrete (fine aggregates).

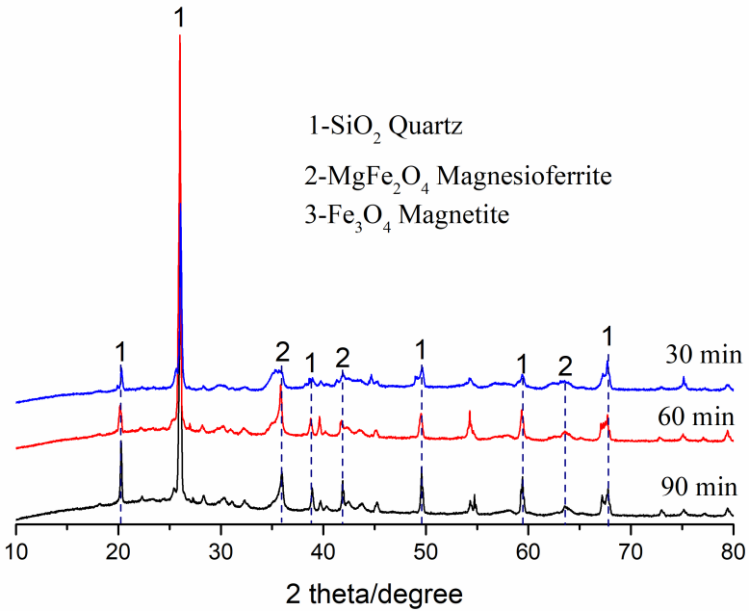


**Figure 3-8** XRD patterns of residues after second stage leaching at different time

**Table 3-4** shows the XRF analysis after second stage leaching at 60 °C as well as the extraction yields for each element. After this stage of 90 min, the extraction yields for $Fe^{3+}$, $Mg^{2+}$ and $Ca^{2+}$ reach 53.83%, 34.84% and 38.98%, respectively. Residual analysis shows that the remaining $Fe_2O_3$, CaO and MgO account for 9.61%, 0.53% and 2.77% of the starting amount, respectively.

**Table 3-4** XRF and yield of second leaching

| | **Residue Composition (*wt%*)** | | | **Extraction Yield (%)** | | |
|---|---|---|---|---|---|---|
| | 30 min | 60 min | 90 min | 30 min | 60 min | 90 min |
| $SiO_2$ | 36.32 | 36.05 | 37.92 | | | |
| $Al_2O_3$ | 9.32 | 8.92 | 8.64 | 0 | 3.25 | 13.97 |
| $Fe_2O_3$ | 13.23 | 11.08 | 9.61 | 29.86 | 41.95 | 53.83 |
| CaO | 0.62 | 0.58 | 0.53 | 21.61 | 28.07 | 38.98 |

| | | | | | | |
|---|---|---|---|---|---|---|
| MgO | 3.77 | 3.16 | 2.77 | 2.22 | 19.1 | 34.84 |
| $SO_3$ | 1.74 | 1.93 | 1.91 | 35.97 | 30 | 36.17 |
| $TiO_2$ | 1.42 | 1.49 | 1.6 | | | |
| LOI | 32.9 | 35.86 | 36.21 | | | |

**Figure 3-9** shows the XRD patterns for raw fly ash and all the leaching residues from the two-stage cross-flow hydrochloric acid leaching at high temperature(60ºC)-high temperature(60ºC). It demonstrates that for all the residues, quartz is the predominant phase. A prolonged leaching time will further decrease the amount of magnesioferrite remained in the residual since its intensity in XRD patterns became weaker. However, increasing leaching time will not significantly improve the extraction yields of these elements. As shown in **Figure 3-10**, the overall comparison of extraction yields at 20 min first stage, 30 min second stage, 60 min second stage and 90 min second stage: $Mg^{2+}$ is 92.15%, 92.32%, 93.65% and 94.88%. $Fe^{3+}$ is 83.42%, 88.37%, 90.37% and 92.34%. $Ca^{2+}$ is 95.71%, 96.64%, 96.92% and 97.39%. All the increases are marginal with the change on the second leaching time.

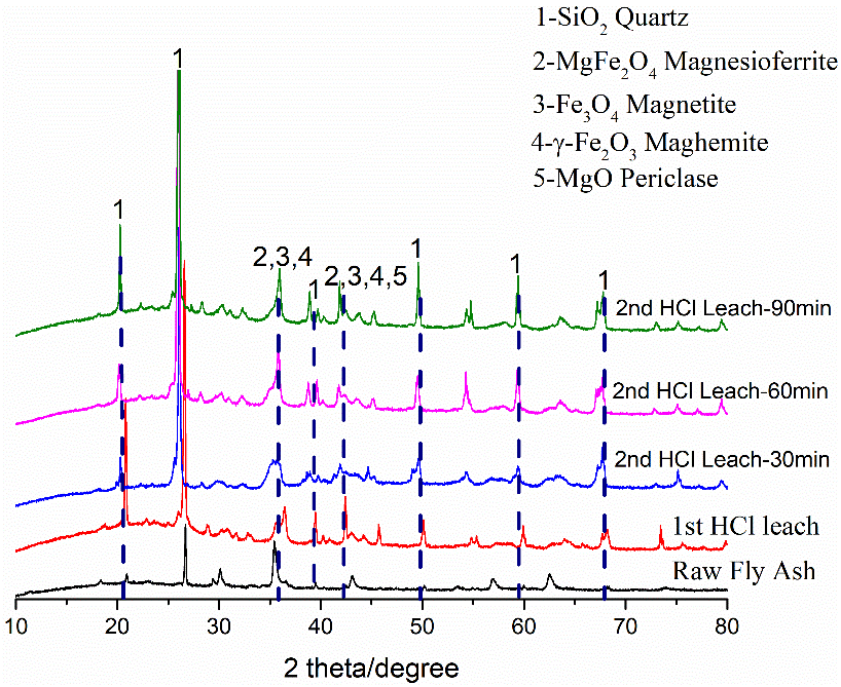


**Figure 3-9** Comparison of XRD patterns of samples before and after HCl leaching

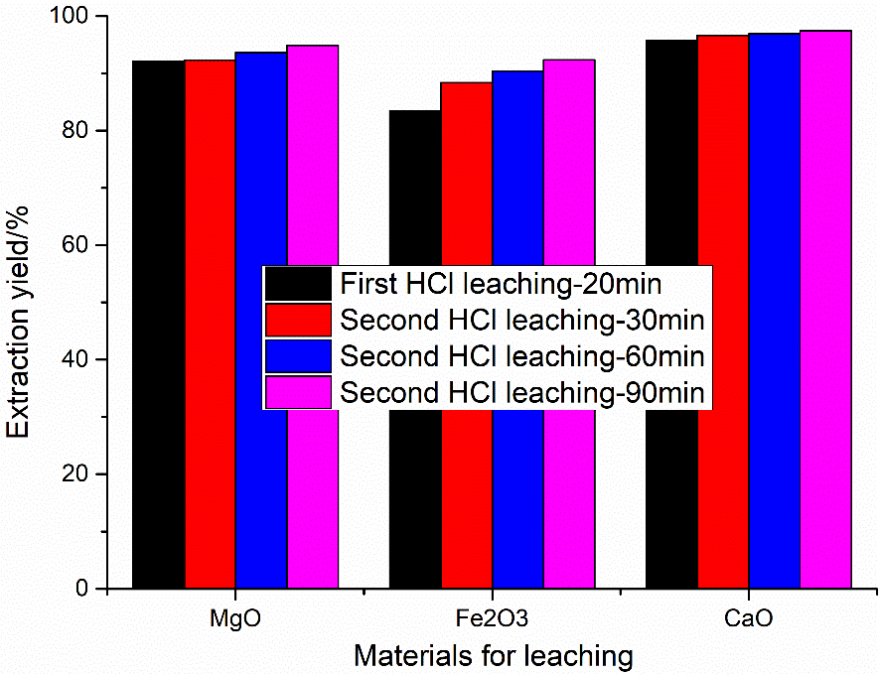


**Figure 3-10** Extraction yields of major elements

In addition to the two-step cross-current both at high temperature (HT) 60°C leaching method, other leaching methods such as one step room temperature (RT), two-step both at RT, one-step at 60°C, RT-HT at 40°C, RT-HT at 60°C, and HT-HT both at RT-HT at 60°C with counter-

current method were also conducted to compare the extraction yield of Fe, Mg and Ca. **Figure 3-11** shows overall comparison of extraction yields for eight different leaching methods: (1) one step at room temperature, (2) two-step both at room temperature, (3) one step high temperature at 60°C, (4) first step room temperature -second step high temperature at 40°C, (5) first step room temperature - second step high temperature at 60°C, (6) two-step both at high temperature of 60°C, (7) two step counter-current both at high temperature of 60°C and (8) two step counter-current both at high temperature of 60°C using sulfuric acid. Considering the extraction yields of the three elements, two-step both at high temperature of 60°C leaching is apparently the best method of all. However, it is obvious that the first step room temperature - second step high temperature at 60°C leaching method is also a good alternative method because the extraction yields of Fe, Mg and Ca only decrease 1.75%, 0.44% and 0.93%.

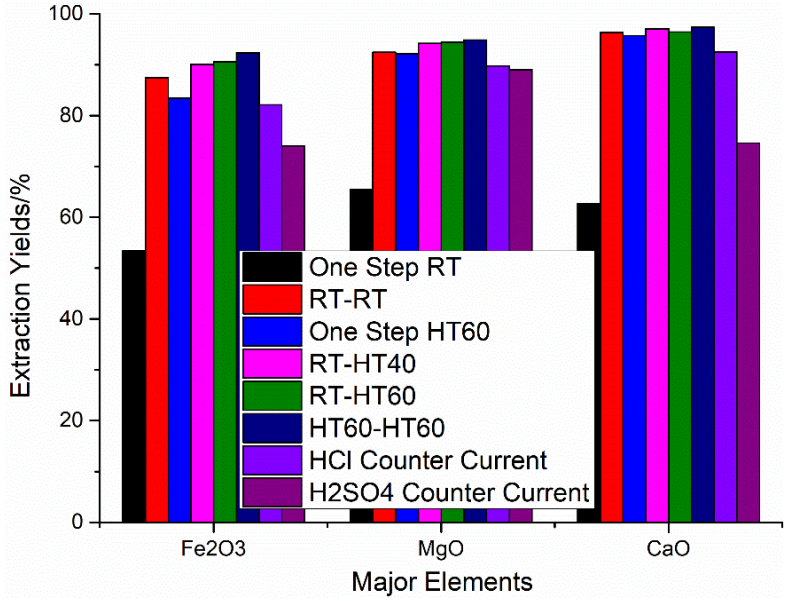


**Figure 3-11** Comparison of extraction yields of major elements from all leaching methods

**Table 3-5** XRF for residuals from 8 leaching methods

| | **Residue Composition (*wt%*)** | | | | | | | | |
|---|---|---|---|---|---|---|---|---|---|
| Oxide | Raw Ash | One Step RT | RT-RT | One Step HT60 | RT-HT40 | RT-HT60 | HT60-HT60 | HCl-Counter Current | $H_2SO_4$-Counter Current |
| $SiO_2$ | 12.05 | 13.95 | 33.94 | 30.44 | 33.82 | 35.69 | 37.92 | 35.83 | 24.02 |
| $Al_2O_3$ | 7.28 | 5.88 | 8.8 | 8.14 | 9.07 | 8.78 | 8.64 | 8.55 | 6.37 |
| $Fe_2O_3$ | 33.35 | 22.89 | 15.59 | 16.86 | 15.86 | 11.47 | 9.61 | 12.19 | 20.41 |
| CaO | 5.2 | 2.85 | 0.71 | 0.7 | 0.73 | 0.67 | 0.53 | 0.79 | 3.11 |
| MgO | 14.21 | 7.22 | 4.02 | 3.45 | 3.93 | 2.9 | 2.77 | 2.98 | 3.67 |
| $SO_3$ | 1.42 | 5.32 | 2.21 | 2.43 | 2.47 | 3.22 | 1.91 | 2.62 | 7.65 |
| $TiO_2$ | 0.79 | 0.72 | 1.49 | 1.59 | 1.53 | 1.46 | 1.62 | 1.64 | 1.02 |
| LOI | 24.33 | 40.15 | 32.92 | 33.54 | 32.18 | 35.52 | 36.21 | 34.95 | 33.44 |

**Table 3-5** shows the XRF analysis for the leaching residuals from the eight leaching methods. In accordance with the highest extraction yields, the best residue is from the two-step cross current leaching method with temperature of both 60ºC. The content of $Fe_2O_3$, CaO and MgO is 9.61%, 0.53% and 2.77%. Similarly, the residual from first step room temperature -second step high temperature at 60ºC leaching method is also competitive with the content of $Fe_2O_3$, CaO and MgO is 11.47%, 0.67% and 2.9%.

### 3.3.4 Hydrothermal synthesis

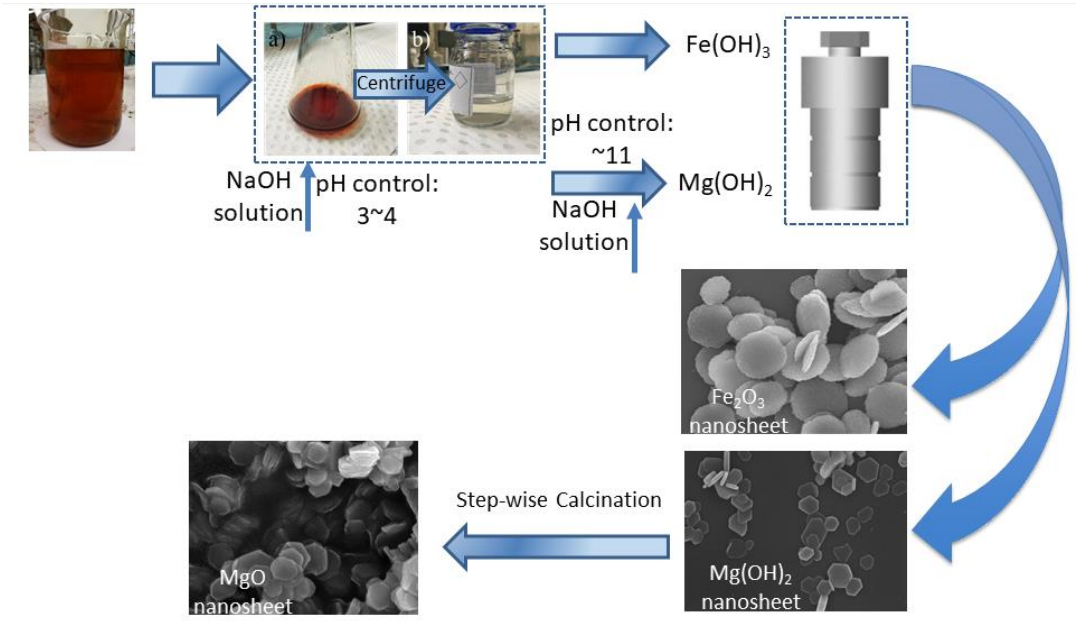


**Figure 3-12** Schematic illustration of the synthesis process

**Figure 3-12** shows the process from leachate to final $Fe_2O_3$/$Mg(OH)_2$/MgO nanoparticles.

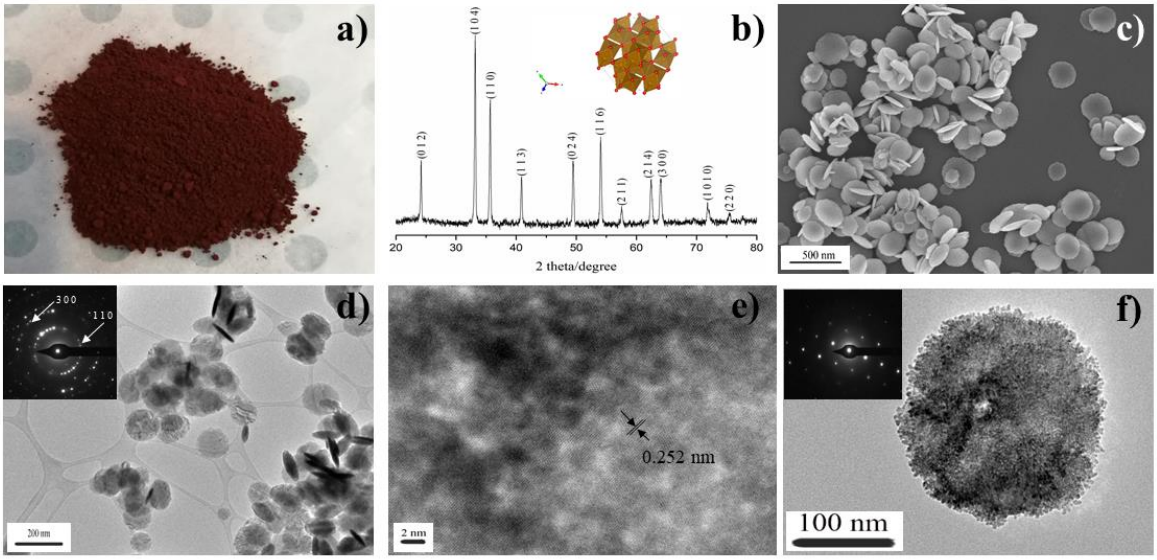


**Figure 3-13** a) α-$Fe_2O_3$ nanosheets sample; b) XRD pattern (Inset: α-$Fe_2O_3$ polyhedral model); c) SEM image; d) HRTEM image (Inset: SAED pattern from d); e) HRTEM with lattice fringes; f) a single α-$Fe_2O_3$ crystal (Inset: SAED pattern from f)

**Figure 3-13(a)** shows a typical sample for as-synthesized α-$Fe_2O_3$ nanosheets. XRD pattern in **Figure 3-13(b)** depicts the crystal details for α-$Fe_2O_3$, indicating that it is the hematite structure (ICSD #22505) in the trigonal system with the lattice constant of a = 5.038 Å and c = 13.772 Å. The surface morphology of the as-synthesized α-$Fe_2O_3$ was observed by high-resolution SEM imaging in **Figure 3-13(c)**. It is confirmed that the as-synthesized α-$Fe_2O_3$ nanosheets exhibit a diameter of 200–400 nm and its nanostructure is different from the previous results using additives. Through using polyethylene glycol and sodium acetate, hexagonal nanosheets or quasi-spherical nanoplates of hematite were synthesized [23], through the use of glycine, cubic-like or spherical hematite nanoparticles can be obtained [41].

**Figure 3-13(d), (e)** and **(f)** further show the representative high-resolution TEM images of the as-synthesized α-$Fe_2O_3$ nanosheet. As shown in **Figure 3-13(d)**, these products are confirmed to display a round lamellar morphology with an averaged size of ~300 nm. Some of the α-$Fe_2O_3$ particles stand straight on the copper grid, indicating a thickness of approximately 50 nm. Inset is the selected area electron diffraction (SAED) patterns taken from **Figure 3-13(d)**, exhibiting the inner-outside rings corresponding to (1 1 0) and (3 0 0) planes of α-$Fe_2O_3$ and the incomplete diffraction ring spots imply the disordered and unsystematic crystal orientation for nanosized α-$Fe_2O_3$. **Figure 3-13(e)** illustrates a HRTEM image of as-synthesized α-$Fe_2O_3$ nanosheet, where the lattice fringes separated by the d-spacing of 0.252 nm can be indexed to the (1 1 0) plane. **Figure 3-13(f)** illustrates a single α-$Fe_2O_3$ nanosheet with obvious round outline. The corresponding SAED pattern (Inset) can be indexed to the [0 0 1] zone axis diffraction of α-$Fe_2O_3$ nanosheets for {1 1 0} crystal facts.

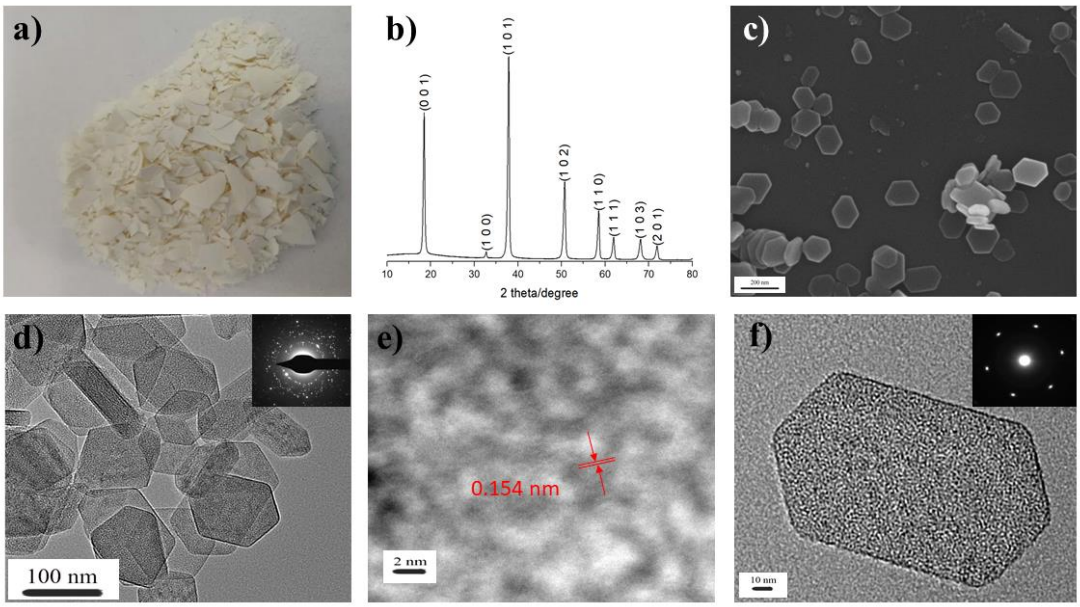


**Figure 3-14** a) $Mg(OH)_2$ nanosheets sample; b) XRD pattern; c) SEM image; d) HRTEM image (Inset: SAED pattern from d); e) HRTEM with lattice fringes; f) a single $Mg(OH)_2$ crystal (Inset: SAED pattern from f)

**Figure 3-14(a)** shows a typical sample for as-synthesized $Mg(OH)_2$ nanosheets. The crystal structure of the as-synthesized $Mg(OH)_2$ nanosheets was determined by XRD and shown in **Figure 3-14(b)**. It is clear that all the diffraction peaks can be indexed to the brucite structure (ICSD #64722). The surface morphology of the as-synthesized $Mg(OH)_2$ was observed by high-resolution SEM imaging in **Figure 3-14(c)**. It is confirmed that the as-synthesized $Mg(OH)_2$ nanosheets exhibit a diameter of 100–200 nm. **Figure 3-14(d)**, **(e)** and **(f)** further depict the representative high-resolution TEM images of the as-synthesized MgO nanosheet. As shown in **Figure 3-14(d)**, the $Mg(OH)_2$ displays a hexagonal lamellar morphology with an averaged size of ~100 nm. It is also notable that the particles standing straight on the copper grid may demonstrate the thickness between 10 nm and 30 nm. Insect is the SAED for nanosheets in **Figure 3-14(d)**, the disorderly and unsystematic diffraction spots imply the various crystal orientation for $Mg(OH)_2$. **Figure 3-14(e)** illustrates HRTEM image of as-

synthesized $Mg(OH)_2$ nanosheet, the lattice fringes separated by a distance of 0.154 nm which can be attributed to the (1 1 0) plane of $Mg(OH)_2$. **Figure 3-14(f)** illustrates an individual $Mg(OH)_2$ nanosheet with obvious hexagonal outline. The SAED pattern, with calculated d-spacing 1.795 Å, can be indexed to the (1 0 2) plane of brucite structure $Mg(OH)_2$.

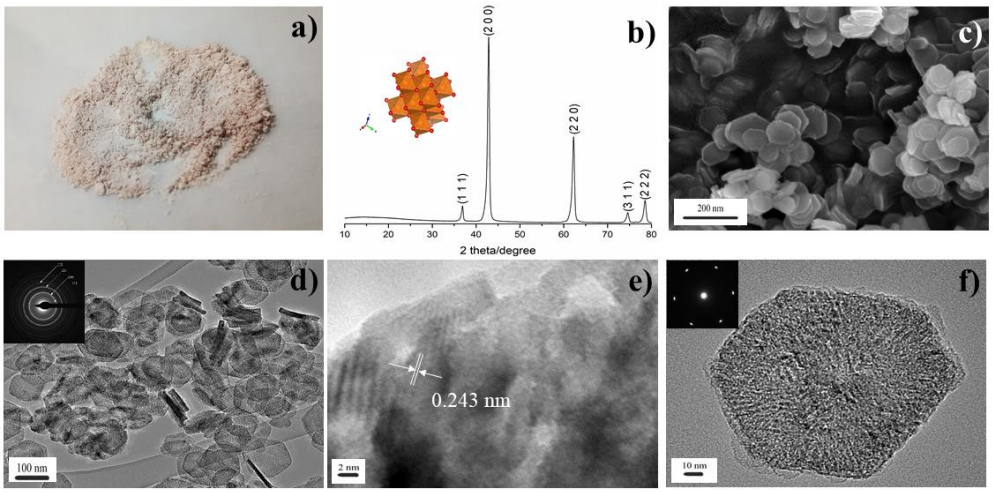


**Figure 3-15** a) MgO nanosheets sample; b) XRD pattern (Inset: MgO polyhedral model); c) SEM image; d) HRTEM (Inset: SAED pattern from d); e) HRTEM with lattice fringes; f) a single MgO crystal (Inset: SAED pattern from f)

**Figure 3-15(a**) shows the final product of the MgO nanosheets. The crystal structure of the as-synthesized MgO nanosheets was determined by XRD and shown in **Figure 3-15(b)**. It is clear that all the diffraction peaks can be indexed to the FCC periclase structure (ICSD #26958) with a lattice constant of a = 4.203 Å. However, one noteworthy exception has been observed here: the diffraction peaks of the synthesized nano-MgO show a slight shift from the periclase standard, due to a trace of magnesium iron oxide ($Mg_{1-x}Fe_xO$) formed by $Fe^{3+}$ impurity being incorporated into MgO during the precipitation process. A low amount of $Fe^{3+}$ can dissolve into MgO lattice producing very little distortion that is undetectable by the XRD [42].

The surface morphology of the as-synthesized MgO was observed by a high-resolution SEM imaging in **Figure 3-15(c)**. It can be seen that the MgO nanosheet has been successfully synthesized. The MgO nanosheets exhibit a diameter of 100–200 nm, which is consistent with the previous results using $NH_3 \cdot H_2O$ or ethylenediamine as the precipitation agent and chemical-grade $MgSO_4$ as the feedstock [16]. Therefore, the averaged diameter of 100-200 nm synthesized here is applicable and able to show a distinctively different property compared to the bulk sample. For the catalyst applications, a minimum diameter of 100 nm is essential for the MgO nanosheet [43].

Additionally, it is noteworthy that the overall hexagonal morphology of these lamellar-like particles is consistent with the hexagonal crystallographic characteristics of brucite ($Mg(OH)_2$), evidencing that the structure of brucite was well retained in the multi-step calcination stage.

**Figure 3-15(d), (e)** and **(f)** further depict the representative high-resolution TEM images of the as-synthesized MgO nanosheet. As shown in **Figure 3-15(d)**, these products are further confirmed to display a hexagonal lamellar morphology with an averaged size of ~100 nm. By checking the MgO particles standing straight on the copper grid, it is also referable that these nanosheets have a thickness of approximately 10 nm. Such a thickness is still comparable with those synthesized from using pure chemicals, which can be attributed to the strong dispersion effect of ethanol added to the hydrothermal precipitation stage [44]. Inset is the selected area electron diffraction (SAED) patterns taken from **Figure 3-15(d)**, exhibiting inner-outside rings corresponding to (1 1 1), (2 0 0), (2 2 0) and (2 2 2) planes of MgO. **Figure 3-15(e)** illustrates the HRTEM image of as-synthesized MgO nanosheet, the lattice fringes separated by a distance of 0.243 nm which can be attributed to the (1 1 1) plane of MgO. **Figure 3-15(f)** illustrates an individual MgO nanosheet with an obvious hexagonal outline. The six-fold symmetry of the

corresponding SAED pattern (Inset) can be indexed to the [1 -1 1] or [1 -1 -1] zone axis diffraction of MgO nanosheets for {2 2 0} crystal facts.

## 3.4 Conclusions

In summary, 2-D α-$Fe_2O_3$ and MgO nanosheets have for the first time been successfully synthesized from brown coal fly ash, an otherwise valueless waste. This study differs from the previous researches that focused on the cement additive or the

synthesis of alumina and zeolite from fly ash. Instead, it opens a new application for brown coal fly ash that is mostly landfilled or used as a low-value additive in the construction industry. The synthesized two-dimensional nano-$Fe_2O_3$ and nano-MgO can be used in a broad variety of high-value applications. For the Victorian brown coal fly ash used here, the typical results confirmed a mass yield of around 25% and a purity of 98.23 *wt* % for the final MgO nanosheet and 45% with a purity of 94.34 *wt*% for α-$Fe_2O_3$ nanosheet. The α-$Fe_2O_3$ nanosheet has a hematite structure with an averaged diameter of 200−400 and 50 nm in thickness for the individual round sheet, and the MgO nanosheet possesses a periclase structure with an averaged diameter of 100−200 and 10 nm in thickness for the single hexagonal lamella. These two kinds of nanosheets are small enough to have distinct properties when compared to the bulk $Fe_2O_3$ or MgO samples.

## References

[1] Iijima, S. Helical microtubules of graphitic carbon. *Nature* **1991**, 354 (6348), 56−58.

[2] Bronner, C.; Durr, R. A.; Rizzo, D. J.; Lee, Y.-L.; Marangoni, T.; Kalayjian, A. M.; Rodriguez, H.; Zhao, W.; Louie, S. G.; Fischer, F. R.; Crommie, M. F. Hierarchical On-Surface Synthesis of Graphene Nanoribbon Heterojunctions. *ACS Nano* **2018**, 12, 2193−2200.

[3] He, R.; Zhang, A.; Ding, Y.; Kong, T.; Xiao, Q.; Li, H.; Liu, Y.; Zeng, J. Achieving the Widest Range of Syngas Proportions at High Current Density over Cadmium Sulfoselenide Nanorods in $CO_2$ Electroreduction. *Advanced Materials* **2018**, 30, 1705872.

[4] Law, M.; Greene, L. E.; Johnson, J. C.; Saykally, R.; Yang, P. Nanowire dye-sensitized solar cells. *Nature Materials* **2005**, 4, 455.

[5] Jia, H.; Gao, Y.; Huang, Q.; Cui, S.; Du, P. Facile three-step synthesis and photophysical properties of [8]-, [9]-, and [12] cyclo1,4-naphthalene nanorings via platinum-mediated reductive elimination. *Chemical Communications* **2018**, 54, 988−991.

[6] Coleman, J. N.; Lotya, M.; O'Neill, A.; Bergin, S. D.; King, P. J.; Khan, U.; Young, K.; Gaucher, A.; De, S.; Smith, R. J.; Shvets, I. V.; Arora, S. K.; Stanton, G.; Kim, H.-Y.; Lee, K.; Kim, G. T.; Duesberg, G. S.; Hallam, T.; Boland, J. J.; Wang, J. J.; Donegan, J. F.; Grunlan, J. C.; Moriarty, G.; Shmeliov, A.; Nicholls, R. J.; Perkins, J. M.; Grieveson, E. M.; Theuwissen, K.; McComb, D. W.; Nellist, P. D.; Nicolosi, V. Two-Dimensional Nanosheets Produced by Liquid Exfoliation of Layered Materials. *Science* **2011**, 331, 568−571.

[7] Richards, R.; Li, W.; Decker, S.; Davidson, C.; Koper, O.; Zaikovski, V.; Volodin, A.; Rieker, T.; Klabunde, K. J. Consolidation of Metal Oxide Nanocrystals. Reactive Pellets with Controllable Pore Structure That Represent a New Family of Porous, Inorganic Materials. *Journal of the American Chemical Society* **2000**, 122, 4921−4925.

[8] Marella, R. K.; Prasad Neeli, C. K.; Rao Kamaraju, S. R.; Burri, D. R. Highly active

Cu/MgO catalysts for selective dehydrogenation of benzyl alcohol into benzaldehyde using neither $O_2$ nor $H_2$ acceptor. *Catalysis Science & Technology* **2012**, 2, 1833−1838.

[9] Serena, S.; Sainz, M. A.; Caballero, A. The system Clinker− MgO−$CaZrO_3$ and its application to the corrosion behaviour of $CaZrO_3$/MgO refractory matrix by clinker. *Journal of the European Ceramic Society* **2009**, 29, 2199−2209.

[10] Krishnamoorthy, K.; Moon, J. Y.; Hyun, H. B.; Cho, S. K.; Kim, S.-J. Mechanistic investigation on the toxicity of MgO nanoparticles toward cancer cells. *Journal of Materials Chemistry* **2012**, 22, 24610−24617.

[11] Makhluf, S.; Dror, R.; Nitzan, Y.; Abramovich, Y.; Jelinek, R.; Gedanken, A. Microwave-Assisted Synthesis of Nanocrystalline MgO and Its Use as a Bacteriocide. *Advanced Functional Materials* **2005**, 15, 1708− 1715.

[12] Bhargava, A.; Alarco, J. A.; Mackinnon, I. D. R.; Page, D.; Ilyushechkin, A. Synthesis and characterisation of nanoscale magnesium oxide powders and their application in thick films of $Bi_2Sr_2CaCu_2O_8$. *Materials Letters* **1998**, 34, 133−142.

[13] Chen, J.; Xu, L.; Li, W.; Gou, X. α-$Fe_2O_3$ Nanotubes in Gas Sensor and Lithium-Ion Battery Applications. *Advanced Materials* **2005**, 17, 582−586.

[14] Navale, S. T.; Bandgar, D. K.; Nalage, S. R.; Khuspe, G. D.; Chougule, M. A.; Kolekar, Y. D.; Sen, S.; Patil, V. B. Synthesis of $Fe_2O_3$ nanoparticles for nitrogen dioxide gas sensing applications. C*eramics International.* **2013**, 39, 6453−6460.

[15] Peerakiatkhajohn, P.; Yun, J.; Chen, H.; Lyu, M.; Butburee, T.; Wang, L. Stable Hematite Nanosheet Photoanodes for Enhanced Photoelectrochemical Water Splitting. *Advanced Materials* **2016**, 28, 6405− 6410.

[16] Ding, Y.; Zhang, G.; Wu, H.; Hai, B.; Wang, L.; Qian, Y. Nanoscale Magnesium Hydroxide and Magnesium Oxide Powders: Control over Size, Shape, and Structure via Hydrothermal Synthesis. *Chemistry of Materials* **2001**, 13, 435−440.

[17] Watari, T.; Nakayoshi, K.; Kato, A. Preparation of submicron magnesium oxide powders by vapor-phase reaction of magnesium and oxygen. *Nippon Kagaku Kaishi* **1984**, 6, 1075−1076.

[18] Utamapanya, S.; Klabunde, K. J.; Schlup, J. R. Nanoscale metal oxide particles/clusters as chemical reagents, Synthesis and properties of ultrahigh surface area magnesium hydroxide and magnesium oxide. *Chemistry of Materials* **1991**, 3, 175−181.

[19] Guan, H.; Wang, P.; Zhao, B.; Zhu, Y.; Xie, Y. Synthesis of high surface area nanometer magnesia by solid-state chemical reaction. *Frontiers of Chemistry in China* **2007**, 2 (2), 204−208.

[20] Beruto, D.; Botter, R.; Searcy, A. W. H2O-Catalyzed Sintering of ~ 2-nm-Cross- Section Particles of MgO. *Journal of the American Chemical Society* **1987**, 70, 155−159.

[21] Ristić, M.; Musić, S.; Godec, M. Properties of γ-FeOOH, α-FeOOH and α-$Fe_2O_3$ particles precipitated by hydrolysis of $Fe^{3+}$ ions in perchlorate containing aqueous solutions. J*ournal of Alloys and Compounds* **2006**, 417, 292−299.

[22] Liu, J.; Liang, C.; Zhang, H.; Zhang, S.; Tian, Z. Silicon-doped hematite nanosheets with superlattice structure. *Chemical Communications* **2011**, 47, 8040−8042.

[23] Hao, H.; Sun, D.; Xu, Y.; Liu, P.; Zhang, G.; Sun, Y.; Gao, D. Hematite nanoplates: Controllable synthesis, gas sensing, photocatalytic and magnetic properties. *Journal of Colloid and Interface Science* **2016**, 462, 315−324.

[24] Henrist, C.; Mathieu, J. P.; Vogels, C.; Rulmont, A.; Cloots, R. Morphological study of magnesium hydroxide nanoparticles precipitated in dilute aqueous solution. *Journal of Crystal Growth* **2003**, 249, 321− 330.

[25] Tadic, M.; Panjan, M.; Damnjanovic, V.; Milosevic, I. Magnetic properties of hematite (α-$Fe_2O_3$) nanoparticles prepared by hydrothermal synthesis method. *Appled Surface Science* **2014**, 320, 183−187.

[26] Ma, X.; Ma, H.; Jiang, X.; Jiang, Z. Preparation of magnesium hydroxide nanoflowers from boron mud via anti-drop precipitation method. *Materials Research Bulletin* **2014**, 56, 113−118.

[27] Prasad, B.; Ghosh, C.; Chakraborty, A.; Bandyopadhyay, N.; Ray, R. K. Adsorption of arsenite ($As^{3+}$) on nano-sized $Fe_2O_3$ waste powder from the steel industry. *Desalination* **2011**, 274, 105−112.

[28] Rajamma, R.; Ball, R. J.; Tarelho, L. A. C.; Allen, G. C.; Labrincha, J. A.; Ferreira, V. M. Characterisation and use of biomass fly ash in cement-based materials. *Journal of Hazardous Materials* **2009**, 172, 1049− 1060.

[29] Fraay, A. L. A.; Bijen, J. M.; de Haan, Y. M. The reaction of fly ash in concrete a critical examination. *Cement and Concrete Research* **1989**, 19, 235−246.

[30] Ferreira, C.; Ribeiro, A.; Ottosen, L. Possible applications for municipal solid waste fly ash. *Journal of Hazardous Materials* **2003**, 96, 201−216.

[31] Yan, F.; Jiang, J.; Tian, S.; Liu, Z.; Shi, J.; Li, K.; Chen, X.; Xu, Y. A Green and Facile Synthesis of Ordered Mesoporous Nanosilica Using Coal Fly Ash. *ACS Sustainable Chemistry & Engineering* **2016**, 4, 4654−4661.

[32] Lee, Y.; Soe, J.; Zhang, S.; Ahn, J.; Park, M.; Ahn, W. Synthesis of nanoporous materials via recycling coal fly ash and other solid wastes: A mini review. *Chemical Engineering Journal* **2017**, 317, 821−843.

[33] Sivalingam, S.; Sen, S. *Applied Surface Science* **2019**, 463, 190−196.

[34] DUNENS, O. M.; MACKENZIE, K. J.; HARRIS, A. T. Synthesis of Multiwalled Carbon Nanotubes on Fly Ash Derived Catalysts. *Environmental Science & Technology* **2009**, 43, 7889−7894.

[35] Sahoo, P. K.; Kim, K.; Powell, M. A.; Equeenuddin, S. M. Recovery of metals and other beneficial products from coal fly ash: a sustainable approach for fly ash management.

*International Journal of Coal Science Technology* **2016**, 3, 267−283.

[36] Valeev, D.; Mikhailova, A.; Atmadzhidi, A. Kinetics of Iron Extraction from Coal Fly Ash by Hydrochloric Acid Leaching. *Metals* **2018**, 8 (7), 533.

[37] Hosseini, T.; Selomulya, C.; Haque, N.; Zhang, L. Indirect carbonation of Victorian brown coal fly ash for $CO_2$ sequestration: multiple-cycle leaching-carbonation and magnesium leaching kinetic modelling. *Energy Fuels* **2014**, 28, 6481−6493.

[38] Valentim, B.; Białecka, B.; Gonçalves, P.; Guedes, A.; Guimarães, R.; Cruceru, M.; Całus-Moszko, J.; Popescu, L.; Predeanu, G.; Santos, A. Undifferentiated Inorganics in Coal Fly Ash and Bottom Ash: Calcispheres, Magnesiacalcispheres, and Magnesiaspheres. *Minerals* **2018**, 8, 140.

[39] Beaudoin, G.; Nowamooz, A.; Assima, G. P.; Lechat, K.; Gras, A.; Entezari, A.; Kandji, E. H. B.; Awoh, A.-S.; Horswill, M.; Turcotte, S.; Larachi, F.; Dupuis, C.; Molson, J.; Lemieux, J.-M.; Maldague, X.; Plante, B.; Bussière, B.; Constantin, M.; Duchesne, J.; Therrien, R.; Fortier, R. Passive Mineral Carbonation of Mg-rich Mine Wastes by Atmospheric $CO_2$. *Energy Procedia* **2017**, 114, 6083−6086.

[40] Barrios, M. S.; González, L. V. F.; Rodríguez, M. A. V.; Pozas, J. M. M. Acid activation of a palygorskite with HCl: Development of physico-chemical, textural and surface properties. *Applied Clay Science* **1995**, 10, 247−258.

[41] Trpkov, D.; Panjan, M.; Kopanja, L.; Tadic, M. Hydrothermal synthesis, morphology, magnetic properties and self-assembly of hierarchical α-$Fe_2O_3$ (hematite) mushroom-, cube- and sphere-like superstructures. *Applied Surface Science* **2018**, 457, 427−438.

[42] Marchetti, S. G.; Spretz, R.; Ulla, M. A.; Lombardo, E. A. Identification of the species formed in the Fe/MgO system: A Raman and Mössbauer study. *Hyperfine Interactions* **2000**, 128, 453−466.

[43] Selvamani, T.; Yagyu, T.; Kawasaki, S.; Mukhopadhyay, I. Easy and effective synthesis of

micrometer-sized rectangular MgO sheets with very high catalytic activity. *Catalysis Communications* **2010**, 11, 537−541.

[44] Kumari, L.; Li, W. Z.; Vannoy, C. H.; Leblanc, R. M.; Wang, D. Z. Synthesis, characterization and optical properties of $Mg(OH)_2$ micro-/nanostructure and its conversion to MgO. *Ceramics International* **2009**, 35, 3355−3364.

# Chapter 4 Synthesis of *in-situ* $Al^{3+}$-defected iron oxide nanoflakes from coal ash: A detailed study on the structure, evolution mechanism and application to water remediation

It has been concluded in Chapter 3 that Fe can be efficiently extracted out from fly ash and then it is a feedstock to synthesize nanosized α-$Fe_2O_3$. However, it is obvious that there are some inherent impurities such Al, Ca and Mg that will be existent in the synthesized α-$Fe_2O_3$. The potential influences of these impurities on the growth and performance on α-$Fe_2O_3$ are still not clear. This chapter has studied the effect of Al on the growth mechanism, atomic environment, crystal structure and water treatment performance of as-synthesized α-$Fe_2O_3$. This chapter has been published in ***Journal of Hazardous Materials:*** **Binbin Qian**, Cheng Liu, Jun Lu, Meipeng Jian, Xiaoyi Hu, Song Zhou, Tara Hosseini, Barbara Etschmann, Xiwang Zhang, Huanting Wang, Lian Zhang*, *Synthesis of in-situ $Al^{3+}$-defected iron oxide nanoflakes from coal ash: A detailed study on the structure, evolution mechanism and application to water remediation*, ***Journal of Hazardous Materials***, 2020, 395, 122696.

## Abstract

The recovery of value-added materials from coal ash waste is of highly economic value and sustainable significance. However, researches on the synthesis of defect-engineering nanomaterials from coal ash are still blank. Herein, iron oxide ($Fe_{1.72}Al_{0.28}O_3$, simplified as FAO) nanoflakes were successfully synthesized from a brown coal fly ash (BCFA) waste. The obtained FAO nanoflakes possess a round-shape morphology with a diameter of around 300 nm and 50 nm in thickness. With the progress of hydrothermal treatment, the impure $Al^{3+}$ gradually replaced part of the $Fe^{3+}$ in the α-$Fe_2O_3$ crystal. Specifically, $Al^{3+}$ was preferentially adsorbed on the (001) facet, hindering the growth of $Fe^{3+}$ on the [001] direction and thus causing the flattening of the resultant FAO. The introduced $Al^{3+}$ also serves as the disordered defects on the hematite surface, leading to decreased crystal parameters for hematite, the formation of a compact first shell and a reduced periodical symmetry for the central cation $Fe^{3+}$. The defects were also found to significantly improve the adsorption capacity of the resultant FAO for Cr(VI), As(V), As(III) and Congo red in waste water, with the maximum adsorption capacity of 68.3, 80.6, 61.1 and 213.8 mg $g^{-1}$, respectively. A relatively strong stability was also confirmed for the as-synthesized adsorbents.

Keywords: crystal growth, defect engineering, nanoflakes, water chemistry, waste recovery

## 4.1 Introduction

Reducing the waste volume and even reusing the waste in value-added ways are critical for a sustainable development of the future economy. Over years, the environmental concerns related to the waste management have been receiving increased attention [1,2]. Out of the most common industrial wastes, coal fly ash is one largest contributor as a solid waste, due to the fact that coal remains as the single largest solid fuel for power generation in most of the

countries. Each year, around 750 million tonnes of coal fly ash is generated in the world [3]. In Australia, the annual production of coal fly ash waste is estimated to reach over ten million tonnes, however, most of which is directly dumped into ash ponds, contaminating the soil and groundwater. Therefore, the utilization of this abundant solid waste has been raised as an urgent local and even global issue. Traditionally, coal fly ash is used as a low-value additive into the cement or concrete [4], geotechnology [5] and others [6]. Recently, for the sake of the environmental sustainability, plenty of efforts have been made to synthesize various nanomaterials from fly ash, such as $Ca_5Si_5Al(OH)O_{16}{\cdot}5H_2O$ nanosheets [7], carbon nanotubes [8], $SO_4^{2-}$-$SnO_2$ catalyst [9], mesoporous nanosilica [10], zeolite [11,12] and others [13,14]. However, most of these synthesized nanomaterials are relevant to alumina and/or silica which are the matrix for the coal ashes derived from high-rank coals. For the ash derived from a low-rank coal such as brown coal, it is implausible to synthesize these Al-/Si-rich nano-particles, due to the shortage of these two elements in the respective ashes.

Owing to the unique properties and excellent applications, nanomaterials with lower value in one dimension such as nanosheets, nanoflakes, nanodisks and nanocakes have been widely developed in the nanoparticle research field [15-17]. With the use of pure reagent grade chemicals, a variety of new methodologies have been developed for the synthesis of these nanomaterials. However, the synthesis of low-dimensional nanomaterials from solid waste including fly ash is rarely reported, which provides an opportunity and challenge for low-cost nanomaterial production [18-21]. Hereby, considering that the BCFA collected from a local power generation station in the state of Victoria, Australia is rich in Fe [22-24], we hypothesized that this Fe-rich coal fly ash could be a potential raw material to synthesize Fe-based low-dimensional nanomaterials. If successful, the fly ash-derived Fe-based nanomaterials could be used to replace those derived from pure reagent grade chemicals, such

as α-$Fe_2O_3$, γ-$Fe_2O_3$, $Fe_3O_4$ and FeOOH. Consequently, this would greatly improve the diversification of low-rank coal ash utilization and the values of its derivatives. In addition, considering that fly ash is a mixture of a broad variation of different elements, it is unknown how the impure cations such as $Al^{3+}$ would affect the structure and function of the resultant Fe-bearing nanoparticles. Answering such a question is another key research goal of this chapter, which is believed to contribute to the fundamental science underpinning the nanoparticle growth.

Herein, for the first time, we report the synthesis of a new *in-situ* $Al^{3+}$-substituted α-$Fe_2O_3$ nanoflakes from BCFA waste, through an initial acid leaching-alkaline precipitation process and subsequent hydrothermal treatment. The evolution of morphologies, lattice parameters, crystal structures and atomic environments have been investigated intensively, in order to elaborate the influence of $Al^{3+}$, an impure and inherent cation derived from fly ash that is unlikely fully separated out of fly ash leachate. In addition, to validate the high performance of the as-synthesized nanoflakes, adsorption tests including cyclic trials have been conducted extensively for a variety of typical heavy metal ions and inorganic dyes in waste water, including Cr(VI), As(V), As(III) and Congo red. These contaminants in waste water are highly toxic and carcinogenic [25-28]. The Fe-bearing nanostructures are environmentally friendly, non-toxic, and corrosion-resistant, and hence, have been tested widely in this field [29-34]. However, compared with the pure chemicals, the presence of impure $Al^{3+}$ within the BCFA is supposed to alter the crystal structure of hematite, thereby resulting in enhanced adsorption performance. To the best of our knowledge, there is still a lack of studies on the influence of impurities on the structure and performance of Fe-bearing nanoflake. Therefore, this work is expected to establish new knowledge and to open a new avenue to synthesize α-$Fe_2O_3$ nanoflakes from low-rank coal fly ash, an otherwise valueless solid waste.

## 4.2 Experimental

### 4.2.1 Materials

The BCFA waste was collected from the Energy Australia Yallourn power plant located in the Latrobe Valley, Victoria, Australia. **Table S4-1** shows the chemical composition of the fly ash sample. It is clear that iron (Fe) is the most abundant element in this fly ash. The as-received fly ash sample was washed at a liquid to solid (L/S) mass ratio of 10 to remove part of the unburnt carbon and water-soluble species. Subsequently, the fly ash sample was dried in an oven at 105°C for 12 h and then ground using a tungsten-carbide vibratory ring pulverizer, producing a particle size of less than 150 μm prior to use. All the chemicals including NaOH, $FeCl_3 \cdot 6H_2O$, $Al(NO_3)_3 \cdot 9H_2O$, HCl (32 *wt%*), $HNO_3$ (65 *wt%*), $K_2Cr_2O_7$, $Na_2HAsO_4 \cdot 7H_2O$ and Congo red were purchased from Sigma-Aldrich. Milli-Q water was used throughout all the experiments.

### 4.2.2 Synthesis of FAO nanoflakes

A two-step cross-current leaching method was used to extract $Fe^{3+}$ from the Victorian BCFA, as shown in **Figure S4-1**. Due to the presence of most of the $Fe^{3+}$ in a stable spinel structure such as magnesium ferrite ($MgFe_2O_4$) [22], in each step, 32 *wt%* HCl was used as the leaching agent to mix with water-washed fly ash or the leaching residue derived from the previous step, at a L/S mass ratio of around two in a closed 250 mL conical flask. The flask was further put in a thermostatically controlled water bath at 60 °C and stirred for a period of 90 min. The stirring rate was controlled at 300 rpm throughout all the runs. After leaching, the slurry was immediately filtered via a vacuum pump and a filter paper with a cut-off size of 450 $\mu m$. As shown in **Figure S4-2**, the resultant leachate is dominated by $Fe^{3+}$ and $Mg^{2+}$ due to the breakage

of the spinel. However, a small amount of $Ca^{2+}$ and $Al^{3+}$ is also introduced into the leachate, probably due to their co-existence with $Fe^{3+}$ and $Mg^{2+}$ in the spinel. Subsequently, 1 mol/L NaOH was added dropwise into the leachate until its pH reached 3.6, forming a slurry that was then centrifuged at 10000 rpm for 10 min to obtain the $Fe(OH)_3$ precipitate. The precipitate was washed three times with Milli-Q water. Afterwards, the precipitate was mixed with 40 mL of Milli-Q water and put into an ultrasonic bath for 1 h. Then 1 mol/L of NaOH solution was further dropped into the resultant slurry to adjust its final pH to 6, resulting in new slurry that was transferred into a number of 150 mL autoclaves and placed inside a preheated hot-air oven maintained at 180°C. At different time intervals, the autoclaves were taken out and cooled down to room temperature naturally. The obtained precipitates were filtered and immersed in ethanol for 24 h, filtered and washed with distilled water three times to remove NaOH and then with ethanol to reduce the agglomeration, and finally dried at 80°C for 2 h.

As a control experiment, synthesis of pure standard α-$Fe_2O_3$ nanoparticles based on the use of chemical grade $FeCl_3{\cdot}6H_2O$ with and without the doping of $Al^{3+}$ was also conducted. In a typical experiment, around 3.25 g of $FeCl_3{\cdot}6H_2O$ was dissolved in 20 mL Milli-Q water, forming a solution of 0.1625 g/mL $FeCl_3{\cdot}6H_2O$ that is comparable with the leachate derived from fly ash. The following steps for the precipitation of α-$Fe_2O_3$ out of this solution are exactly the same as those described above.

### 4.2.3 Adsorption Experiment

Cr(VI) and As(III and V) solutions were made by dissolving $K_2Cr_2O_7$, $NaAsO_2$ and $Na_2HAsO_4{\cdot}7H_2O$ into Milli-Q water, respectively. Adsorption isotherm experiments were conducted in 200 mL beakers containing these heavy metal ion solutions with concentrations

from 5 to 500 mg $L^{-1}$. The pH of the solution was adjusted to 6.0 ± 0.1 with dilute HCl and NaOH. After 0.03 g of adsorbents was added to the 50 mL of each solution in a glass beaker, the whole solution was stirred magnetically at 200 rpm at 25.0 ± 1°C for 24 h. The solid and liquid were separated by centrifuge to measure the concentrations of the remaining arsenic and chromium in the liquid solutions. To determine the adsorption kinetic, the initial concentrations of these heavy metal ions were fixed at 40 mg $L^{-1}$, and the test lasted 300 min for each run. All the other conditions are the same as the isotherm experiments.

Congo red ($C_{32}H_{22}N_6O_6S_2Na_2$) was selected as a typical organic water pollutant [31]. Different amounts of adsorbents were mixed with 50 mL of 100 mg $L^{-1}$ Congo red solutions. After each solution (loaded with adsorbent) was stirred magnetically for 12 h, the adsorbents were separated by centrifuge and the supernatant solutions were analyzed by UV-vis spectroscopy (Shimadzu, Model 2600). The remaining concentration of Congo red was determined by the absorbance bands at $\lambda_{max}$=498 nm using a linear calibration curve over 5-80 mg $L^{-1}$. To evaluate the maximum adsorption capacity, the initial concentrations of Congo red was varied from 10-500 mg $L^{-1}$ and 0.025 g adsorbent was added into 50 mL (0.5 g $L^{-1}$) of the Congo red solutions in 200 mL beakers. These beakers were further stirred magnetically at 200 rpm at 25.0 ± 1 °C for 12 h. Afterwards, the solid and liquid were separated by centrifuge and UV-vis spectroscopy was further employed to measure the remaining Congo red concentrations in the supernatant. To determine the adsorption kinetic, the initial concentration of these heavy metal ions was fixed at 100 mg $L^{-1}$, and the test lasted 300 min for each run. All the other conditions are the same as the isotherm experiments. Note that cyclic tests were also conducted to test the stability of the synthesized FAO. For the cyclic heavy metal adsorption test, the spent FAO nanoflake was washed by 0.05 mol $L^{-1}$ NaOH solution for 12 h and then Milli-Q water to reach a neutral pH prior to the next cycle. For the cyclic Congo red adsorption test, the spent FAO nanoflake

was washed by ethanol under ultrasonication three times, and further washed by Milli-Q water prior to next cycle. The conditions were the same as adsorption kinetic experimental parameters.

### 4.2.4 Material Characterization

X-ray diffraction (XRD) analysis was used for phase identification and the determination of unit cell parameters. The XRD patterns were recorded on a Rigaku SmartLab 3000A diffractometer with Cu Kα radiation (λ = 0.15406 nm). The X-ray tube was operated at 40 kV and 15 mA. The synthesized samples were scanned between 20° and 80° with a D/teX Ultra detector, at a scanning speed of 5°/min. Morphologies and structures of the as-synthesized materials were characterized by scanning electron microscopy (SEM) (FEI Nova NanoSEM 450 FEGSEM) and scanning transmission electron microscopy (STEM) (FEI Tecnai G2 F20 S-TWIN STEM). X-ray photoelectron spectra (XPS) was determined by using an AXIS Ultra spectrometer (Escalab 250Xi, Thermo Fisher Scientific, USA) with an Al Kα anode. Fe K-edge X-ray absorption near-edge spectroscopy (XANES) and extended X-ray absorption fine structure spectroscopy (EXAFS) were conducted at Beamline BL16A1 of NSRRC (National Synchrotron Research Radiation Centre) in Taiwan. Fe K-edge XANES spectra were processed using ATHENA software (a part of DEMETER package) and Fe EXAFS data were fitted using Artemis (part of Demeter) with FEFF version 8. Nitrogen sorption isotherms were performed using a surface characterization analyzer (Micromeritics 3Flex), and the samples were degassed at 160 °C for 24 h before the measurements. Low pressure volumetric $N_2$ adsorption isotherms up to 1 bar were measured with a Micromeritics 3 Flex gas sorption analyzer. BET surface area and pore size were determined by measuring $N_2$ isotherms in a liquid nitrogen bath and then using the Micromeritics software for calculations.

Inductively coupled plasma optical emission spectroscopy (ICP-OES, Optima 7000 DV,

PerkinElmer) was used to quantify the ratio of Al in the as-synthesized FAO nanoflakes and the concentration of Cr and As after adsorption experiments. To determine the atomic composition of the as-synthesized products, about 0.01 g FAO nanoflakes was used and dissolved into 50 mL of 65 *wt%* $HNO_3$ at room temperature. After 24 h, the solid sample was found completely dissolved, forming a clear yellow solution that is ready for the ICP analysis.

UV-vis spectroscopy (Shimadzu, Model 2600) was used to determine the concentrations of remaining Congo red after adsorption experiments.

## 4.3 Results and discussion

### 4.3.1 Synthesis of FAO nanoflakes

Since the BCFA waste contains a significant amount of $Fe_2O_3$ (33.5 *wt%*, **Table S4-1**), and the two-step strong HCl leaching process (**Figure S4-1**) is successful in breaking the spinel structure, approximately 95% of iron was leached out of fly ash and all of the resultant $Fe^{3+}$ precipitated out upon the increase of the leachate pH up to 3.6. Meanwhile, a small fraction of $Al^{3+}$ was also leached out and partially co-precipitated out with $Fe^{3+}$ due to the overlapped pH precipitation range [35]. Effort has been made by fine tuning the leachate pH value to eliminate the precipitation of $Al^{3+}$. However, it was unsuccessful, causing either incomplete precipitation of $Fe^{3+}$, or the precipitation of other cations such as $Ca^{2+}$ and $Mg^{2+}$, which were also leached out and preferentially precipitated at higher pH value. In this sense, the final pH value was optimised at 3.6, causing the presence of around 7.23 *wt%* $Al^{3+}$ in the form of $Al_2O_3$ and a few trace elements such as CaO and MgO in the final precipitate, as shown in **Table S4-1**. However, the yield of the resultant FAO is high, reaching 32% on the mass basis of water-washed and dried fly ash. To date, such a high yield has yet to be reported for the synthesis of any other

nano-sized materials from coal fly ash. More specifically, the as-synthesized precipitate from fly ash was found to bear a BET specific surface area of 80.12 $m^2$ $g^{-1}$, which is far larger than the pure α-$Fe_2O_3$ nanoparticle (synthesized under the same condition as FAO) with a specific surface area of only 31.73 $m^2$ $g^{-1}$, as shown in **Figure S4-3(a)**. The pore size analysis of the FAO is shown in **Figure S4-3(b)**. It is obvious that a sharp pore distribution with an average diameter of 3.7 nm is estimated by the Barrett−Joyner−Halenda (BJH) method. In addition, it is noteworthy that the final leaching residue possesses a chemical composition (**Table S4-1**) that is close to silicon adjustment raw material [4], which is a potential material to be used in the Portland cement clinker manufacturing industry.

### 4.3.2 Micro-structural morphology of as-synthesized FAO nanoflakes

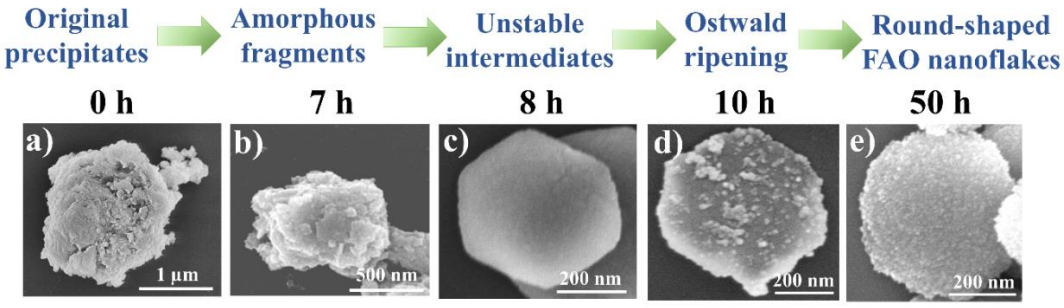


**Figure 4-1** SEM images and growing process of hydrothermal products synthesized from BCFA at different hydrothermal treatment duration. (a) 0 h, (b) 7 h, (c) 8 h, (d) 10 h, and (e) 50 h

**Figure 4-1** visualizes the growth dynamic underpinning the crystal precipitation in the hydrothermal treatment stage. For the original precipitate prior to the hydrothermal treatment, the $Fe^{3+}$-bearing particle suspended in the slurry shows an irregular structure with individual seeds agglomerating into clusters of 1-2 μm in diameter (**Figure 4-1(a)**). The irregularity remained unchanged in the first five hours for the hydrothermal treatment, as demonstrated in **Figure S4-4(a)-(c)**. Starting from the duration of 7 h in **Figure 4-1(b)**, the coarse clusters

commenced to collapse into smaller fragments with a size less than 1 μm on average. Interestingly, remarkable changes occurred when the hydrothermal time increased to 8 h. The clusters are fully gone and replaced by individual particles with tiny wrinkles on surface. The entire morphology for each single particle also shows a uniformly regular hexagonal structure with a nominal diameter of around 500 nm (**Figure 4-1(c)**). The evolution of the morphology continued when the hydrothermal time was further extended to 10 h. As shown in **Figure 4-1(d)**, the surface turned rough again, with numerous debris deposited on the surface of the hexagonal hematite. However, most of the debris disappeared in another 10 h, whilst the hexagonal shape gradually turned into a round shape with a comparatively smooth surface shown in **Figure S4-4(e)**. This is mainly due to the Ostwald ripening effect, which can be briefly described as the growth of larger crystals at the expense of smaller ones deposited on them [36,37]. In our study, a longer hydrothermal process benefits the growth of the unstable crystals and the deposition of smaller debris (crystals) on larger the particles. Eventually, the smaller debris will be embedded within the matrix to form round nanoflakes. With the hydrothermal treatment duration being extended beyond 20 h, the shape transition is almost complete here.

Finally, the product achieved for the longest hydrothermal treatment duration of 50 h, as shown in **Figure 4-1(e)**, was found to consist predominantly of round nanoparticles with a diameter of around 300 nm each. These nanoparticles formed here are also rather flat, as demonstrated in **Figure S4-4(f)**. For simplification, this final product is termed as FAO nanoflakes hereafter. In addition, a close view of the single particle surface, as shown in **Figure 4-1(e)**, still confirmed a non-smooth surface with abundance of tiny seeds, which might be associated with the effect of impure $Al^{3+}$ on the growth process.

To prove this hypothesis, two extra efforts were made to synthesize the α-$Fe_2O_3$ nanoparticles based on the use of pure $Fe^{3+}$ solution (made from $FeCl_3 \cdot 6H_2O$) with and without the addition of $Al^{3+}$ at a same concentration to the fly ash leachate, respectively. As demonstrated in **Figure S4-5**, in the case of using pure $FeCl_3$ with the absence of $Al^{3+}$, the final product exhibits a polyhedron structure with an average size of around 100 nm in **Figure S4-5(a)**, whereas the addition of extra $Al^{3+}$ induced the flattening of the particle and the formation of a relatively rough surface with plenty of defects in **Figure S4-5(b)**. The final morphology in **Figure S4-5(b)** also resembles well with the $Al^{3+}$-substituted α-$Fe_2O_3$ nanoflake synthesized from fly ash in **Figure 4-1(e)**.

### 4.3.3 $Al^{3+}$-defect determination and formation mechanism

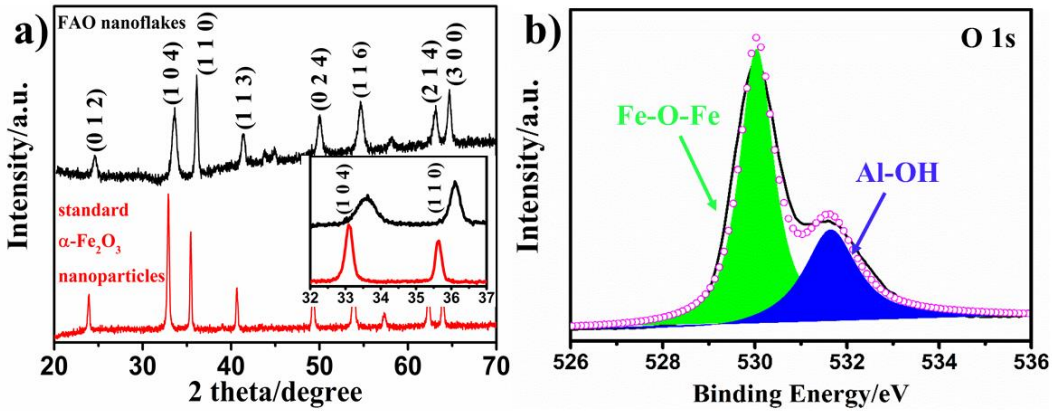


**Figure 4-2** XRD and XPS analysis of as-synthesized samples. (a) XRD pattern of standard α-$Fe_2O_3$ nanoparticles and FAO nanoflakes (Inset: selected 2 theta range from 32-37 degree), (b) The measured (solid line) and corresponding fitting curve (dashed line) of XPS O 1s of FAO nanoflakes

**Figure 4-2(a)** shows the XRD patterns of the as-synthesized standard α-$Fe_2O_3$ nanoparticles

and FAO nanoflake in 50 h. The diffraction peaks of FAO nanoflakes match well with those of standard α-$Fe_2O_3$ nanoparticles, indicating that the entire crystal structure of FAO nanoflakes is the rhombohedral α-$Fe_2O_3$. However, there is a slight shift to higher degree of the 2θ positions for FAO, which is demonstrated in **Figure 4-2(a)** inset. According to the Bragg laws of $2d\sin\theta=n\lambda$, for an identical X-ray wavelength of λ=0.15406 nm at first diffraction (n=1), the increase in 2θ corresponds to a decrease in the d-spacing, which is an indicator of the reduction on the magnitude of the lattice parameters of hematite. Again, such a decrease in lattice parameters should be mainly attributed to the presence of impure $Al^{3+}$ within the FAO nanoflake. During the hydrothermal treatment step, the impure $Al^{3+}$ would enter into the α-$Fe_2O_3$ lattice and replace a portion of $Fe^{3+}$ ion to form an *in-situ* substitutional solid solution of $Fe_{2-x}Al_xO_3$. The ionic radius of 0.053 nm for $Al^{3+}$ is smaller than $Fe^{3+}$ at 0.06 nm, and hence, the substitutional solid solution $Fe_{2-x}Al_xO_3$ meets the Hume-Rothery rules satisfactorily [38], as shown in **Equation 4-1**:

$$\%\ difference = \left|\frac{r_1 - r_2}{r_2}\right| \times 100\% \leq 15\% \qquad \textbf{Equation 4-1}$$

Where $r_1$ is the solute ionic radius for $Al^{3+}$ and $r_2$ is the solvent ionic radius for $Fe^{3+}$. The difference of 11.67% between these two radiuses is smaller than 15%, favouring the formation of $Fe_{2-x}Al_xO_3$. Regarding the other impure ions such as $Ca^{2+}$, it can be ruled out here because the radius of $Ca^{2+}$ is 0.1 nm and its difference to $Fe^{3+}$ is 66.67%, which is not favourable to form a stable solid solution.

To further verify the $Al^{3+}$-induced defects in FAO nanoflakes, XPS spectrum of the as synthesized FAO nanoflakes was recorded to determine the O 1s chemical states, as shown in **Figure 4-2(b)**. Only two peaks were observed, 529.3 eV and 531.8 eV, which are attributed to

the Fe-O-Fe bond [39] and the Al-OH bond [40,41], respectively. The existence of Al–OH bonds rather than Al-O-Al proved a preferential bonding of impure $Al^{3+}$ with the hydroxyl functional group on the surface. Additionally, XPS spectra for Fe 2p and Al 2p were also conducted (**Figure S4-6**). The two major peaks together with two satellites (sat.) in Fe 2p spectrum are clearly observed, which are located at 711.3 eV ($Fe2p_{3/2}$), 725.0 eV ($Fe2p_{1/2}$), 719.8 eV ($Fe2p_{3/2}$ sat.), and 733.9 eV ($Fe2p_{1/2}$ sat.), respectively. And one peak for Al 2p spectra is located at 73.9 eV. All these are the features for the co-existence of chemical states of $Fe^{3+}$ and $Al^{3+}$ in the FAO nanoflakes [39,41]. Surface functional groups of the FAO nanoflakes were further characterized by Fourer Transformed Infrared Spectroscopy (FTIR), as shown in Figure S7. The adsorption bands around 440 and 530 $cm^{-1}$ are attributed to the Fe-O bond vibration from crystalline $\alpha$-$Fe_2O_3$ [27]. The bonds near 1000 $cm^{-1}$ correspond to residual hydroxyl groups [29]. In addition, some weak peaks distributed around 3700 $cm^{-1}$ also correspond to the hydroxyl groups [27].

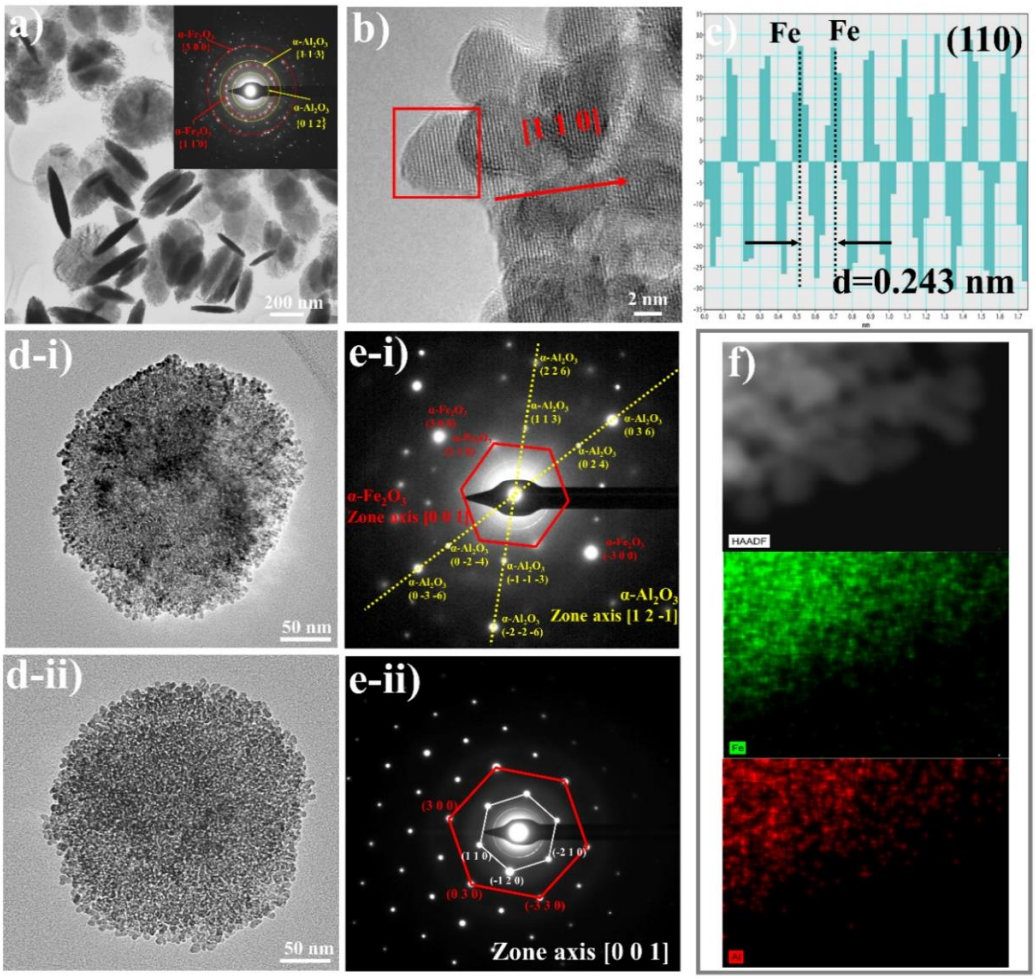


**Figure 4-3** TEM images of FAO nanoflakes (hydrothermal treatment time of 50 h) synthesized from BCFA. (a) An overall view of round-shaped FAO nanoflakes with various orientations (inset: SAED of (a)), (b) High magnification TEM from (a), (c) The corresponding intensity profiles of the red box from (b), (d-i) and (d-ii) are two crystallized cases of single FAO nanoflake, (e-i) and (e-ii) are SAED of (d-i) and (d-ii), respectively, (f) From top to bottom: HAADF-STEM image of region characterization from (d), element mapping of Fe (green) and Al (red)

TEM imaging analyses of the final FAO nanoflakes synthesized in 50 h hydrothermal treatment are shown in **Figure 4-3**. In **Figure 4-3(a)**, one can further verify the formation of a round shape with an averaged diameter of ~300 nm and a thickness of approximately 50 nm. In

addition, the inset of **Figure 4-3(a)** for the corresponding selected area electron diffraction (SAED) pattern demonstrates the presence of multiple-ring diffraction spots for the various orientations of the as-synthesized nanoflake. In addition to the {1 1 0} and {3 0 0} equivalent facets (red in inset) from α-$Fe_2O_3$, another set of diffraction spots is also detected, which can be indexed to the {0 1 2} and {1 1 3} equivalent facets from α-$Al_2O_3$. **Figure 4-3(b)** demonstrates that the building blocks of a single FAO nanoflake are individually around 5 nm in size. Interestingly, these nanoparticles seemingly self-orientate together to form an ultimately round nanoflake. The clear fringe d-spacing value in **Figure 4-3(b)** was measured as ~ 0.251 nm that concurs well with the interplanar spacing of (1 1 0) for α-$Fe_2O_3$. Clearly, the individual crystals preferentially assembled on this direction for the formation of flat nanoflake observed here. Additionally, owing to the preferential orientation of (1 1 0) facet, the X-ray diffraction intensity for this facet was enhanced remarkably, as evident in **Figure 4-2(a)**.

**Figure 4-3(c)** is the corresponding intensity line profile from the red box in **Figure 3(b)**. It clearly demonstrates a adjacent Fe position value (d-spacing value) of 0.243 nm, which falls right between the $d_{(1\,1\,0)}$ of 0.251 nm for α-$Fe_2O_3$ and $d_{(1\,1\,0)}$ of 0.238 nm for α-$Al_2O_3$, indicating that $Al^{3+}$ replaced $Fe^{3+}$ position from the original α-$Fe_2O_3$ and caused the reduction on the d-spacing of (1 1 0). The reduced d-spacing is highly consistent with the XRD results of $2\theta_{(1\,1\,0)}$ of around 36.15° (Cu Kα) based on the Bragg laws.

**Figure 4-3(d-i) and (d-ii)** are two typical crystal structures for the single nanoflakes. Intriguingly, the whole single nanoflake exhibits a "single-crystal" feature, as suggested by the respective SAED patterns in **Figure 4-3(e-i)** and **(e-ii)**, respectively. From **Figure 4-3(e-i)**, the SAED pattern is composed of two sets of diffraction spots, corresponding to an electron beam parallel to the zone axis [0 0 1] of α-$Fe_2O_3$ and [1 2 -1] of α-$Al_2O_3$. From **Figure 4-3(e-ii)**, the

inter-cross hexagonal diffraction spots can be indexed to the [0 0 1] zone axis for single-crystal structured rhombohedral α-$Fe_2O_3$. However, the round-shaped nanoflake still has an incomplete morphology (indented outlines) compared with a perfect hexagonal nanoparticle derived from a single crystal. Thereby, the resultant nanoflake should be deemed as a "pseudo-single-crystal hematite" structure. Clearly, for the lattice distortions, the corresponding SAED (**Figure 4-3(e-i)**) is simply a spatial overlay composed of two sets of diffraction spots from α-$Fe_2O_3$ and α-$Al_2O_3$ rather than within a periodic superlattice structure. Therefore, this implies that the $Al^{3+}$-induced crystal defects are present in a highly disordered manner within the FAO nanoflake. This is also substantiated by the noticeable difference between the diffraction patterns in **Figure 4-3(d-ii)** and **(e-ii)**). The similar phenomena have been reported for the doping of tin (Sn) as dopant into α-$Fe_2O_3$ [42].

Finally, **Figure 4-3(f)** is a close-up region from **Figure 4-3(d-i)** in high-angle annular dark-field (HAADF)-STEM. The corresponding elemental mapping images reveal that Fe and Al are homogeneously distributed inside the nanoflake. In other words, $Al^{3+}$ is atomically dispersed within the hematite matrix. In contrast, other impure ions from the leaching of fly ash including $Ca^{2+}$ and $Mg^{2+}$ are undetectable, confirming that they did not enter into hematite crystal structure in the hydrothermal treatment. More specifically, the impure $Al^{3+}$ was adsorbed preferentially on the (001) facet that is rich in hydroxyl groups due to the difference of surface hydroxy group configuration of the various crystal facets of hematite. The double coordination nature of hydroxyl functions [43] in turn hindered the growth of $Fe^{3+}$ on the [001] direction. The presence of hydroxyl group and its preferential bonding with $Al^{3+}$ has been demonstrated in **Figure 4-2(b)**. Finally, the as-synthesized $Al^{3+}$-substituted α-$Fe_2O_3$ nanoflake can be deemed to have a nominal chemical formula of $Fe_{2-x}Al_xO_3$. Based on the atomic compositions determined by ICP-OES, the mole ratio of Fe to Al was found to be 8.51.

Therefore, the final formula can be regarded as $Fe_{1.72}Al_{0.28}O_3$ with respect to the final as-synthesized FAO nanoflake in 50 h.

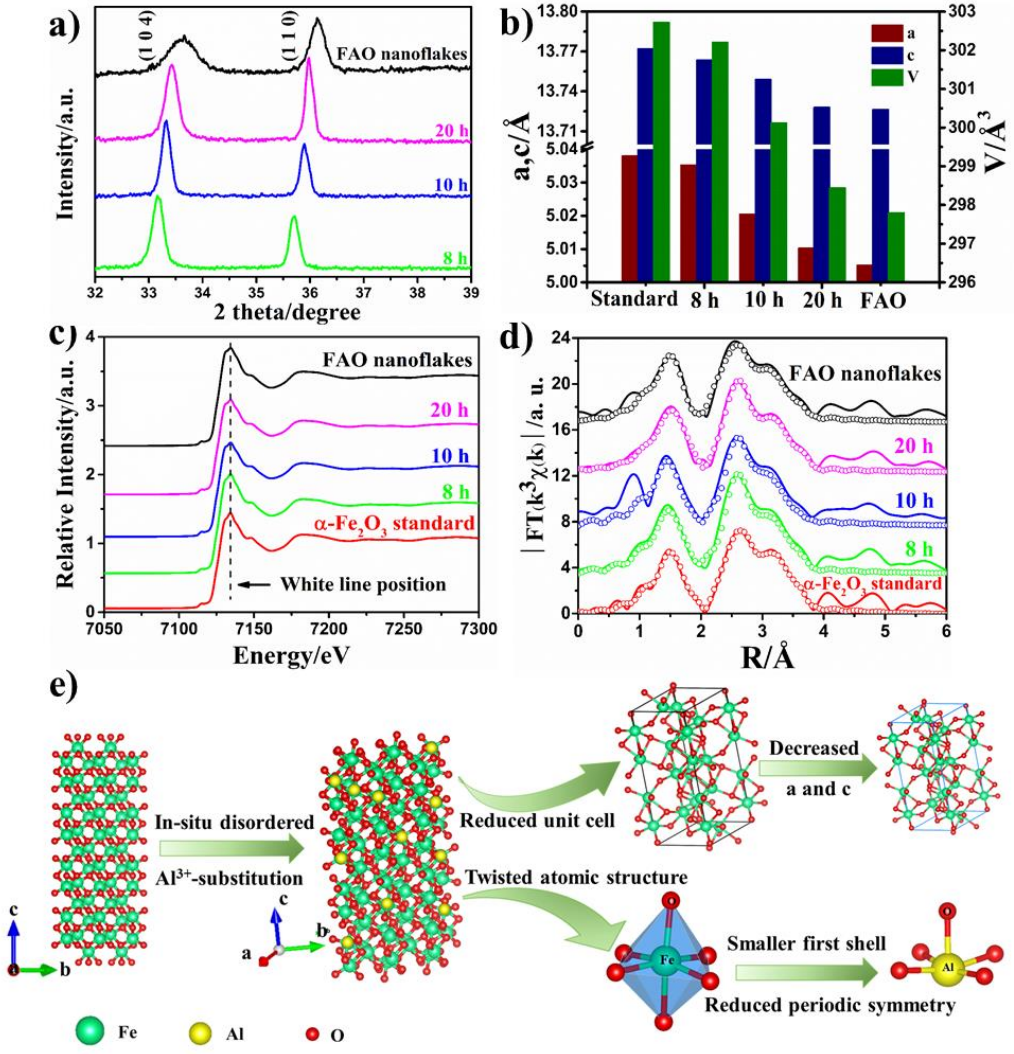


**Figure 4-4** XRD and XAS analysis of as-synthesized α-$Fe_2O_3$ products synthesized from BCFA. (a) A selected range of XRD patterns of $Fe_2O_3$ at the hydrothermal treatment duration of 8 h, 10 h, 20 h and 50 h (FAO nanoflakes), (b) Lattice parameters of a value, c value and cell volume of $Fe_2O_3$ calculated based on the Rietveld refinement method, (c) Fe K-edge XANES spectra of FAO nanoflakes and α-$Fe_2O_3$ reference, (d) The measured (solid line) and corresponding fitting curve (dashed line) of $k^3$-weighted EXAFS spectra of α-$Fe_2O_3$ products compared with α-$Fe_2O_3$ standard, (e) Schematic illustration of crystal defects formation

**Table 4-1** Structural parameters calculated from EXAFS analysis

| Samples | Shell | N | R/Å | $\delta^2$/Å$^{-2}$ | R factor |
|---|---|---|---|---|---|
| α-$Fe_2O_3$ standard | Fe-O | 5.9(0.3) | 2.01(0.01) | 0.0135 | 0.044 |
| | Fe-Fe | 3.8(0.6) | 2.95(0.83) | 0.0073 | |
| 8 h | Fe-O | 5.2(0.7) | 1.98(0.05) | 0.0117 | 0.028 |
| | Fe-Fe | 3.6(0.2) | 2.98(1.07) | 0.0026 | |
| 10 h | Fe-O | 4.7(0.6) | 1.97(0.07) | 0.0101 | 0.039 |
| | Fe-Fe | 4.8(0.9) | 2.96(0.75) | 0.0048 | |
| 20 h | Fe-O | 4.8(1.5) | 1.97(0.06) | 0.0132 | 0.012 |
| | Fe-Fe | 4.0(1.2) | 2.94(0.37) | 0.0014 | |
| 50 h | Fe-O | 4.5(0.3) | 1.95(0.21) | 0.0130 | 0.036 |
| | Fe-Fe | 4.1(0.9) | 2.95(0.13) | 0.0051 | |

### 4.3.4 Atomic Coordination of $Fe^{3+}$ and Its Time-Resolved Evolution

**Figure 4-4(a)** shows the XRD patterns of the Fe-bearing precipitates formed in different hydrothermal treatment duration. To reiterate, the products demonstrate a poor crystallinity in the first 7 h. Once the hydrothermal treatment time is increased to 8-10 h, substantial changes are confirmed for all the diffraction peaks. The sample exhibits a high degree of crystallinity and all the diffraction peaks are in conformity with rhombohedral α-$Fe_2O_3$, which is highly consistent with the changes of the morphology from random clusters to regular hexagonal particles in **Figure 4-1**. Extending the hydrothermal time beyond 10 h does not alter the XRD pattern any more. Instead, as discussed above, the 2θ positions of (1 0 4) and (1 1 0) facets gradually shifts right as the hydrothermal treatment time prolongs. The Rietveld refinement

method based on the program X'Pert HighScore was used to determine the lattice parameters of the precipitates, and the results are illustrated in **Figure 4-4(b)**. It is obvious that with the prolonging of the hydrothermal treatment time, the lattice parameters of a, c and cell volume V decrease from 5.038(67), 13.772(18) and 302.722(5) Å of standard α-$Fe_2O_3$ nanoparticles (**Table S4-2**) to 5.005(43), 13.727(44) and 297.853(3) Å at 50 h, respectively. With the increase on the hydrothermal treatment duration, the isovalent *in-situ* substitution of $Fe^{3+}$ by $Al^{3+}$ is enhanced stably, as evident by a continuing reduction on the magnitude of the three lattice parameters summarized in **Table S4-2**, with all the respective XRD patterns and fitting results illustrated in **Figure S4-8-S4-12**.

Detailed atomic structure of the as-synthesized FAO nanoflake is further verified through Fe K-edge XANES and EXAFS. As depicted in **Figure 4-4(c)**, the XANES curves prove that the white line position of all the precipitate samples closely resembles that of standard α-$Fe_2O_3$. However, a close view of the pre-edge position, as depicted **Figure S4-13,** reveals a gradual shift of the white-line, which is a qualitative indicator of the change/distortion in the local geometry with increasing hydrothermal annealing time [44,45]. To quantitatively clarify the effect of Al on the local structure of Fe in atomic level, Fe K-edge EXAFS spectra in **Figure 4-4(d)** were analyzed using Artemis. This analysis is expected to offer the atomic coordination details of $Fe^{3+}$, including bond distance (R), coordination number (N) and Debye-Waller factor ($\sigma^2$) of ligands coordinated to the absorbing element.

**Table 4-1** demonstrates that with the hydrothermal time prolongs, the Fe-O bond distance decreases from the standard α-$Fe_2O_3$ (2.01(0.01) Å) to the final 50 h product (1.95(0.21) Å), which is attributed to the intrusion of the smaller $Al^{3+}$ into the crystal lattice of hematite. The mixed Fe-O and Al-O bonds contribute to the first shell jointly and result in a smaller crystal

lattice that has been discussed in the XRD part. In contrast, the second shell for the Fe-Fe bond is rather constant in terms of the bond distance, which is also very close to standard α-$Fe_2O_3$ nanoparticles, indicating that the distortion of $Fe_{2-x}Al_xO_3$ lattice is mainly attributed to intrusion of $Al^{3+}$ into the short-range first shell. With regards the coordination number (N), the refined N value of standard sample is 5.9(0.3) and 3.8(0.6) for Fe-O and Fe-Fe, respectively, which are close to the theoretical values of 6 and 4 [43]. However, the value of N of the first shell decreases from 5.2(0.7) in 8 h to 4.5(0.3) in 50 h, indicating a gradual and slow intrusion of $Al^{3+}$ into the α-$Fe_2O_3$ lattice. Finally, as a summary, **Figure 4-4(e)** illustrates the evolution of the *in-situ* disorder replacement of $Al^{3+}$ into the hematite structure upon hydrothermal treatment, which results in reduced unit cell and twisted atomic structure for $Fe^{3+}$ that preferentially grows on its (1 1 0) crystal direction.

### 4.3.5 Adsorption performance

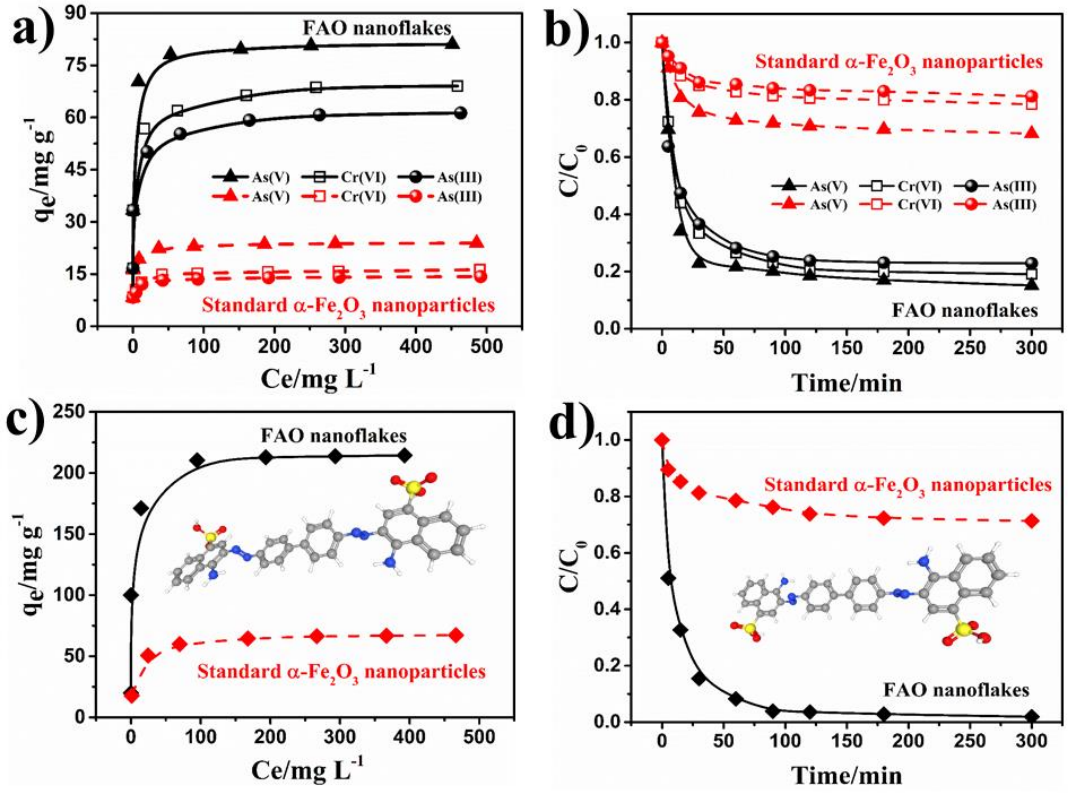


**Figure 4-5** Adsorption properties of the fresh as-synthesized FAO nanoflakes. (a) Langmuir adsorption isotherms of Cr(VI), As(V), As(III), (b) Adsorption rate curves of Cr(VI), As(V), As(III), (c) Langmuir adsorption isotherm of Congo red, (d) Adsorption rate curves of Congo red. (In all the four figures, solid lines are for the FAO nanoflakes and dashed lines are for the standard α-$Fe_2O_3$ nanoparticles. In (c) and (d), inset is the molecule structure for Congo red with C (grey), H (white), N (blue), O (red) and S (yellow))

Finally, the adsorption experiments were conducted to evaluate the potential applications of the as-synthesized FAO nanoflakes in water treatment. **Figure 4-5(a)** shows the adsorption isotherms for Cr(VI), As(V) and As(III) of the fresh as-synthesized FAO nanoflakes and standard α-$Fe_2O_3$ nanoparticles prepared from pure $FeCl_3 \cdot 6H_2O$, respectively. The Langmuir

adsorption equation (**Equation 4-2**) was used to model the adsorption data over the concentration range of 5 to 500 mg $L^{-1}$ and to calculate the maximum adsorption capacity:

$$q_e = \frac{q_m b c_e}{1+bc_e} \qquad \textbf{Equation 4-2}$$

Where $C_e$ (mg $L^{-1}$) is the equilibrium concentration of heavy metal ions, $q_e$ (mg $g^{-1}$) is the amount of heavy-metal ions adsorbed per unit weight of the adsorbent at equilibrium, $q_m$ (mg $g^{-1}$) is the theoretical maximum adsorption capacity, and $b$ is the equilibrium constant. Results show that the Langmuir model fits all the experimental data fit well. Note that the Freundlich model was also used to fit the isotherm adsorption data, as shown in **Figure S4-14**. Clearly, the Langmuir fittings are better than the Freundlich fittings, which are further quantified by the $R^2$ coefficient summarized in **Table S4-3.** This indicates that the adsorption proceeds more likely via a monolayer chemical adsorption on the adsorbent surface.

Back to **Figure 4-5**, a large difference is notably observed between the fresh as-synthesized FAO nanoflakes and the standard α-$Fe_2O_3$ nanoparticles. Based on the isotherms, the calculated maximum adsorption capacity, $q_m$ of the fresh FAO nanoflake reaches 68.3 mg $g^{-1}$ for Cr(VI), 80.6 mg $g^{-1}$ for As(V) and 61.1 mg $g^{-1}$ for As(III). These values are significantly higher than the respective $q_m$ of the standard α-$Fe_2O_3$ nanoparticles, which is around 15.7, 22.7 and 10.6 mg $g^{-1}$ for the three respective cations. Furthermore, it is noteworthy that the adsorption capacities of the FAO nanoflakes are comparable and even higher in comparison with the reported nanomaterials, such as α-$Fe_2O_3$ nanostructures [30,46-49], $Fe_3O_4$ [33], FeOOH [34], CuO [50] and $CeO_2$ [51], as listed in **Table S4-4**. Specifically, although the as-synthesized hematite in this study does not possess the largest specific surface area, its maximum removal

capacity for the three heave metal cations are larger than all the other samples except the nanowire hematite. This should be due to its unique structure as elaborated before, and also the strong hydrophilicity as evident in **Figure 4-2(b)**. In addition, the adsorption kinetics experiments of Cr(VI), As(V) and As(III) ions with an initial concentration of 40 mg $L^{-1}$ were also conducted, as shown **Figure 4-5(b)**. Obviously, as for the fresh crystal-defect FAO nanoflake, the adsorption reaction moves rapidly in the initial 120 min, achieving the removal percentages of about 80% for Cr(VI), 82% for As(V) and 76% for As(III). In comparison, for the standard α-$Fe_2O_3$ nanoparticles, only 17% of Cr(VI), 29% of As(V) and 16% of As(III) were removed.

To investigate the applicability of the crystal-defect FAO nanoflakes towards water remediation, adsorption experiments using Congo red were also conducted. **Figure S4-15** shows the effect of fresh FAO nanoflakes dosage from 0 to 1 g $L^{-1}$ on the removal of Congo red with an initial concentration 100 mg $L^{-1}$ in 12 h. Upon the increase of the dosage to 0.5 g $L^{-1}$, 99.6% of the Congo red was removed out of water (shown in **Figure S4-15** inset). Accordingly, the dosage of 0.5 g $L^{-1}$ was then used to evaluate the maximum adsorption capacity of both FAO nanoflake and standard α-$Fe_2O_3$ nanoparticle. **Figure 4-5(c)** shows the respective adsorption isotherms. Based on the Langmuir adsorption equation, the maximum adsorption capacity for fresh FAO nanoflakes and standard α-$Fe_2O_3$ nanoparticles was found to reach 213.8 mg $g^{-1}$ and 65.9 mg $g^{-1}$, respectively. Here again, the obtained adsorption capacity of our FAO nanoflake is higher than similar materials, such as α-$Fe_2O_3$ nanostructures [30,47,52,53], γ-$Fe_2O_3$ [54], FeOOH [34], $MnO_2$ [55], γ-$Al_2O_3$ [56] and boehmite [57], as listed in **Table S4-5**. Similarly, it should be partially due to the unique structure and strong hydrophilicity of our hematite. To evaluate the adsorption rate of FAO nanoflakes, the adsorption kinetics experiments of Congo red with an initial concentration of 100 mg $L^{-1}$ were also conducted, as shown **Figure 4-5(d)**. Clearly,

as for the defected FAO nanoflake, the adsorption reaction occurred rapidly in the initial 120 min, achieving a removal percentage of about 97% for Congo red. This is much higher than the standard α-$Fe_2O_3$ nanoparticles for the removal of only 26% Congo red in the same duration.

Regarding the spent FAO nanoflakes, the morphology remains unchanged, as indicated in **Figure 4-S16**. This is an indicator of its strong stability. Additionally, the cyclic test results in **Figure S4-17 and Figure S4-18** further confirmed a strong adsorption performance of the spent FAO nanoflake. The gradual loss of the FAO nanoflake capacity from the third cycle is mainly attributed to the loss of its surface activity, as has been observed for the other adsorbents elsewhere [30,47,53,58]. Nevertheless, even after four cycles, the regenerated FAO nanoflake still bears a much better removal capacity than the standard α-$Fe_2O_3$ nanoparticles.

### 4.3.6 Implications

Herein, a nanoflake structured hematite has been successful synthesized from a local coal fly ash waste. Its larger adsorption capacity than the literature was also confirmed by testing various traces metals and Congo red in aqueous solution. Such an effort is clearly beneficial in valorizing this local waste, and hence, this study is expected to cast a profound impact from the practical perspective. Moreover, through the intensive characterization, detailed knowledge for the structure of the $Al^{3+}$-substituted hematite has been established, which is expected to extend and cast a broad implication on the use of this structure or similar ones in the other areas such as catalysis. As a key catalyst precursor, hematite is usually doped with $Al^{3+}$ or other cations with an ionic radius close to $Fe^{3+}$ to promote its textural parameter, and consequently its catalytic performance [59]. However, as far as the authors are aware, no study has yet to be made to elaborate the fundamentals underpinning the structural role of $Al^{3+}$ and the time-resolved evolution and optimization of the structure. Clearly, the results here have the potential

to assist in fine-tuning the structure of the $Al^{3+}$-doped hematite such as through a hydrothermal annealing to improve its catalytic performance, which is underway by us.

## 4.4 Conclusions

A unique $Fe_{1.72}Al_{0.28}O_3$ (FAO) nanoflake has for the first time been successfully synthesized from BCFA waste, an otherwise valueless industry by-product. The product achieved a yield of 32%, based on the mass of water-washed, dried fly ash. Crystal defects of the FAO nanoflakes were introduced through the *in-situ* isovalent replacement of $Fe^{3+}$ by $Al^{3+}$ upon hydrothermal treatment. Consequently, a flattened nanoflake-like morphology with a diameter of around 300 nm and 50 nm in thickness was achieved, and a relatively large specific surface area of 80.12 $m^2$ $g^{-2}$ was secured. Detailed structure characterization indicates that, the $Al^{3+}$ dopant distorted the original atomic structure of standard α-$Fe_2O_3$, resulting in reduced lattice parameters (a=5.005(43) Å, c=13.727 (44) Å), a smaller first shell (Fe-O bond distance of 1.95(0.21) Å) and a reduced periodic symmetry (Fe coordination number of 4.5(0.3)). Compared with the standard nanosized α-$Fe_2O_3$ and even those reported in the literature, the as-synthesized FAO nanoflakes exhibit higher efficiency and enhanced adsorption performance with a maximum adsorption capacity of 68.3, 80.6, 61.1 and 213.8 mg $g^{-1}$ of Cr(VI), As(V), As(III) and Congo red, respectively. These values are around 3-5 times larger than the standard α-$Fe_2O_3$ nanoparticles that is free in $Al^{3+}$. This work demonstrates the viability of converting the low-rank coal ash waste into value-added materials that are highly efficient for wastewater remediation.

# Supporting Results

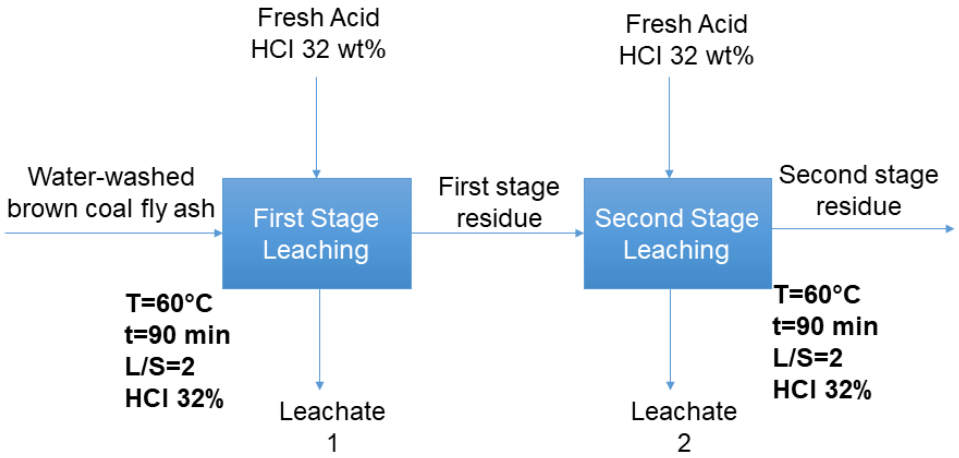


**Figure S4-1** Block flow diagram of the two-stage cross flow leaching of water-washed brown coal fly ash

**Table S4-1** XRF analysis of water washed fly ash FAO nanoflakes after hydrothermal treatment time of 50 h (*wt*%)

| Oxides | Percent (%) | | |
|---|---|---|---|
| | Raw fly ash | FAO nanoflakes | Leaching residue |
| $SiO_2$ | 12.45 | 0 | 37.92 |
| $Al_2O_3$ | 7.47 | 7.23 | 8.64 |
| $Fe_2O_3$ | 33.35 | 92.04 | 9.61 |
| CaO | 5.22 | 0.48 | 0.53 |
| MgO | 14.51 | 0.15 | 2.77 |
| $K_2O$ | 0.06 | 0 | 0.22 |
| $SO_3$ | 1.42 | 0.05 | 1.91 |
| MnO | 0.41 | 0.02 | 0.57 |
| $TiO_2$ | 0.79 | 0.03 | 1.62 |
| Loss of Ignition | 24.32 | 0 | 36.21 |

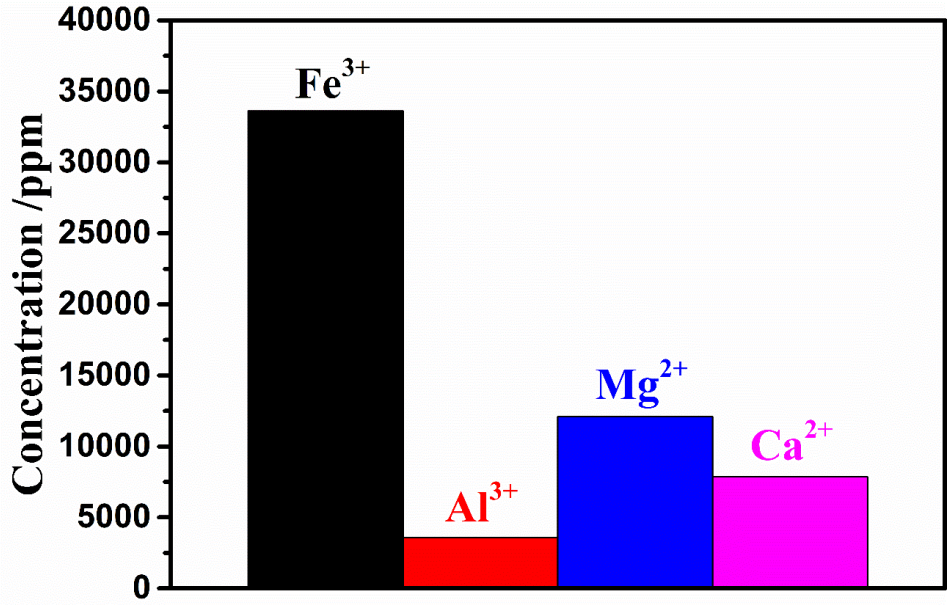


**Figure S4-2** Concentrations of major cations from initial leachate

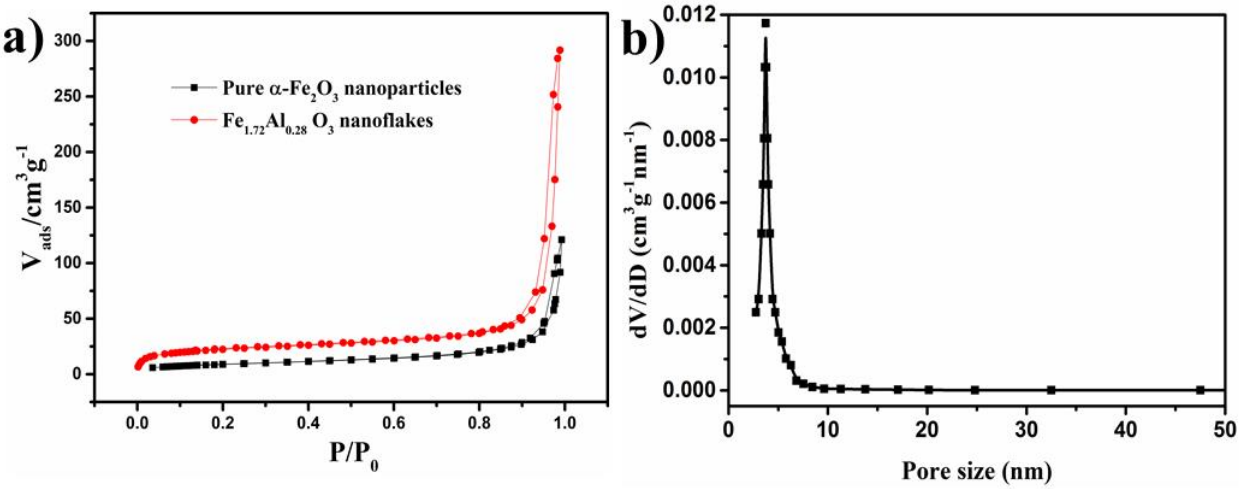


**Figure S4-3** (a) adsorption-desorption isotherm of as-synthesized FAO nanoflakes and pure α-$Fe_2O_3$ nanoparticles. (b) pore size distribution of as-synthesized FAO nanoflakes

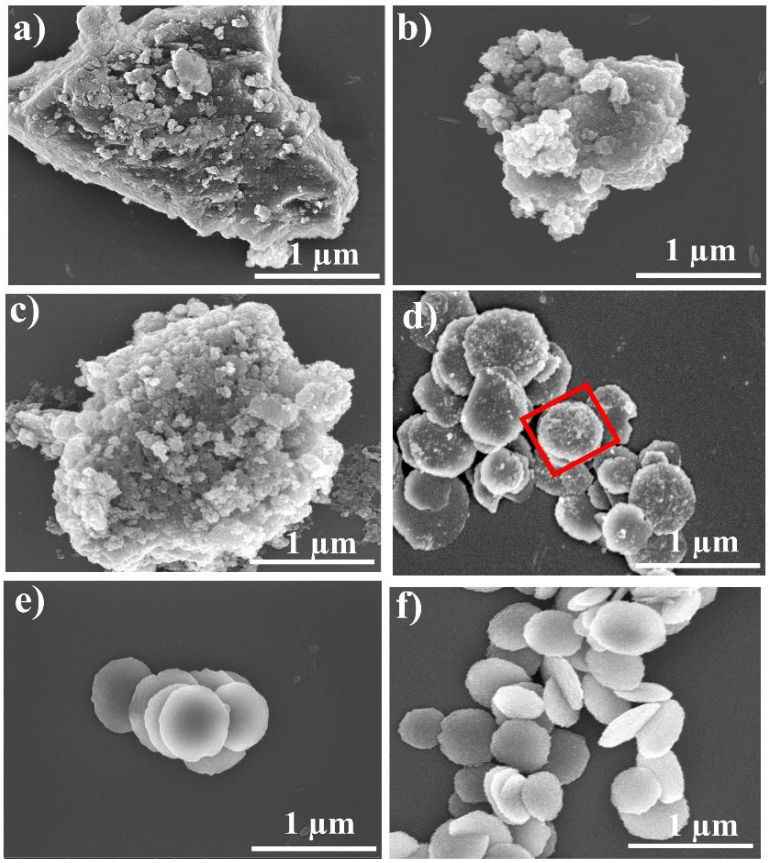


**Figure S4-4** SEM images of hydrothermal products from brown coal fly ash at different hydrothermal treatment duration. (a) 1 h, (b) 3 h, (c) 5 h, (d) 10 h, (e) 20 h and (f) 50 h

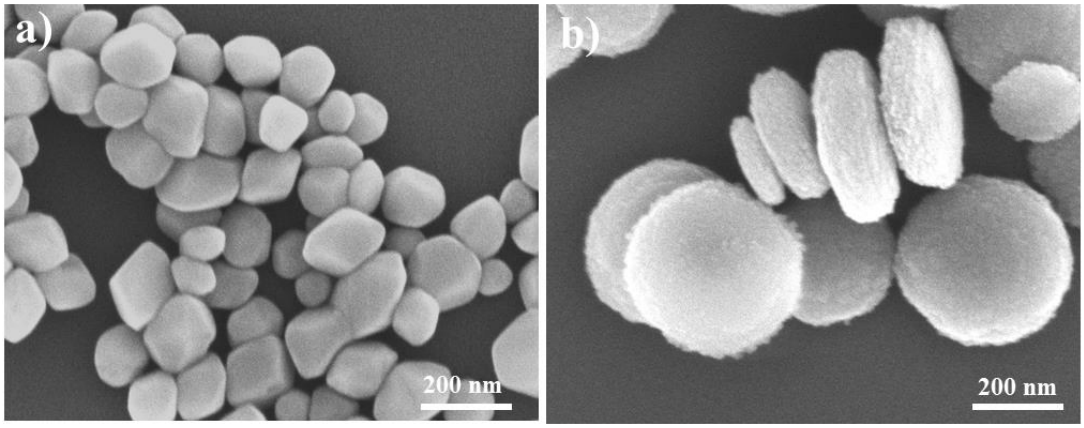


**Figure S4-5** SEM images of α-$Fe_2O_3$ nanoparticles synthesized from reagent grade chemicals. (a) Without additional $Al^{3+}$, (b) With additional $Al^{3+}$

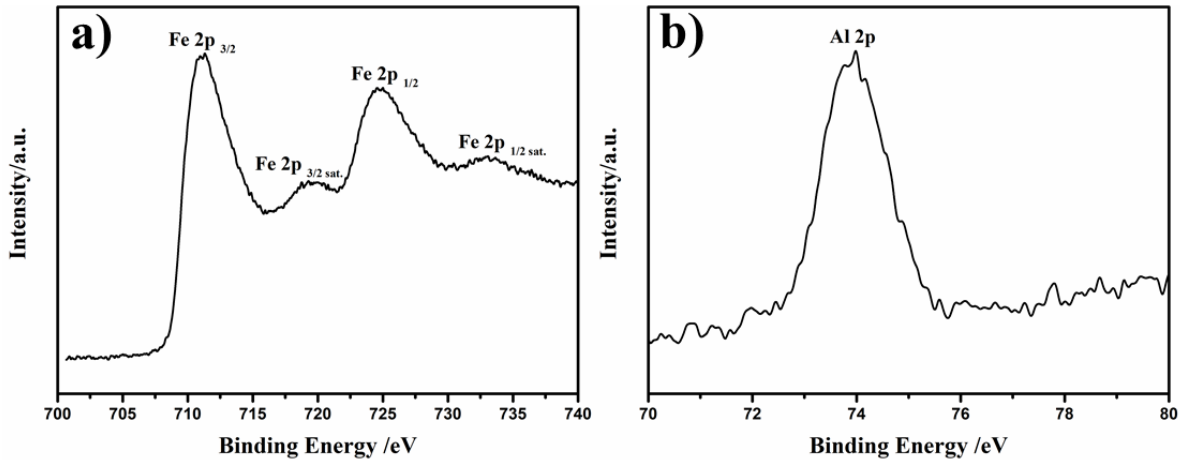


**Figure S4-6** XPS spectrum of FAO nanoflakes synthesized at 50 h

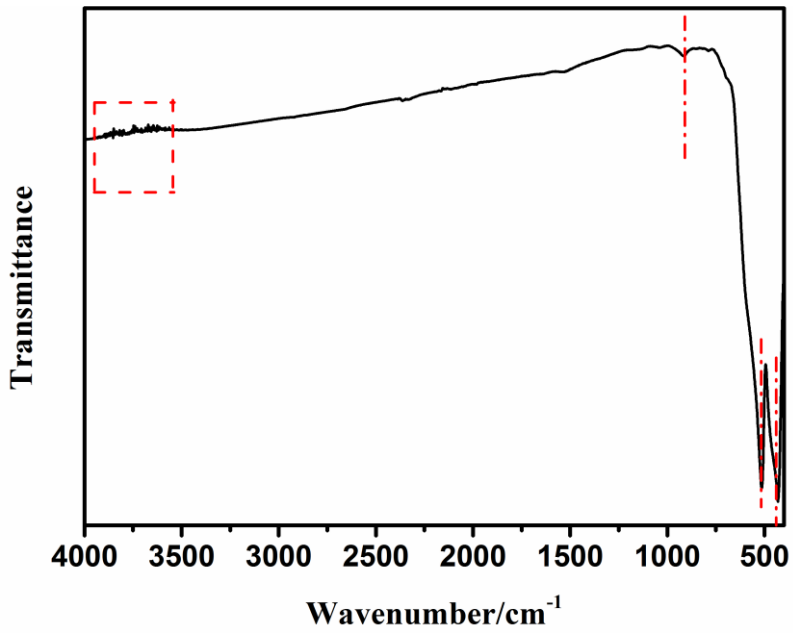


**Figure S4-7** FTIR spectrum of FAO nanoflakes synthesized at 50 h

The XRD results were quantified using the software X'Pert HighScore Plus. The overall refined parameters were the zero-shift error, background polynomial parameters, phase scale factors, unit-cell parameters, peak-shape parameters (GU, GV and GW) and preferred orientation coefficient.

**Table S4-2.** Lattice parameters of $Al^{3+}$-substituted α-$Fe_2O_3$ obtained from Rietveld refinement

| Samples | Lattice parameters | | | Rwp/% | Good of fitness |
|---|---|---|---|---|---|
| | a/Å | c/Å | V/Å$^3$ | | |
| Standard α-$Fe_2O_3$ nanoparticles | 5.038(67) | 13.772(18) | 302.722(5) | 4.52 | 1.21 |
| 8 h | 5.035(25) | 13.763(43) | 302.203(4) | 2.63 | 1.25 |
| 10 h | 5.020(52) | 13.748(82) | 300.118(6) | 1.83 | 0.89 |
| 20 h | 5.010(25) | 13.727(96) | 298.438(9) | 2.51 | 1.07 |
| FAO (50 h) | 5.005(43) | 13.727(44) | 297.853(3) | 2.45 | 1.94 |

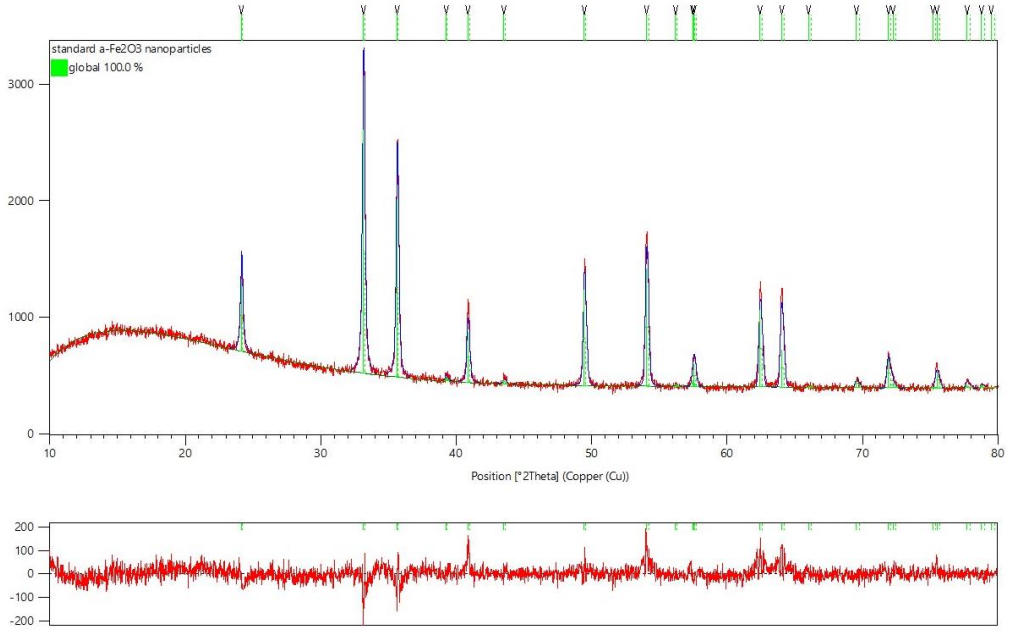


**Figure S4-8** Rietveld refinement of standard α-$Fe_2O_3$ nanoparticles

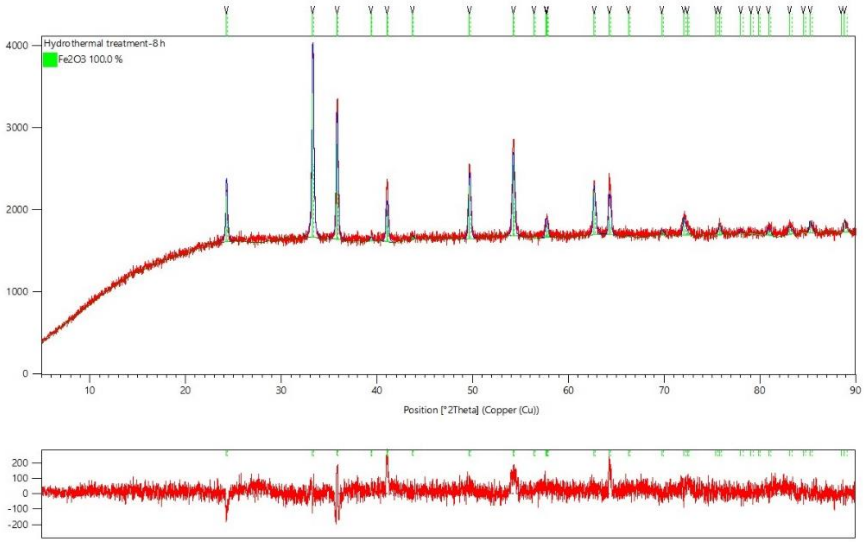


**Figure S4-9** Rietveld refinement of α-$Fe_2O_3$ nanoflakes synthesized in hydrothermal 8 h

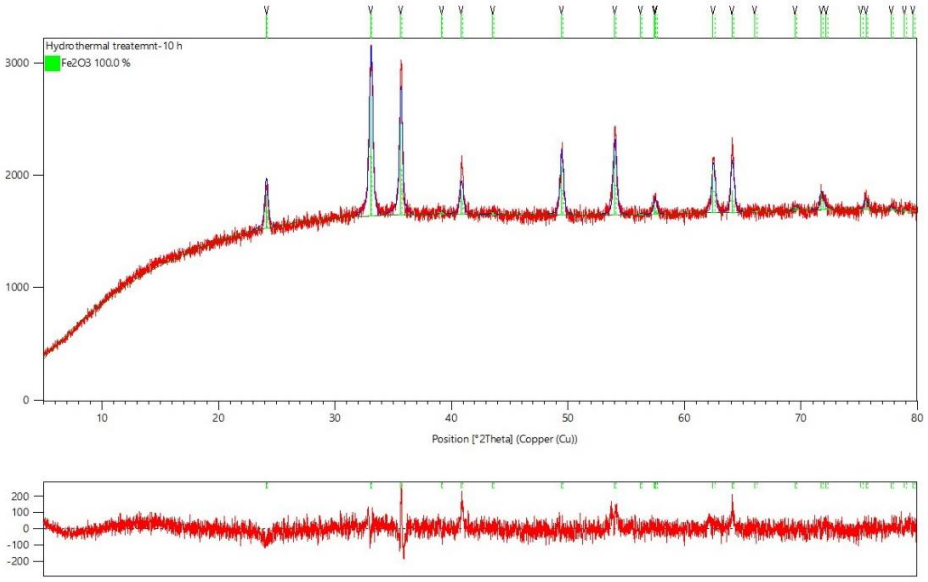


**Figure S4-10** Rietveld refinement of α-$Fe_2O_3$ nanoflakes synthesized in hydrothermal 10 h

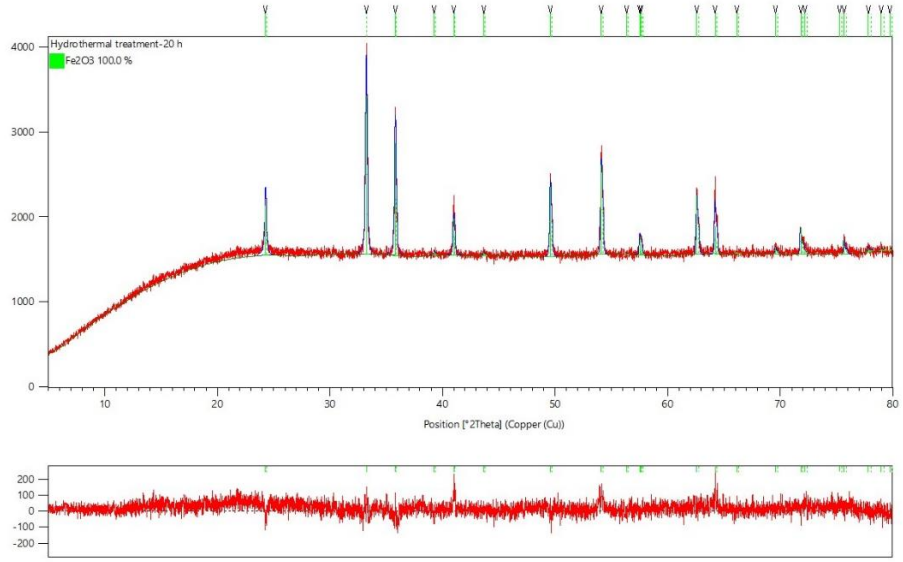


**Figure S4-11** Rietveld refinement of α-$Fe_2O_3$ nanoflakes synthesized in hydrothermal 20 h

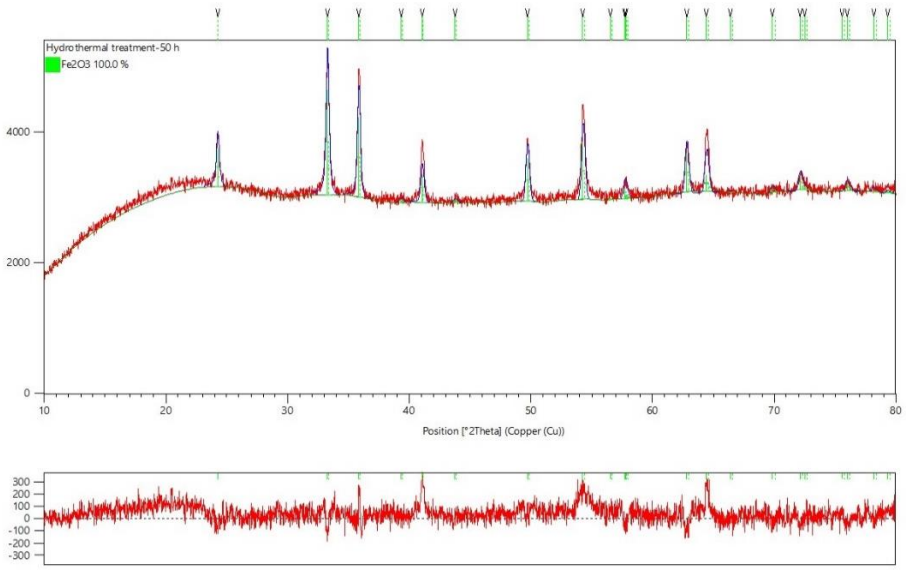


**Figure S4-12** Rietveld refinement of α-$Fe_2O_3$ nanoflakes synthesized in hydrothermal 50 h

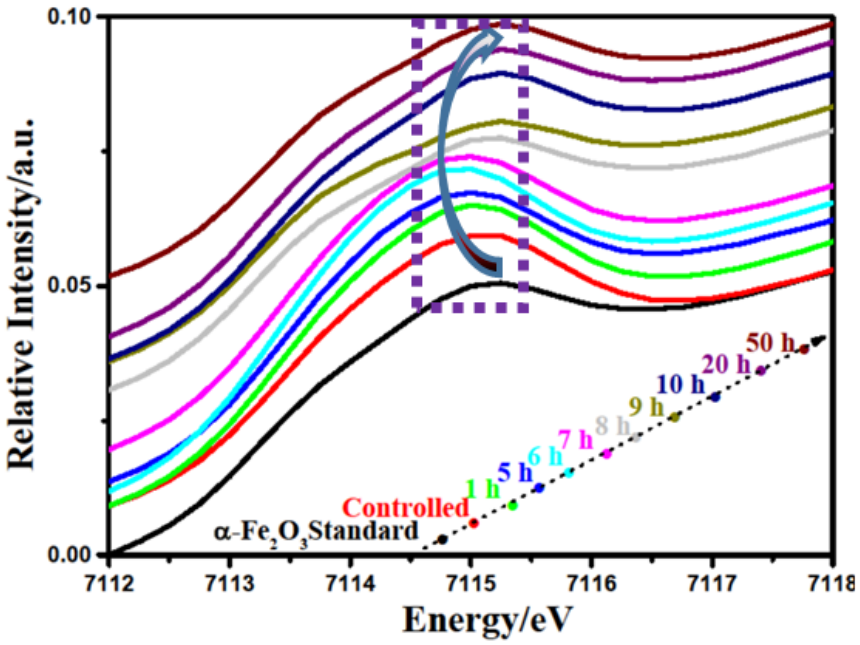


**Figure S4-13** Pre-edge features of products synthesized in different hydrothermal treatment periods

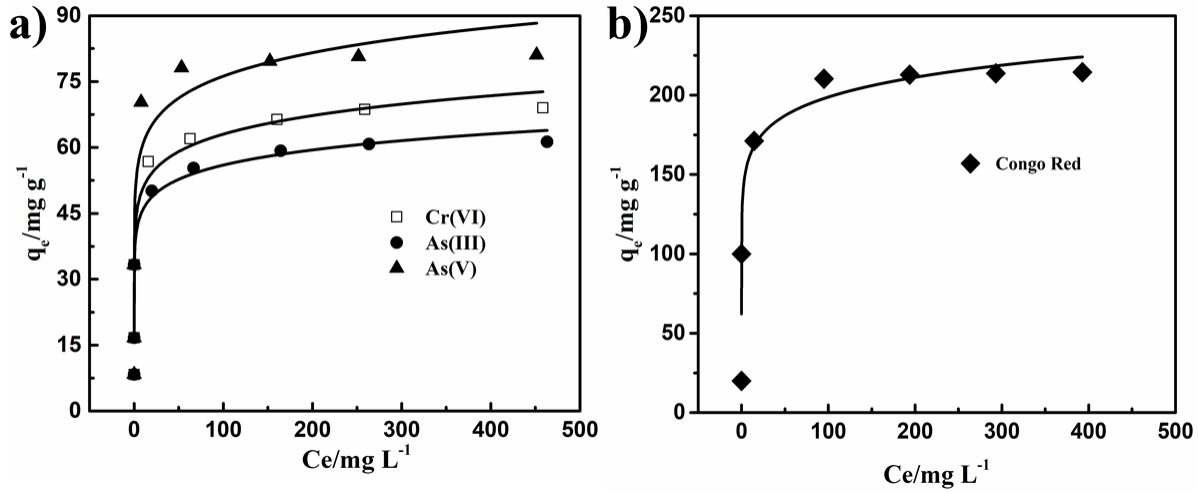


**Figure S4-14** (a) Freundlich adsorption isotherms of Cr(VI), As(V) and As(III), (b) Freundlich adsorption isotherm of Congo red

**Table S4-3** Summary of R-square values for Langmuir and Freundlich fittings

| Models | R-square | | | |
|---|---|---|---|---|
| | Cr(VI) | As(V) | As(III) | Congo red |
| Langmuir | 0.9521 | 0.9764 | 0.9855 | 0.9817 |
| Freundlich | 0.8944 | 0.9132 | 0.9001 | 0.8832 |

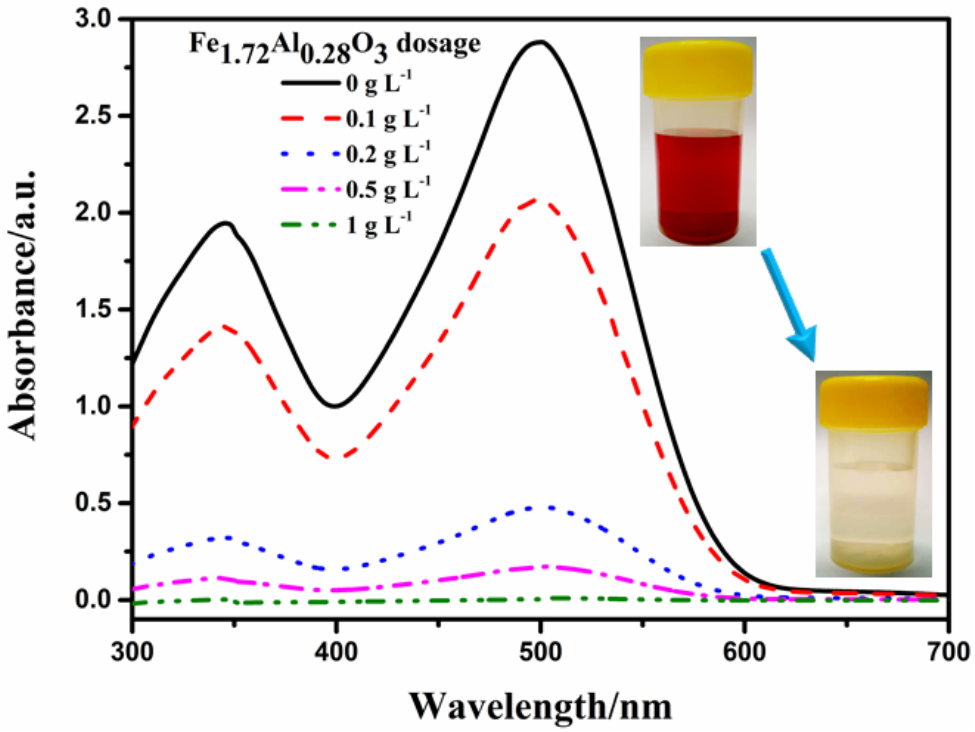


**Figure S4-15** UV-vis absorption spectra of Congo red solutions treated by the FAO nanoflakes with different dosages

**Table S4-4** Comparison of Cr(VI), As(V) and As(III) adsorption capacity with various adsorbents in the references

| Adsorbents | Morphology | BET surface area ($m^2$ $g^{-1}$) | Maximum removal capacity (mg $g^{-1}$) | | | Reference |
|---|---|---|---|---|---|---|
| | | | Cr(VI) | As(V) | As(III) | |
| $\alpha$-$Fe_2O_3$ | Round nanoflakes | 80.12 | 68.3 | 80.6 | 61.1 | This study |
| | Polyhedron nanoparticles | 31.73 | 15.7 | 22.7 | 10.6 | |
| $\alpha$-$Fe_2O_3$ | Hollow nestlike spheres | 152.42 | 58.6 | 75.3 | - | 30 |
| $\alpha$-$Fe_2O_3$ | Flowerlike nanostructures | 130 | 30 | 51 | - | 46 |
| $\alpha$-$Fe_2O_3$ | Irregular spherical nanoparticles | 164.1 | 17 | - | - | 47 |
| $\alpha$-$Fe_2O_3$ | 3D flowerlike nanostructures | 40 | 4.47 | 5.31 | - | 29 |
| $\alpha$-$Fe_2O_3$ | Nanowires deposited diatomite | 30 | - | 81.2 | 60.6 | 48 |
| $\alpha$-$Fe_2O_3$ | Uniform granular | 173 | - | - | 51.8 | 49 |

| | | | | | | |
|---|---|---|---|---|---|---|
| | crystals | | | | | |
| $Fe_3O_4$ | Pineal-like nanoparticles | 32.75 | | 7.23 | 6.77 | 33 |
| FeOOH | Hollow urchin-like spheres | 96.9 | - | 58 | - | 34 |
| $CeO_2$ | Hollow nanospheres | 72 | 15.4 | 22.4 | - | 51 |
| CuO | Uniform spherical shape | 85 | - | 22.6 | 26.9 | 50 |

**Table S4-5** Comparison of Congo Red and adsorption capacity with various adsorbents in the references

| Adsorbents | Morphology | BET surface area ($m^2$ $g^{-1}$) | Maximum removal capacity (mg $g^{-1}$) | Reference |
|---|---|---|---|---|
| α-$Fe_2O_3$ | Round nanoflakes | 80.12 | 213.8 | This study |
| | Polyhedron nanoparticles | 31.73 | 65.9 | |
| α-$Fe_2O_3$ | Hollow nestlike spheres | 152.42 | 160 | 30 |
| α-$Fe_2O_3$ | - | 124.56 | 139.86 | 52 |
| α-$Fe_2O_3$ | Rod-like nanostructures | 98 | 57.2 | 53 |
| γ-$Fe_2O_3$ | Hierarchical Nanostructures | 114 | 58.2 | 54 |

| | | | | |
|---|---|---|---|---|
| $\gamma$-$Al_2O_3$ | Hierarchical spindle-like particles | 149 | 90 | 56 |
| $MnO_2$ | Hierarchical hollow structures | - | 80 | 55 |
| Boehmite | Hollow core/shell microspheres | 269 | 111.3 | 57 |

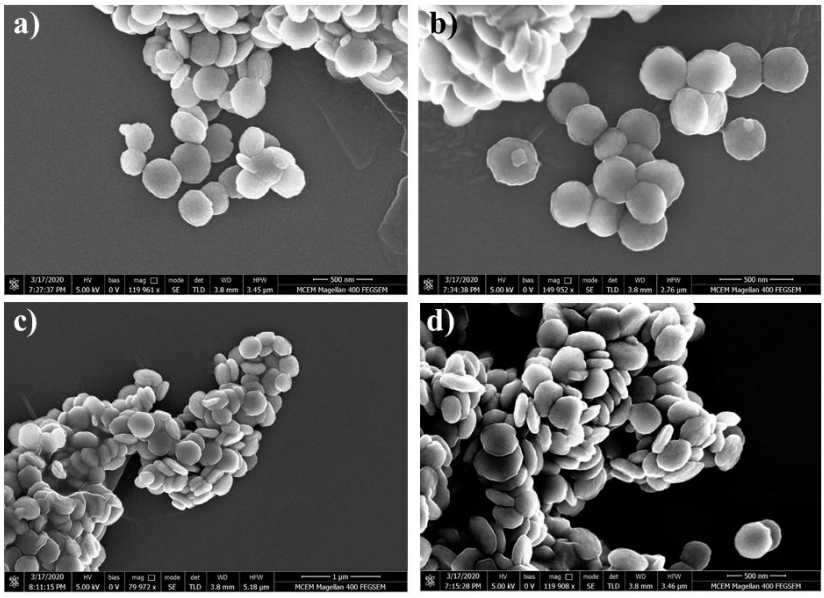


**Figure S4-16** SEM images of as-synthesized $\alpha$-$Fe_2O_3$ nanoflakes after water remediation. (a) after Cr(VI) adsorption, (b) after As(V) adsorption, (c) after As(III) adsorption and (d) after Congo red adsorption

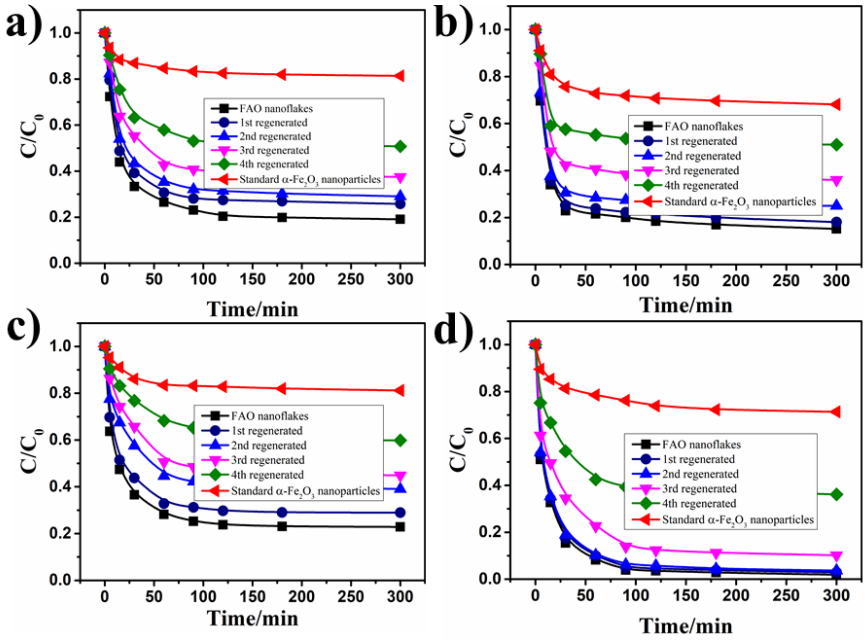


**Figure S4-17** Adsorption rate curves of the as-prepared and the regenerated FAO nanoflakes compared with the standard α-$Fe_2O_3$ nanoparticles. (a) Cr(VI) adsorption, (b) As(V) adsorption, (c) As(III) adsorption and (d) Congo red adsorption

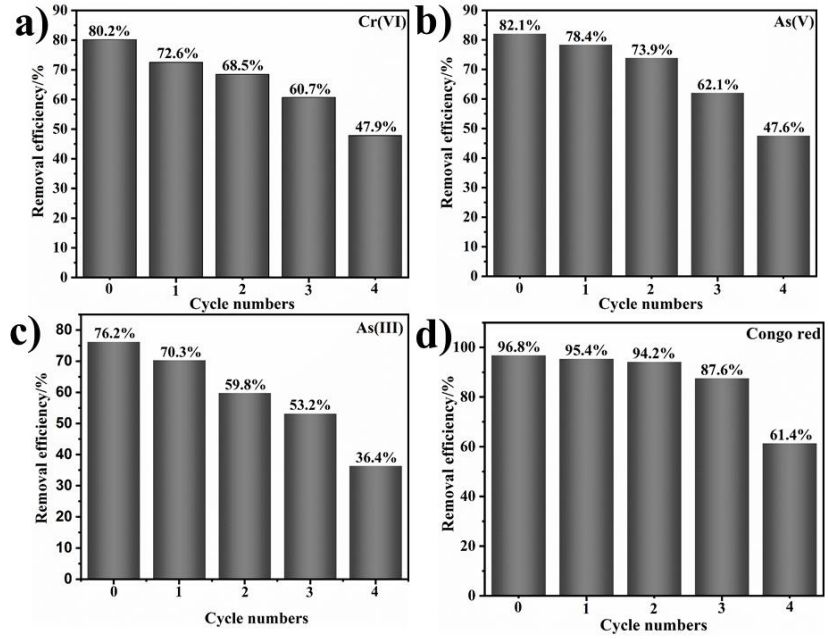


**Figure S4-18** The final removal efficiency of the as-prepared and the regenerated FAO nanoflakes. (a) Cr(VI) adsorption, (b) As(V) adsorption, (c) As(III) adsorption and (d) Congo red adsorption

# References

[1] Schwarzenbach R. P.; Escher B. I.; Fenner K.; Hofstetter T. B.; Johnson C. A.; Gunten U. V.; Wehrli B. The Challenge of Micropollutants in Aquatic Systems. *Science* **2006**, 313, 1072-1077.

[2] Colón J.; Cadena E.; Pognani M.; Barrena R.; Sánchez A.; Font X.; Artola A. Determination of the energy and environmental burdens associated with the biological treatment of source-separated Municipal Solid Wastes. *Energy & Environmental Science* **2012**, 5, 5731-5741.

[3] Blissett R. S.; Rowson N. A. A review of the multi-component utilisation of coal fly ash. *Fuel* **2012**, 97, 1-23.

[4] Palomo A.; Grutzeck M. W.; Blanco M. T. Alkali-activated fly ashes: A cement for the future. *Cement and Concrete Research* **1999**, 29, 1323-1329.

[5] Rogbeck J.; Hartlén J. Ash gravel — A material for recycling. *Waste Management* **1996**, 16, 109-112.

[6] Pandey V. C.; Singh N. Impact of fly ash incorporation in soil systems. *Agriculture, Ecosystems & Environment* **2010**, 136, 16-27.

[7] Bai J. L.; Li Y. Z.; Ren L.; Mao M. Y.; Zeng M.; Zhao X. J. Thermal Insulation Monolith of Aluminum Tobermorite Nanosheets Prepared from Fly Ash. *ACS Sustainable Chemistry & Engineering* **2015**, 3, 2866-2873.

[8] Dunens O. M.; MacKenzie K. J.; Harris A. T. Synthesis of Multiwalled Carbon Nanotubes on Fly Ash Derived Catalysts. *Environmental Science & Technology* **2009**, 43, 7889-7894.

[9] Thirumurthy K.; Thirunarayanan G. A facilely designed, highly efficient green synthetic strategy of a peony flower-like $SO_4^{2-}$–$SnO_2$-fly ash nano-catalyst for the three component synthesis of a serendipitous product with dimedone in water. *RSC Advances* **2015**, 5, 33595-33606.

[10] Yan F.; Jiang J. G.; Tian S. C.; Liu Z. W.; Shi J.; Li K. M.; Chen X. J.; Xu Y. W. A Green and Facile Synthesis of Ordered Mesoporous Nanosilica Using Coal Fly Ash. *ACS Sustainable Chemistry & Engineering* **2016**, 4, 4654-4661.

[11] Wang D. J.; Zhang Y. H.; Dong A. G.; Tang Y.; Wang Y. J.; Xia J. C.; Ren N. Conversion of Fly Ash Cenosphere to Hollow Microspheres with Zeolite/Mullite Composite Shells. *Advanced Functional Materials* **2003**, 13, 563-567.

[12] Liu M. M.; Xi B. D.; Hou L. A.; Yu S. L. Magnetic multi-functional nano-fly ash-derived zeolite composites for environmental applications. *Journal of Materials Chemistry A* **2013**, 1, 12617-12626.

[13] Khatri C.; Rani A. Synthesis of a nano-crystalline solid acid catalyst from fly ash and its catalytic performance. *Fuel* **2008**, 87, 2886-2892.

[14] Li Y.; Zhang F. S. Catalytic oxidation of Methyl Orange by an amorphous FeOOH catalyst developed from a high iron-containing fly ash. *Chemical Engineering Journal* **2010**, 158, 148-153.

[15] Coleman J. N.; Lotya M.; O'Neill A.; Bergin S. D.; King P. J.; Khan U.; Young K.; Gaucher A.; De S.; Smith R. J.; Shvets I. V.; Arora S. K.; Stanton G.; Kim H. Y.; Lee K.; Kim G. T.; Duesberg G. S.; Hallam T.; Boland J. J.; Wang J. J.; Donegan J. F.; Grunlan J. C.; Moriarty G.; Shmeliov A.; Nicholls R. J.; Perkins J. M.; Grieveson E. M.; Theuwissen K.; McComb D. W.; Nellist P. D.; Nicolosi V. Two-Dimensional Nanosheets Produced by Liquid Exfoliation of Layered Materials. *Science* **2011**, 331, 568-571.

[16] Alnasser F.; Castagnola V.; Boselli L.; Esquivel-Gaon M.; Efeoglu E.; McIntyre J.; Byrne H. J.; Dawson K. A. Graphene Nanoflake Uptake Mediated by Scavenger Receptors. *Nano Letters* **2019**, 19, 1260-1268.

[17] Zhang, X.; Cheng, H.; Zhang, H. Recent Progress in the Preparation, Assembly, Transformation, and Applications of Layer-Structured Nanodisks beyond Graphene. *Advanced*

*Materials* **2017**, 29 (35), 1701704.

[18] Ruan G. D.; Sun Z. Z.; Peng Z. W.; Tour J. M. Growth of Graphene from Food, Insects, and Waste. *ACS Nano* **2011**, 5, 7601-7607.

[19] Genovese M.; Jiang J. H.; Lian K.; Holm N. High capacitive performance of exfoliated biochar nanosheets from biomass waste corn cob. *Journal of Materials Chemistry A* **2015**, 3, 2903-2913.

[20] Gong J.; Liu J.; Chen X. C.; Jiang Z. W.; Wen X.; Mijowska E.; Tang T. Converting real-world mixed waste plastics into porous carbon nanosheets with excellent performance in the adsorption of an organic dye from wastewater. *Journal of Materials Chemistry A* **2015**, 3, 341-351..

[21] Qian B. B.; Hosseini T.; Zhang X. W.; Liu Y.; Wang H. T.; Zhang L. Coal Waste to Two-Dimensional Materials: Fabrication of α-$Fe_2O_3$ Nanosheets and MgO Nanosheets from Brown Coal Fly Ash. *ACS Sustainable Chemistry & Engineering* **2018**, 6, 15982-15987.

[22] Choo T. K.; Song Y.; Zhang L.; Selomulya C.; Zhang L. Mechanisms Underpinning the Mobilization of Iron and Magnesium Cations from Victorian Brown Coal Fly Ash. *Energy & Fuels* **2014**, 28, 4051-4061.

[23] Choo T. K.; Cashion J.; Selomulya C.; Zhang L. Reductive Leaching of Iron and Magnesium out of Magnesioferrite from Victorian Brown Coal Fly Ash. *Energy & Fuels* **2016**, 30, 1162-1170.

[24] Hosseini T.; Selomulya C.; Haque N.; Zhang L. Indirect Carbonation of Victorian Brown Coal Fly Ash for $CO_2$ Sequestration: Multiple-Cycle Leaching-Carbonation and Magnesium Leaching Kinetic Modeling. *Energy & Fuels* **2014**, 28, 6481-6493.

[25] Nordstrom D. K. Worldwide Occurrences of Arsenic in Ground Water. *Science* **2002**, 296, 2143-2145.

[26] Mattagajasingh, S. N.; Misra, B. R.; Misra, H. P. Carcinogenic chromium(VI)-induced

protein oxidation and lipid peroxidation: implications in DNA–protein crosslinking, *Journal of Applied Toxicology* **2008**, 28 (8), 987-997.

[27] Kang, D. J.; Hu, C. Q.; Zhu, Q. S. Morphology controlled synthesis of hierarchical structured $Fe_2O_3$ from natural ilmenite and its high performance for dyes adsorption. *Applied Surface Science* **2018**, 459, 327-335.

[28] Cramer A. J.; Cole J. M. Removal or storage of environmental pollutants and alternative fuel sources with inorganic adsorbents via host–guest encapsulation. *Journal of Materials Chemistry A***2017**, 5, 10746-10771.

[29] Ai, Z.; Lu, L.; Li, J.; Zhang, L.; Qiu, J.; Wu, M. Fe@$Fe_2O_3$ Core− shell nanowires as the iron reagent. 2. An efficient and reusable sono-fenton system working at neutral pH. *The Journal of Physical Chemistry C* **2007**, 111 (20), 7430-7436.

[30] Wei Z. H.; Xing R.; Zhang X.; Liu S.; Yu H. H.; Li P. C. Facile Template-Free Fabrication of Hollow Nestlike α-$Fe_2O_3$ Nanostructures for Water Treatment. *ACS Applied Materials & Interfaces* **2013**, 5, 598-604.

[31] Gómez-Pastora, J.; Bringas, E.; Ortiz, I. Recent progress and future challenges on the use of high performance magnetic nano-adsorbents in environmental applications. *Chemical Engineering Journal* **2014**, 256, 187-204.

[32] Yang J.; Zhang H. W.; Yu M. H.; Emmanuelawati I.; Zou J.; Yuan Z. G.; Yu C. Z. High-Content, Well-Dispersed γ-$Fe_2O_3$ Nanoparticles Encapsulated in Macroporous Silica with Superior Arsenic Removal Performance. *Advanced Functional Materials* **2014**, 24, 1354-1363

[33] Wang T.; Zhang L. Y.; Wang H. Y.; Yang W. C.; Fu Y. C.; Zhou W. L.; Yu W. T.; Xiang K. S.; Su Z.; Dai S.; Chai L. Y. Controllable Synthesis of Hierarchical Porous $Fe_3O_4$ Particles Mediated by Poly (diallyldimethylammonium chloride) and Their Application in Arsenic Removal. *ACS Applied Materials & Interfaces* **2013**, 5, 12449-12459.

[34] Wang B.; Wu H. B.; Yu L.; Xu R.; Lim T. T.; Lou X. W. Template-free Formation of Uniform

Urchin-like α-FeOOH Hollow Spheres with Superior Capability for Water Treatment. *Advanced Materials* **2012**, 24, 1111-1116.

[35] Dyer, J. A.; Scrivner, N. C.; Dentel, S. K. A practical guide for determining the solubility of metal hydroxides and oxides in water. *Environmental progress* **1998**, 17 (1), 1-8.

[36] Xie, J.; Zhang, X.; Zhang, H.; Zhang, J.; Li, S.; Wang, R.; Xie, Y. Intralayered Ostwald ripening to ultrathin nanomesh catalyst with robust oxygen‐evolving performance. *Advanced Materials* **2017**, 29 (10), 1604765.

[37] Yu L.; Han R. X.; Sang X. H.; Liu J.; Thomas M. P.; Hudak B. M.; Patel A.; Page K.; Guiton B. S. Shell-Induced Ostwald Ripening: Simultaneous Structure, Composition, and Morphology Transformations during the Creation of Hollow Iron Oxide Nanocapsules. *ACS Nano* **2018**, 12, 9051-9059.

[38] de Laissardière, G. T.; Nguyen-Manh, D.; Mayou, D. Electronic structure of complex Hume-Rothery phases and quasicrystals in transition metal aluminides. *Progress in Materials Science* **2005**, 50 (6), 679-788.

[39] Yu Q.; Meng X. G.; Wang T.; Li P.; Ye J. H. Hematite Films Decorated with Nanostructured Ferric Oxyhydroxide as Photoanodes for Efficient and Stable Photoelectrochemical Water Splitting. *Advanced Functional Materials* **2015**, 25, 2686-2692.

[40] Sun C. L.; Zeng R. X.; Zhang J. K.; Qiu Z. J.; Wu D. P. Effects of UV-Ozone Treatment on Sensing Behaviours of EGFETs with $Al_2O_3$ Sensing Film. *Materials* **2017**, 10, 1432.

[41] Fang R. C.; Sun Q. Q.; Zhou P.; Yang W.; Wang P. F.; Zhang D. W. High-performance bilayer flexible resistive random access memory based on low-temperature thermal atomic layer deposition. *Nanoscale Research Letters* **2013**, 8, 92.

[42] Aoshima M.; Ozaki M.; Satoh A. Structural Analysis of Self-Assembled Lattice Structures Composed of Cubic Hematite Particles. *The Journal of Physical Chemistry C* **2012**, 116, 17862-17871.

[43] Jia C. J.; Sun L. D.; Yan Z. G.; You L. P.; Luo F.; Han X. D.; Pang Y. C.; Zhang Z.; Yan C. H. Single-Crystalline Iron Oxide Nanotubes. *Angewandte Chemie International Edition* **2005**, 117, 4402-4407.

[44] Chen L. X.; Zhang X.; Shelby M. Recent advances on ultrafast X-ray spectroscopy in the chemical sciences. *Chemical Science* **2014**, 5, 4136-4152.

[45] Wilke M.; Farges F.; Petit P. E.; Brown G. E.; Martin F. Oxidation state and coordination of Fe in minerals: An Fe K-XANES spectroscopic study. *American Mineralogist* **2001**, 86, 714-730.

[46] Cao C. Y.; Qu J.; Yan W. S.; Zhu J. F.; Wu Z. Y.; Song W. G. Low-Cost Synthesis of Flowerlike α-$Fe_2O_3$ Nanostructures for Heavy Metal Ion Removal: Adsorption Property and Mechanism. *Langmuir* **2012**, 28, 4573-4579.

[47] Hao T.; Yang C.; Rao X. H.; Wang J. D.; Niu C. G.; Su X. T. Facile additive-free synthesis of iron oxide nanoparticles for efficient adsorptive removal of Congo red and Cr(VI). *Applied Surface Science* **2014**, 292, 174-180.

[48] Du Y. C.; Fan H. G.; Wang L. P.; Wang J. S.; Wu J. S.; Dai H. X. α-$Fe_2O_3$ nanowires deposited diatomite: highly efficient absorbents for the removal of arsenic. *Journal of Materials Chemistry A* **2013**, 1, 7729-7737.

[49] Qiu G. H.; Huang H.; Genuino H.; Opembe N.; Stafford L.; Dharmarathna S.; Suib S. L. Microwave-Assisted Hydrothermal Synthesis of Nanosized α-$Fe_2O_3$ for Catalysts and Adsorbents. *The Journal of Physical Chemistry C* **2011**, 115, 19626-19631.

[50] Martinson C. A.; Reddy K. J. Adsorption of arsenic(III) and arsenic(V) by cupric oxide nanoparticles. *Journal of Colloid and Interface Science* **2009**, 336, 406-411.

[51] Cao C. Y.; Cui Z. M.; Chen C. Q.; Song W. G.; Cai W. Ceria Hollow Nanospheres Produced by a Template-Free Microwave-Assisted Hydrothermal Method for Heavy Metal Ion Removal and Catalysis. *The Journal of Physical Chemistry C* **2010**, 114, 9865-9870.

[52] Jia Z. G.; Liu J. H.; Wang Q. Z.; Li S. B.; Qi Q.; Zhu R. S. Synthesis of 3D hierarchical porous iron oxides for adsorption of Congo red from dye wastewater. *Journal of Alloys and Compounds* **2015**, 622, 587-595.

[53] Maiti D.; Mukhopadhyay S.; Devi P. S. Evaluation of Mechanism on Selective, Rapid, and Superior Adsorption of Congo Red by Reusable Mesoporous α-$Fe_2O_3$ Nanorods. *ACS Sustainable Chemistry & Engineering* **2017**, 5, 11255-11267.

[54] Fei J. B.; Zhao J.; Du C. L.; Ma H. C.; Zhang H.; Li J. B. The facile 3D self-assembly of porous iron hydroxide and oxide hierarchical nanostructures for removing dyes from wastewater. *Journal of Materials Chemistry A* **2013**, 1, 10300-10305.

[55] Fei J. B.; Cui Y.; Yan X. H.; Qi W.; Yang Y.; Wang K. W.; He Q.; Li J. B. Controlled Preparation of $MnO_2$ Hierarchical Hollow Nanostructures and Their Application in Water Treatment. *Advanced Materials* **2008**, 20, 452-456.

[56] Cai W. Q.; Yu J. G. ; Jaroniec M. Template-free synthesis of hierarchical spindle-like γ-$Al_2O_3$ materials and their adsorption affinity towards organic and inorganic pollutants in water. *Journal of Materials Chemistry* **2010**, 20, 4587-4594.

[57] Cai W. Q.; Yu J. G.; Cheng B.; Su B. L.; Jaroniec M. Synthesis of Boehmite Hollow Core/Shell and Hollow Microspheres via Sodium Tartrate-Mediated Phase Transformation and Their Enhanced Adsorption Performance in Water Treatment. *Journal of Physical Chemistry C* **2009**, 113, 14739-14746.

[58] Lee, H. U.; Lee, S. C.; Lee, Y. C.; Vrtnik, S.; Kim, C., Lee, S.; Lee, J. Sea-urchin-like iron oxide nanostructures for water treatment. *Journal of Hazardous Materials* **2013**, 262, 130-136.

[59] Pal, D. B.; Chand, R.; Upadhyay, S. N.; Mishra, P. K. Performance of water gas shift reaction catalysts: a review. *Renewable and Sustainable Energy Reviews* **2018**, 93, 549-565.

# Chapter 5 Synthesis of (111) facet-engineered MgO nanosheet from coal fly ash and its superior catalytic performance for high-temperature water gas shift reaction

It has been reviewed in Chapter 2 that the synthesis of facet-engineered nano-$Mg(OH)_2$ from coal fly ash is still blank. Based on the efficient leaching of Mg from fly ash, the resultant Mg-rich leachate was used as the feedstock to synthesize the nanosized $Mg(OH)_2$ and it was employed as a support to fabricate the facet-engineered Mg-Fe-O catalyst for the WGSR. This chapter has studied the growth of (001) facet-rich $Mg(OH)_2$, the conversion from (001) facet-rich $Mg(OH)_2$ to (111) facet-rich MgO and its catalytic performance towards the WGSR after loading 30 *wt.*% Fe. This chapter has been published in ***Applied Catalysis A: General:*** **Binbin Qian**, Jianghao Zhang, Song Zhou, Jun Lu, Yue Liu, Baiqian Dai, Cheng Liu, Yong Wang, Huanting Wang, Lian Zhang*, *Synthesis of (111) facet-engineered MgO nanosheet from coal fly ash and its superior catalytic performance for high-temperature water gas shift reaction*, ***Applied Catalysis A: General***, 2021, 618, 118132.

## Abstract

Synthesis of high-value products from coal ash, an otherwise valueless waste is crucial to both sustainable waste treatment and low-cost material fabrication. However, research in this area is still sparse, with majority of the researches being conducted on the synthesis of alumina/silica-based nanomaterials such as zeolite. Herein, we report a facile synthesis of high-purity, magnesium hydroxide ($Mg(OH)_2$) nanosheet from a brown coal fly ash (BCFA) waste via leaching, precipitation and ethanol-mediated hydrothermal process in sequence. The resultant nanosheet from fly ash bears a specific surface area of around 100 $m^2/g$, and an averaged aspect ratio of 11.8, as opposed to only 1.5 for the commercial $Mg(OH)_2$ and the one synthesed without the mediation of ethanol during hydrothermal processing. The fly ash derived $Mg(OH)_2$ nanosheet was subsequently loaded with 30 *wt%* $Fe^{3+}$ (as $Fe_2O_3$) via incipient wetness impregnation and calcined into a (111) facet-rich MgO, which was proved for a superior catalysis performance for high-temperature water gas shift reaction (HT-WGSR). At the reaction temperatures of 400-450 $^oC$, the CO conversion was increased by a factor of two compared to a reference catalyst consisting of identical Fe loading on a $Mg(OH)_2$ support synthesized without ethanol, and by a factor of seven compared to a nano-sized hematite catalyst synthesized from same hydrothermal process without ethanol addition. This is mainly due to the abundant oxygen vacancy on the (111) facet of the MgO nanosheet support, which improved the reducibility of $Fe^{3+}$ as well as facilitated the formation and decomposition of intermediate formates that in turn promoted the forward reaction. This study is expected to open a new direction for the valorisation of fly ash and any Mg-bearing solid wastes into high-value materials such as catalyst or catalyst support for a broad range of industrial applications.

**Keywords:** Coal fly ash, Facet engineering, MgO nanosheet, Waste treatment, Water gas shift

reaction

## 5.1 Introduction

Due to the continuous use of coal as the single largest solid fuel for the power generation in most countries, coal fly ash is one of the largest solid wastes with an annual yield of approximate 750 million tons, among which 10 million tons is discharged in Australia [1,2]. Conventionally, coal fly ash can be used as a low-value additive into cement-based construction materials [3], road base [4] and agriculture [5]. With the increased awareness of the superiority of nanoparticles, various nanomaterials have been synthesized from fly ash, such as silicon nanorods [6], carbon nanofibers [7], geopolymer [8], mesoporous nanosilica [9], zeolite [10] and ordered mesoporous molecular sieves [11]. Despite of these findings, most of the reported nanomaterials are limited to alumina ($Al_2O_3$) and/or silica ($SiO_2$), which are abundant in the coal ashes produced from high-rank coals. For the ash produced from a low-rank coal such as brown coal, it is implausible to synthesize these Al-/Si-based nanomaterials as they are generally lean in the low-rank coal ashes.

As a continuation of our effort on the synthesis of hematite ($\alpha$-$Fe_2O_3$) nanoflake from a Mg-rich local coal ash, namely BCFA [12], in this work, we further report the synthesis of high-purity, magnesium hydroxide ($Mg(OH)_2$) nanosheet from the same fly ash, and a successful demonstration of its high-value application for the use as catalyst promoting the hydrogen production from HT-WGSR. The principal motivation for an effort is to utilize the Mg-rich fly ash as a substitute for natural dolomite or chrysotile for the production of high-purity brucite ($Mg(OH)_2$) and magnesia (MgO). On the one hand, as a by-product derived from high-temperature coal combustion, fly ash bears negligible fibrous-asbestiform crystal habitus that is however present in natural dolomite and serpentine. Therefore, the use of fly ash is expected

to cause less/negligible risk to the development of malignant mesothelioma and lung cancers induced by the environmental exposure to asbestos [13]. On the other hand, the presence of alkali and alkaline earth metals including $Mg^{2+}$ in fly ash hinders its use as an additive to cement, which would otherwise lead to the breakage of the road and bridge [14].

In addition, from the scientific perspective, this research aims to synthesize a facet-rich nanosheet structure for $Mg(OH)_2$ and MgO from fly ash, based on the rational that the crystal materials with a controlled facet at nanoscale level is crucial for boosting their performance in catalysis [15-18]. For the target oxide MgO, its (111) is composed exclusively of alternating polar monolayers of $O^{2-}$ and $Mg^{2+}$, and hence, a strong electrostatic field perpendicular to the (111) facet is created, which has abundant Lewis basicity $O^{2-}$ sites (oxygen vacancy). This in turn makes the (111) facet ideal for the storage of hydrogen [19], carbon capture [20] and catalysis [21]. To date, most of the proposed synthesis procedures are complex and/or energy-intensive, including the deposition of MgO on a facet-rich substrate such as Si(100), Ag(111) or GaAs(001) [22], mechanical polishing followed by acid etching [23], ion bombardment [24], electron beam annealing (1000 °C) in an ultrahigh vacuum (UHV) [25], benzyl alcohol-assisted supercritical synthesis [26] and multistep MgO-$Mg(OH)_2$-MgO transformation upon heating under dynamic vacuum [27]. For the catalysis performance evaluation, the HT-WGSR was chosen here. This is because his reaction has been remaining as the most practical reaction for hydrogen production, contributing to over 95% of hydrogen produced by steam methane reforming of hydrocarbon fuels followed by WGSR [28]. For the hydrogen production from renewable biogas reforming, the WGSR is also one of the three principal steps [29]. In addition, although plenty of catalysts have been developed for the HT-WGSR, the development of non-toxic substitutes for the commercial Cr-laden hematite is still ongoing and the reaction mechanism is also in dispute [30]. There is still a lack of application of the facet-dependent

nanocrystal catalysts to the HT-WGSR [15].

In this study, we demonstrate a novel synthesis of high-purity, (111) facet-dominant MgO from BCFA, as per a facile leaching-precipitation-hydrothermal scheme in **Figure 5-1**. In brief, upon an initial crushing and water-washing, the BCFA powders are treated by leaching, precipitation and ethanol-mediated hydrothermal treatment sequentially, leading to the production of $Mg(OH)_2$ nanosheet with a high purity, high yield and high selectivity. Afterwards, it was impregnated with 30 *wt*% $Fe^{3+}$ and calcined successfully into an (111)-facet rich MgO-supported catalyst. Extensive characterizations based on XRD, TEM, XPS and synchrotron X-ray adsorption spectroscopy (XAS) have been conducted to elucidate the properties of the resultant products. For HT-WGSR catalysis performance evaluation, apart from CO conversion and time-on-stream testing, *in-situ* DRIFTS, CO-TPR and $H_2$-TPR were also conducted to elucidate the unique reducibility of $Fe^{3+}$ and reaction mechanism on the (111)-facet directional MgO. The results reported hereby are expected to cast a broad impact on the sustainable utilization of solid wastes and low-cost synthesis of facet-engineered catalysts in the clean energy research area.

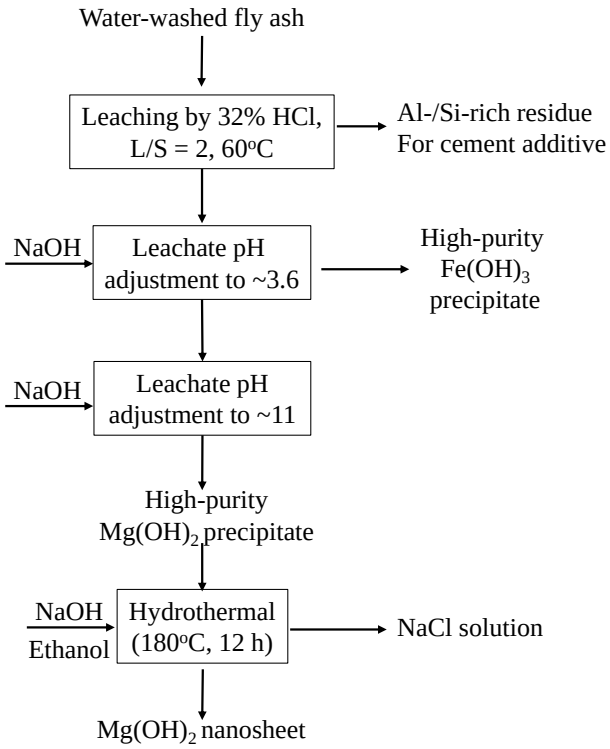


**Figure 5-1**. Scheme of synthesis of high-purity $Mg(OH)_2$ nanosheet from BCFA. Note that all the three products including Al-/Si-rich residue, high-purity $Fe(OH)_3$ and $Mg(OH)_2$ nanosheet can be used rather than landfilled, enabling a full recovery and reuse of this special fly ash.

## 5.2 Experimental

### 5.2.1 Materials

The BCFA waste was collected from the Energy Australia Yallourn power plant located in the Latrobe Valley, Victoria, Australia. **Table 5-1** shows the elemental composition of the BCFA sample. It is clear that both Fe and Mg are abundant in this fly ash, whereas Al and Si are rather lean. The as-received fly ash sample was washed at a liquid to solid (L/S) mass ratio of 10 to remove the unburnt carbon and water-soluble species. Subsequently, it was dried in an oven at 105 °C for 12 h and ground using a tungsten-carbide vibratory ring pulveriser, producing a particle size of <150 μm prior to use.

All the other chemicals including HCl (32 *wt*%), NaOH, MgO, ethanol, silicon carbide (SiC), $FeCl_3 \cdot 6H_2O$ and $Fe(NO_3)_3 \cdot 9H_2O$ were purchased from Sigma-Aldrich. Milli-Q water was used throughout all the experiments. Note that SiC was sieved to a narrow size of 105-165 μm, pre-ultrasonicated and dried prior to the HT-WGSR experiments.

### 5.2.2 Synthesis of $Mg(OH)_2$ Nanosheets and Fe-Mg-O Catalysts

The leaching process was consistent with our previous research [12]. To be specific, a two-step cross-current leaching method was used to extract $Mg^{2+}$ from the Victorian BCFA, as shown in **Figure S5-1** in the Supporting Information (SI). In each step, 32 *wt*% HCl was used as the leaching agent to mix with water-washed fly ash or the leaching residue derived from the previous step, at a L/S mass ratio of around two in a closed 250 mL conical flask. The flask was further placed in a thermostatically controlled water bath at 60 °C and stirred for a period of 90 min. The stirring rate was controlled at 300 rpm throughout all the runs. Afterwards, the slurry was filtered via a vacuum pump and a filter paper with a cut-off size of 450 μm. As shown in **Figure S5-2**, the resultant leachate is dominated by $Fe^{3+}$ and $Mg^{2+}$, accompanied by a small amount for $Ca^{2+}$ and $Al^{3+}$. Subsequently, 1 mol/L NaOH was added dropwise into the leachate until its pH reached ~3.6, forming a slurry that was then centrifuged at 10,000 rpm for 10 min to remove the $Fe(OH)_3$ precipitate. For the resultant $Mg^{2+}$-rich leachate, 1 M NaOH solution was further added dropwise until its pH reached ~11. Consequently, a white slurry was obtained, and centrifuged at 8000 rpm for 10 min to obtain the $Mg(OH)_2$ precipitate. The $Mg(OH)_2$ precipitate was further suspended into Milli-Q water and ultrasonicated for approximately 1 h. Subsequently, 1 mol/L of NaOH solution was dropped into the slurry via a peristaltic pump at a discharge rate of 9.6 mL/min. The resultant suspending solution was placed at room temperature and stirred continuously at 100 rpm. Its pH was closely monitored every 2 min in the first 20 min and then every 30 s. Once the pH reached 11, approximately 10

ml of ethanol was added into the suspension to prevent the agglomeration of the particles and tune the growth of $Mg(OH)_2$ as an organic additive [31]. For each condition, three repeats were conducted to secure a high accuracy and sufficient sample. The resultant suspending solutions were combined and transferred into a 120 mL autoclave. The closed autoclave was finally placed inside a preheated hot-air oven maintained at 180 °C for 12 h, followed by a natural cooling down to room temperature. The obtained precipitate was filtered, washed with distilled water to remove the excessive NaOH and then with ethanol to reduce the agglomeration, and finally dried at 80 °C for 2 h.

Three reference materials were synthesized and tested, including $Mg(OH)_2$ nanoparticles that were synthesized from the same BCFA, and by exactly the same procedure without the addition of ethanol in the hydrothermal step; commercial MgO purchased from Sigma-Aldrich, and hematite ($Fe_2O_3$) nanoparticles synthesized from using pure $FeCl_3$ solution as the precursor, as per a similar hydrothermal procedure detailed in our previous research [12].

An impregnation method was used to load $Fe^{3+}$ on a MgO support. Specifically, the as-synthesized $Mg(OH)_2$ was first mixed with $Fe(NO_3)_3{\cdot}9H_2O$ at a mass percentage of 30 *wt%* for $Fe_2O_3$ (Hereafter, the loading amount of iron is described as 30 *wt%* $Fe^{3+}$). A very small amount of water (I.e. 1-2 ml per unit gram of $Mg(OH)_2$) was then gradually added into the mixture which was also continuously stirred until it turned pulpy. The resultant pulp was then dried at 80 °C overnight and calcined in air at 400 ºC for 4 h. The $Fe^{3+}$-MgO catalysts with ethanol treatment (facet-engineered), without ethanol treatment and from commercial purchase are denoted as FEMNS, NMNS and CMP, respectively. Notably, before the XRD analysis of the reduced FEMNS, NMNs and CMP, they were dispersed in ethanol and the resultant suspensions were dropped onto a clean glass substrate with subsequent drying at room

temperature for one day and further heating in the muffle furnace at 350 °C for 2h, which is expected to make the (111) facet perpendicular to the diffraction vector ***s*** (the vector that bisects the angle between the incident and diffracted beam) to produce more collectible scattered beams [32]. It is also noteworthy that, only 30 *wt%* of $Fe^{3+}$ was tested in this study, aiming to demonstrate the superiority of the fly ash-derived MgO nanosheet over its counterparts. Regarding the optimization of the mass fraction of $Fe^{3+}$ and other conditions such as those for HT-WGSR, it is out of the scope.

### 5.2.3 HT-WGSR Testing

Catalytic performance was evaluated in a continuous-flow fixed bed reactor at 400-450 ºC and under the atmospheric pressure. For each run, 50-170 mg of a synthesized catalyst was blended and co-loaded with ten times the amount of pre-cleaned SiC, and then heated to 400 ºC under the protection of $N_2$ at a heating rate of 10 °C/min, which simultaneously removed the surface contaminants. Afterwards, the dry CO gas at a concentration of ~ 4.5 vol% was fed into the system at a flow rate of 200 ml/min for 1-2 h, until the $CO_2$ signal was negligible (<0.1%) in the outlet gas. Note that the dry CO gas functioned as a reducing agent for an *in-situ* reduction of $Fe^{3+}$ into ferrous $Fe^{2+}$, which is expected to be the active site [33,34]. Catalysts were reduced at both 400 and 450 °C and it is found that the CO conversion for catalysts reduced at 400 °C is higher, as shown in **Figure S5-3**. Therefore, the reduction temperature was set at 400 °C for all the runs. After catalyst reduction, CO and steam were introduced at a concentration of ~ 4.5-5 vol% each to commission the HT-WGSR for ~60 min for most of the cases. For two typical catalysts, time-on-stream testing in 10 h was also conducted. The overall gas flow rate remained at 200 mL/min, resulting in a space velocity of 0.23-0.89 $m^3\ g_{Fe2O3}^{-1}\ h^{-1}$.

The outlet gas stream was on-line monitored by an MKS Multigas$^{TM}$ 2030 Fourier-transform

infrared spectroscopy (FTIR) continuous gas analyzer for CO, $CO_2$, $H_2O$ and $CH_4$. It was also periodically sampled for the quantification of $H_2$, CO, $CO_2$ and $CH_4$ by an Agilent gas chromatography (GC) coupled with a TCD detector. The analysis showed a good consistence between the two analytic instruments. A closed mass balance for carbon was also confirmed. For the catalyst performance evaluation, the CO conversion based on the difference of inlet and outlet CO concentrations was used primarily.

### 5.2.4 Catalyst Characterization

A number of advanced facilities, including X-ray diffraction (XRD), scanning electron microscopy (SEM), transmission electron microscopy (TEM), small area electron diffraction (SAED), X-ray photoelectron spectroscopy (XPS) and synchrotron soft X-ray near-edge X-ray absorption fine structure (NEXAFS) have been employed to characterize the solid samples. Details for each analysis procedure can be found in the SI. Note that the (NEXAFS analysis was conducted on the total electron yield (TEY) mode that is highly surface intensive [35].

For the catalysis mechanistic study, *In-situ* diffuse reflectance infrared Fourier transform spectroscopy (DRIFTS), CO-Temperature Programmed Reduction (TPR) and $H_2$-TPR were performed, with the detail for each analysis procedure given in the supporting results.

## 5.3 Results and discussion

### 5.3.1 Synthesis and Properties of BCFA derived $Mg(OH)_2$ and Fe-Mg-O Catalysts

**Table 5-1.** Mass yield, elemental compositions, specific surface area and aspect ratio of raw fly ash and as-synthesized $Mg(OH)_2$ nanoparticles (*wt*%).

| | Percent (%) | | |
|---|---|---|---|
| | Raw fly ash | $Mg(OH)_2$ nanosheet synthesized with the use of ethanol | $Mg(OH)_2$ nanoparticles synthesized without the use of ethanol |
| Mass yield, *wt%* on unit fly ash mass | -- | 19.9 | |
| Elemental composition, *wt%* | | | |
| $SiO_2$ | 12.45 | N.D.[1] | N.D. |
| $Al_2O_3$ | 7.47 | N.D. | N.D. |
| $Fe_2O_3$ | 33.35 | 0.45 | 0.29 |
| CaO | 5.22 | 0.49 | 0.57 |
| MgO | 14.51 | 68.39 | 69.21 |
| $K_2O$ | 0.06 | N.D. | N.D. |
| $SO_3$ | 1.42 | N.D. | N.D. |
| MnO | 0.41 | N.D. | N.D. |
| $TiO_2$ | 0.79 | N.D. | N.D. |
| Loss of Ignition[3] | 24.32 | 30.67 | 29.93 |
| Physical properties | | | |
| Aspect ratio, [-] | - | 11.8 | 1.5 |
| Specific surface | - | 103.7 | 78.2 |

| | | | |
|---|---|---|---|
| area ($m^2 g^{-1}$) | | 340.7 (Calcined) | 321.7 (Calcined) |
| | | 104.5 (FEMNS)[2] | 100.8 (NMNS)[2] |

[1] N.D.: Not detectable by XRF; [2]: after the loading with 30 *wt*% $Fe^{3+}$ and further calcination at 400ºC for 4 hr. [3]: LOI was measured by heating a sample up to 800 ºC in air in TGA. The LOI for a commercial $Mg(OH)_2$ was found to be around 31 *wt*%.

As demonstrated in **Table 5-1**, the $Mg(OH)_2$ precipitate from fly ash has a mass yield of around 19.9% on the basis of water-washed fly ash, this is due to a successful extraction of the majority of the inherent $Mg^{2+}$ out of fly ash matrix, leaving MgO with a content of around 1.3 *wt%* in the leaching residue [36]. In addition, **Table 5-1** indicates a high purity for the two nano-$Mg(OH)_2$ derived from the hydrothermal step, with a MgO content of around 69 *wt%* and an LOI content of around 31 *wt*% that is very close to the commercial $Mg(OH)_2$. Interestingly, the impurities such as $Fe^{3+}$ and $Ca^{2+}$ are controlled at a negligible level, whist the other elements are indeed negligible. This further demonstrates a high selectivity for the extraction of $Mg^{2+}$ from fly ash. Regarding the physical properties of the two $Mg(OH)_2$ products, the one formed upon the addition of ethanol has a BET specific surface area of around 103.7 $m^2/g$, which is slightly higher than the one without ethanol. Nevertheless, these BET values are comparable and even superior to the nano $Mg(OH)_2$ synthesized from pure chemicals elsewhere [37,38]. After calcination at 400ºC, The BET surface area for the resultant MgO was further improved to 340.7 $m^3/g$ and 321.7 $m^2/g$ for the $Mg(OH)_2$ synthesis with and without ethanol, respectively. These values are comparable and even superior to previous findings [39-41]. The loading of 30 *wt*% $Fe^{3+}$ clearly occupied some of the pores, and hence, reverted the surface area to around 100 $m^2/g$.

XRD patterns for $Mg(OH)_2$ nanosheets prepared with and without ethanol treatment are shown

in **Figure 5-2(a)**. All diffraction peaks can be indexed to the hexagonal brucite structure of $Mg(OH)_2$ (ICSD 34401) with lattice constants of a = 3.148 Å and c = 4.787 Å. The fact that no peaks associated other phases were observed further confirmed the high-purity of the $Mg(OH)_2$ nanosheets synthesized. Moreover, the addition of ethanol in the hydrothermal stage led to an enhanced intensity of the (0 0 1) peak. More specifically, the intensity ratio of peak (0 0 1) to (1 0 1) reaches 1.32 after the addition of ethanol, relative to merely 0.71 in the absence of ethanol and 0.79 in the standard file ICSD #34401. This is a clear evidence of the preferential orientation of $Mg(OH)_2$ on the (0 0 1) facet. Such a phenomenon is associated with the change of the surface energy upon the adsorption of organic molecules during hydrothermal modification [42,43]. The ethanol used here should work both as a dispersant and an anionic surfactant that was apparently adsorbed more readily on the (0 0 1) facet to reduce the high potential energy of the system, hindering the growth of nanoparticle in the [0 0 1] direction while promoting the edgewise growth normal to c-axis. Note that the trace impurities including $Ca^{2+}$ and $Fe^{3+}$ from fly ash leachate can be ruled out here, as the use of pure $MgCl_2$ solution lead to exactly the same structure for $Mg(OH)_2$, as demonstrated in **Figure S5-4**.

The SEM images of the $Mg(OH)_2$ samples are shown in **Figures 5-2(b)** and **5-2(c)**, respectively. **Figure 5-2(c)** confirms a regular hexagonal structure for $Mg(OH)_2$ synthesized without the presence of ethanol. The averaged diameter reaches 113 nm and the mean thickness is 76 nm (**Figure S5-5** and **S5-6**). These thickened sheets clearly tended to grow at a comparable rate in both c- and a- directions, thereby culminating in the shape of roughly equiaxed particles. In contrast, upon the addition of ethanol in the hydrothermal stage, **Figure 5-2(b)** shows the abundance of well-grown thinner nanosheet with an averaged diameter of 212 nm and a mean thickness of 18 nm (**Figure S5-5** and **S5-6**). Consequently, the aspect ratio of diameter to thickness for $Mg(OH)_2$ has been increased dramatically, reaching 11.8 for the use of ethanol

versus merely 1.5 without ethanol, as shown in **Table 5-1**.

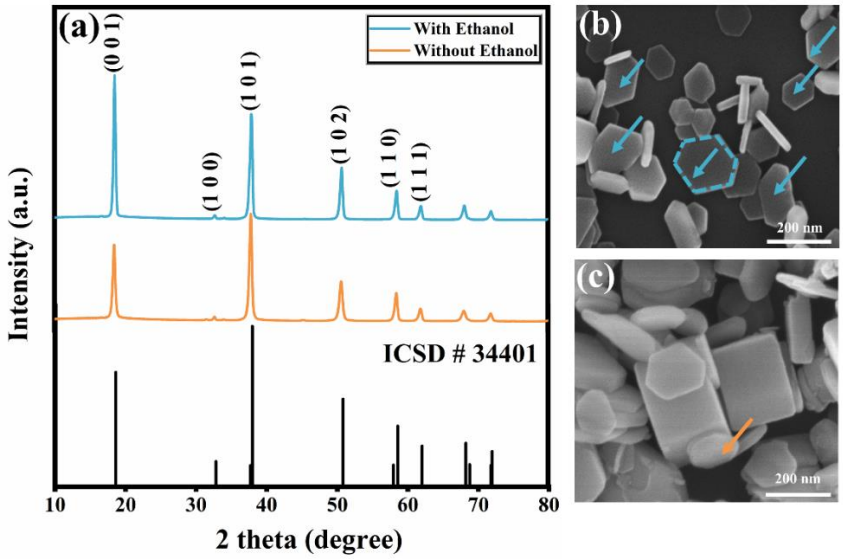


**Figure 5-2.** (a) XRD patterns for $Mg(OH)_2$ nanosheets with and without ethanol treatment. (b) and (c) are SEM images for $Mg(OH)_2$ nanosheets with and without ethanol, respectively.

In the temperature window of 400-450 ºC employed for calcination, reduction and HT-WGSR in this study, the as-synthesized $Mg(OH)_2$ is supposed to dehydroxylate into MgO crystal and a vapor-phase $H_2O$. For the resultant MgO, its (111) facet was found equivalent to facet (001) in the original $Mg(OH)_2$ in terms of orientation [44]. In other words, the (001) facet in $Mg(OH)_2$ can contribute to the exposure of unstable (111) facet for MgO, as depicted in **Figure 5-3(a)**. **Figure 5-3(b)** for the XRD patterns of the reduced Fe-Mg-O catalysts confirmed the hypothetical transformation route in **Figure 5-3(a)**. All the diffraction peaks can be indexed to the standard FCC periclase (MgO) structure (ICSD #26958) with a lattice constant of a = 4.203 Å. More interestingly, the calcined FEMNS based on the (001) facet-rich $Mg(OH)_2$ nanosheet bears a stronger crystallinity degree (manifested as peak sharpness) and intensity for the (111) and (222) diffraction peaks than its counterpart, calcined NMNS without the use of ethanol. This confirms the transformation route in **Figure 5-3(a)**. The HRTEM image in **Figure 5-3(c1)**

attests the abundance of irregular nanoparticles derived from the reduction of NMNS crystals. In contrast, the calcined FEMNS in **Figure 5-3(c2)** displays a well-defined, intact hexagonal lamellar morphology with an average diameter of ~100 nm. These nanosheets also feature a thickness of approximately 10 nm that is comparable with its (001) facet-rich $Mg(OH)_2$ precursor. More specifically, the HRTEM image in **Figure 5-3(c3)** of the standing nanosheet (blue region in (**c2**)), and its corresponding FFT pattern and line intensity profile in **Figure 5-3(c4)** exhibit the characteristic lattice fringes with a distance of 0.242 nm, which is in good agreement with the (111) lattice spacings in MgO [26]. Furthermore, the structure of a single calcined FEMNS single particle is amplified in **Figure 5-3(d)**, which exhibits an obvious hexagonal outline and a 6-fold symmetry of the corresponding SAED pattern that can be indexed to the [111] zone axis diffraction for the {2 -2 0} crystal facts. More intriguingly, regardless of the MgO precursor, the diffraction spot from the loaded $Fe^{3+}$ is undetectable by XRD, indicating that $Fe^{3+}$ is highly dispersed rather than forming any crystalline such as magnetite ($Fe_3O_4$) or magnesium ferrite ($MgFe_2O_4$) that has been reported as the active site for HT-WGSR [34,45]. Probably, it is present as a solid solution such as $Fe_xMg_{1-x}O$ with a non-stoichiometric formula. **Figure 5-3(e)** and **(f)** shows the bright field HRTEM for the Fe-laden FEMNS and NMNS, respectively. The bright areas in **Figure 5-3(e)** for FEMNS represent the MgO crystals with a lattice d-spacing of 0.148 nm and 0.211 nm for the {022} and {002} facets, respectively. The darker areas (blue ovals) are the contrast from Fe species, which again are confirmed with a high dispersion as nano and even sub-nano clusters, without any crystal structure. Similar observation was confirmed for the Fe-laden NMNS in **Figure 5-3(f)**. However, no obvious discrepancy was discerned for the size and dispersion of Fe-clusters between the two supports.

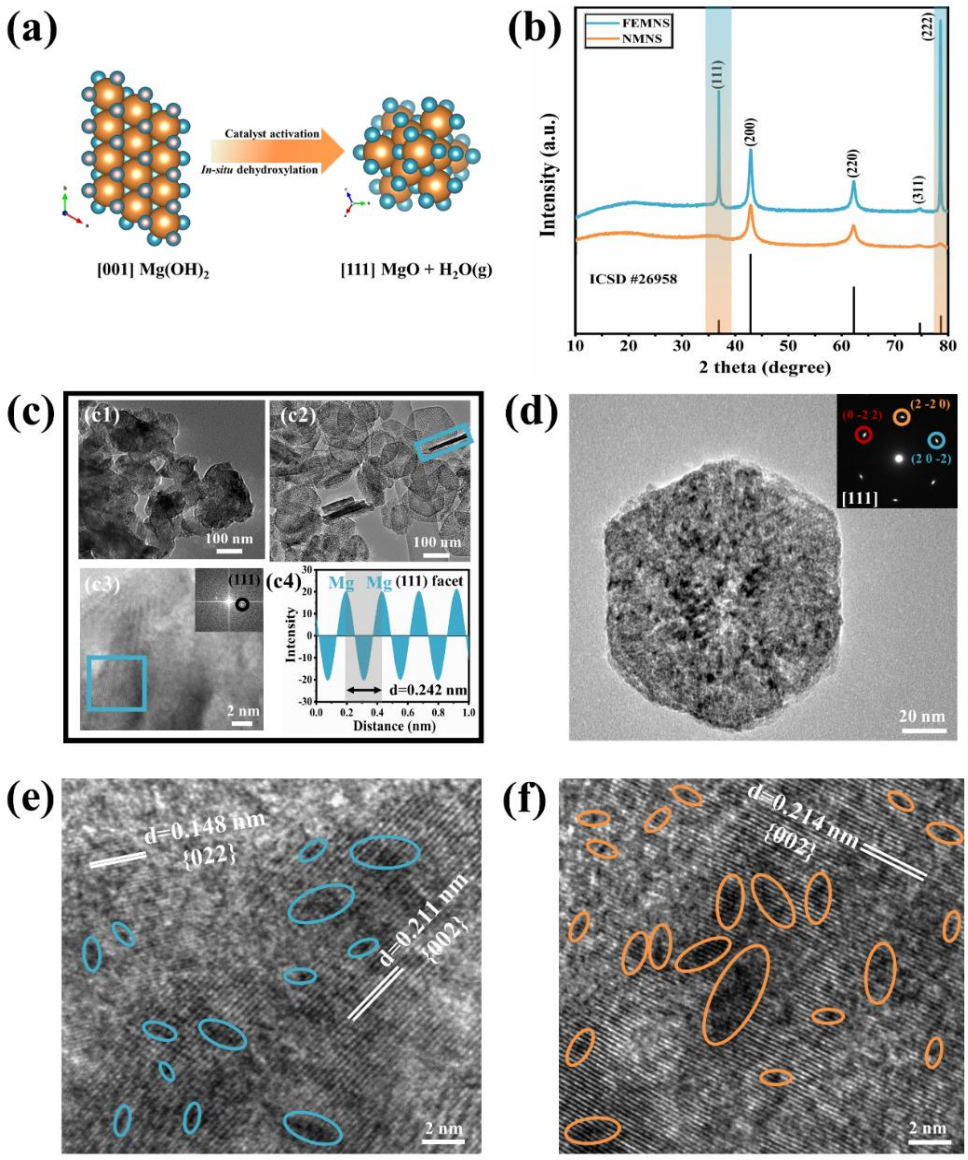


**Figure 5-3.** (a) Equivalent orientations from [001] of $Mg(OH)_2$ to [111] of MgO during *in-situ* dehydroxylation. (b) XRD patterns for FEMNS and NMNS. (c) HRTEM images of catalysts: (c1) NMNS nanoparticles, (c2) FEMNS nanosheets, (c3) high-magnification TEM image from the blue region in (c2) (Inset is the corresponding FFT pattern for blue region) and (c4) line intensity profile from the blue region in (c3). (d) A typical FEMNS single crystal (inset: SAED pattern). (e) and (f) are bright field HRTEM images of FEMNS and NMNS, respectively. The yellow, blue and white spheres represent Mg, O and H, respectively.

### 5.3.2 HT-WGSR Performance of Fe-Mg-O Catalysts

**Figure 5-4** displays the CO conversion data on different catalysts. At the reaction temperature of 400 ºC, as show in **Figure 5-4(a)**, it is evident that the stabilized CO conversion only reached 5% for pure hematite, which is less than the value of 20% reported elsewhere [46]. This should be due to the harsh HT-WGSR conditions (*i.e.* low CO/steam partial pressure and high space velocity) employed here. The HT-WGSR rate is also kinetically controlled by the partial pressures of CO and steam [32,47,48]. Nevertheless, the discrepancy between the three MgO-supporting catalysts is more interesting. The NMNS catalyst clearly bears a comparable activity with the CMP ($Fe^{3+}$ loaded on commercial MgO), both improving the CO conversion to around 10% at 400 ºC. This substantiates a structural similarity of these two catalysts, as well as the insignificance of trace $Ca^{2+}$ within the fly ash derivates. However, the CO conversion reached ~22% for the FEMNS at 400 ºC. It is further demonstrated in **Figure 5-4(b)** that increasing the reaction temperature to 450 °C improved the CO conversion for all the catalysts, while the discrepancy among different catalysts is still remarkable. In particular, the use of FEMNS resulted in a CO conversion of ~35% that is around eight-fold higher than the pure hematite and two-fold higher than the NMNS. The NMNS was also slightly more active than the commercial MgO, which should be due to the abundance of nano-size and thus, a larger specific surface area (**Table S5-1**) of the NMNS catalyst. More specifically, **Table S5-1** quantitatively compared the mass-based specific reaction rates for all the catalysts tested. The value for FEMNS reached $832.14\times10^{-4}$ and $1682.68\times10^{-4}$ $mol_{co}$ $g_{Fe2O3}^{-1}$ $h^{-1}$ at 400 ºC and 450 °C, respectively. Both are nearly one order of magnitude higher than pure hematite. In addition, the superior performance of FEMNS is merely attributed to its facet-engineered feature, rather than the specific surface area. As shown in **Table S5-1**, the BET specific surface area of FEMNS is very close to that of NMNS and even the commercial MgO-supported catalyst. This means that

the preferential orientation of (001) facet was achieved at an expense of the other facets for $Mg(OH)_2$. Additionally, **Figure 5-4(c)** displays the CO conversion of FEMNS and NMNS at 450 °C over a 10-hour time-on-stream (TOS), which obviously substantiates a stronger stability of FEMNS than its counterpart over a long period.

The CO conversion profiles versus space velocity over the FEMNS and NMNS catalysts are presented in **Figure S5-7**. Due to a shortened residence time, a lower CO conversion is expected at a higher space velocity. Nevertheless, even at the highest space velocity of 0.89 $m^3$ $g_{Fe2O3}^{-1}$ $h^{-1}$ studied, the CO conversion of FEMNS at 450 ºC still reached 10.3% that is considerably higher than NMNS at 7.4%.

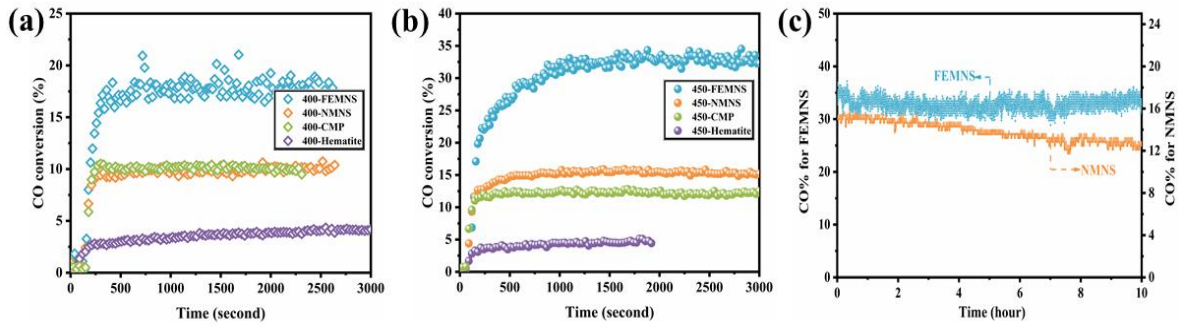


**Figure 5-4.** (a) and (b) are Short-term CO conversion as a function of time-on-stream over FEMNS, NMNS, CMP and hematite at 400 and 450 °C, respectively. (c) Long-term CO conversion as a function of time-on-stream over FEMNS and NMNS at 450 °C The space velocity is 0.23 $m^3$ $g_{Fe2O3}^{-1}$ $h^{-1}$. 4.5% CO and 4.5% $H_2O$ balanced with He.

### 5.3.3 Mechanistic Study

*In-situ* DRIFTS

Identification of the HT-WGSR reaction pathway and surface intermediates on the catalysts was conducted via *in-situ* DRIFTS at 400 ºC. **Figure 5-5(a)** and **(b)** depict a time-dependent

change of the surface upon a continuous injection of 5% CO through the catalyst. Clearly, in terms of peak intensities, nearly all the peak areas on the FEMNS catalyst are higher than the respective ones on its counterpart, which should be derived from the abundant oxygen vacancies on MgO (111) facet produced from dehydration of the $Mg(OH)_2$ (001) facet or from the reduction stage. This strongly indicates the abundance of active site on the former catalyst with a nanosheet structure. Specifically, the intensity of the two strongest doublet bands at 2190 and 2114 $cm^{-1}$ increased stably with the progress of the CO injection. These two peaks are the characteristic gas-phase CO [49,50]. Moreover, the peak at 2848 $cm^{-1}$ is attributed to C−H stretching of bidentate formats [51], while those at 1610 and 1370 $cm^{-1}$ are attributed to the asymmetric and symmetric OCO stretching vibration of bidentate β-formate [51,52]. Inferably, the dosing of CO onto the reduced Fe-MgO catalysts produced formate species as a surface intermediate. Especially, CO is more sensitive to basic $O^{2-}$ sites, which are abundant on the (111) facet from FEMNS. In addition, another two strong doublet peaks at 2354 and 2310 $cm^{-1}$ appeared, signaling the formation of surface $CO_2$ that is likely derived from the decomposition of the surface formate [52,53]. Additionally, there is a shoulder band at 1263 $cm^{-1}$ for FEMNS, which can be attributed to the vibration of the stable bidentate formate that starts to decompose into $CO_2$ and $H_2$ when the temperature is increased above 450 ºC [54]. Nevertheless, the preferential adsorption of CO on these vacancies stabilized the (111) facet, which was in turn detectable by *ex-situ* XRD and TEM in **Figure 5-3**. This phenomenon has also been reported for the carbon adsorption on MgO elsewhere [20,27].

After the injection of CO was ceased, 5% steam was introduced on the catalyst surface system and the resultant DRIFTS spectra were also collected. For both catalysts in **Figure 5-5(b)**, it is clear that the bands at 2190 and 2114 $cm^{-1}$ corresponding to gaseous CO disappeared completely. Simultaneously, the intensity of the bands at 1610 and 1370 $cm^{-1}$ also decreased rapidly, indicative of a continuous decomposition of the surface OCO formate into $H_2$ and $CO_2$.

To clearly demonstrate the decomposition of the OCO formate, peak areas were calculated, as shown in Figure 5 (c) and (d). Figure 5(c) further quantitatively displays the areas of asymmetric OCO formate as a function of reaction time, it is obvious that the initial decomposition for FEMNS (25.24% for the peak area reduction in 1 min) is much faster than NMNS (11.31%). Likewise, for the symmetric OCO formate, the initial decomposition for FEMNS (42.05%) is also faster than NMNS (19.98%). In addition, as the hierarchy of hydroxylated surface energy for low-index MgO facets follows an ascending order of (111) < (100) < (110) [55], the adsorbed water molecule should be most easily adsorbed on the (111) facet, reacting with the adsorbed CO to form formic acid. This further explains an intense peak for the surface α-formate on FEMNS.

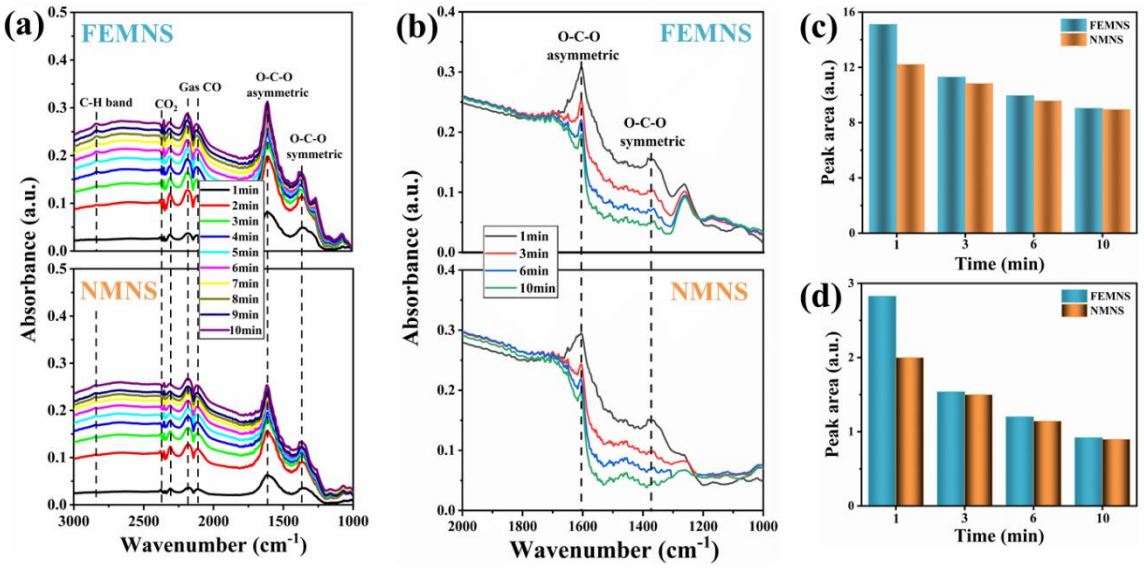


**Figure 5-5.** (a) *In-situ* DRIFTS of CO adsorption for FEMNS (upper) and NMNS (lower), (b) *in-situ* DRIFTS of $H_2O$ adsorption for FEMNS (upper) and NMNS (lower), (c) and (d) are peak areas of asymmetric and symmetric OCO formate, respectively.

$H_2$-TPR and CO-TPR

The above results suggest that the remarkable performance of FEMNS towards HT-WGSR is

due to the formation of abundant formates, which can be attributed to the oxygen vacancies from ferrous $Fe^{2+}$ and/or the high-energy MgO(111) facet, or even from the interface formed between $Fe^{2+}$ and the support MgO [56,57]. To confirm this hypothesis, the reducibility of both catalysts was studied by the $H_2$-TPR and CO-TPR. As shown in **Figure 5-6(a)**, the pure hematite $H_2$-TPR profile consists of fairly separated peaks, with a smaller peak at ~419 ºC for the reduction of hematite to magnetite ($Fe_3O_4$), and a much larger one of ~543 ºC for a further reduction to metallic iron ($Fe^0$) [58]. In contract, for both MgO-supposed catalysts, the former peak for the reduction into magnetite at the similar temperature is predominant, whereas the second one is much weaker and also displays a long tail for a very slow reduction of magnetite. In particular, the FEMNS bears a larger and broader peak after 400 ºC. This suggests a stabilization of $Fe^{2+}$ by MgO into a solid solution such as $Fe_xMg_{1-x}O$, which can lead to a high dispersion of very finely divided $Fe^{2+}$ to promote the HT-WGSR. The CO-TPR in **Figure 5-6(b)** further confirmed the highest reducibility of $Fe^{3+}$ within FEMNS and the stabilization of the reduced $Fe^{2+}$. Both of FEMNS and NMNS also exhibit a larger shoulder peak at 250-265ºC temperatures than pure hematite, which should be due to the high dispersion of $Fe^{3+}$ on the support. The majority of the $Fe^{3+}$ on the supported catalysts is also reduced at 330 ºC that falls in the overlap between the two reduction zones, $Fe_2O_3$ to $Fe_3O_4$ (yellow area) and $Fe_3O_4$ to FeO/Fe (purple area). This reflects a mixing of different oxidation states for Fe and even the presence of structural impurities/defects for the two catalysts. Moreover, the first peak for the FEMNS catalyst is located at 250 °C, which is slightly lower than NMNS at 265 °C. Regarding the second sharp peak located at 330 °C, the FEMNS catalyst clearly presents a much stronger intensity than its counterpart. Such a feature provides another strong evidence of the abundance of MgO(111) facet within the FEMNS catalyst, as a similar $CO_2$ desorption temperature of ~352 ºC has been confirmed from the MgO(111) nanosheet synthesized elsewhere [26], due to the abundance of oxygen vacancy, $O^{2-}$, that functioned as the medium basic sites on MgO(111)

[59,60].

The isothermal CO reduction at 400 ºC in **Figure 5-6(c)** confirmed a quick and easy reduction of $Fe^{3+}$ on FEMNS. The $Fe^{3+}$ on FEMNS exhibits an early shoulder peak at around 2.8 min, which is accompanied by a larger peak at around 3.5 min. The shoulder peak should be assigned as $Fe^{3+}$ on the facets other than (111) of MgO, as it overlaps with the $Fe^{3+}$ on pure hematite and NMNS. In contrast, the principal peak at 3.5 min should be mostly assigned as $Fe^{3+}$ on the MgO(111) facet, where a strong interfacial interaction should exist, leading to a long tail for a slow secondary reduction of $Fe^{2+}$. Furthermore, based on the peak areas in **Figure 5-6(c)**, a quantitative determination of the CO uptake amount for each catalyst was calculated, with the results displayed in **Figure 5-6(d)**. It is evident that all the catalysts were reduced to a non-stoichiometric oxidation state for Fe. However, the reduction extent of each catalyst is very different. For pure hematite, its CO uptake amount falls in between the two theoretical values (e.g. 0.0625 mmol-CO and 0.1875 mmol-CO per 30 mg-$Fe_2O_3$ based on **Equation S5-(2)** and **S5-(3)** for the conversion of hematite to $Fe_3O_4$ and FeO, indicating the accompanient of $Fe^{3+}$ to $Fe^{2+}$ within it. However, for the other two catalysts, their CO uptake amounts are even above the theoretical value for $Fe^{2+}O$ formation. This is not a sign of the formation of metallic $Fe^0$, as the feastuing peak of 1889 $cm^{-1}$ for the chemisorbed CO [57] on a metal is indiscernable in **Figure 5-5**. The Fe-2p XPS spectra (shown in **Figure 5-7(a-b)**) also failed to find any metallic $Fe^0$ that has a featuring binding energy at 706.7 eV. Alternatively, it should be assigned as the loss of the lattice oxygen from the MgO support. Consequently, the $O^{2-}$ from the reduced $Fe^{2+}$ site should be scavenged by the oxygen vacancy, leading to the formation of $Fe_xMg_{1-x}O$ with a non-stoichiometric ratio that is stable enough to inhibit the further reduction of $Fe^{2+}$. As it carries a non-stoichiometric formula, it was also failed to be detected by the XRD and even TEM. Here again, compared to the other facets in MgO, the (111) one is clearly prone to lossing its lattice oxygen, which in turn favors the reduction of the highly dispersed Fe on its surface.

This observation is consistent with the CO-TPR results in **Figure 5-6(b)**.

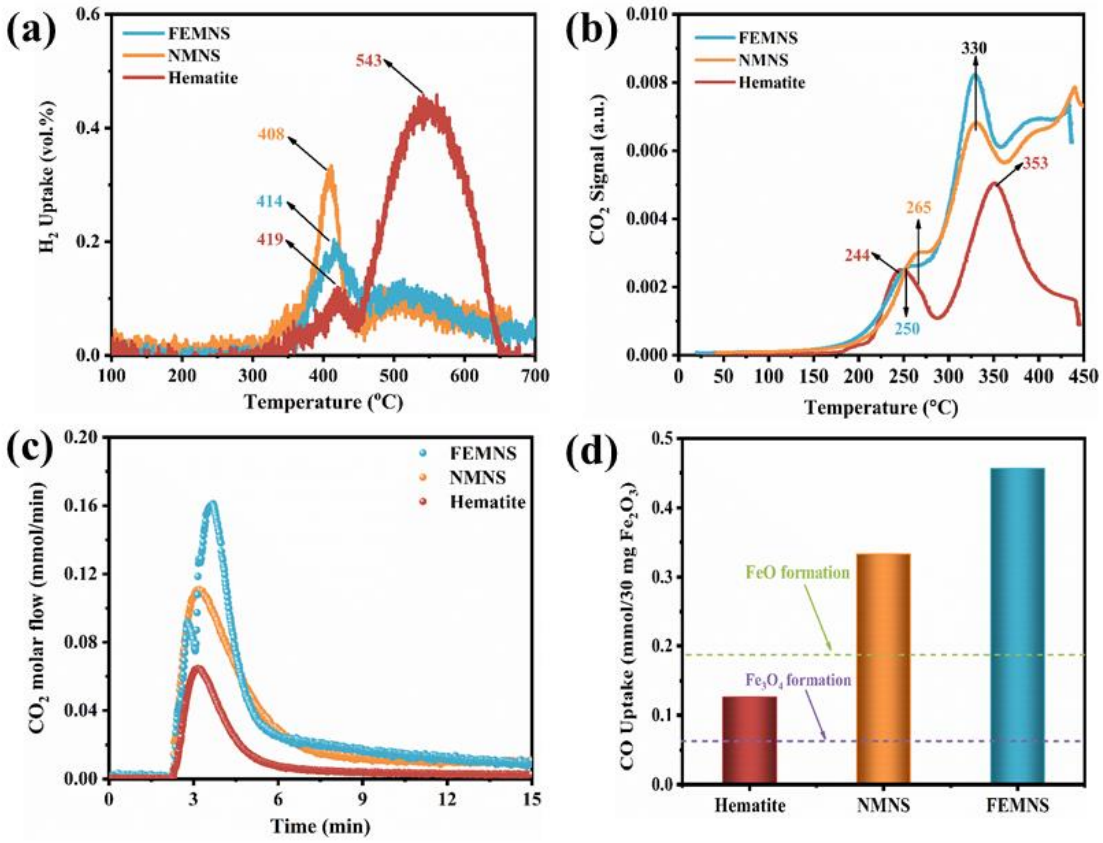


**Figure 5-6.** (a) $H_2$-TPR profiles of FEMNS, NMNS and hematite, (b) CO-TPR profiles of FEMNS, NMNS and hematite, (c) Isothermal CO reduction at 400 °C of FEMNS, NMNS and hematite, (d) CO uptake amount for FEMNS, NMNS and hematite.

XPS and NEXAFS Surface Analysis of Spent Catalysts

**Figure S5-8** shows the XPS survey spectra of the spent FEMNS and NMNS catalysts. It further demonstrates a negligible signal from Ca and Al on the surface. **Figure 5-7(a)** shows the high-resolution XPS spectra of Fe 2p region, which can be attributed to two spin-orbit doublet peaks at 710.8 eV and 724.5 eV corresponding to the Fe $2p_{3/2}$ and Fe $2p_{1/2}$, respectively. The doublet is a characteristic of the peaks for $Fe^{2+}$ and $Fe^{3+}$ [61,62]. The quantitative analysis in **Figure 5-7(b)** confirms a molar percentage of 61.2% for $Fe^{2+}$ from surface Fe on the FEMNS catalyst,

relative to 49.1% $Fe^{2+}$ on the surface of the NMNS counterpart, whereas the metallic $Fe^0$ was not found. This verifies a stronger reducibility for $Fe^{2+}$ and its subsequent stabilization by the oxygen vacancy on the MgO(111) facet, which is mainly attributed to the effect of the oxygen vacancy (basic $O^{2-}$ sites) that was produced by CO reduction. To be specific, CO should be preferentially adsorbed on the oxygen vacancy sites, grabbing the lattice oxygen by nucleophilic attack of basic $O^{2-}$ [27] and thus lowering the valence state of Fe. Moreover, such an observation agrees with previous findings that the catalytic activity of $Fe^{2+}$-$Fe^{3+}$ pairs is enhanced upon an increase on the $Fe^{2+}/Fe^{3+}$ ratio [34,63]. As both catalysts have a rather similar dispersion of Fe (as shown in **Figure 5-3(e)** and **(f)**), the MgO(111) support is clearly the principal factor promoting the reducibility for Fe. It should be mainly due to the presence of abundant oxygen vacancy in the (111) facet, as has been confirmed by the theoretical calculation elsewhere [64]. In addition, **Figure 5-7(c)** depicts the Mg K-edge NEXAFS spectra for both spent catalysts. The entire spectrum pattern as well as their white line positions closely resemble standard MgO, verifying the dominance of MgO rather than $MgFe_2O_4$ on these two catalysts. Moreover, the abundance of oxygen vacancy on FEMNS can be further verified by its stronger intensity than the counterpart. This is in line with the previous experimental and theoretical works that have identified that the introduction of oxygen vacancy can affect the relative intensity of the spectral feature, especially the pre-edge region [65,66]. In particular, an enhanced pre-edge at ~1304 eV is confirmed for the FEMNS catalyst, which is a strong indicator of the presence of oxygen vacancy for the central Mg atom site that is highly non-centrosymmetric on the FEMNS catalyst surface.

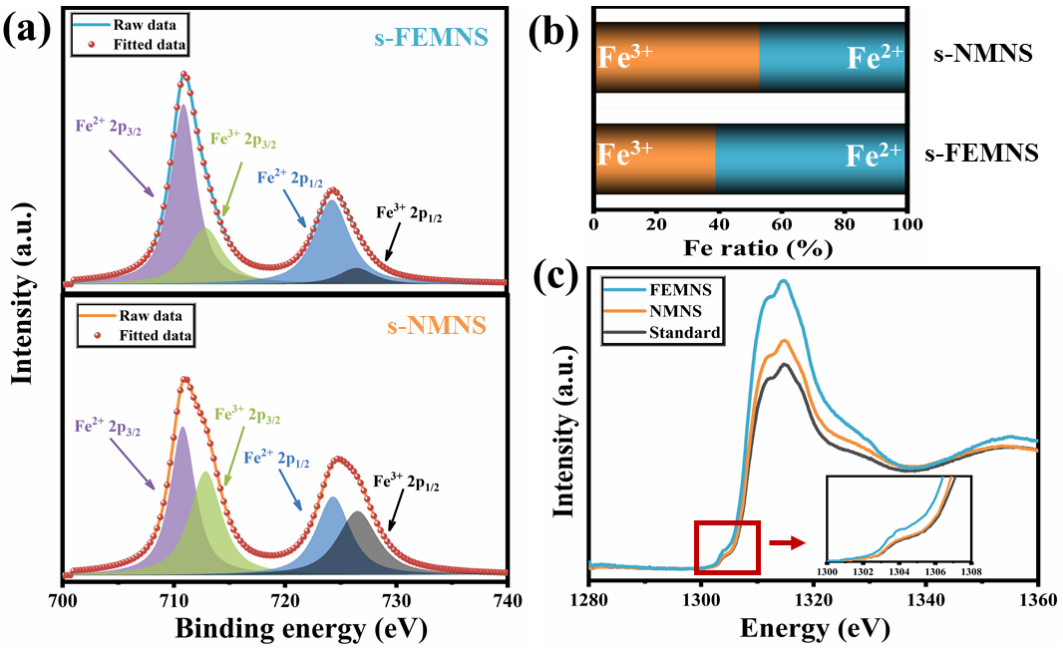


**Figure 5-7.** (a) High-resolution XPS spectra of Fe 2p for spent FEMNS (s-FEMNS) and spent NMNS (s-NMNS), (b) Atomic ratio of $Fe^{2+}$ and $Fe^{3+}$ of s-FEMNS and s-NMNS , (c) Mg K-edge XANES spectra of FEMNS, NMNS and MgO reference (inset: the red area highlights the pre-edge absorption region).

## 5.4 Conclusions

The facile synthesis of a facet-engineered MgO(111)-Fe(III) nanosheet from BCFA waste as a HT-WGSR catalyst was successfully demonstrated in this study, which involves an initial leaching, precipitation and growth of a (001)-facet dominant $Mg(OH)_2$ precursor by an ethanol-mediated hydrothermal process followed by conversion of $Mg(OH)_2$(001) to MgO(111) facet during the HT-WGSR. The resultant products bear a high-purity of >98%, and comparable specific surface area with those synthesized from pure chemical precursors. More intriguingly, upon the loading of 30 *wt%* $Fe^{3+}$, the thermally unstable (001)-facet enhanced $Mg(OH)_2$ nanosheet undertook a dehydroxylation into well-defined MgO(111) after calcination and reduction, which remained as nanosheets with the abundance of oxygen vacancy (Lewis

basicity $O^{2-}$ sites). During the HT-WGSR, the reduced FEMNS is beneficial in promoting the formation and decomposition of surface formates owing to the enhanced CO and $H_2O$ adsorption as well as the reduction of $Fe^{3+}$ on the oxygen vacancy of the (111) facet, leading to increased CO conversion by a factor of two in comparison to the commercial $Mg(OH)_2$ loaded with the same amount of $Fe^{3+}$, and by nearly seven time compared to the nano-sized hematite reference. This study successfully broadens the application of fly ash derivatives in clean energy catalysis areas.

## Supporting results

### Catalyst Characterization

X-ray Fluorescence (XRF) spectrometer was used for analysis of elemental compositions of fly ash and the synthesized $Mg(OH)_2$ nanosheets. X-ray powder diffraction (XRD) analysis was used for phase identification. The XRD patterns were recorded on a Rigaku SmartLab 3000A diffractometer with CuKα radiation (λ = 0.15406 nm). The X-ray tube was operated at 40 kV and 15 mA. The powdered samples were scanned between 10° and 80° by a D/teX Ultra detector at a scanning speed of 5°/min. The optical configuration was a fixed divergence slit (1.25°) and a fixed incident antiscatter slit (2.5°). Measurements were performed in a θ-2θ reflection configuration. Scanning electron microscopy (SEM) was conducted by a FEI Nova NanoSEM 450 FEGSEM. The sample was prepared by placing a single droplet of dilute sample-ethanol suspension on a 1×1 cm section of silicon wafer which allows the ethanol to evaporate quickly. The wafer was then attached to an aluminum sample holder with conductive carbon tab. Finally, the sample was coated with gold to eliminate any possible charging effect. Transmission Electron Microscopy (TEM) imaging and SAED patterns were recorded using an equipment namely FEI Tecnai $G^2$ T20 TWIN TEM with an accelerating voltage of 200 kV. The sample was dispersed ultrasonically in ethanol prior to deposition on a TEM copper grids

with thin carbon films. A single droplet of the solution was then transferred onto the TEM grid for 5-10 minutes until ethanol was completely evaporated. A Nexsa Surface Analysis System with an Al Kα X-ray source was used to obtain X-ray photoelectron spectroscopy (XPS) and the quantitative analysis was performed on Avantage software with Shirley background. In addition, near-edge X-ray absorption fine structure (NEXAFS) was used to elaborate the coordination environment of Mg K-edge (1280-1360 eV) in the spent catalyst, based on the total electron yield (TEY) mode.

*In-situ* diffuse reflectance infrared Fourier transform spectroscopy (DRIFTS) was performed on Bruker Tensor 27 FTIR spectrometer coupled with a Praying Mantis™ Diffuse Reflection Accessory from Harrick. In a typical experiment, the sample was first pretreated with UHP He (40 mL/min) at 400 °C for 1 h. Afterwards, 5 vol% CO/He (40 mL/min) was introduced into the sample cell for 10 min. Thereafter, the gas was switched to 3 vol% $H_2O$/He (40 mL/min) and maintained for another 10 min. The spectra were recorded with a resolution of 4 $cm^{-1}$ between 4000 $cm^{-1}$ and 600 $cm^{-1}$.

CO-Temperature Programmed Reduction (TPR) was conducted using AutoChem II 2920 from Micromeritics, coupled with ThermoStar GSD 320 T Quadrupole Mass Spectrometer (QMS) from Pfeiffer Vacuum, using a Secondary Electron Multiplier. In each experiment, ~60 mg of catalyst was pretreated with 10 vol% $O_2$/He (50 mL/min) at 300 °C for 1 h, followed by ramping down to ambient temperature in 5 vol% Ar/He (50 mL/min). The flowing gas was then switched to 5 vol% CO/He (50 mL/min). After stabilizing for 30 min, the temperature was ramped to 450 °C at a rate of 3 °C/min. Additionally, $H_2$-TPR was conducted at a fix-bed reactor coupled with a Rapidox 5100 gas analyzer which has a built-in thermal conductivity detector (TCD) for real-time H2 detection. For each run, the sample of approximately 100 mg was heated from room temperature to 700 °C at 5 °C/min, with a continuous flow of 10% $H_2/N_2$ at

200 ml/min. Prior to the analysis, the reactor was purged by pure nitrogen for around 1 hr.

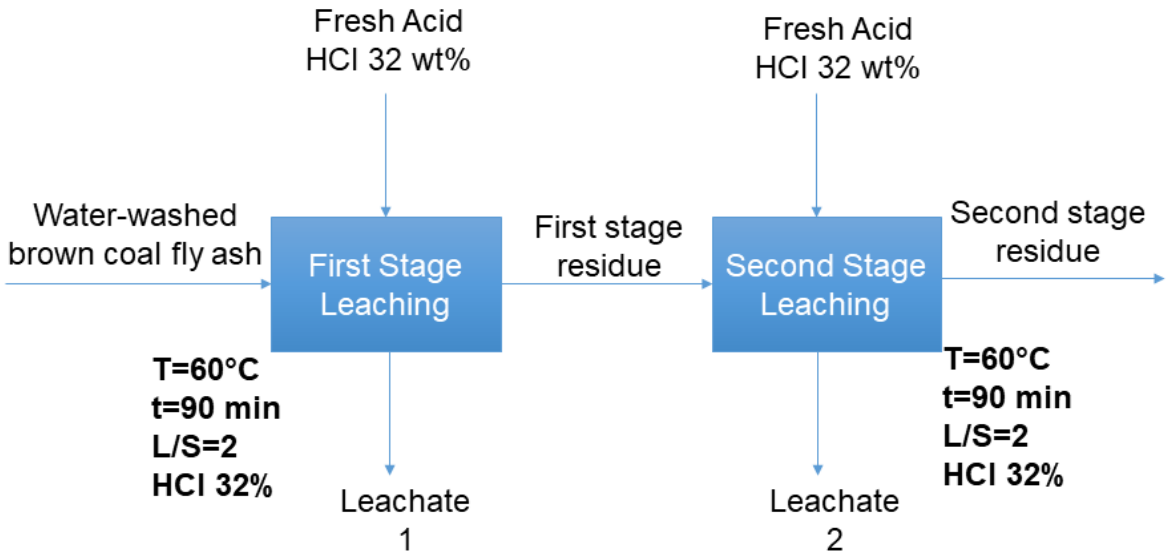


**Figure S5-1.** Block flow diagram of the two-stage cross flow leaching of water-washed brown coal fly ash.

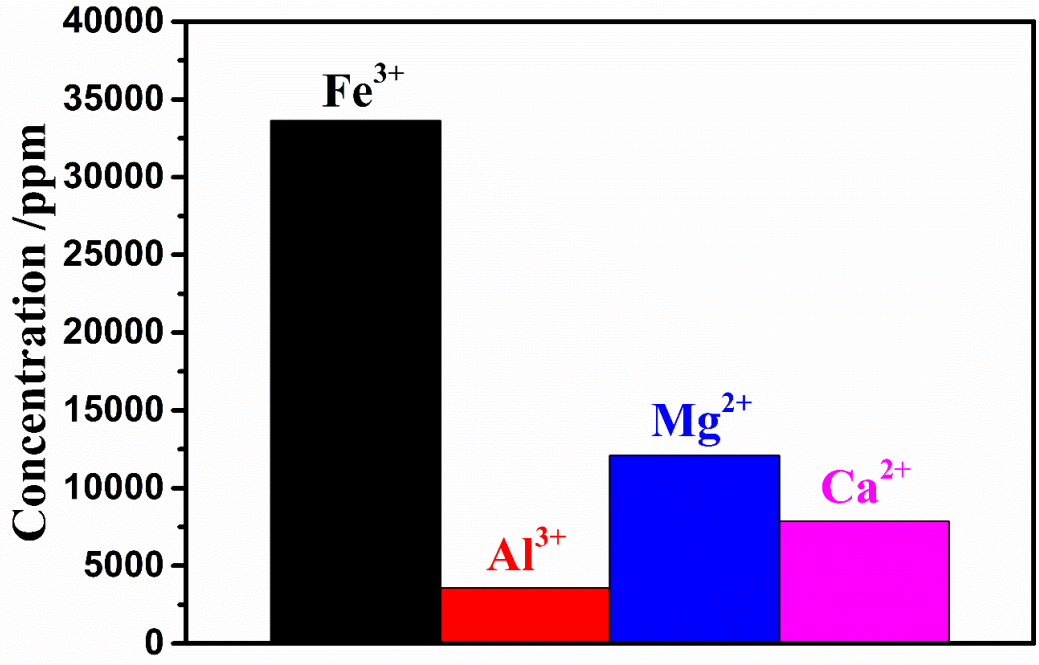


**Figure S5-2.** Concentrations of major cations from initial leachate.

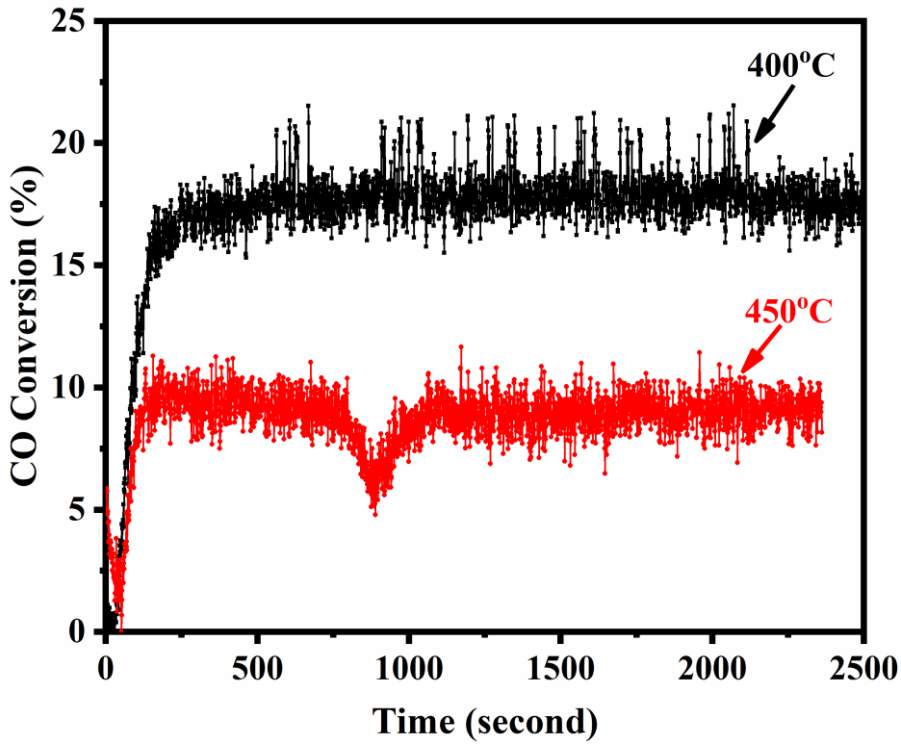


**Figure S5-3.** Effect of reduction temperature on CO conversion during the HT-WGSR.

CO conversion was calculated as **Equation S5-(1)**:

$$\text{CO conversion} = \frac{CO_{in} - CO_{out}}{CO_{in}} \times 100\% \qquad \textbf{Equation S5-(1)}$$

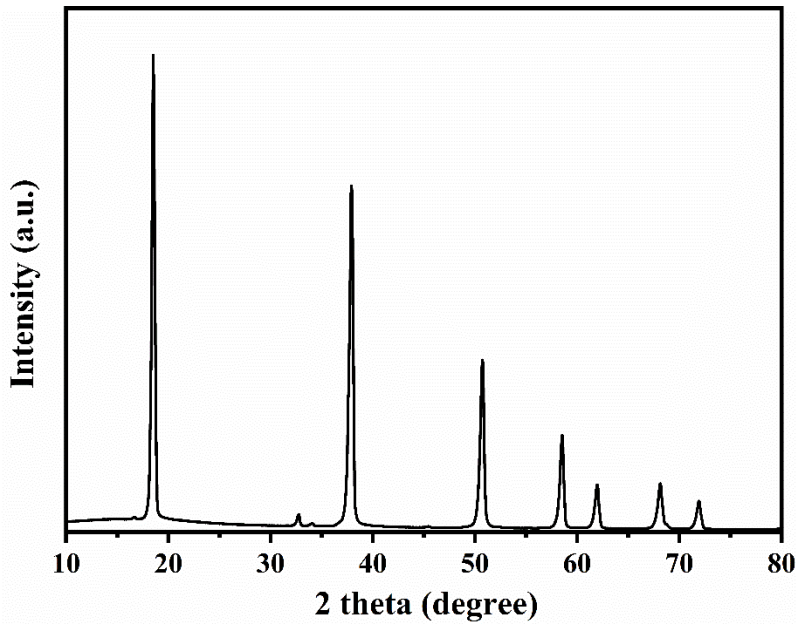


**Figure S5-4.** XRD pattern for $Mg(OH)_2$ synthesized from pure $MgCl_2$ under ethanol-mediated hydrothermal.

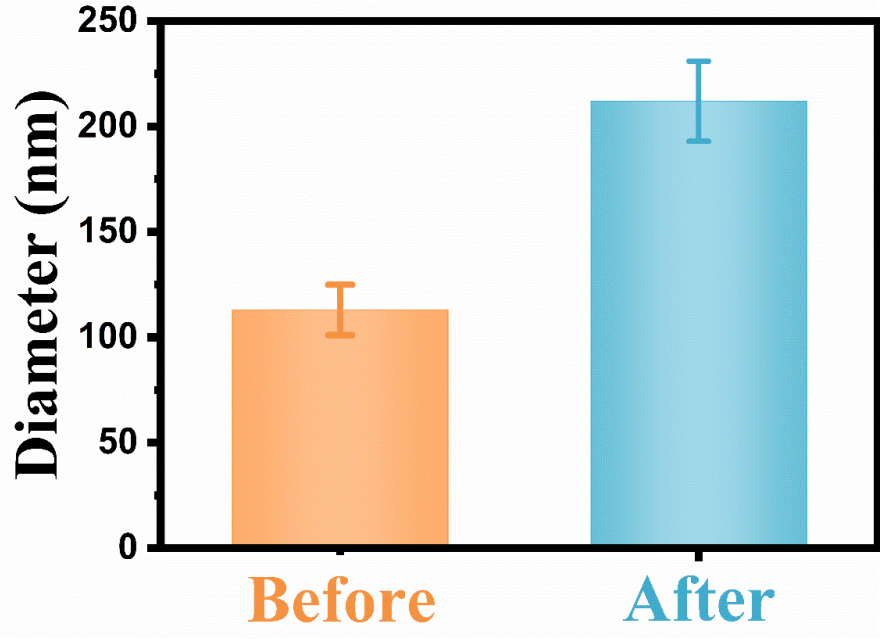


**Figure S5-5.** Statistics diameter of nano-$Mg(OH)_2$ before and after ethanol treatment.

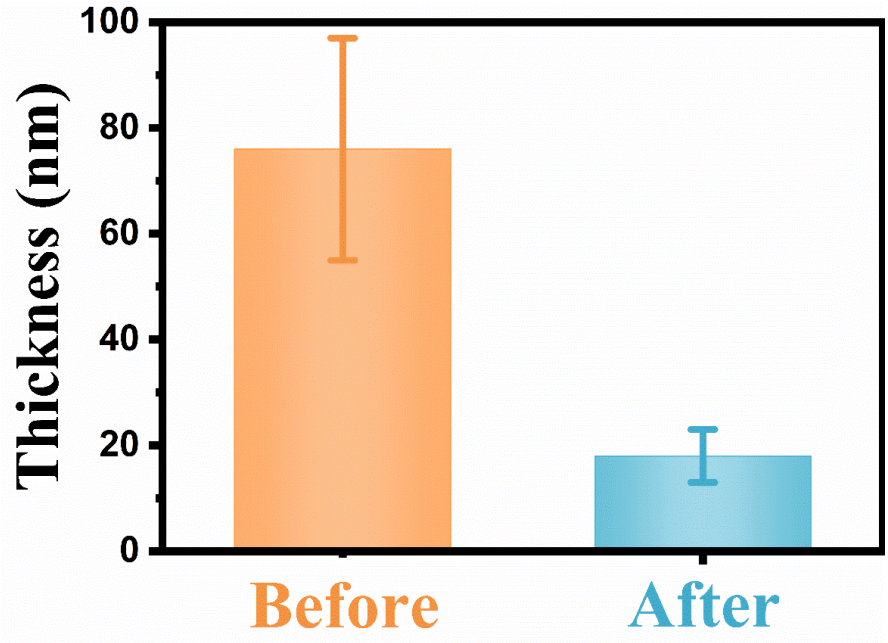


**Figure S5-6.** Statistics thickness of nano-$Mg(OH)_2$ before and after ethanol treatment.

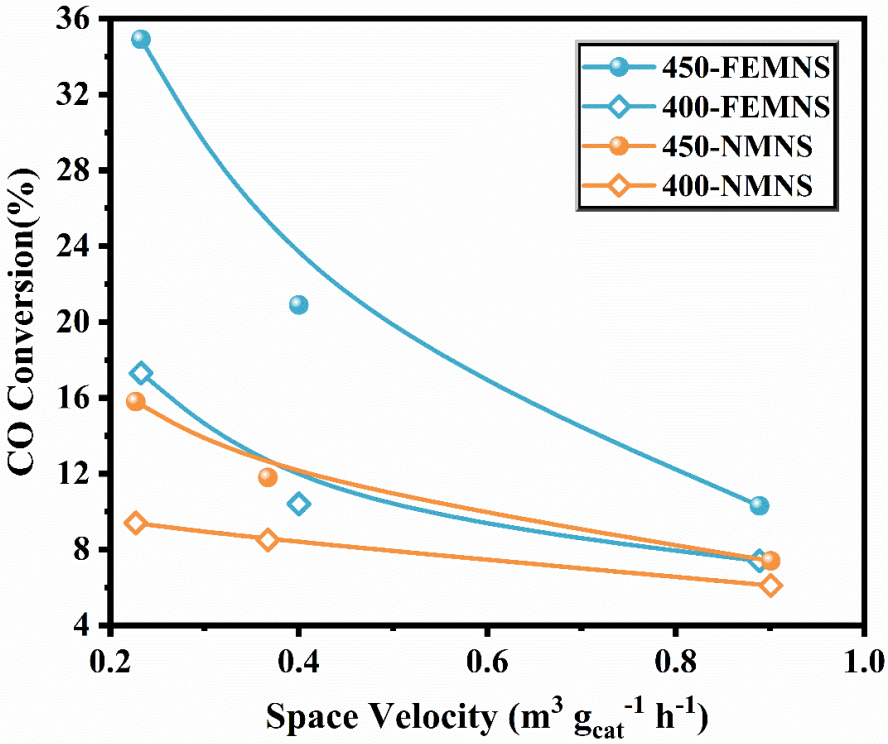


**Figure S5-7** CO conversion as a function of space velocity over FEMNS and NMNS at 400 and 450 °C.

Theoretical CO uptake calculation method:

$3Fe_2O_3+CO=2Fe_3O_4+CO_2$ **Equation S5-(2)**

$Fe_3O_4+CO=3FeO+CO_2$ **Equation S5-(3)**

As per the stoichiometric ratio for above two equations, on a basis of 30 mg $Fe_2O_3$ (0.1875 mmol), 0.0625 mmol CO is required to be reduced into $Fe_3O_4$ per **Equation S5-(2)**, whereas 0.1875 mmol CO is necessary for $Fe_2O_3$ to be reduced into FeO in **Equation S5-(3)**.

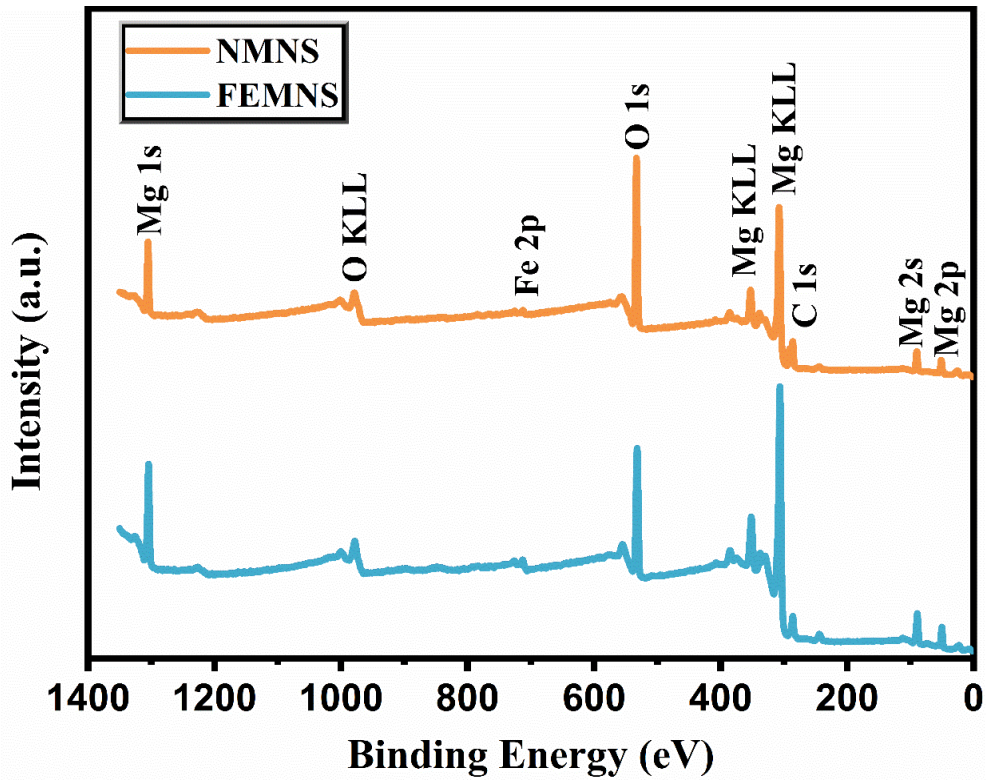


**Figure S5-8.** XPS survey scan spectra for NMNS and FEMNS.

**Table S5-1** Comparison of CO conversion and specific rates of as-synthesized catalysts

| Catalyst | Space velocity ($m^3\ g_{Fe2O3}^{-1}\ h^{-1}$) | Specific Surface area ($m^2\ g^{-1}$) | Temperature (°C) | CO Conversion (%) | Specific rate$^{\nabla}$ ($10^4\ mol_{CO}\ g_{Fe2O3}^{-1}\ h^{-1}$) |
|---|---|---|---|---|---|
| FEMNS* | 0.23 | 104.5 | 400 | 17.3 | 834.12 |
| | | | 450 | 34.9 | 1682.68 |
| NMNS# | | 100.8 | 400 | 9.4 | 455.31 |
| | | | 450 | 15.8 | 761.79 |
| CMP^ | | 83.7 | 400 | 9.1 | 436.82 |
| | | | 450 | 13.2 | 568.93 |
| Hematite | | 14.3 | 400 | 3.5 | 83.64 |
| | | | 450 | 4.3 | 171.15 |

*: 30 *wt%* Fe loaded on $Mg(OH)_2$ nanosheet synthesized from ethanol-meditated hydrothermal condition;

#: 30 *wt%* Fe loaded on $Mg(OH)_2$ nano-particles synthesized from ethanol-free hydrothermal condition;

^: 30 *wt%* Fe loaded on commercial $Mg(OH)_2$ purchased from Sigma-Aldrich.

$^{\nabla}$: Specific reaction rate was determined by normalizing the respective amount (mol/h) of CO converted with the mass (g) of $Fe_2O_3$ for the respective catalyst.

# References

[1] Yao, Z. T.; Ji, X. S.; Sarker, P. K.; Tang, J. H.; Ge, L. Q.; Xia, M. S.; Xi, Y. Q. A comprehensive review on the applications of coal fly ash. *Earth-Science Reviews* **2015**, *141*, 105–121.

[2] Blissett, R.S.; Rowson, N.A. A review of the multi-component utilisation of coal fly ash. *Fuel* **2012**, *97*, 1–23.

[3] Ma, B.; Li, X.; Shen, X.; Mao, Y.; Huang, H. Enhancing the addition of fly ash from thermal power plants in activated high belite sulfoaluminate cement. *Construction and Building Materials* **2014**, *52*, 261–266.

[4] Forteza, R.; Far, M.; Seguí, C.; Cerdá, V. Characterization of bottom ash in municipal solid waste incinerators for its use in road base. *Waste Management* **2004**, *24*, 899–909.

[5] Pandey, V. C.; Singh, N. Impact of fly ash incorporation in soil systems. *Agriculture, Ecosystems & Environment* **2010**, *136*, 16–27.

[6] Jiang, Y.; Zhang, Y.; Yan, X.; Tian, M.; Xiao, W.; Tang, H. A sustainable route from fly ash to silicon nanorods for high performance lithium ion batteries. *Chemical Engineering Journal* **2017**, *330*, 1052–1059.

[7] Hintsho, N.; Shaikjee, A.; Masenda, H.; Naidoo, D.; Billing, D.; Franklyn, P. Durbach, S. Direct synthesis of carbon nanofibers from South African coal fly ash. *Nanoscale Research Letters* **2014**, *9*, 387.

[8] Alzeer, M. I. M.; MacKenzie, K. J. D. Synthesis and Catalytic Properties of New Sustainable Aluminosilicate Heterogeneous Catalysts Derived from Fly Ash. *ACS Sustainable Chemistry & Engineering* **2018**, *6*, 5273–5282.

[9] Yan, F.; Jiang, J.; Tian, S.; Liu, Z.; Shi, J.; Li, K.; Chen, X.; Xu, Y. A Green and Facile Synthesis of Ordered Mesoporous Nanosilica Using Coal Fly Ash. *ACS Sustainable Chemistry & Engineering* **2016**, *4*, 4654−4661.

[10] Feng, W.; Wan, Z.; Daniels, J.; Li, Z.; Xiao, G.; Yu, J.; Xu, D.; Guo, H.; Zhang, D.; May, E. F.; Li, G. Synthesis of high quality zeolites from coal fly ash: Mobility of hazardous elements and environmental applications. *Journal of Cleaner Production* **2018**, *202*, 390-400.

[11] Hui, K. S.; Chao, C. Y. H. Synthesis of MCM-41 from coal fly ash by a green approach: Influence of synthesis pH. *Journal of Hazardous Materials* **2006,** *137*, 1135-1148.

[12] Qian, B.; Liu, C.; Lu, J.; Jian, M.; Hu, X.; Zhou, S.; Hosseini, T.; Etschmann, B.; Zhang, X.; Wang, H.; Zhang, L. Synthesis of *in-situ* $Al^{3+}$-defected iron oxide nanoflakes from coal ash: A detailed study on the structure, evolution mechanism and application to water remediation. *Journal of Hazardous Materials* **2020,** *395*, 122696.

[13] Bloise, A.; Ricchiuti, C.; Giorno, E.; Fuoco, I.; Zumpano, P.; Miriello, D.; Apollaro, C.; Crispini, A.; Rosa, R.; Punturo, R. Assessment of Naturally Occurring Asbestos in the Area of Episcopia (Lucania, Southern Italy). *Fibers* **2019**, *7*.

[14] Wang, G. The Utilization of Slag in Civil Infrastructure Construction, Publisher: *Elsevier* **2016**.

[15] Zhang, Z.; Wang, S.-S.; Song, R.; Cao, T.; Luo, L.; Chen, X.; Gao, Y.; Lu, J.; Li, W.-X.; Huang, W. The most active Cu facet for low-temperature water gas shift reaction. *Nature Communications* **2017,** *8* (1), 488.

[16] Rej, S.; Hsia, C.-F.; Chen, T.-Y.; Lin, F.-C.; Huang, J.-S.; Huang, M. H. Facet-Dependent and Light-Assisted Efficient Hydrogen Evolution from Ammonia Borane Using Gold–Palladium Core–Shell Nanocatalysts. *Angewandte Chemie International Edition* **2016,** *55* (25), 7222-7226.

[17] Zhang, Q.; Wang, H. Facet-Dependent Catalytic Activities of Au Nanoparticles Enclosed by High-Index Facets. *ACS Catalysis* **2014,** *4* (11), 4027-4033.

[18] Zhou, K.; Li, Y. Catalysis Based on Nanocrystals with Well-Defined Facets.

*Angewandte Chemie International Edition* **2012,** *51* (3), 602-613.

[19] Lazarov, V. K.; Plass, R.; Poon, H. C.; Saldin, D. K.; Weinert, M.; Chambers, S. A.; Gajdardziska-Josifovska, M. Structure of the hydrogen-stabilized MgO(111)-(1×1) polar surface: Integrated experimental and theoretical studies. *Physical Review B* **2005,** *71* (11), 115434.

[20] Mutch, G.; Shulda, S.; McCue, A.; Menart, M.; Ciobanu, C.; Ngo, C.; Anderson, J.; Richards, R.; Vega-Maza, D. Carbon Capture by Metal Oxides: Unleashing the Potential of the (111) Facet. *Journal of the American Chemical Society* **2018**, *140* (13), 4736−4742.

[21] Wu, S.; Peng, Y.; Chen, T.; Mo, J.; Large, A.; McPherson, I.; Chou, H.; Wilkinson, I.; Venturini, F.; Grinter, D.; Escorihuela, P.; Held, G.; Tsang, S. Removal of Hydrogen Poisoning by Electrostatically Polar MgO Support for Low-Pressure $NH_3$ Synthesis at a High Rate over the Ru Catalyst. *ACS Catal*ysis **2020**, *10* (10), 5614–5622.

[22] Arita, R.; Tanida, Y.; Entani, S.; Kiguchi, M.; Saiki, K.; Aoki, H. Polar surface engineering in ultrathin MgO(111)/Ag(111): Possibility of a metal-insulator transition and magnetism. *Physical Review B* **2004,** *69* (23), 235423.

[23] Shinozaki, S.; Sato, H. Cleaving of MgO inside an Electron Microscope. *Journal of Applied Physics* **1972,** *43* (2), 701-706.

[24] Henrich, V. E. Thermal faceting of (110) and (111) surfaces of MgO. *Surface Science* **1976,** *57* (1), 385-392.

[25] Lazarov, V. K.; Chambers, S. A.; Gajdardziska-Josifovska, M. Polar Oxide Interface Stabilization by Formation of Metallic Nanocrystals. *Physical Review Letters* **2003,** *90* (21), 216108.

[26] Zhu, K.; Hu, J.; Kübel, C.; Richards, R. Efficient Preparation and Catalytic Activity of MgO(111) Nanosheets. *Angewandte Chemie International Edition* **2006,** *118* (43),

7435-7439.

[27] Liu, P.; Abdala, P.; Goubert, G.; Willinger, M.; Copéret, C. Ultrathin Single-crystalline MgO (111) Nanosheets. *Angewandte Chemie International Edition* **2020**.

[28] Navarro, R. M.; Peña, M. A.; Fierro, J. L. G. Hydrogen Production Reactions from Carbon Feedstocks: Fossil Fuels and Biomass. *Chemical Reviews* **2007,** *107* (10), 3952-3991.

[29] Minh, D.; Siang, T.; Vo, D.; Phan, T.; Ridart, C.; Nzihou, A.; Grouset, D. Chapter 4 - Hydrogen Production From Biogas Reforming: An Overview of Steam Reforming, Dry Reforming, Dual Reforming, and Tri-Reforming of Methane. *Hydrogen Supply Chains* **2018**, 111-166.

[30] Huang, L.; Han, B.; Zhang, Q.; Fan, M.; Cheng, H. Mechanistic Study on Water Gas Shift Reaction on the $Fe_3O_4$ (111) Reconstructed Surface. *The Journal of Physical Chemistry C* **2015**, *119* (52), 28934–28945.

[31] Wang, P.; Li, C.; Gong, H.; Wang, H.; Liu, J. Morphology control and growth mechanism of magnesium hydroxide nanoparticles via a simple wet precipitation method. *Ceramics International* **2011**, *37* (8), 3365-3370.

[32] Tang, M.; Ren, Y.; Hu, Y.; Ye, L.; Yue, B.; He, H. Synthesis and orientational assemblies of MgO nanosheets with exposed (111) facets. *Chinese Chemical Letters* **2018**, *29* (6), 935-938.

[33] Keturakis, C. J.; Zhu, M.; Gibson, E. K.; Daturi, M.; Tao, F.; Frenkel, A. I.; Wachs, I. E. Dynamics of $CrO_3$–$Fe_2O_3$ Catalysts during the High-Temperature Water-Gas Shift Reaction: Molecular Structures and Reactivity. *ACS Catalysis* **2016,** *6* (7), 4786-4798.

[34] Zhu, M.; Wachs, I. E. Iron-Based Catalysts for the High-Temperature Water–Gas Shift (HT-WGS) Reaction: A Review. *ACS Catalysis* **2016,** *6* (2), 722-732.

[35] Feng, Q.; Zhao, S.; Xu, Q.; Chen, W.; Tian, S.; Wang, Y.; Yan, W.; Luo, J.; Wang, D.;

Li, Y. Mesoporous Nitrogen-Doped Carbon-Nanosphere-Supported Isolated Single-Atom Pd Catalyst for Highly Efficient Semihydrogenation of Acetylene. *Advanced Materials* **2019,** *31* (36), 1901024.

[36] Qian, B.; Hosseini, T.; Zhang, X.; Liu, Y.; Wang, H.; Zhang, L. Coal Waste to Two-Dimensional Materials: Fabrication of α‑$Fe_2O_3$ Nanosheets and MgO Nanosheets from Brown Coal Fly Ash. *ACS Sustainable Chemistry & Engineering* **2018**, *6*, 15982−15987.

[37] Liu, M.; Wang, Y.; Chen, L.; Zhang, Y.; Lin, Z. $Mg(OH)_2$ Supported Nanoscale Zero Valent Iron Enhancing the Removal of Pb(II) from Aqueous Solution. *ACS Applied Materials & Interfaces* **2015**, *7*, 7961−7969.

[38] Pan, X.; Xu, Z.; Zheng, Y.; Huang, T.; Li, L.; Chen, Z.; Rao, W.; Chen, S.; Hong, X.; Guan, X. The adsorption features between insecticidal crystal protein and nano-$Mg(OH)_2$. *Royal Society Open Science* **2017**, *4*, 170883.

[39] Ding, Y.; Zhang, G.; Wu, H.; Hai, B.; Wang, L.; Qian, Y. Nanoscale Magnesium Hydroxide and Magnesium Oxide Powders: Control over Size, Shape, and Structure via Hydrothermal Synthesis. *Chemistry of Materials* **2001**, *13*, 435−440.

[40] Selvam, N.; Kumar, R.; Kennedy, L.; Vijaya, J. Comparative study of microwave and conventional methods for the preparation and optical properties of novel MgO-micro and nano-structures. *Journal of Alloys and Compounds* **2011**, *509*, 9809-9815.

[41] Tian, P.; Han, X.; Ning, G.; Fang, H.; Ye, J.; Gong, W.; Lin, Y. Synthesis of Porous Hierarchical MgO and Its Superb Adsorption Properties, *ACS Applied Materials & Interfaces* **2013**, *5*, 12411–12418.

[42] Lee, S.-M.; Cho, S.-N.; Cheon, J. Anisotropic Shape Control of Colloidal Inorganic Nanocrystals. *Advanced Materials* **2003,** *15* (5), 441-444.

[43] Sui, Y.; Fu, W.; Yang, H.; Zeng, Y.; Zhang, Y.; Zhao, Q.; Li, Y.; Zhou, X.; Leng, Y.; Li,

M.; Zou, G. Low Temperature Synthesis of $Cu_2O$ Crystals: Shape Evolution and Growth Mechanism. *Crystal Growth & Design* **2010,** *10* (1), 99-108.

[44] McKelvy, M. J.; Sharma, R.; Chizmeshya, A. V. G.; Carpenter, R. W.; Streib, K. Magnesium Hydroxide Dehydroxylation: In Situ Nanoscale Observations of Lamellar Nucleation and Growth. *Chemistry of Materials* **2001,** *13* (3), 921-926.

[45] Boudjemaa, A.; Auroux, A.; Boumaza, S.; Trari, M.; Cherifi, O.; Bouarab, R. Hydrogen production on iron–magnesium oxide in the high-temperature water-gas shift reaction. *Reaction Kinetics and Catalysis Letters* **2009,** *98* (2), 319-325.

[46] Natesakhawat, S.; Wang, X.; Zhang, L.; Ozkan, U. S. Development of chromium-free iron-based catalysts for high-temperature water-gas shift reaction. *Journal of Molecular Catalysis A: Chemical* **2006**, *260* (1-2), 82-94.

[47] Yao, S.; Zhang, X.; Zhou, W.; Gao, R.; Xu, W.; Ye, Y.; Lin, L.; Wen, X.; Liu, P.; Chen, B.; Crumlin, E.; Guo, J.; Zuo, Z.; Li, W.; Xie, J.; Lu, L.; Kiely, C. J.; Gu, L.; Shi, C.; Rodriguez, J. A.; Ma, D. Atomic-layered Au clusters on α-MoC as catalysts for the low-temperature water-gas shift reaction. *Science* **2017,** *357* (6349), 389-393.

[48] Zhang, J.; Yan, W.; An, Z.; Song, H.; He, J. Interface–Promoted Dehydrogenation and Water–Gas Shift toward High-Efficient $H_2$ Production from Aqueous Phase Reforming of Cellulose. *ACS Sustainable Chemistry & Engineering* **2018**, 6 (6), 7313-7324.

[49] Fu, X.-P.; Guo, L.-W.; Wang, W.-W.; Ma, C.; Jia, C.-J.; Wu, K.; Si, R.; Sun, L.-D.; Yan, C.-H. Direct Identification of Active Surface Species for the Water–Gas Shift Reaction on a Gold–Ceria Catalyst. *Journal of the American Chemical Society* **2019,** *141* (11), 4613-4623.

[50] Sun, X.; Lin, J.; Zhou, Y.; Li, L.; Su, Y.; Wang, X.; Zhang, T. $FeO_x$ supported single-atom Pd bifunctional catalyst for water gas shift reaction. *AIChE Journal* **2017,** *63* (9), 4022-4031.

[51] Chen, Y.; Lin, J.; Li, L.; Qiao, B.; Liu, J.; Su, Y.; Wang, X. Identifying Size Effects of Pt as Single Atoms and Nanoparticles Supported on $FeO_x$ for the Water-Gas Shift Reaction. *ACS Catalysis* **2018,** *8* (2), 859-868.

[52] Li, J.; Liang, J.-X.; Lin, J.; Liu, J.; Wang, X.; Zhang, T. Dual metal active sites in an $Ir_1/FeO_x$ single-atom catalyst: a redox mechanism for the water-gas-shift reaction. *Angewandte Chemie International Edition* **2020,** *59*, 2-10.

[53] Ribeiro, M. C.; Jacobs, G.; Linganiso, L.; Azzam, K. G.; Graham, U. M.; Davis, B. H. Low Temperature Water Gas Shift: Evaluation of $Pt/HfO_2$ and Correlation between Reaction Mechanism and Periodic Trends in Tetravalent (Ti, Zr, Hf, Ce, Th) Metal Oxides. *ACS Catalysis* **2011,** *1* (10), 1375-1383.

[54] Shido, T.; Asakura, K.; Iwasawa, Y. Reactant-promoted reaction mechanism for catalytic water-gas shift reaction on MgO. *Journal of Catalysis* **1990,** *122* (1), 55-67.

[55] Geysermans, P.; Finocchi, F.; Goniakowski, J.; Hacquart, R.; Jupille, J. Combination of (100), (110) and (111) facets in MgO crystals shapes from dry to wet environment. *Physical Chemistry Chemical Physics.* **2009**, *11* (13), 2228-2233.

[56] Ruiz Puigdollers, A.; Schlexer, P.; Tosoni, S.; Pacchioni, G. Increasing oxide reducibility: the role of metal/oxide interfaces in the formation of oxygen vacancies. *ACS Catalysis* **2017**, *7* (10), 6493-6513.

[57] Bond, G.; Molloy, K. C.; Stone, F. S. Reduction of MgO-supported iron oxide: formation and characterization of Fe/MgO catalysts. *Solid State Ionics* **1997**, *101*, 697-705.

[58] Jozwiak, W. K.; Kaczmarek, E.; Maniecki, T. P.; Ignaczak, W.; Maniukiewicz, W. Reduction behavior of iron oxides in hydrogen and carbon monoxide atmospheres. *Applied Catalysis A: General* **2007**, *326* (1), 17-27.

[59] Liu, Z.; Cortés-Concepción, J. A.; Mustian, M.; Amiridis, M. D. Effect of basic properties of MgO on the heterogeneous synthesis of flavanone. *Applied Catalysis A:*

*General* **2006**, *302* (2), 232-236.

[60] Choudary, B. M.; Kantam, M. L.; Ranganath, K. V. S.; Mahendar, K.; Sreedhar, B. Bifunctional Nanocrystalline MgO for Chiral Epoxy Ketones via Claisen−Schmidt Condensation−Asymmetric Epoxidation Reactions. *Journal of the American Chemical Society* **2004**, *126* (11), 3396-3397.

[61] Han, F.; Ma, L.; Sun, Q.; Lei, C.; Lu, A. Rationally designed carbon-coated $Fe_3O_4$ coaxial nanotubes with hierarchical porosity as high-rate anodes for lithium ion batteries. *Nano Research* **2014,** *7* (11), 1706-1717.

[62] Pan, L.; Zhu, X.-D.; Xie, X.-M.; Liu, Y.-T. Smart Hybridization of $TiO_2$ Nanorods and $Fe_3O_4$ Nanoparticles with Pristine Graphene Nanosheets: Hierarchically Nanoengineered Ternary Heterostructures for High-Rate Lithium Storage. *Advanced Functional Materials* **2015,** *25* (22), 3341-3350.

[63] Cherkezova-Zheleva, Z.; Mitov, I. *In situ* Mössbauer investigation of iron oxide catalyst in water gas shift reaction – Impact of oxyreduction potential and temperature. *Journal of Physics: Conference Serie* **2010**, *217*, 012044.

[64] Tusche, C.; Meyerheim, H. L.; Jedrecy, N.; Renaud, G.; Ernst, A.; Henk, J.; Bruno, P.; Kirschner, J. Oxygen-Induced Symmetrization and Structural Coherency in Fe/MgO/Fe(001) Magnetic Tunnel Junctions. *Physical Review Letters* **2005,** *95* (17), 176101.

[65] Wan, J.; Chen, W.; Jia, C.; Zheng, L.; Dong, J.; Zheng, X.; Wang, Y.; Yan, W.; Chen, C.; Peng, Q.; Wang, D.; Li, Y. Defect Effects on $TiO_2$ Nanosheets: Stabilizing Single Atomic Site Au and Promoting Catalytic Properties. *Advanced Materials* **2018,** *30* (11), 1705369.

[66] Kuzmin, A.; Chaboy, J. EXAFS and XANES analysis of oxides at the nanoscale. *IUCrJ* **2014,** *1* (Pt 6), 571-589.

# Chapter 6 Synthesis of magnetite with a surrounded core-shell structure from fly ash waste and its superior catalysis performance for high-temperature water gas shift reaction

It has been concluded in Chapter 3 that Fe can be efficiently extracted out from fly ash and Chapter 4 has clarified the effect of Al impurity on nanosized α-$Fe_2O_3$ during synthesis process. This chapter will further demonstrate a facile process for the design of magnetite-based, surrounded catalysts with a core-shell structure from coal fly ash, an industrial solid waste, and the application to classic high temperature water-gas shift reaction (WGSR). This chapter has been organized and submitted to ***Green Chemistry***.

# Abstract

In this section, we demonstrate a facile process for the design of magnetite-based, surrounded catalysts with a core-shell structure from coal fly ash, an industrial solid waste, and the application to classic high temperature water-gas shift reaction (WGSR). The feedstock was initially synthesized through a leaching-precipitation-hydrothermal process, leading to the formation of a nanosheet-like hematite precursor consisting of $Fe^{3+}$ as principal element and trace cations including $Al^{3+}$, $Mg^{2+}$ and other cations (*e.g.* $Ca^{2+}$, $Ti^{4+}$ and $Mn^{2+}$). Upon a subsequent thermal reduction, the nanosheet broke into smaller particles with a core in form of magnetite and a diameter of ~20 nm, whereas the inherent impurity elements were activated to migrate to the outer surface forming a shell with a thickness in a few nanometres. The elemental composition, porosity and thickness of the shell are highly tunable. Upon the addition of ethanol during the hydrothermal stage, a slightly higher content of $Al^{3+}$ (8.92 *wt%*) and $Mg^{2+}$ (2.58 *wt%*) were successfully embedded within the shell of the catalyst, which in turn increased the shell thickness by nearly twice, and created more nanochannels in mesopore scale within the shell. Due to the protection effect of shell, the two catalysts exhibited higher activity, thermal stability and long-term durability for HT-WGSR at 400ºC and 450ºC. In particular, the catalyst synthesized with a thicker shell slightly more impurities exhibited the highest activity at a temperature. Compared to the pure hematite, the best activity increased the CO conversion by nearly four times and decreased the magnitude of the deactivation rate constant by four times too. Additionally, apart from $Al^{3+}$ being a textual promoter enhancing the interfacial area of the catalysts, the trace impurity elements, in particular 2.58 *wt%* $Mg^{2+}$ was confirmed to promote the redox rate of catalysts by promoting the formation of formate, the adsorption rate of CO and the desorption of $CO_2$ molecules on the catalyst surface too. These trace impurities are supposed to atomically disperse within the nano-scale shell, thereby creating extra active sites to interact strongly with the magnetite core. This study opens a new direction on the

valorization of solid waste into high-value catalysts, thereby promoting the sustainability of solid waste management, but it also provides an alternative, cost-effective and scalable approach for the design and fine-tuning of surrounded catalysts.

Keywords: Coal fly ash, Core-shell structure, Magnetite, Waste treatment, Water gas shift reaction

## 6.1 Introduction

Heterogeneous catalysis is the core of most of the chemical reactions. From the practical perspective, supported catalyst featuring a high dispersion of the active phase on a support is the most widely used type. In addition to providing a matrix with a large surface area to disperse the active phases/particles, the support also influences the electronic and geometrical structures of the active phase. Traditionally, the impregnation or precipitation method is employed to load a metal precursor, usually in a water-soluble salt form onto the outer surface of a support. This, however, renders limited contact area and relatively weak interfacial interaction between support and the active phase, which in turn causes an easy agglomeration and deactivation of the active phase [1]. Alternatively, through the design of a core-shell structure in which the active phase, as the core is surrounded by the support as a shell, the catalyst bears a larger interfacial area facilitating a strong metal-support interaction (SMSI) [2] and improved activity, thermal stability and durability [3]. Recently, extensive studies have demonstrated the superiority of this structure, including surrounded Ni@$Al_2O_3$ catalyst [1], hierarchical Sn-Cu/$SnO_x$ catalyst [4], nanostructured (Pt-Enriched Cage)@$CeO_2$ catalyst [5], FeOx@Rh [6] and numerous core-shell catalysts for water-gas shift reaction (WGSR), including Pd@$CeO_2$ catalyst hybridized with multi-walled carbon nanotubes [7], bimetallic nickel–copper [8], Pd@$CeO_2$/$Al_2O_3$ [9], transition-metal (TM)@$Cu_{12}$ [10] and cobalt@gold nanocluster [11].

However, all these catalysts either involve a complex synthesis processes including galvanic replacement [6], ion-exchange [1] and electrodeposition-oxidation [4], or focus on the use of noble metals that increase the catalyst cost and environmental impact for its final disposal.

In this section, we report a facile and noble metal-free route for the synthesis of magnetite ($Fe_3O_4$) with a core-shell structure from fly ash, an otherwise valueless solid waste with an annual yield of 750 Mt in the world [12]. More specifically, the $Fe^{3+}$ within fly ash is purposely extracted out as the principal precursor cation to convert into magnetite, whereas the inherently present impurities including $Al^{3+}$ and $Mg^{2+}$ are also selectively extracted out in a trace amount, functioning as promoters comprising a shell to stabilise magnetite. The primary motivation is that, out of the commonly discharged industrial wastes, coal ash is a large contributor produced from a continuous use of coal as the predominant source for power and heat generation in the world. With a substantial amount being disposed of in landfills or lagoons, a portion of fly ash rich in alumina and silica is merely used as a low-value additive into the cement. However, this method is not applicable to low-rank coal fly ash and even bio-ash which is rich in the elements including alkali and alkaline earth elements and even iron. In Australia, over ten million tons of low-rank coal fly ash had been produced annually in the last thirty years [13], most of which is simply dumped into ash ponds. Nevertheless, from a catalyst synthesis perspective, the aforementioned elements other than alumina and silica are the essential elements for a broad range of applications. Due to its low toxicity and economic viability, iron oxide has been used as catalysts for numerous reactions [14-17], whereas $Al^{3+}$ and $Mg^{2+}$ have been reported as textual promoters in lieu of potentially toxic chromium (Cr) for the WGSR [18-21]. Presumably, through a carefully tuning procedure, these three elements can be selectively extracted out of fly ash, and further turn into an effective magnetite-based catalyst, whereas the remaining residue of fly ash is depleted in these elements, and it could thus be used as an additive in the

existing cement industry. Ultimately, the fly ash feedstock would be fully valorized rather than being landfilled causing substantially negative environmental impact.

As illustrated in **Figure 6-1(a)**, the proposed process commences from an acid-leaching of a pre-treated fly ash (after water-washing and crushing) to selectively leach out $Fe^{3+}$ as the principal cation, which is accompanied by impurity cations including $Al^{3+}$, $Mg^{2+}$, $Ca^{2+}$, $Mn^{2+}$ and even $Ti^{4+}$ from the same fly ash matrix. Subsequently, the pH of the leachate is increased to approximately 3 to precipitate out $Fe^{3+}$ as hydroxide ($Fe(OH)_3$), with the co-precipitation of a portion of the aforementioned cations, in particular $Al^{3+}$ due to an overlapping of their hydroxide precipitation around this pH value [22]. Afterwards, upon a further hydrothermal treatment, calcination and thermal reduction in sequence, a core-shell structured catalyst is formed, with a core of nanosized magnetite ($Fe_3O_4$) formed from the partial reduction of the principal $Fe^{3+}$ cation, and a shell formed from a preferential outward migration of the aforementioned impurities to the surface of magnetite. Such a facile strategy is based on the discrepancy of the diffusion of individual cations within the defects, vacancies and interstitials of a crystal structure [23]. More specifically, $Al^{3+}$ forms metastable solid solution of $Fe_{2-x}Al_xO_3$ at high temperature [24], which is prone to diffuse out of magnetite lattice. Similarly, induced by thermal activation and the discrepancy of atomic radius to Fe, alkali and alkaline earth metals easily segregate at the surface of magnetite, as has been confirmed at an annealing temperature of ~1000 K [25].

Herein, we demonstrate this core-shell structure of two typical surrounded magnetite catalysts formed from a local fly ash, and their strong catalytic activity in high-temperature WGSR (HT-WGSR). The impurity elements including $Al^{3+}$, $Mg^{2+}$, $Ca^{2+}$, $Mn^{2+}$ and $Ti^{4+}$ with a concentration ranging from <1 *wt%* to ~ 5 *wt%* each have been successfully converted into a shell on the

magnetite surface. Additionally, through the use of advanced facilities for both bulk and surface characterizations, and *in-situ* spectroscopic analysis, the knowledge underpinning the role of $Al^{3+}$ (~ 5 *wt%*) and $Mg^{2+}$ (~ 1-2 *wt%*) have been further expanded. To date, through co-precipitation with $Fe^{3+}$ at a molar ratio of 1:10, $Al^{3+}$ has been revealed as an effective textural promoter of increasing the specific surface area and sintering resistance of iron oxide, and hence, its catalytic activity on HT-WGSR [21]. On the other hand, through being used as a large surface area support, MgO is able to disperse and stabilize $Fe^{3+}$ as spinel for a high sintering resistance and catalytic activity in HT-WGSR [19]. However, neither of these studies have examined such low concentrations for the promoters. In addition, for the other Cr-free Fe-based catalysts, as summarized in **Table S6-1**, the added promoters usually form a single phase/structure with Fe, rather than being segregated as a unique core-shell structure. Ultimately, this study is expected to cast a significant impact on the valorization of fly ash and other iron-rich solid wastes into high-value catalysts for a broad range of catalysis applications, thereby promoting the sustainability of the future economy.

# 6.2 Materials and methods

## 6.2.1 Materials

The low-rank coal fly ash, namely brown coal fly ash was collected from the Energy Australia Yallourn power plant located in the Latrobe Valley, Victoria, Australia. **Table 6-1** shows its typical elemental composition. It is clear that iron (Fe) is the most abundant element, followed by Mg being the second most abundant one. The as-received fly ash sample was washed at a liquid to solid (L/S) mass ratio of 10 to remove the unburnt carbon and water-soluble species. Subsequently, it was oven-dried at 105°C for 12 h and grounded using a tungsten-carbide vibratory ring pulverizer, producing a particle size of <150 μm prior to use. All the chemicals

including NaOH, HCl (32 *wt%*), $FeCl_3$•6H2O and ethanol were purchased from Sigma-Aldrich. Milli-Q water was used throughout all the experiments.

## 6.2.2 Synthesis of magnetite with a core-shell structure

As illustrated in **Figure 6-1(b)**, after a pretreatment by water-washing, drying and crushing mentioned above, the resultant fly ash was subjected to acid leaching, precipitation, hydrothermal processing and reduction in sequence, leading to desired core-shell structure for high-purity magnetite. Approximately 95% of Fe was successfully extracted out of fly ash matrix, which was also nearly fully converted into high-purity magnetite [13]. Therefore, the mass yield of magnetite catalyst reaches 32% on the mass basis of dried fly ash. The detail of each step for catalyst synthesis is given below.

Acid leaching and hydroxide precipitation

A two-step cross-current leaching method was used to extract $Fe^{3+}$ from the Victorian BCFA, as reported in our previous research [26]. Due to the presence of most of the $Fe^{3+}$ in a stable spinel structure such as magnesium ferrite ($MgFe_2O_4$) [27], as shown in **Figure S6-1**, in each step, 32 *wt%* HCl was used as the leaching agent to mix with water-washed fly ash or the leaching residue derived from the previous step, at a L/S mass ratio of around two in a closed 250 mL conical flask. The flask was then placed in a thermostatically controlled water bath at 60 °C and stirred for a period of 90 min. The stirring rate was controlled at 300 rpm throughout all the runs. After leaching, the slurry was immediately filtered via a vacuum pump and a filter paper with a cut-off size of 450 μm. Around 95% of Fe and 94% of Mg have been successfully extracted out, leading to the formation of a reddish leachate as shown in **Figure 6-1(a)**. Note that a small amount of $Ca^{2+}$ and $Al^{3+}$ was also introduced into the leachate. Nevertheless, the remaining residue is rich in $Al_2O_3$ and $SiO_2$, as shown in **Table 6-1**. It is thus suitable for the

use as cement additive. With regards the leachate rich in $Fe^{3+}$ and $Mg^{2+}$, 1 mol/L NaOH was added dropwise until the pH of the leachate reached 3.6, forming a slurry that was then centrifuged at 10000 rpm for 10 min to obtain the $Fe(OH)_3$ precipitate. The precipitate was washed three times with Milli-Q water to remove the water-soluble cations on it. Afterwards, the precipitate was further mixed with 40 mL of Milli-Q water and placed into an ultrasonic bath for 1 h.

Hydrothermal processing of hydroxide into $\alpha$-$Fe_2O_3$

For the mixture of iron hydroxide with Milli-Q water, after sonication, 1 mol/L of NaOH solution was further dropped into the resultant slurry to adjust its final pH to 6. For the resultant slurry, it was split into two batches, with one being further blended with 10 mL ethanol, and another as it was. The addition of ethanol is expected to tune the growth of $\alpha$-$Fe_2O_3$. Afterwards, both batches were transferred into a 150 mL autoclave each, and placed inside a preheated hot-air oven maintained at 180°C. After 24 h, the autoclaves were removed and cooled down to room temperature naturally. The obtained precipitates were filtered and immersed in ethanol for 24 h, filtered and washed with distilled water three times to remove NaOH and then with ethanol to mitigate the particle agglomeration, and finally dried at 80°C for 2 h. In addition, as a reference, pure hematite nanoparticles were also synthesized based on the use of pure $FeCl_3$ solution as the precursor, as per a similar hydrothermal procedure detailed in our previous research [26].

Thermal Reduction of $\alpha$-$Fe_2O_3$ into magnetite

Thermal reduction is the final step for the conversion of $\alpha$-$Fe_2O_3$ into magnetite, as well as the migration of impurity cations to the surface of the resultant magnetite. Here ~4.5% CO in $N_2$ of 200 ml/min was used as the reductant, and the reduction was conducted so-thermally at

400ºC for 1-2 h, with the $CO_2$ signal from outlet gas down to a negligible level (<0.1 vol%) in the on-line FTIR gas analyzer. For most of the cases, this step was conducted *in-situ* and followed by the HT-WGSR test directly at 400ºC. For the HT-WGSR testing at 450ºC, the gas of 5% CO in $N_2$ was switched to pure $N_2$, and the reduced catalyst was heated from 400ºC to 450ºC. Afterwards, the reactive gases including 5% $CO_2$ and 5% steam were switched on for a continuous HT-WGSR testing. Effort was also made to *ex-situ* reduce the fly ash derived α-$Fe_2O_3$ by 5% $H_2$ at 400°C for around 1 h. The reduced catalyst was subsequently cooled down and passivated in 1% $O_2$ at room temperature. However, in terms of the HT-WGSR catalytic activity, negligible difference was observed between the two differently reduced catalysts.

### 6.2.3 HT-WGSR tests

Catalytic performance was evaluated in a continuous-flow fixed bed reactor with 100-200 mg of a synthesized catalyst at 400-450 ºC under the atmospheric pressure. In each run, the catalyst was mixed with ten times the amount of pre-cleaned SiC, and then heated to 400ºC under the protection of $N_2$ at a heating rate of 10°C/min, which simultaneously removed the surface contaminants. For *in-situ* reduction, to reiterate, dry CO gas of ~ 4.5 vol% was fed into the system at a flow rate of 200 mL/min for 1-2 h, until the $CO_2$ signal was negligible (<0.1%) in the outlet gas. This step is however omitted in the case the catalyst was prior reduced in $H_2$. Afterwards, CO and steam were introduced at ~ 4.5-5 vol% each to commission the HT-WGSR. The overall gas flow rate remained at 200 mL/min, resulting in a gas hourly space velocity (GHSV) of 0.23-0.89 $m^3\ g_{Fe2O3}^{-1}\ h^{-1}$. Note that the concentrations of CO and $H_2O$ are much lower, whilst the space velocity here is much higher than the values such as 0.018 and 0.06 $m^3\ g_{cat}^{-1}\ h^{-1}$ used elsewhere [21].

The outlet gas stream was monitored on-line by an MKS Multigas™ 2030 Fourier-transform

infrared spectroscopy (FTIR) continuous gas analyzer for CO, $CO_2$, $H_2O$ and $CH_4$. It was also periodically sampled for the quantification of $H_2$, CO, $CO_2$ and $CH_4$ by an Agilent gas chromatography (GC) coupled with a (thermal conductivity detector) TCD detector. The analysis showed a good agreement between the two analytical measurements. A closed mass balance for carbon was also confirmed. For the catalyst performance evaluation, the CO conversion based on the difference of inlet and outlet CO concentrations was used primarily.

The deactivation rate constants were calculated based on a pseudo-first-order kinetics in the initial 2 h. To derive the deactivation rate constants (k), the natural logarithms of the relative rates (rate at a time divided by the initial rate) were plotted against the time-on-stream (TOS), as shown in **Equation 6-1**. Note that the reaction rate at TOS = 0.25 h was assumed as an initial rate ($r_0$):

$$\ln\left(\frac{r}{r_0}\right) = -k(t - 0.25) \qquad \textbf{Equation 6-1}$$

## 6.2.4 Material Characterization

X-ray diffraction (XRD) analysis was used for phase identification and the determination of unit cell parameters. The XRD patterns were recorded on a Rigaku SmartLab 3000A diffractometer with Cu Kα radiation (λ = 0.15406 nm). The X-ray tube was operated at 40 kV and 15 mA. Each sample was scanned between 20° and 80° with a D/teX Ultra detector, at a scanning speed of 5°/min. Morphologies and structures of the as-synthesized materials were characterized by scanning electron microscopy (SEM) (FEI Nova NanoSEM 450 FEGSEM) and scanning transmission electron microscopy (STEM) (FEI Tecnai G2 F20 S-TWIN STEM). X-ray photoelectron spectra (XPS) were measured with using an AXIS Ultra spectrometer (Escalab 250Xi, Thermo Fisher Scientific, USA) with an Al Kα anode. Fe K-edge X-ray

absorption near-edge spectroscopy (XANES) and extended X-ray absorption fine structure spectroscopy (EXAFS) were conducted at Beamline BL16A1 of NSRRC (National Synchrotron Research Radiation Centre) in Taiwan. Fe K-edge XANES spectra were processed using ATHENA software (a part of DEMETER package) and Fe EXAFS data were fitted using Artemis (part of Demeter) with FEFF version 8. In addition, near-edge X-ray absorption fine structure (NEXAFS) was used to elaborate the coordination environment of Mg K-edge (1280-1360 eV), Al K-edge (1540-1620 eV) and Fe L-edge (700-730 eV) in the spent catalyst, based on the total electron yield (TEY) mode that is highly surface sensitive for an average depth of a few of nanometres down the surface [28, 29].

*In-situ* diffuse reflectance infrared Fourier transform spectroscopy (DRIFTS) was performed on Bruker Tensor 27 FTIR spectrometer coupled with a Praying Mantis™ Diffuse Reflection Accessory from Harrick. In a typical experiment, the sample was first pretreated with UHP He (40 mL/min) at 400 °C for 1 h. Afterwards, 5 vol% CO/He (40 mL/min) was introduced into the sample cell for 10 min. Thereafter, the gas was switched to 3 vol% $H_2O$/He (40 mL/min) and maintained for another 10 min. The spectra were recorded with a resolution of 4 $cm^{-1}$ between 4000 $cm^{-1}$ and 600 $cm^{-1}$.

CO-Temperature Programmed Reduction (TPR) was conducted using AutoChem II 2920 from Micromeritics, coupled with ThermoStar GSD 320 T Quadrupole Mass Spectrometer (QMS) from Pfeiffer Vacuum, using a Secondary Electron Multiplier. In each experiment, ~60 mg of catalyst was pretreated with 10 vol% $O_2$/He (50 mL/min) at 300 °C for 1 h, followed by ramping down to ambient temperature in 5 vol% Ar/He (50 mL/min). The flowing gas was then switched to 5 vol% CO/He (50 mL/min). After stabilizing for 30 min, the temperature was ramped to 450 °C at a rate of 3 °C/min. Additionally, $H_2$-TPR was conducted at a fix-bed reactor

coupled with a Rapidox 5100 gas analyser which has a built-in thermal conductivity detector (TCD) for real-time $H_2$ detection. For each run, a sample of approximately 100 mg was heated from room temperature to 700 °C at 5 °C/min, with a continuous flow of 10% $H_2/N_2$ at 200 ml/min. Prior to the analysis, the reactor was purged by pure nitrogen for around 1 hr.

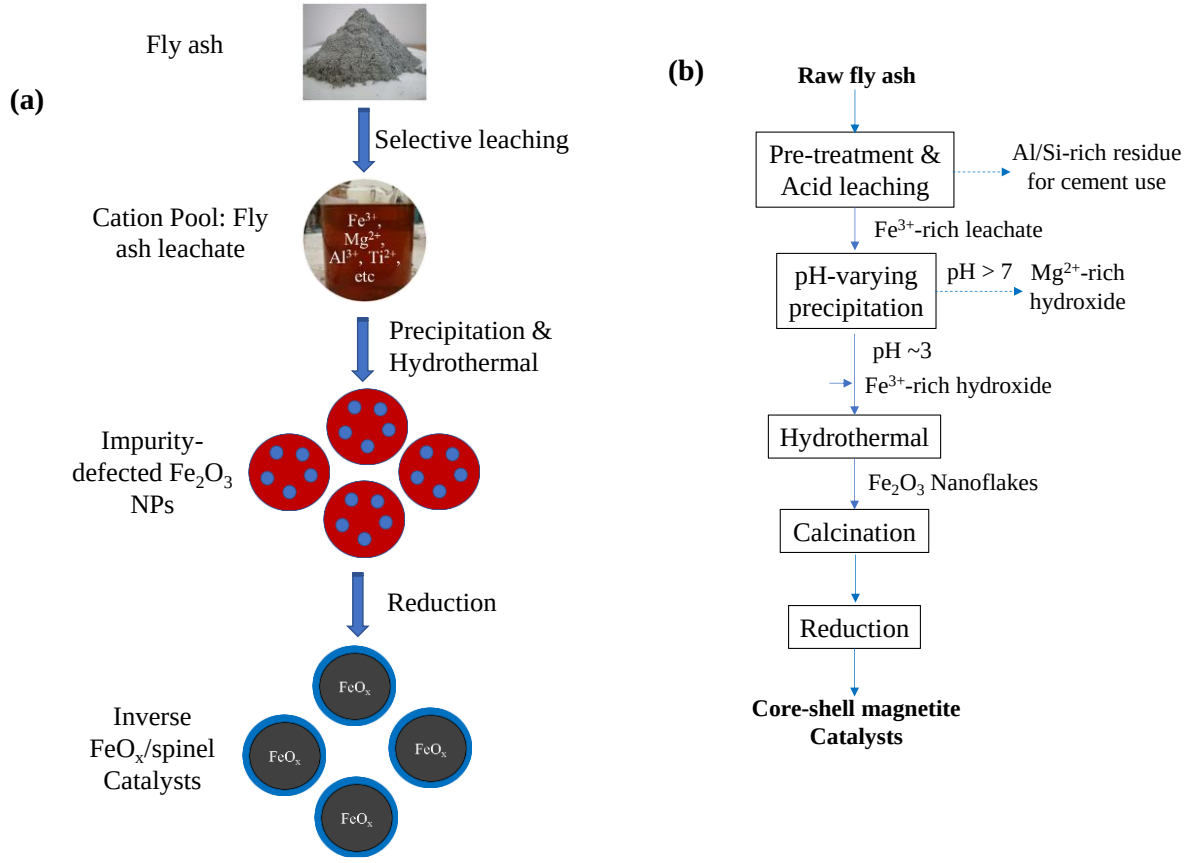


**Figure 6-1**(a) Schematic illustration of synthesis of magnetite with a core-shell structure from fly ash waste, and (b) for the detailed stepwise procedure for the synthesis.

## 6.3 Results and Discussion

### 6.3.1 Bulk properties of α-$Fe_2O_3$ nanoparticles and $Fe_3O_4$ catalysts with a core-shell structure synthesized from fly ash

**Elemental Compositions, Surface Area, Porosity and Microstructures**

**Table 6-1** also displays the elemental compositions of the two α-$Fe_2O_3$ precursors achieved after the hydrothermal treatment of the fly ash derived hydroxide, with and without the addition of ethanol in the hydrothermal autoclave. For simplification, the two oxide precursors were abbreviated as RNF and INS hereafter, representing the oxides formed in the absence and presence of ethanol, respectively.

In terms of the most stable oxide, $Fe_2O_3$ is clearly the principal oxide for both precursors, counting for 88.12 *wt%* and 92.74 *wt%* for the case with and without ethanol, respectively. In addition, a number of impurity elements with varying contents were detected, with $Al_2O_3$ being the most abundant for a content of 5.8-8.9 *wt%*, followed by MgO of 1-2.6 *wt%* and all the others less than 0.2 *wt%*. More interestingly, the specific surface areas of the two precursors are also considerably different. Upon the addition of ethanol, the oxide formed bears a relatively small surface area of 35.7 $m^2/g$, whereas the absence of ethanol increased the surface area up to 52.8 $m^2/g$. As the same batch of leachate from fly ash leaching and same iron hydroxide precipitate were used, the difference of these two precursors shall be solely attributed to the ethanol in the hydrothermal stage. The added ethanol could be selectively adsorbed on the α-$Fe_2O_3$ and thus changed the growth of individual cations from the fly ash leachate to α-$Fe_2O_3$ matrix, leading to the formation of sheet-like morphology and variable chemical composition [30, 31]. In terms of total pore volume, both two fresh precursors carry a pore volume of around 0.1 $cm^3/g$, and their difference is rather marginal. The pore size distribution

in **Figure S6-2** also suggested marginal difference between the two samples. In general, a very broad pore size distribution from micropores to macropores were found within the two fresh precursors. In particular, the fresh INS with an irregular shape carries more macropores, which should be relevant to the edge defects.

The surface morphology of the $Fe_2O_3$ precursors is shown in **Figure 6-2(a1)-(a3)** and **(b1)-(b3)**. For the INS precursor formed from the case of ethanol addition in **(a1)-(a3)**, it exhibits a diameter of around 1 μm, and an irregular nanosheet-like structure. The TEM morphology for a single particle demonstrates the indented outlines and defects on the edge. The inset for an inter-cross of hexagonal diffraction spots can be indexed to the [0 0 1] zone axis for a single-crystal structured rhombohedral α-$Fe_2O_3$. The detailed facets for this precursor are further confirmed by HRTEM in **(a3)**, demonstrating three equivalent facets of (110), (-120) and (-210) with a d-spacing of 0.252 nm and apart at 120° from one another. All these feature facets belong to the [001] zone axis of α-$Fe_2O_3$.

The RNF precursor formed in the absence of ethanol in **Figure 6-2(b1)-(b3)** displays a small diameter of approximately 300 nm and a round nanoflake structure. The smaller diameter for the latter precursor explains its larger surface area in **Table 6-1**, which further demonstrates the critical role of ethanol on the growth of α-$Fe_2O_3$. Meanwhile, from the TEM picture in **(b2)**, one can further see a clearly round shape for this precursor. The corresponding SAED pattern (inset) can also be indexed to the [0 0 1] zone axis of α-$Fe_2O_3$. Similarly, for the HRTEM picture in **(b3)**, the clear fringe d-spacing value measured as ~0.252 nm concurs well with the interplanar spacing of (1 1 0) facets for α-$Fe_2O_3$.

More strikingly, **Figure 6-2(a4)** and **(b4)** demonstrate the bright field TEM images of the two

spent (simplified as **s** as the prefix before RNF and INS hereafter) catalysts after the HT-WGSR at 450ºC. Both samples demonstrate a clear core-shell structure, with darker contrast (elements with higher atomic numbers) embedded as the "core" and lighter contrast (elements with lower atomic numbers) as the surrounding "shell". For the spent INS catalyst with an irregular shape for the precursor, its core is composed of crystalline $Fe_3O_4$ with a d-spacing of 0.209 nm corresponding to the (400) facet. However, its shell is closer to a poorly-crystallized $Al_2O_3$ with a d-spacing of 0.196 nm corresponding to the (202) facet of $Al_2O_3$. Likewise, for the spent RNF catalyst with a round shape, its core was also confirmed as the crystalline $Fe_3O_4$ with a d-spacing of 0.161 nm for the respective (511) facet. The shell part exhibits a poorly-crystallized $Al_2O_3$ with a d-spacing of 0.255 nm corresponding to the (104) facet. This observation proved our hypothesis for a preferential migration of impurity elements, in particular $Al^{3+}$ to the outer surface of magnetite. The other impurity elements were not detected, which shall be due to their extremely low concentration and low contrast to Fe for their small atomic numbers. Regarding the difference between the two spent catalysts, the particle size for the magnetite core is quite comparable, reaching around 20 nm in diameter. Nevertheless, the thickness of the shell varies remarkably, showing a value of 4-5 nm for the INS precursor and only 2-3 nm for the RNF. This shall be attributed to the quantity of the impurity elements within the two catalysts. As shown in **Table 6-1**, the RNF precursor bears 5.81 *wt%* $Al^{3+}$ and only 1.03 *wt%* $Mg^{2+}$, opposed to 8.92 *wt%* $Al^{3+}$ and 2.58 *wt%* $Mg^{2+}$ in its counterpart. Clearly, although these differences are small, they had exerted a considerable effect on the catalyst structure. Inferably, the catalyst performance would differ as well.

**Table 6-1** Mass yield, elemental compositions and specific surface area of raw fly ash and as-synthesized INS and RNF

| | Percent (%) | | | |
|---|---|---|---|---|
| | Raw fly ash | $\alpha$-$Fe_2O_3$ without ethanol addition in hydrothermal (RNF) | $\alpha$-$Fe_2O_3$ with ethanol addition in hydrothermal (INS) | Leaching residue |
| Mass yield, *wt%* on unit fly ash mass | -- | 32 | | 67 |
| Elemental composition, *wt%* | | | | |
| $SiO_2$ | 12.45 | N.D.[#] | N.D. | 37.92 |
| $Al_2O_3$ | 7.47 | 5.81 | 8.92 | 8.64 |
| $Fe_2O_3$ | 33.35 | 92.74 | 88.12 | 9.61 |
| CaO | 5.22 | 0.15 | 0.08 | 0.53 |
| MgO | 14.51 | 1.03 | 2.58 | 2.77 |
| $K_2O$ | 0.06 | N.D. | N.D. | 0.22 |
| $SO_3$ | 1.42 | N.D. | N.D. | 1.91 |
| MnO | 0.41 | 0.09 | 0.13 | 0.57 |
| $TiO_2$ | 0.79 | 0.18 | 0.17 | 1.62 |
| Loss of Ignition[*] | 24.32 | -- | -- | 36.21 |
| Physical properties | | | | |
| Specific surface area ($m^2\ g^{-1}$) | -- | 52.8 (41.1$^{\Delta}$) | 35.7 (34.2$^{\Delta}$) | -- |
| BJH adsorption volume of pores ($cm^3 g^{-1}$) | -- | 0.1163 (0.1022$^{\Delta}$) | 0.1098 (0.1053$^{\Delta}$) | -- |

[#] N.D.: Not detectable by XRF; [*]: LOI was measured by heating a sample up to 300°C in air. [Δ]: Post reduction in $H_2$ at 400°C.

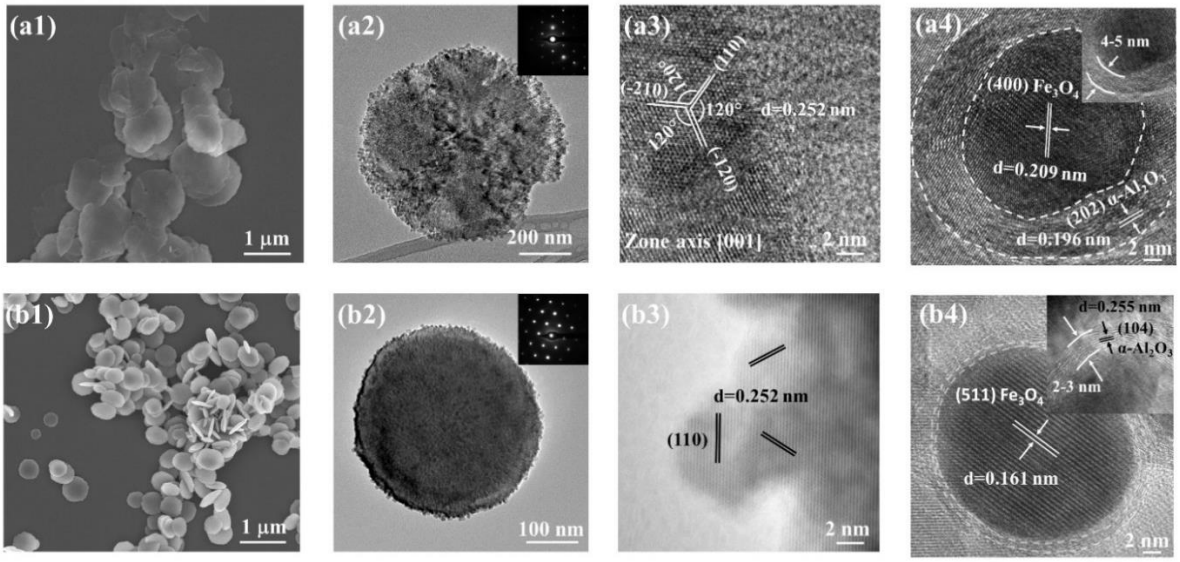


**Figure 6-2** (a1) and (b1) are SEM images for f-INS and f-RNF, respectively. (a2-a3) and (b2-b3) are TEM images for f-INS and f-RNF, respectively. (a4) and (b4) are TEM images for s-INS and s-RNF, respectively.

**XRD and Synchrotron XAS characterization**

The XRD patterns of fresh INS and RNF are shown in **Figure 6-3(a1)** and are also compared with standard rhombohedral hematite (JCPDS No. 33-0664) with lattice constants of a = 5.038 Å and c = 13.772 Å. The well-resolved diffraction peaks reveal the good crystallinity of iron oxide within the two precursors. The species for impurity cations including $Al^{3+}$ and $Mg^{2+}$ were not detected, which shall also be due to their low concentration, or implies an amorphous state such as solid solution for these two elements within the $\alpha$-$Fe_2O_3$ lattice. The XRD patterns for $Al^{3+}$ and $Mg^{2+}$ bearing ferrites also overlap with iron oxides such as hematite and magnetite significantly [32].

Detailed atomic structure of the two precursors is further verified through Fe K-edge XANES and EXAFS. As depicted in **Figure 6-3(a2)**, the XANES curves prove that the white line

position of both samples closely resembles that of standard hematite. More quantitatively, through a Fourier transforming of the EXAFS spectra in **Figure 6-3(a3)**, the bond distance (R), coordination number (N) and Debye-Waller factor ($\sigma^2$) of ligands coordinated to $Fe^{3+}$ are tabulated in **Table S6-2**. As shown in this Table, for both fresh precursors, their Fe-$O_{oct}$ bond distance reaches 1.94(23) Å and 2.01(15) Å for the RNF and INS, respectively. Both values fall within the error of the standard α-$Fe_2O_3$ (2.08(2) Å). In terms of bond distance, the second shells for the $FeO_{oct}$-$FeO_{oct}$ bond of both precursors are also constant and close to that of standard α-$Fe_2O_3$. However, in terms of refined coordination number (N), the pure nano-hematite synthesized reaches 5.9(3) and 3.8(4) for Fe-$O_{oct}$ and $FeO_{oct}$-$FeO_{oct}$, respectively, which are close to the theoretical values of 6 and 4 [33]. In contrast, the N values of the first shell Fe-$O_{oct}$ for the RNF and INS reaches 4.5(2) and 4.2(3), respectively. This is an indicator of a flattened nanosheet structure for the two precursors, which are remarkably different from the three-dimensional pure hematite nanoparticles (**Figure S6-3**). In particular, the impurity elements can replace a portion of Fe in hematite lattice, thereby reducing the coordination number of Fe in first shell Fe-$O_{oct}$ [26].

The XRD patterns of the two spent catalysts are shown in **Figure 6-3(b1)**. Note that both are contaminated with SiC (JCPDS No. 65-3107) that were used to blend with catalyst at a mass ratio of 10:1 for the HT-WGSR testing. Nevertheless, the face-centered cubic magnetite structure has been confirmed, matching the standard one (JCPDS No. 29-1126). Additionally, **Figure 6-3(b2)** confirmed that both Fe K-edge XANES curves and their white line position for the spent catalysts are highly consistent with that of the standard, demonstrating the predominance of magnetite phase for the two catalysts. However, the corresponding Fourier transform of the EXAFS spectra in **Figure 6-3(b3)** and the respective structural parameters in **Table S6-2** indicate the considerable discrepancy of the two catalysts from pure magnetite, as

well as the difference between the two catalysts. In general**,** there are four scattering paths for magnetite model, with the first and second shells corresponding to $FeO_4$ tetrahedron (Fe-$O_{tet}$) with a bond length R of 1.87 Å and $FeO_6$ (Fe-$O_{oct}$) octahedron with R of 2.04 Å, respectively, whilst the third and fourth shells at 2.97 Å and 3.48 Å, respectively, are attributed to the $FeO_{oct}$-$FeO_{oct}$ and $FeO_{oct}$-$FeO_{tet}$ multiple scattering paths. For the spent pure hematite, both of the refined N and R values derived from the four shells are very close to the standard magnetite, further proving the appropriateness of the reduction conditions (*i.e.* 400ºC, 4.5 % CO in $N_2$ and around 1-2 h) for the generation of magnetite.

In contrast, significant changes on the atomic environment of Fe were observed for the two spent catalysts. As detailed in **Table S6-2**, compared to the standard magnetite, the s-RNF exhibits a shorter bonding distance of Fe-$O_{tet}$ and Fe-$O_{oct}$, which is probably due to the incorporation of smaller $Al^{3+}$ ions into the two shells. Similar results were also obtained in ion-doped hematite [34, 35]. More strikingly, for the s-INS, its first two shells for distinct Fe-$O_{tet}$ and Fe-$O_{oct}$ scattering paths merged into one single shell (Fe-$O_{com}$), strongly suggesting a spatial distortion of Fe from a periodic symmetry. In addition, its Fe-$O_{com}$ bond distance is longer than the standard magnetite, which is an evidence for the intrusion of foreign $Al^{3+}$ and $Mg^{2+}$ into magnetite lattice, resulting in distorted lattice and altered bond distance [36]. In contrast, for the $FeO_{oct}$-$FeO_{tet}$ bond distances referring to the third shell around Fe, both two spent catalysts are almost the same and hence, it is inferred that the impurities such as $Al^{3+}$ and $Mg^{2+}$ are mostly bound within the vicinity of Fe. This is further reflected by the remarkable decrease on the coordination number (N) for the two spent catalysts. Apparently, a chemical bonding derived from the substitution of impurity elements for Fe within magnetite at tetrahedral and/or octahedral sites have occurred, which was similarly observed for Zn and Ce [37-39]. This should be initiated by the reduction of $Fe^{3+}$ on the surface of the hematite

precursor, thereby creating oxygen vacancy for the impurity elements to migrate and bind with the surface $Fe^{2+}$ and/or $Fe^{3+}$ into a solid solution such as $Fe_{1-x}Al_{x2}O_3$ or a ferrite such as $Mg_{1-x}Fe_{2+x}O_4$ as has been suggested for $Ca^{2+}$ within magnetite [25].

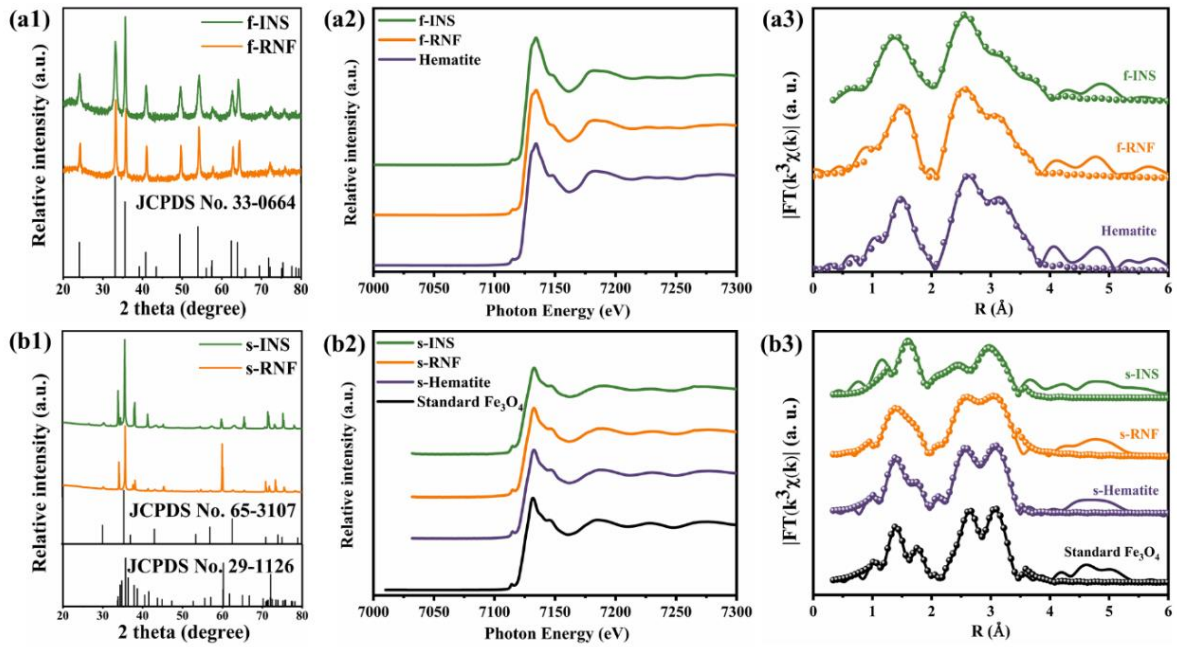


**Figure 6-3** XRD patterns (a1 and b1), Fe K-edge XANES spectra (a2 and b2) and the corresponding $k^3$-weighted Fourier transformed EXAFS spectra with measured (solid line) and fitting curve (scatter line) (a3 and b3) for as-synthesized fresh and spent INS and RNF. Phases in XRD patterns are α-$Fe_2O_3$ (JCPDS No. 33-0664), $Fe_3O_4$ (JCPDS No. 29-1126) and SiC (JCPDS No. 65-3107).

### CO-TPR and Isothermal Reduction Profiles

**Figure 6-4** displays the reducibility of both fly ash derivatives and their comparison with pure one. As shown in **Figure 6-4(a)**, the $H_2$-TPR profile for the pure hematite consists of two well separated peaks, with a small peak at ~370°C for the reduction of hematite to magnetite ($Fe_3O_4$), and a large peak at ~500°C for the further reduction to FeO and metallic iron ($Fe^0$) [40]. In

contrast, the reduction profiles for the two fly ash derivatives is much broader. The first peak for hematite to magnetite is also much less intense, which is an indicator of the establishment of the shell that provides a resistance against hydrogen diffusion. In particular, this is the case for the INS precursor, reflecting the previous observations that the shell of the INS is thicker due to the inclusion of slightly more $Al^{3+}$ and $Mg^{2+}$. The breadth for the second peak located around 585°C is also an indicator of the formation of aforementioned ferrites, which establishes a strong solution with the magnetite core, such as $Fe_3O_4$-$FeAl_2O_4$ at their interface to hinder the reduction of magnetite, as has been confirmed for the addition of 6-12 *wt%* $Al_2O_3$ into pure hematite [41]. Similarly, the CO-TPR in **Figure 6-4(b)** also confirmed the formation of a larger intensity for the second peak beyond 400°C for the two fly ash derivatives, which is another sign for the establishment of a complex ferrite/solid solution for the shells upon the thermal reduction. However, the isothermal CO reduction profiles in **Figure 6-4(c)** demonstrates a long tail for the reduction of the RNF precursor. This difference can be explained by the pore size distribution of the two reduced precursors in **Figure S6-2**. Interestingly, for the CO-reduced RNF, its peak pore size is around 10 nm, which shall be mainly assigned as nanochannels within the shell which allows the CO molecules to go through and interact with the inner magnetite. In conreast, the pore or nanochannel within the reduced INS show a bimodal distribution with two peak mesopores at ~ 10 nm and ~25 nm. Consequently, the gas molecule diffusion through its shell is enhanced.

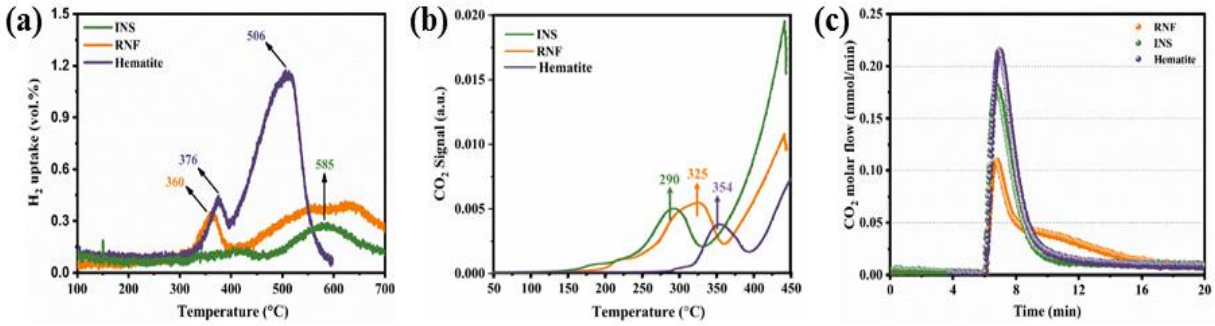


**Figure 6-4** (a) $H_2$-TPR profiles of INS, RNF and hematite, (b) CO-TPR profiles of INS, RNF and hematite, (c) Isothermal CO reduction at 400ºC of INS, RNF and hematite.

## 6.3.2 Surface property analysis by XPS and NEXAFS

Surface analysis by XPS and NEXAFS is conducted to confirm the enrichment and oxidation states of impurity $Al^{3+}$ and $Mg^{2+}$, as well as that of $Fe^{2+}/Fe^{3+}$ on the two spent catalyst surfaces. As these two instruments are only able to provide the information for an average depth of 5 nm, the information received is supposedly for the shell rather than the core of the two catalysts. **Figure S6-4** and **S6-5** show the XPS survey spectra of both the fresh and spent catalysts, which covers the signals detected from Mg, Al, Fe, O and C (ascribed to the carbon tape from the sample holder) whereas the other impurity elements in <0.2 *wt%* are still negligible. Additionally, the XPS spectra Mg 1s and Al 2p in **Figure 6-5(a)** and **(b)** confirmed a weak signal of these elements, in particular Mg on the fresh precursors. This is another sign of a uniform distribution of these impurities within hematite matrix, as has been suggested by the EXAFS fitting results in **Table S6-2**. The increase of the signal for these two elements on the spent catalyst surface is dramatic, which again is in support of the TEM observation in **Figure 6-2(a4)** and **(b4)**) for a preferential migration of Al and Mg to form a shell surrounding the magnetite core. For the fresh INS (i.e. f-INS), it bears an atomic ratio of 0.16 for Al/Fe and 0.05 for Mg/Fe, as shown in **Figure 6-5(c)** and **Table S6-3**. However, after the HT-WGSR, the Al/Fe and Mg/Fe ratios increased dramatically to 2.67 and 0.29, respectively. Likewise, for the

RNF precursor, the two ratios also demonstrate a dramatic rise from 0.11 to 2.42 for Al/Fe, and from 0.04 to 0.25 for Mg/Fe. Clearly, these two elements, in particular $Al^{3+}$ preferentially migrated to the outer surface, thereby creating a core-shell structure for the two catalysts. More importantly, in combination with the results in **Figure 6-2** and **Figure S6-2**, the results here further indicate that, the establishment of the core-shell should initiate from the breakage of the nanosheet and its macropores for each of the precursor during the thermal reduction process. Consequently, plenty of smaller nanoparticles of ~20 nm in diameter were formed. Afterwards, the outward migration of impurity elements was thermally induced, creating plenty of mesopores or nanochannels within the shell.

**Figure 6-5(d)** show the high-resolution XPS spectra for the Fe 2p region, which can be attributed to two spin-orbit doublet peaks at 710.8 eV and 724.5 eV for Fe $2p_{3/2}$ and Fe $2p_{1/2}$, respectively. The doublet is a characteristic of the peaks for $Fe^{2+}$ and $Fe^{3+}$ [42, 43]. Peak fitting confirmed an enrichment of $Fe^{2+}$ on the spent catalyst surface, accounting for 67.8% and 59.3% of the entire Fe for the INS and RNF precursor, respectively. Such a larger loss of the lattice oxygen around $Fe^{3+}$ should be due to the continuous exposure of the surface to the reducing gases. It also facilitated the creation of interstitial vacancy that in turn promoted the migration of impurity elements. In addition, both of them are much higher than the $Fe^{2+}$ on the surface of the spent hematite, as shown in **Figure S6-6**. Again, this is due to the easy agglomeration of the pure hematite particles (as shown in **Figure S6-7** for the spent hematite), which thus lost its contact area with the cases.

For the two spent catalysts, **Figure 6-5(e)** displays the Al 2p XPS spectra that are deconvoluted into two bands, 73.6 eV and 74.4eV featuring the characteristic positions for interfacially defective $AlO_x$ and well-oxidized $Al_2O_3$, respectively [44, 45]. Clearly, for both spent catalysts,

the former species is predominant, accounting for 74.9% of the entire surface Al on the s-INS catalyst, and 64.6% of Al on the surface of the s-RNF. Similarly, **Figure 6-5(f)** for the Al K-edge NEXAFS confirmed that the white line position of Al on the surface of the two spent catalysts is located around 1567.8 eV, falling between the tetrahedral $AlO_4$ (1566 eV) and octahedral $AlO_6$ (1568 eV) [46]. This confirmed the abundance of $AlO_x$ that shall play a role on the stabilization of $Fe^{2+}$ and even other impurity elements into a $MAlO_x$ solid state within the catalyst shell. With regards another key impurity element, Mg, its XPS K-edge spectra is too weak to be deconvoluted with a high accuracy. Alternatively, the Mg K-edge NEXAFS spectra in **Figure 6-5(g)** confirmed that the white line position in the two spent catalysts largely aligns with the standard MgO [47]. This indicates a close bonding of $Mg^{2+}$ with O on its first shell, which however could be further bound with $Fe^{3+}$ in a form of $Mg_xFe_{1-x}O_3$, as has been found for the impurity Ca within magnetite [25], or the formed MgO should be highly dispersed within the shell. Regardless, the presence of MgO within the shell is beneficial in creating the oxygen vacancy, as indicated by a slight left shift for the s-INS catalyst to a lower energy.

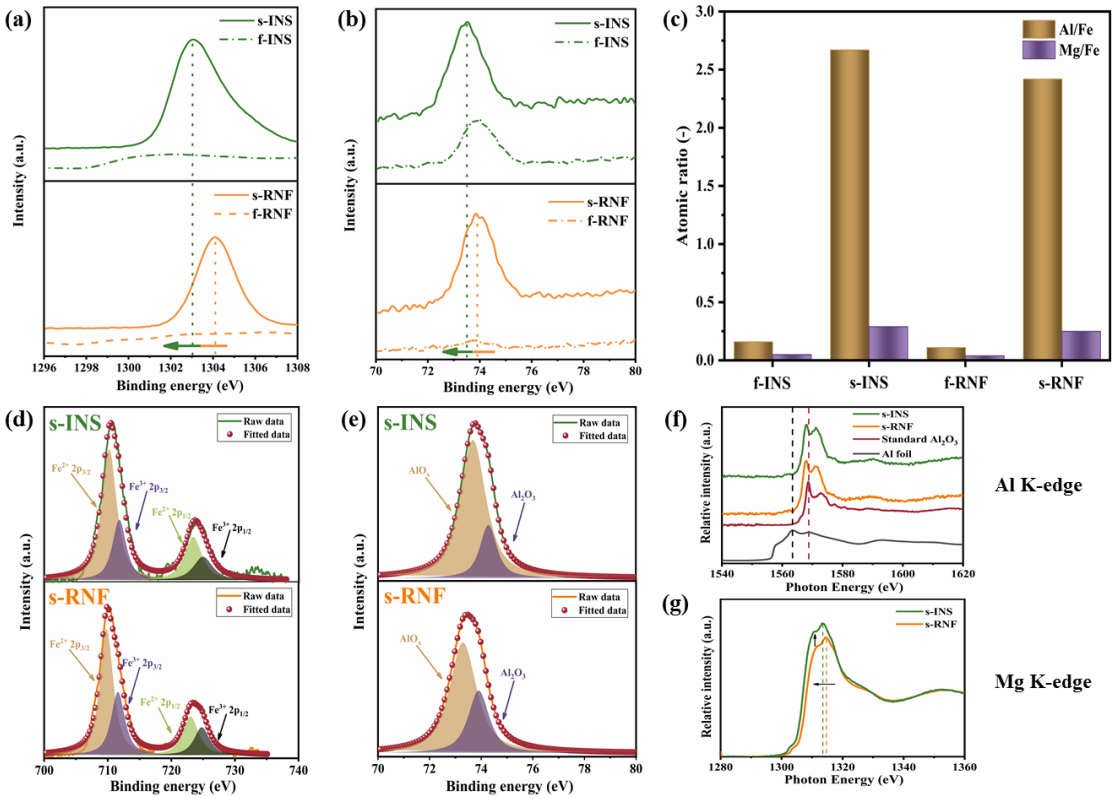


**Figure 6-5** High-resolution XPS spectra of Mg 1s (a) and Al 2p (b) of fresh and spent INS and RNF, (c) is the quantitative results of atomic ratio, (d) and (e) are high-resolution XPS spectra of Fe 2p and Al 2p, respectively, (The upper spectra are for s-INS and the lower spectra are for the s-RNF), (f) Al K-edge XANES spectra of s-INS, s-RNF, standard α-$Al_2O_3$ and Al foil, (g) Mg K-edge XANES spectra of s-INS and s-RNF.

## 6.3.3 HT-WGSR Catalytic Performance

**Figure 6-6(a)** and **(b)** display the CO conversion results for the two catalysts derived from fly ash at 400 and 450 °C, respectively. To reiterate, the precursors were calcined at 400°C and *in-situ* reduced in 4.5% CO at 400°C. Afterwards the HT-WGSR was either conducted at the same temperature or at 450°C. The waster-washed fly ash was also tested and showed negligible activity at 450°C in **Figure S6-8**. In contrast, at 400°C, the stabilized CO conversion for pure hematite, RNF and INS reached 3%, 8% and 19%, respectively, demonstrating a higher activity

of RNF and INS. Similarly, at 450ºC, the stabilized CO conversion reached 7% for pure hematite. In contrast, both fly ash derived catalysts exhibited considerably higher activity, with the CO conversion reaching 13% for the RNF and 26% for the INS catalyst. Upon the doubling of the INS amount, the CO conversion reached close to ~45%. Similar enhanced CO conversion results were also observed at 400ºC in **Figure 6-6(a)**. **Table S6-4** quantitatively compared the mass-based specific reaction rates for all the catalysts tested. For the best catalyst derived from the INS precursor, the specific reaction rate reached $489\times10^{-4}$ and $668\times10^{-4}$ $mol_{co}$ $g_{Fe2O3}^{-1}$ $h^{-1}$ at 400 ºC and 450°C, respectively. Both are dramatically higher than pure hematite. Additionally, **Figure 6-6(c)** demonstrates a strong durability of the best catalyst over a 10-hour time-on-stream (TOS) testing. More quantitatively, the deactivation rate constants were calculated based on a pseudo-first-order kinetics in **Figure 6-6(d)**. The deactivation rate constant for the best catalyst observed here only reaches 0.017 $h^{-1}$, which is far less than the value of 0.042 $h^{-1}$ determined for the pure hematite precursor.

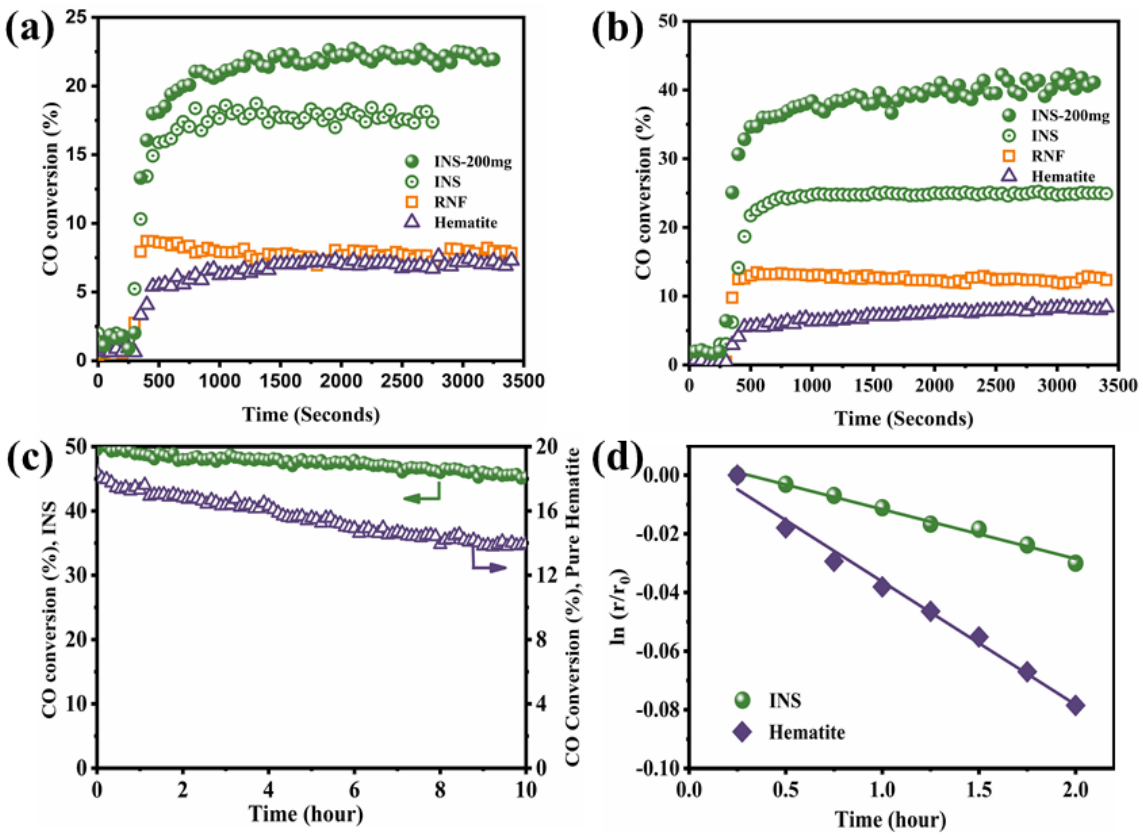


**Figure 6-6** (a) and (b) are CO conversion as a function of time-on-stream over INS, RNF and hematite at 400 and 450°C, respectively. 4.5% CO and 4.5% $H_2O$ balanced with He. (c) Stability test of INS and hematite at 450 °C. The GHSV is 120, 000 mL/($g_{Fe2O3}$·h). 4.5% CO and 4.5% $H_2O$ balanced with He. (d) pseudo-first order deactivation kinetics during initial reaction stage (T ≤ 2 h).

These catalyst performance results clearly substantiate the compositional and structural differences that have been confirmed between the two fly ash derivatives, as well as between them and pure hematite. More specifically, as the active phase of magnetite is exclusively identical and predominant for all the three catalysts, the unique core-shell structure formed for the two fly ash derivatives should be the principal factor accounting for their remarkable catalytic activity in **Figure 6-6**. In particular, the impurity element-bearing shell is responsive, which have effectively isolated the active magnetite particles and thus prevented their sintering

for a long-term testing. Moreover, the core-shell structure should also be responsive for the large specific surface area observed for the two catalysts derived from fly ash, 35.7-52.8 $m^2/g$ in **Table 6-1**. For comparison, the pure nanosized hematite synthesized under the same hydrothermal condition only carries a specific surface area of 14.3 $m^2/g$. This confirmed a strong role of the impurity elements, in particular the most abundant $Al^{3+}$ as a textual promoter providing a large interfacial surface area, and also isolating the active magnetite as individual nanoparticles for a higher activity. The content of $Al_2O_3$ within the two fly ash derivatives is also comparable with the optimum 10 *wt%* recommended for the addition into hematite [21]. However, the impurity elements should not merely function as a textual promoter, otherwise the RNF with a larger specific surface area (52.8 $m^2/g$) than INS (35.7 $m^2/g$) should bear a larger activity. Apparently, these impurity elements have also played a chemical role in altering the reaction pathway on the core-shell interface. In particular, the trace $Mg^{2+}$ distributed within the nano-shell shall be chemically highly active. Interestingly, its content is far less than that has been reported elsewhere, where MgO was used as a support loaded with maximum 30 *wt%* $Fe^{3+}$ [19].

*In-situ* DRIFTS and transient analysis of products at 400ºC were conducted to reveal the chemical roles of the impurities. Apart from the three catalysts mentioned here, another two were also examined, including pure Fe-Mg-O and Fe-Al-O nanosheets. The former catalyst was prepared by loading 30 *wt%* $Fe^{3+}$ on MgO nanosheet that was produced from the similar process [13], and the latter one was prepared by an initial co-precipitation of 10 *wt%* $Al_2O_3$ with hematite. The resultant precipitate was subsequently dried, calcined and treated by hydrothermal under the same conditions as for fly ash derivatives [26]. The *in-situ* CO-DRIFTS results for these two catalysts and pure hematite are displayed in **Figures S6-9—S6-11**. **Figure 6-7** depict a time-dependent change of the surface upon a continuous flow of 5% CO through

the two fly ash derivatives. For both catalysts, upon the introduction of CO to the surface, there is an intense negative peak at the high frequency wavenumbers (3600-4000 $cm^{-1}$) and up-shift of the overall baseline of the spectra, which can be attributed to the production of oxygen vacancies for the reduction of $Fe^{3+}$ to $Fe^{2+}$ [48]. Clearly, the lattice O within the catalyst can be abstracted quickly from the gaseous or adsorbed CO, in particular for the INS catalyst. Regarding the difference between the two fly ash derivatives, for the RNF, the peaks at 2181 and 2106 $cm^{-1}$ for the gas-phase CO [49, 50] are most intense. These two peaks appeared in the first two minutes and grew further stably in intensity. Simultaneously, another small peak located at 2305 $cm^{-1}$ for surface $CO_2$ also appeared in the first two minutes, which, however, gradually decayed in intensity. Clearly, this catalyst is capable of quickly adsorbing CO for the surface $Fe^{3+}$ reduction, whereas the resultant $CO_2$ product was also rapidly desorbed into the bulk gas. In comparison, the pure hematite in **Figure S6-9** showed a similar pattern with the appearance of aforementioned peaks for CO and $CO_2$. However, the peak intensities are much weaker. All the peaks only appeared in three minutes, and almost fully disappeared in five minutes. Clearly, due to a lack of the isolation measure from the impurity element-dominant shell, the pure hematite particles were sintered or agglomerated quickly, and hence, its surface adsorption capability was also lost quickly. This echoes the low activity and yet quick deactivation for pure hematite in **Figure 6-6**. In contrast, the strong and stable intensity for the gas-phase CO in **Figure 6-7(a)** confirmed a significant role of impurity elements on the adsorption of CO, as well as the reduction rate of hematite. Presumably, the enhanced CO adsorption should be attributed to an enlarged interface between magnetite and the shell, creating plenty of adsorptive sites that are just adjacent to the un-reduced $Fe^{3+}$ in bulk hematite. Subsequently, reduction of $Fe^{3+}$ took place instantaneously, and the generated $CO_2$ on the same site was quickly desorbed and diffused out through the mesopores/nanochannels within the shell. As there are no other intermediates detected, it is also inferable that the classic redox

mechanism shall apply to both pure hematite and the RNF catalyst. This agrees with the pure and $Al^{3+}$-doped hematite tested under the similar HT-WGSR conditions [21].

For the INS in **Figure 6-7(b)**, in addition to aforementioned gas-phase CO and $CO_2$ peaks, two extra peaks at 1457 and 1271 $cm^{-1}$ were also formed. In particular, the latter peak is the most intense and its intensity was increased stably over time. As these two peaks refer to the stretching vibration of formate [51], it is apparent that the associative mechanism also applies to the catalytic reaction pathway on this catalyst. That is, once being adsorbed on the catalyst interface, the adsorbed CO abstracted the lattice O from $Fe^{3+}$ to convert into an intermediate O-C-O vibration, rather than the $CO_2$ molecule. This shall not be attributed to $Al^{3+}$ which has an improved content in the INS precursor (see **Table 6-1**) than the RNF, as pure Fe-Al-O catalyst in **Figure S6-10** failed to show any formate signal. Alternatively, it can be assigned to the basic elements such as $Mg^{2+}$ and $Ca^{2+}$ that are able to anchor the intermediates on their Lewis acid sites, as has been confirmed in **Figure S11**. Clearly, if that is the case, the slightly higher content of MgO (*i.e.* 2.58 *wt%*) in the INS precursor should be partially responsive for the higher activity of this catalyst. However, to date, MgO was merely tested as a support (with $Fe_2O_3$ up to 30 *wt%*), whereas no study has examined such a low content of MgO as an impurity element within magnetite. In this sense, the majority (if not all) of MgO should migrate into and also atomically disperse within the shell with a thickness of 4-5 nm. The relatively large nanochannels within the shell also warranted a quick access of the gas molecules to the $Mg^{2+}$-centered active sites, and the formation of formate with a larger molecular size than $CO_2$.

The influence of other impurity elements within the two fly ash derivatives cannot be ruled out here. However, their concentrations are too low to be detected by any facilities used in this study. Moreover, the literature study on the role of these elements is also contradictory, as

summarised in **Table S6-1**. For $Ca^{2+}$, its presence with Fe-rich red mud was reported to promote the sintering of catalyst (thus decrease on the activity) [52], whereas another study on the synthesis of $CuO/MO_x$-$Fe_2O_3$ proposed a positive role of $Ca^{2+}$ on the formation of solid solution, which in turn promotes the redox activity of catalyst [53]. Regarding another impurity element Ti, it was merely tested as a support for the loading of $Fe^{3+}$. Due to its weak Lewis acidity, $TiO_2$ was confirmed to exert a less influential role than MgO on the activity of catalyst. Nevertheless, neither of the studies have examined these impurities with a content down to <0.2 *wt%* on catalyst. Presumably, due to the difference of their atomic radius to $Fe^{2+}/Fe^{3+}$, these impurities should also migrate preferentially towards the outer surface of magnetite, and hence, are atomically dispersed within the nano-scale shell promoting the redox and catalyst activity. Additionally, since all the impurities are inherently present within fly ash, a fine-tuning of the catalyst synthesis condition is clearly crucial in improving the catalyst performance. In other words, both the composition and structure of fly ash derived catalyst are highly tunable, as has been demonstrated by the two catalysts in this study. This is another advantage of using solid waste as precursor for the synthesis of magnesite-based catalysts. Nevertheless, extra works are still needed to elucidate the role of individual trace elements and further optimizing the catalyst performance, which are underway by us.

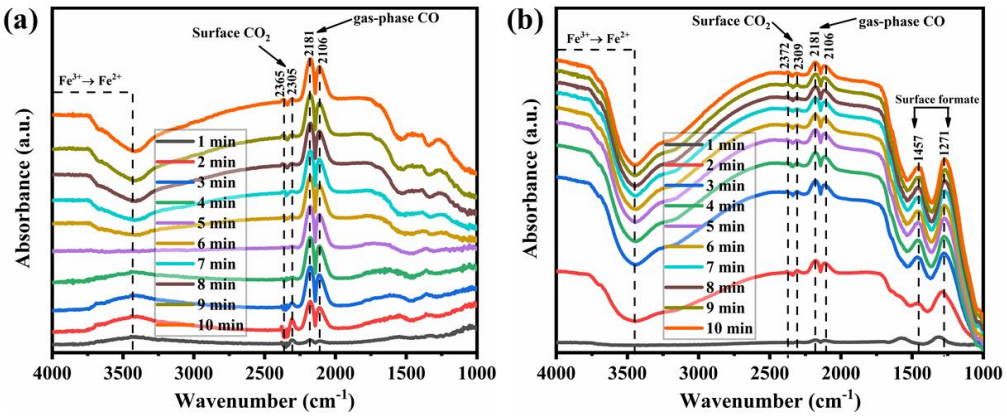


**Figure 6-7** *In-situ* DRIFTS of CO adsorption for (a) RNF and (b) INS

## 6.4 Conclusion

Synthesis of two magnetite-based catalysts with a core-shell structure and tunable composition was successfully achieved from brown coal fly ash, an industrial solid waste, and they were also applied in the HT-WGSR. The key conclusions achieved from this study can be draw as follows:

1) Through a leaching-precipitation-hydrothermal process, $Fe^{3+}$ was selectively extracted out as the principal element from solid fly ash. It was also accompanied by $Al^{3+}$, $Mg^{2+}$ and other trace cations (*e.g.* $Ca^{2+}$, $Ti^{4+}$ and $Mn^{2+}$) that are inherently present within fly ash matrix. Upon a subsequent reduction, the nanosheet-like $Fe^{3+}$ hydroxide precursor broke into smaller particles with a core in form of magnetite and a diameter of ~20 nm, whereas the impurity elements were activated to migrate to the outer surface forming a shell with a thickness in a few nanometres.

2) The elemental composition, porosity and thickness of the shell are highly tunable upon the addition of ethanol during the hydrothermal stage. Upon the addition of ethanol, a slightly higher content of $Al^{3+}$ (8.92 *wt%*) and $Mg^{2+}$ (2.58 *wt%*) were successfully embedded within the shell of the catalyst, which in turn increased the shell thickness by nearly twice, and created more nanochannels in mesopore scale within the shell.

3) Due to the protection of shell on the sintering, the two catalysts derived from fly ash exhibited higher activity, thermal stability and long-term durability for HT-WGSR at 400ºC and 450ºC. In particular, the catalyst synthesized with a thicker shell slightly more impurities exhibited the highest activity at a temperature. Compared to the pure hematite, the best activity increased the CO conversion by nearly four times and decreased the magnitude of the deactivation rate constant by four times too.

4) Apart from $Al^{3+}$ being a textual promoter enhancing the interfacial area of the

catalysts, the trace impurity elements, in particular 2.58 *wt%* $Mg^{2+}$ was confirmed to promote the redox rate of catalysts by improving the formation of formate, the adsorption rate of CO and the desorption of $CO_2$ molecules on the catalyst surface. These trace impurities are supposed to atomically disperse within the nano-scale shell, thereby creating extra active sites to interact strongly with the magnetite core.

# Supporting results

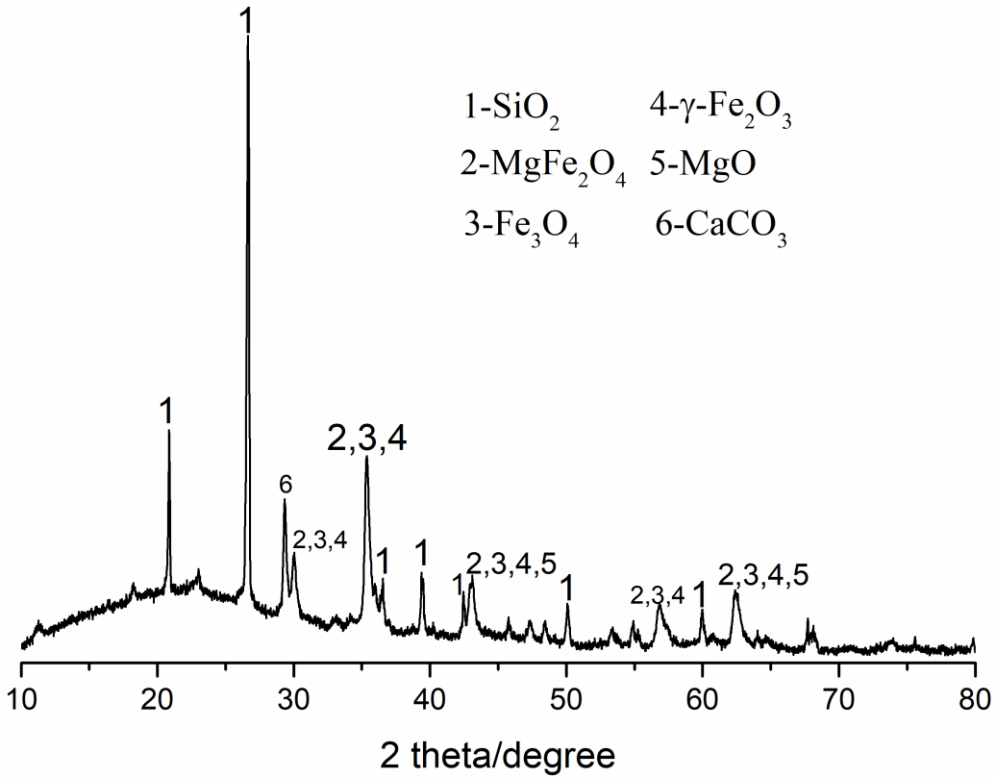


**Figure S6-1** XRD pattern for raw fly ash

CO conversion was calculated as Equation S(1):

$$\text{CO conversion} = \frac{\text{CO}_{\text{in}} - \text{CO}_{\text{out}}}{\text{CO}_{\text{in}}} \times 100\% \qquad \textbf{Equation S6-(1)}$$

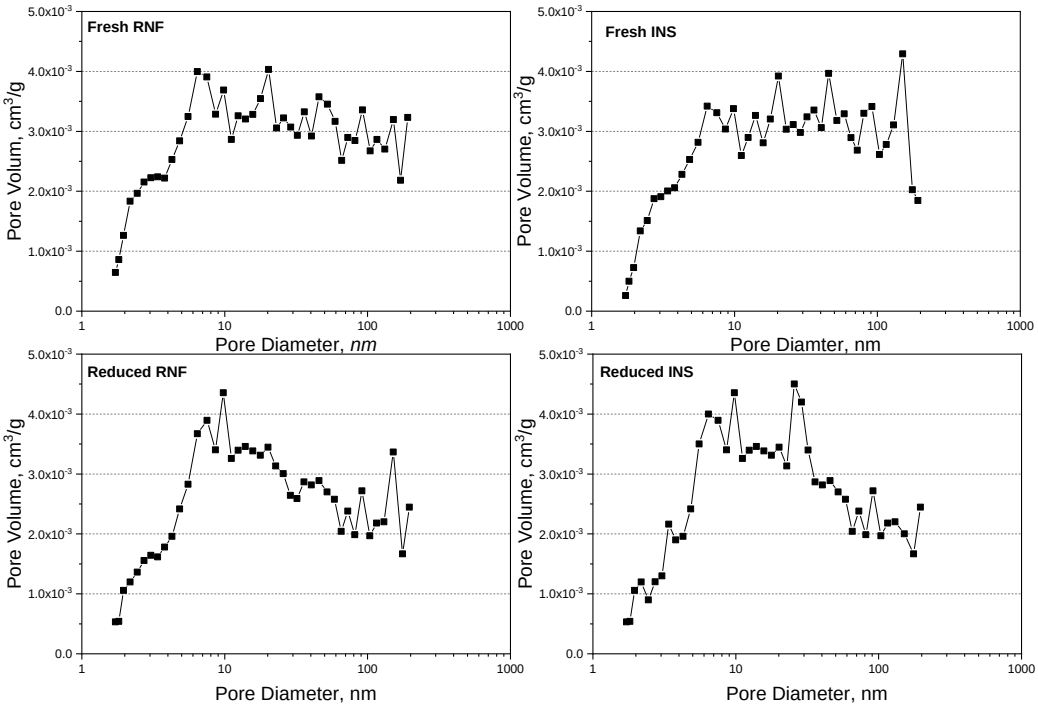


**Figure S6-2** Barrett-Joyner-Halenda (BJH) pore size and volume analysis.

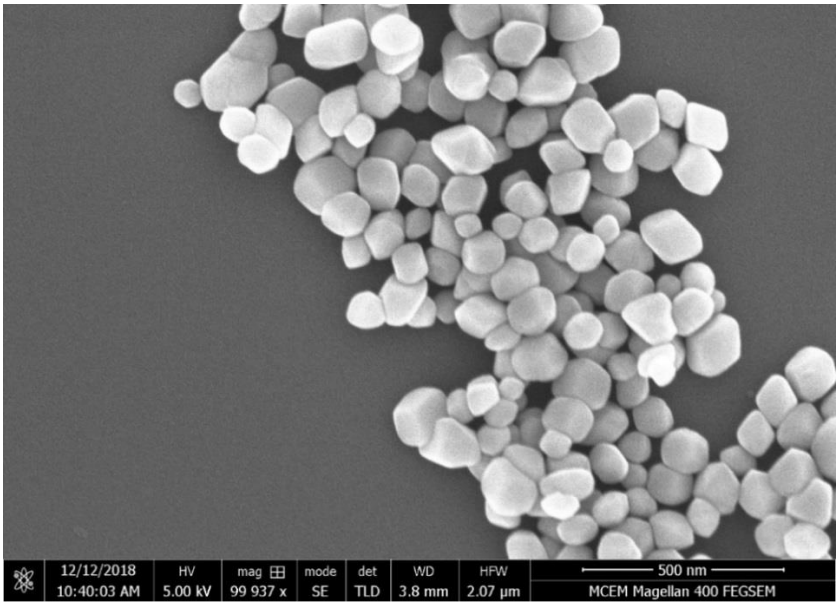


**Figure S6-3** SEM image of α-$Fe_2O_3$ nanoparticles synthesized from pure $FeCl_3$

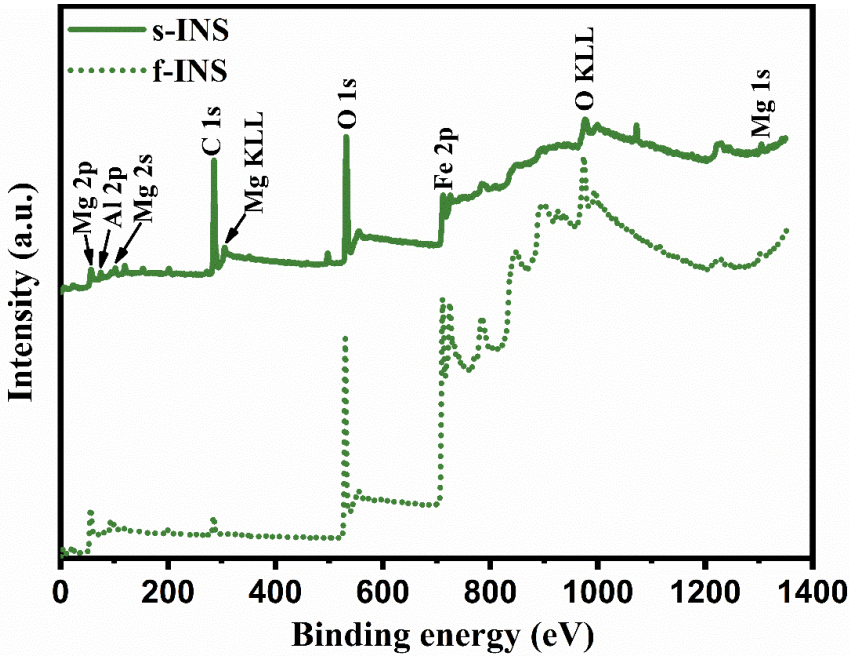


**Figure S6-4** XPS full survey scan spectra for of fresh and spent INS

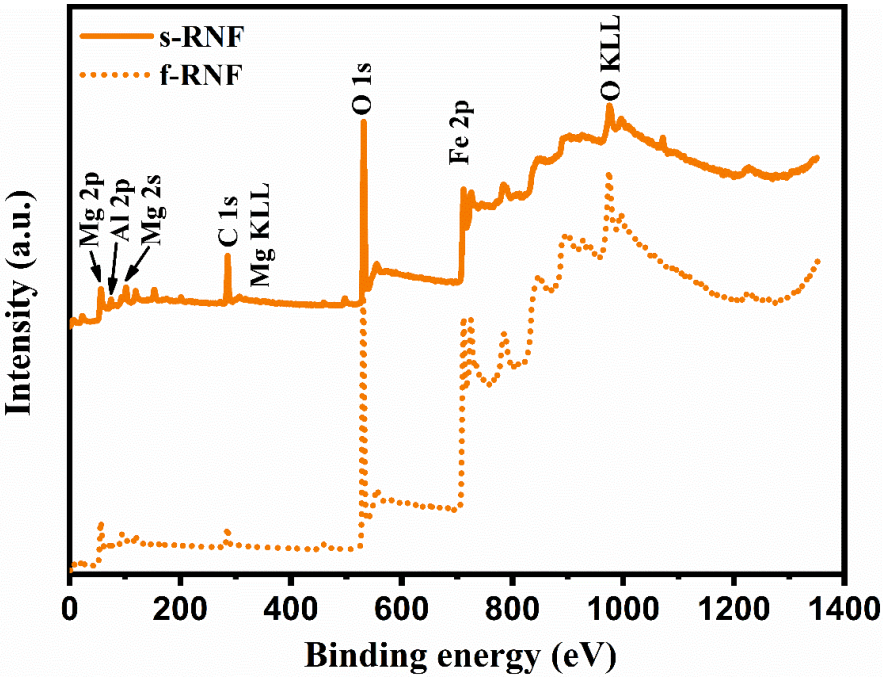


**Figure S6-5** XPS full survey scan spectra for of fresh and spent RNF

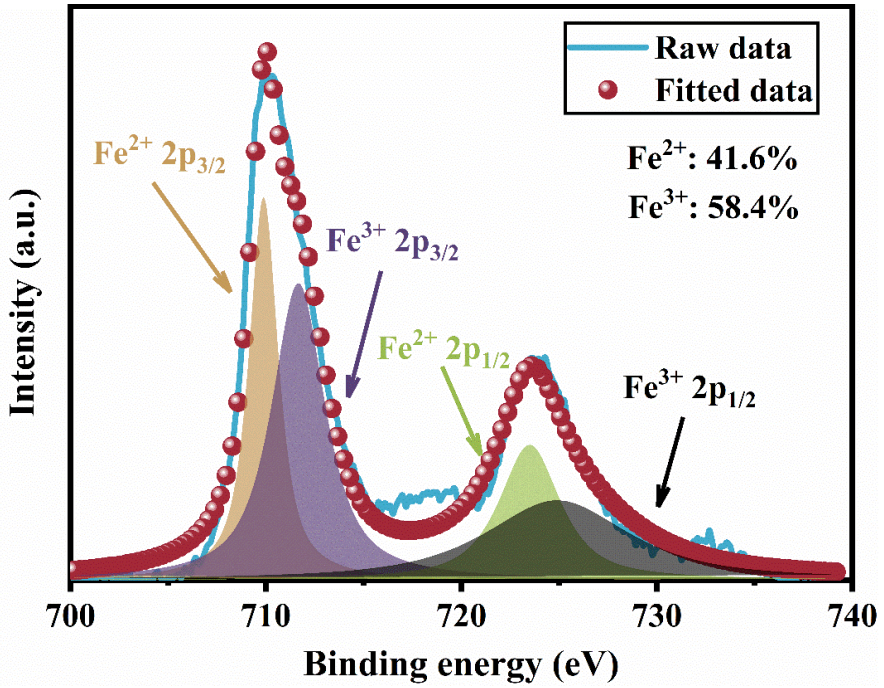


**Figure S6-6** High-resolution XPS Fe 2p spectra of spent hematite catalyst

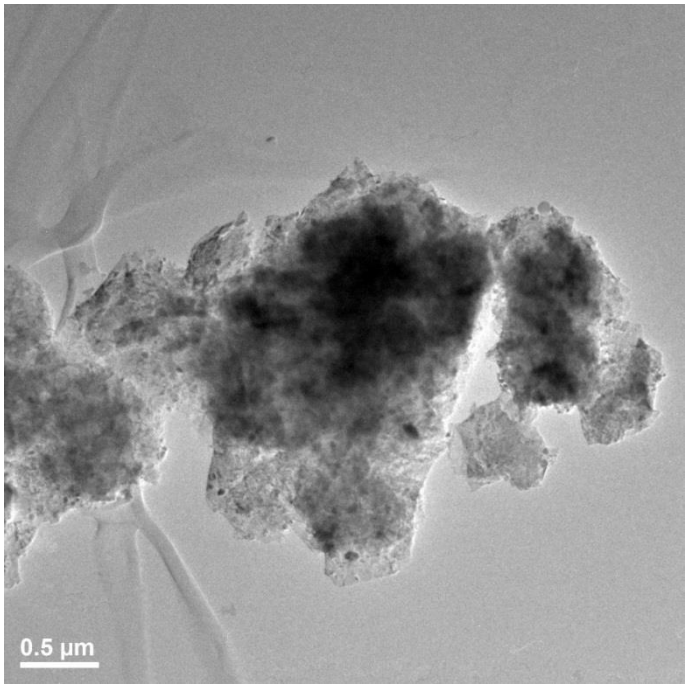


**Figure S6-7** TEM image for spent hematite catalyst

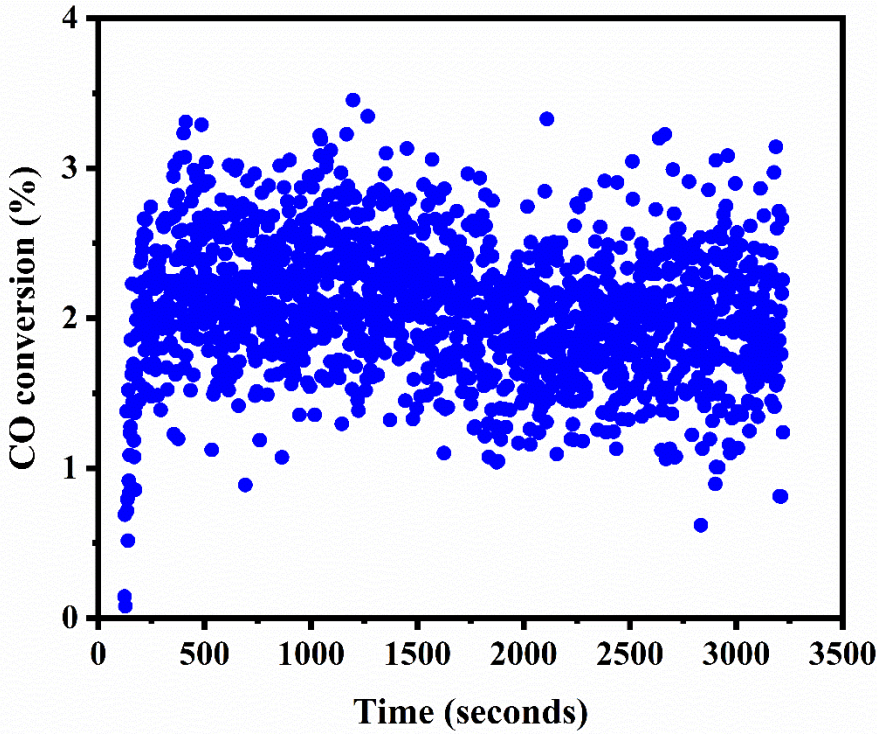


**Figure S6-8** CO conversion as a function of time-on-stream over raw fly ash at 450°C

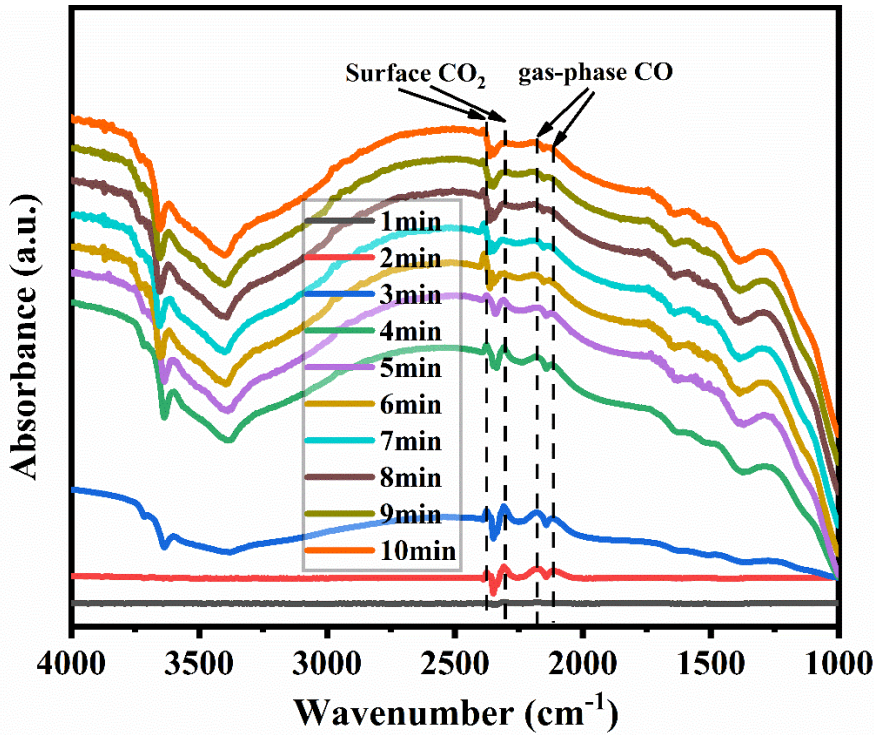


**Figure S6-9** *In-situ* DRIFTS of CO adsorption for pure hematite

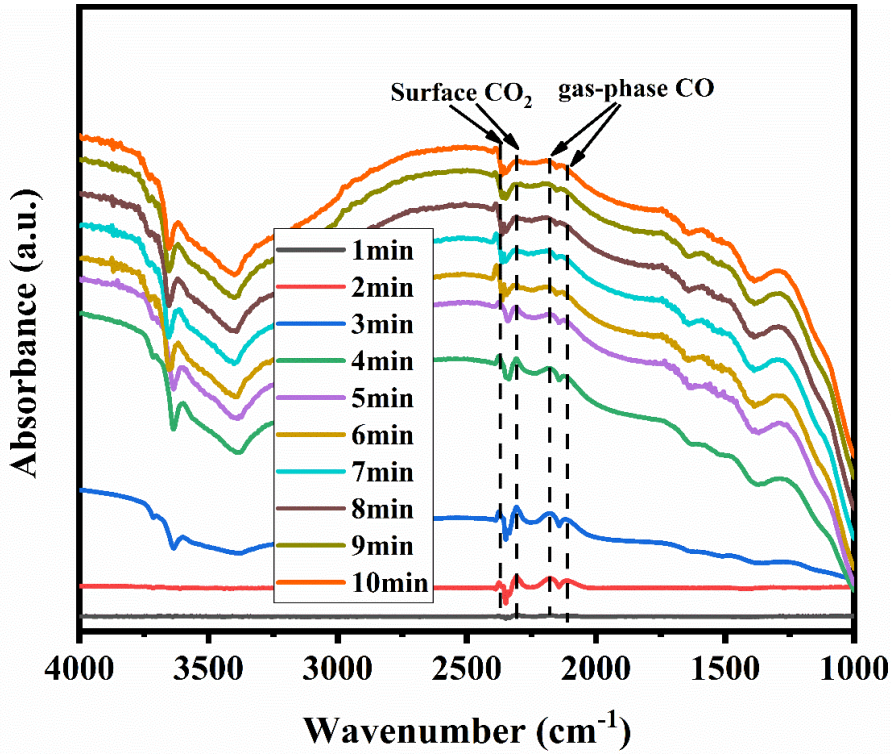


**Figure S6-10** *In-situ* DRIFTS of CO adsorption for Fe-Al-O

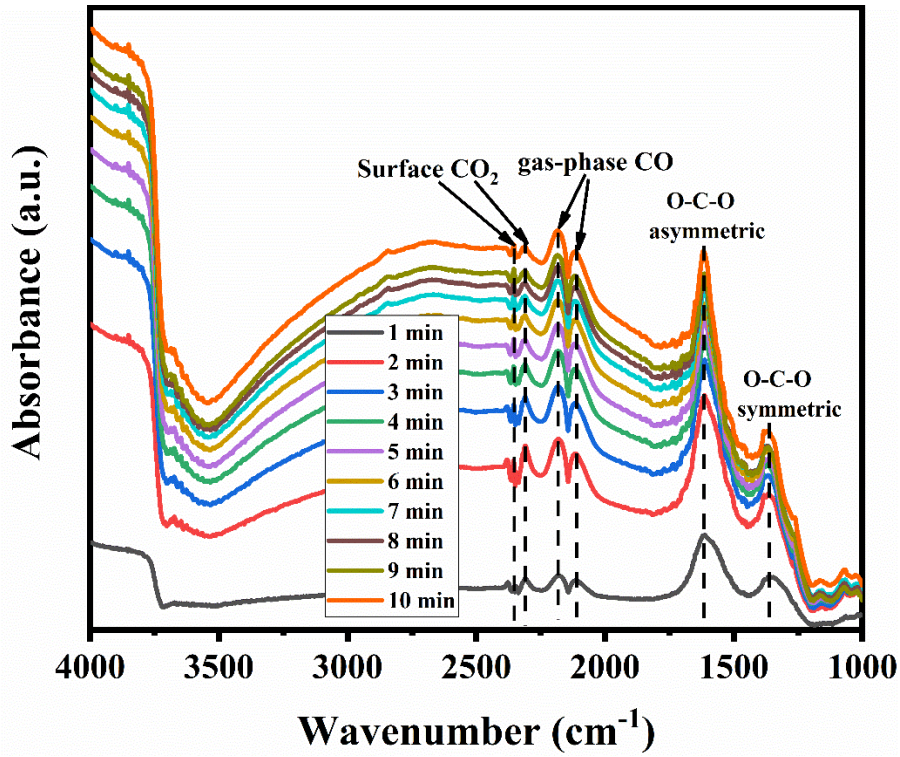


**Figure S6-11** *In-situ* DRIFTS of CO adsorption for Fe-Mg-O

**Table S6-1** Summary of synthesized Cr-free Fe-based catalysts for WGSR

| Catalyst | Catalyst Synthesis method | Operating Conditions | Activation and WGSR conditions | Characterisation Techniques used | Findings and limitations | Ref. |
|---|---|---|---|---|---|---|
| **Fe-Gd** | Sol-gel | Samples analysed: Gd/Fe molar ratio = 0.05, 0.1 and 0.15.<br>Pressure = 1atm<br>Final pH = 11<br>Calcination at 800°C | Pressure = 1atm<br>T = 250-400°C<br>Steam rate = 135mL/min<br>Steam to process gas ratio = 0.6 (3.7% CO, 3.7% $CO_2$, 22.2% $H_2$, 70.4% $N_2$) (steam/CO molar ratio 16:1) | Thermogravimetry, DRIFTS, XRD, specific surface area measurements, MES, TPR | -Gd made $Fe^{3+}$ and $Fe^{2+}$ reduction more difficult and produced minor quantities of iron carbides during WGSR (increase activity)<br>-Gd/Fe (molar ratio) = 0.1 had highest activity due to greater SA.<br>-Conflict with production of iron carbides compared to previous work done, SA is also comparatively lower (due to high calcination temp)<br>-Gd acts as textual promoter/spacer | [54] |
| **Fe-V** | Coprecipitation | Two vanadium-doped samples analysed with V/Fe molar ratio = 0.03 and 0.1. Calcination at | Pressure = 1atm<br>T = 370°C<br>Steam to process gas ratio of 0.2 and 0.6 (10% CO, | XRD, DRIFTS, TPR, XPS, High resolution TEM, MES, specific surface area | -Vanadium found on the surface of magnetite structure where there was a higher surface area and higher activity.<br>-Proved to be more active and structure stable under S/G=0.6. It also assisted in the redox mechanism during the | [55] |

| | | | | | | |
|---|---|---|---|---|---|---|
| | | 400°C.<br>Final pH = 10<br>Ammonium metavanadate and iron nitrate were used as precursors | 10% $CO_2$, 60% $H_2$, 20% $N_2$)<br>Duration: 6h | measurements | reaction, preventing over-reduction and sintering of catalyst.<br>-V acts as primarily as structural promoter | |
| **Fe-Co** | Coprecipitation | Samples analysed: Co/Fe (molar ratio) = 0.05 and 1.0. Final pH = 11.<br>Calcination at 500°C | Pretreatment: heated up at a rate of 10°C/min to 160°C (nitrogen flow)<br>Reduced from 30-1000°C using 5% $H_2/N_2$ gas mixture<br>WGSR: T= 370°C<br>P= 1 atm<br>Steam to process gas ratio of 0.6 (10% CO, 10% $CO_2$, 60% $H_2$, 20% $N_2$) | Specific surface area measurements, XRD, TPR, XPS, DRIFTS | -Potential to work under low steam conditions (minimise cost)<br>-Cobalt ferrite and $Co_3Fe_7$ alloys are produced, active sites depended on Co content<br>-Co acts as textual promoter (increase in SA: Co>$Fe_2O_3$) | [56] |

| | | | | | | |
|---|---|---|---|---|---|---|
| **Fe-Th-Cu** | Coprecipitation | Fe/Th, Cu (molar ratio) = 10.<br>Final pH = 11.<br>Calcination at 500°C | <u>WGSR:</u><br>T= 370°C<br>P= 1 atm<br>Steam to process gas ratio of 0.6 (10% CO, 10% $CO_2$, 50% $H_2$, 30% $N_2$) | BET, XRD, TPR, MES | -Can be prepared in the active phase/magnetite found in fresh catalyst<br>-Cu (structural promoter) found to increase metallic iron production whilst Th prevents this at high temperature ranges.<br>-Magnetite activity is higher with the presence of both Th-Cu due to increased surface area (resulted from surface inter-particle repulsion effects)<br>-Limitation: Th alone found to damage some active sites | [57] |
| **Fe-Al-Cu** | 2 step Coprecipitation - impregnation | Fe/Al (molar ratio) = 10<br>Fe/Cu (molar ratio) = 20<br>Final pH = 11.<br>Calcination at 500°C | <u>WGSR:</u><br>T= 350°C, 370°C and 400°C<br>P= 1 atm<br>Steam to process gas ratio of 0.2, 0.4 and 0.6 (10% CO, 10% $CO_2$, 60% $H_2$, 20% $N_2$) | XRD, Specific surface area measurements, TPR, XRM | -Proved to be efficient under conditions of lower S/G molar ratio of 0.4 and temperature of 350°C<br>-Cu acts like a structural promoter whilst Al acts as a textual promoter/spacer<br>-Solids with 8%+ Cu content favours sinterization of Fe-based catalysts<br>-Similarity in ionic radius sizing of Al, Cu and Fe allowed for the dopants to enter into the magnetite lattice | [20] |

| | | | | | | |
|---|---|---|---|---|---|---|
| | | | | | -Patterns detected extend to how aluminium caused strain in the lattice structure which directly affects catalyst surface area | |
| **Fe-Al-Ce** | Wet precipitation | Fe/Al/Ce (molar ratio) = 1:0.04,0.2) | <u>Pre-treatment condition:</u><br>Reduced at T = 530°C, 3000$h^{-1}$ for 15h<br>Gas mixture: (26% CO, 8% $CO_2$, 40% $H_2$, 26% $N_2$)<br><br><u>WGSR:</u><br>P = 1atm<br>T= 350°C, 3000$h^{-1}$ (dry-gas basis)<br>Same feed process gas mixture used as activation | BET, XRD, MES, TPD, TPR (surface) | -A redox regenerative mechanism pathway is proposed based of TPD and TPSR results<br>-Active and thermo-stable catalyst for HT-WGS<br>-Idealised magnetite structure that is comparable to commercial catalyst was observed after reduction and reaction<br>-Al and Ce precursors found to be distributed evenly through fresh and spent catalysts | [58] |

| | | | | | | |
|---|---|---|---|---|---|---|
| **Fe-Al-Cu (with Ba, Ca, Mg, Sr and Mn)** | Coprecipitation | Final pH = 10<br>Calcination temperature = 400°C | <u>Pre-treatment conditions:</u><br>T= 400°C<br>Steam to dry gas ratio of 0.6 (30% CO, 10% $CO_2$, 60% $H_2$)<br>Duration of 2h<br><u>WGSR:</u><br>T= 300-500°C<br>(increments of 50°C)<br>Process gas mixture of 30% CO, 10% $CO_2$, 60% $H_2$ | XRD, BET, TPR, TEM | -Cu allows for decreases temperature for reduction reaction<br>-Fe/Al = 10 and Fe/Cu = 5 (wt ratio) show optimal activity<br>-9*wt%* Ba promoted Fe-Al-Cu catalyst is experimentally a suitable replacement as it has the highest BET area and recorded activity. Any higher and SA and activity would decrease.<br>-These promoters didn't have a recognisable effect on reducibility of Fe-Al-Cu catalyst<br>-Ba addition resulted in suppression of methanation (side reaction to WGSR) | [20] |
| **Fe-Ni-Cu** | 2 step Coprecipitation-Impregnation | Final pH = 10.5<br>Calcination temperature = 400°C<br>$Fe_2O_3$ support was prepared by precipitation and then wet | <u>Pre-treatment conditions:</u><br>Reduced in 2% $H_2/N_2$<br>T= 400°C (from heating rate of 4.6°C/min)<br><u>WGSR:</u><br>T= 350-550°C | XPS, XRD, BET, TPR | -High catalytic activity detected due to lattice strain increase and binding energy of lattice oxygen decrease<br>-Highest CO conversion occurring at $X_{CO}$ = 85%, 400°C<br>-Surface CuNi alloy formation sighted which increased CO adsorption | [59] |

| | | | | | | |
|---|---|---|---|---|---|---|
| | | impregnation methods were employed with nitrate precursors of Ni and Cu. $CuNi/Fe_2O_3$ (*wt%* ratio) = 1:1 | P = 1atm<br>Feed: Steam to process gas ratio of 2.0 (38% CO, 21.33% $CO_2$, 2.3% $CH_4$, 29.3% $H_2$, and 9.07% $N_2$) | | -Strong chemical interactions between Ni and Cu resulted in reducing major side reaction (methanation), however further in-situ characterisation needs to be done in detail<br>-Limitation: Ni alone favours undesirable methanation, which reduces WGS selectivity | |
| **Fe-MgO**<br>**Fe-$TiO_2$**<br>**(<u>support</u>)** | Co-precipitation<br>Impregnation | Hematite catalyst was first synthesized by co precipitation<br>Calcination at 400°C | <u>Pre-treatment conditions:</u><br>Activated in situ with 48% $H_2/N_2$<br>T= 350-450°C<br><u>WGSR:</u><br>T= 350-450°C<br>P= 1atm<br>$H_2O$/CO (molar ratio) = 4.4<br>Flow rate of 33mL/min | BET, XRD, TPR, TG | -When large quantities of $H_2O$ was present, MgO support (basic) prevented sintering in iron phase<br>-Spinel oxide phase ($MgFe_2O_4$) assist in increased stability<br>-An associative mechanism pathway is proposed<br>-Mg-rich catalysts are comparatively more active than commercial catalysts<br>-$TiO_2$ support found to be less active than MgO<br>-Good example to establish a relationship between acid-base properties of catalysts and activity where MgO>$TiO_2$<br>-XRD found Fe(3+) phase in the hematite for $TiO_2$ supported catalyst | [60] |

| | | | | | | |
|---|---|---|---|---|---|---|
| | | | | | -$TiO_2$ is not as effective as MgO – $CO_2$ adsorption (relative to basicity) and basic surface site strength is comparatively lower for $TiO_2$ | |
| **B, Cu, Ba, Pb, Hg, Ag promoted Fe-Cr** | Co-precipitation | Promoted catalysts: 91.5% iron oxide, 6.5%chromium oxide and 2 % promoter Unpromoted $Fe_3O_4/Cr_2O_3$ catalyst: 92.5% iron oxide and 7.5% chromium oxide Calcination at 300°C | <u>Pre-treatment conditions:</u> Reduction in situ 400°C 2 bar pressure Dry gas composition: $H_2$ (50 vol%), CO (12 vol%), $CO_2$ (8vol%) and $N_2$(30vol%) Steam was added (55 vol%) to give a R-factor of 1.0 <u>WGSR:</u> 350–440°C 400psi Dry gas composition: 50 vol% $H_2$, CO 12.5 vol%, | N/A | -B poisons activity slightly -Relative improvement to HT-WGS activity (within the investigated temperature range 350-440°C) is in the order: Hg > Ag; Ba > Cu > Pb > unpromoted > B -Beneficial effects of Hg, Ag or Ba dopants were ascribed to the differences between their ionic sizes and that of Fe, which allows the additives to influence the electronic nature of the active $Fe^{3+}$ cation. -WGS reaction was found to be first order in CO, zero order in $H_2O$ (for both the unpromoted and Cu-promoted Fe/Cr catalysts). This suggests that adsorption of CO is an important factor in the overall energetics of the process. | [61] |

| | | | | | | |
|---|---|---|---|---|---|---|
| | | | $N_2$ 37.5 vol%<br>Gas hourly space velocity GHSV = 1.2 x $10^6$ ml gas/ml catalyst/h.<br>Steam volume = 75 vol% of the dry gas<br>0.1g catalyst | | | |
| **Fe-Cr-CuO** | Ammonia assisted co-precipitation method | Calcination at 400°C, in static air, for 3 h<br>Weight ratio = 3 wt % CuO, 8 wt % $Cr_2O_3$, and 89 wt % $Fe_2O_3$ | <u>Pre-treatment conditions:</u><br>$CO_2$:$H_2$ = 1:1<br>1 hour OR CO:$H_2O$ = 1:1<br>at 350°C | XRD, in situ Raman, NAP-XPS (near ambient pressure), HS-LEIS (high sensitivity low energy ion scattering spectroscopy), XAS, TPR | -Presence of metallic copper nanoparticles allows Cu to act as a chemical promoter for the HT-WGS reaction<br>-Cr only acts as a structural stabilizer; disproves contribution of $Cr^{6+}$ and $Cr^{3+}$ valence states towards the HT-WGS redox cycle | [62] |
| **Promoters M = Cr, Ca, Co, Ni,** | 2 step Co-precipitation-impregnation | Final pH = 8.5<br>Calcination at 400°C, under static air, | <u>Pre-treatment conditions:</u><br>T = 400°C 90 mins<br>10 mL/min 10% CO/Ar | BET, HS-LEIS, CO-TPR and CO+$H_2O$ TPSR, SS-WGS | -The study related the addition of promoters, to the formation of $FeO_x$-Cu interfacial sites, and the catalyst's | [53] |

| | | | | | | |
|---|---|---|---|---|---|---|
| **Ge in CuO/MOx-$Fe_2O_3$ catalysts** | | for 4 h | 30 mL/min He<br>$H_2O/CO$~1<br>WGSR:<br>10 mL/min 10% CO/Ar and 30 mL/min He<br>T = 450°C (10°C/min ramp rate) | Activity | redox ability, suggesting $FeO_x$-Cu interfacial areas serve as the active sites for promoted Fe-Cu WGS catalysts.<br>-Ca and Ni were identified as suitable substitutes to Cr (improved catalytic performance relative to the Cr counterpart).<br>-Promotion by Ca, Ni and Cr allowed highly active $FeO_x$-Cu interfacial redox areas (thin $FeO_x$ oxide overlayers on the CuO nanoparticles) to form, enhancing the redox ability of the respective catalysts.<br>-Conversely, Co and Ge promoted catalysts exhibited poorer performance in the WGS reaction (potentially due to the lack of active $FeO_x$-Cu interfacial sites formed)<br>- This also diminished the catalysts' ability to participate in redox reactions.<br>- Co inability to stabilize the iron oxide surface area against sintering likely also contributed to the low WGS activity. | |

| | | | | | | |
|---|---|---|---|---|---|---|
| | | | | | - Other related findings include the ability for Cr, Ni and Ca promoters to form solid solutions with $Fe_3O_4$, and the tendency for Ge to segregate on the surface. | |
| **Fe-Al, Fe-Mn, Fe-Ga**<br><br>**Fe-Al-Co, Fe-Al-Zn, Fe-Al-Cu** | One-step coprecipitation (Fe-Al, Fe-Mn, Fe-Ga, and Fe-Al-Cu catalysts)<br>Two-step coprecipitation-impregnation (Fe-Al-Cu catalysts) | Fe-Al, Fe-Mn, Fe-Ga<br>Molar ratio = (Fe/textural promoter=10:1)<br><br>Fe-Al-Co, Fe-Al-Zn, Fe-Al-Cu<br>Molar ratio = (Fe/structural promoter = 20:1)<br>Final pH level = 9<br>Calcination at 450°C, under air (ramp rate = 2.5°C /min) for 4h | <u>Pre-treatment conditions:</u><br>Reduction in situ under 20% $H_2/N_2$ at 50 cm3 (STP)/min 350°C<br>2 hours<br><u>WGSR:</u><br>250-450°C; mostly 400°C<br>$CO/H_2O/N_2$ = 1/1/8 ($CO/H_2O$ ratio matches that in coal-derived syngas)<br>Feed flow rate = 100 $cm^3$ (STP)/min | BET, XRD, XPS, DRIFTS, TPR | -Al is a promising replacement for Cr as a textural promoter, retarding reduction of magnetite to FeO/Fe and improving sintering resistance<br>-TPR studies showed shift of the magnetite-to-FeO/Fe reduction feature to higher temperatures<br>-In situ XRD studies during reduction identified the presence of smaller hematite crystallite sizes compared to Fe-only catalysts<br><br>-Fe-Al-Zn did not offer higher catalytic activity, compared to Fe-Al<br>-Addition of Co and Cu as structural promoters to Fe-Al both increased CO conversion | [52] |

| | | | | | | |
|---|---|---|---|---|---|---|
| | | | | | -Fe-Al-Cu exhibited high stability and activity<br>-Promotional effect of Cu was dependent on catalyst preparation method<br>-XPS and TPR found Cu to be enriched on the iron oxide surface. (2-step) These Cu species subsequently became reduced to metallic Cu, therein providing additional active sites. High activity was observed at low temperatures, but high temperatures resulted in sintering of metallic Cu, leading to decay of the Cu promotional effect and a loss of WGS activity<br>-Incorporated within the lattice, Cu acts as an electronic promoter. (1-step method) The spacer function of iron oxide meant that the bulk Cu was less prone to severe sintering, compared to surface Cu. Some surface Cu still became reduced to metallic Cu, providing additional active sites to enhance activity.<br>-Major proportion of Cu precipitated with Al and Fe into a solid solution when prepared with 1-step method | |

| | | | | | | |
|---|---|---|---|---|---|---|
| **Red Mud** | - | - | - | - | Literature finding summary:<br>-Contains Fe, Al, Cl, Ti, Ca, Si, Na, S elements/impurities<br>-Similarities between TPR studies on red mud and hematite was observed (peak at 400°C)<br>-Na and Ca impurities play a role in sintering promotion (decrease in catalytic activity)<br>-Enhancement of catalytic activity is driven by Fe and Ti content | [21] |

**Table S6-2** Structural parameters calculated from EXAFS analysis.

| Samples | Shell | N | R/Å | $\delta^2$/Å$^{-2}$ | R factor |
|---|---|---|---|---|---|
| Hematite | Fe-$O_{oct}$ | 5.9(3) | 2.08(2) | 0.0063 | 0.027 |
| | $FeO_{oct}$-$FeO_{oct}$ | 3.8(4) | 2.93(11) | 0.0055 | |
| f-RNF | Fe-$O_{oct}$ | 4.5(2) | 1.94(23) | 0.0122 | 0.045 |
| | $FeO_{oct}$-$FeO_{oct}$ | 4.1(5) | 2.89(12) | 0.0084 | |
| f-INS | Fe-$O_{oct}$ | 4.2(3) | 2.01(15) | 0.0133 | 0.033 |
| | $FeO_{oct}$-$FeO_{oct}$ | 3.9(2) | 2.95(9) | 0.0028 | |
| Standard α-$Fe_3O_4$ | Fe-$O_{tet}$ | 3.8(2) | 1.87(3) | 0.0035 | 0.012 |
| | Fe-$O_{oct}$ | 6.1(1) | 2.04(2) | 0.0019 | |
| | $FeO_{oct}$-$FeO_{oct}$ | 5.9(2) | 2.97(2) | 0.0092 | |
| | $FeO_{oct}$-$FeO_{tet}$ | 4.2(1) | 3.48(3) | 0.0094 | |
| s-Hematite | Fe-$O_{tet}$ | 3.9(3) | 1.86(1) | 0.0138 | 0.035 |
| | Fe-$O_{oct}$ | 6.1(3) | 2.02(4) | 0.0127 | |
| | $FeO_{oct}$-$FeO_{oct}$ | 5.8(2) | 2.96(1) | 0.0044 | |
| | $FeO_{oct}$-$FeO_{tet}$ | 3.9(1) | 3.50(6) | 0.0146 | |
| s-RNF | Fe-$O_{tet}$ | 3.5(2) | 1.69(4) | 0.0066 | 0.029 |
| | Fe-$O_{oct}$ | 5.3(4) | 1.91(5) | 0.0083 | |
| | $FeO_{oct}$-$FeO_{oct}$ | 5.5(3) | 2.83(2) | 0.0123 | |
| | $FeO_{oct}$-$FeO_{tet}$ | 3.9(3) | 3.45(1) | 0.0072 | |

| | | | | | |
|---|---|---|---|---|---|
| s-INS | $Fe\text{-}O_{com}$ | 5.1(6) | 2.01(6) | 0.0049 | 0.018 |
| | $FeO_{oct}\text{-}FeO_{oct}$ | 5.2(2) | 2.94(1) | 0.0098 | |
| | $FeO_{oct}\text{-}FeO_{tet}$ | 3.3(2) | 3.44(5) | 0.0107 | |

**Table S6-3** quantitative analysis of tested elements

| | | Fe | Al | Mg | O |
|---|---|---|---|---|---|
| INS | Fresh | 32.7 | 5.3 | 1.8 | 60.2 |
| | Spent | 11.5 | 30.7 | 3.4 | 54.4 |
| RNF | Fresh | 34.1 | 3.5 | 1.3 | 61.1 |
| | Spent | 10.3 | 24.9 | 2.6 | 62.2 |

**Table S6-4** Comparison of CO conversion and specific rates of as-synthesized catalysts

| Catalyst | Space velocity ($m^3\ g_{Fe2O3}^{-1}\ h^{-1}$) | Specific Surface area ($m^2\ g^{-1}$) | Temperature (°C) | CO Conversion (%) | Specific rate$^{\nabla}$ ($10^4\ mol_{CO}\ g_{Fe2O3}^{-1}\ h^{-1}$) |
|---|---|---|---|---|---|
| INS | 0.23 | 35.7 | 400 | 19.2 | 489 |
| | | | 450 | 26.7 | 668 |

| | | | | | |
|---|---|---|---|---|---|
| RNF | | 52.8 | 400 | 8.1 | 205 |
| | | | 450 | 13.2 | 330 |
| Hematite | | 14.3 | 400 | 3.5 | 83.64 |
| | | | 450 | 7.1 | 171.15 |

$^{\nabla}$: Specific reaction rate was determined by normalizing the respective amount (mol/h) of CO converted with the mass (g) of $Fe_2O_3$ for the respective catalyst.

# References

[1] Hao, P.; Xie, M.; Chen, S.; Li, M.; Bi, F.; Zhang, Y.; Lin, M.; Guo, X.; Ding, W.; Guo, X. Surrounded catalysts prepared by ion-exchange inverse loading. *Science Advances* **2020**, *6*, eaay7031.

[2] Tauster, S. J.; Fung, S. C.; Garten, R. L. Strong metal-support interactions. Group 8 noble metals supported on titanium dioxide. *Journal of the American Chemical Society* **1978**, *100*, 170-175.

[3] Das, S.; Pérez-Ramírez, J.; Gong, J.; Dewangan, N.; Hidajat, K.; Gates, B. C.; Kawi, S. Core–shell structured catalysts for thermocatalytic, photocatalytic, and electrocatalytic conversion of $CO_2$. *Chemical Society Reviews* **2020**, *49*, 2937-3004.

[4] Ye, K.; Zhou, Z.; Shao, J.; Lin, L.; Gao, D.; Ta, N.; Si, R.; Wang, G.; Bao, X. In Situ Reconstruction of a Hierarchical Sn-Cu/$SnO_x$ Core/Shell Catalyst for High-Performance $CO_2$ Electroreduction. *Angewandte Chemie International Edition* **2020**, *59*, 4814-4821.

[5] Song, S.; Liu, X.; Li, J.; Pan, J.; Wang, F.; Xing, Y.; Wang, X.; Liu, X.; Zhang, H. Confining the Nucleation of Pt to In Situ Form (Pt-Enriched Cage)@$CeO_2$ Core@Shell Nanostructure as Excellent Catalysts for Hydrogenation Reactions. *Advanced Materials* **2017**, *29*, 1700495.

[6] Zhu, Y.; Zhang, X.; Koh, K.; Kovarik, L.; Fulton, J. L.; Rosso, K. M.; Gutiérrez, O. Y. Inverse iron oxide/metal catalysts from galvanic replacement. *Nature*

*Communications* **2020**, *11*, 3269.

[7] Beltram, A.; Melchionna, M.; Montini, T.; Nasi, L.; Gorte, R. J.; Prato, M.; Fornasiero, P. Improved activity and stability of Pd@$CeO_2$ core–shell catalysts hybridized with multi-walled carbon nanotubes in the water gas shift reaction. *Catalysis Today* **2015**, *253*, 142-148.

[8] Saw, E. T.; Oemar, U.; Ang, M. L.; Hidajat, K.; Kawi, S. Highly Active and Stable Bimetallic Nickel–Copper Core–Ceria Shell Catalyst for High-Temperature Water–Gas Shift Reaction. *ChemCatChem* **2015**, *7*, 3358-3367.

[9] Wieder, N. L.; Cargnello, M.; Bakhmutsky, K.; Montini, T.; Fornasiero, P.; Gorte, R. J. Study of the Water-Gas-Shift Reaction on Pd@$CeO_2$/$Al_2O_3$ Core−Shell Catalysts. *The Journal of Physical Chemistry C* **2011**, *115*, 915-919.

[10] Guo, L.; Li, A.; An, X.; Cao, Z.; Liu, N. Catalytic activity of TM@$Cu_{12}$ core–shell nanoclusters for water gas shift reaction. *International Journal of Hydrogen Energy* **2015**, *40*, 8330-8340.

[11] Wu, S.-K.; Lin, R.-J.; Jang, S.; Chen, H.-L.; Wang, S.-M.; Li, F.-Y. Theoretical Investigation of the Mechanism of the Water–Gas Shift Reaction on Cobalt@Gold Core–Shell Nanocluster. *The Journal of Physical Chemistry C* **2014**, *118*, 298-309.

[12] Blissett, R. S.; Rowson, N. A. A review of the multi-component utilisation of coal fly ash. *Fuel* **2012**, *97*, 1-23.

[13] Qian, B.; Hosseini, T.; Zhang, X.; Liu, Y.; Wang, H.; Zhang, L. Coal Waste to

Two-Dimensional Materials: Fabrication of α-$Fe_2O_3$ Nanosheets and MgO Nanosheets from Brown Coal Fly Ash. *ACS Sustainable Chemistry & Engineering* **2018**, *6*, 15982-15987.

[14] Zhu, M.; Wachs, I. E. Iron-Based Catalysts for the High-Temperature Water–Gas Shift (HT-WGS) Reaction: A Review. *ACS Catalysis* **2016**, *6*, 722-732.

[15] Ji, M.; Chen, G.; Wang, J.; Wang, X.; Zhang, T. Dehydrogenation of ethylbenzene to styrene with $CO_2$ over iron oxide-based catalysts. *Catalysis Today* **2010**, *158*, 464-469.

[16] Fabbri, E.; Habereder, A.; Waltar, K.; Kötz, R.; Schmidt, T. J. Developments and perspectives of oxide-based catalysts for the oxygen evolution reaction. *Catalysis Science & Technology* **2014**, *4*, 3800-3821.

[17] Achola, L. A.; Ghebrehiwet, A.; Macharia, J.; Kerns, P.; He, J.; Fee, J.; Tinson, C.; Shi, J.; March, S.; Jain, M.; Suib, S. L. Enhanced visible-light-assisted peroxymonosulfate activation on cobalt-doped mesoporous iron oxide for orange II degradation. *Applied Catalysis B: Environmental* **2020**, *263*, 118332.

[18] Boudjemaa, A.; Auroux, A.; Boumaza, S.; Trari, M.; Cherifi, O.; Bouarab, R. Hydrogen production on iron–magnesium oxide in the high-temperature water-gas shift reaction. *Reaction Kinetics and Catalysis Letters* **2009**, *98*, 319-325.

[19] Boudjemaa, A.; Daniel, C.; Mirodatos, C.; Trari, M.; Auroux, A.; Bouarab, R. In situ DRIFTS studies of high-temperature water-gas shift reaction on chromium-free iron oxide catalysts. *Comptes Rendus Chimie* **2011**, *14*, 534-538.

[20] de Araújo, G. C.; do Carmo Rangel, M. An environmental friendly dopant for the high-temperature shift catalysts. *Catalysis Today* **2000**, *62*, 201-207.

[21] Natesakhawat, S.; Wang, X.; Zhang, L.; Ozkan, U. S. Development of chromium-free iron-based catalysts for high-temperature water-gas shift reaction. *Journal of Molecular Catalysis A: Chemical* **2006**, *260*, 82-94.

[22] Dyer, J. A.; Scrivner, N. C.; Dentel, S. K. A practical guide for determining the solubility of metal hydroxides and oxides in water. *Environmental Progress* **1998**, *17*, 1-8.

[23] Dieckmann, R.; Hilton, M. R.; Mason, T. O. Defects and Cation Diffusion in Magnetite (VIII): Migration Enthalpies for Iron and Impurity Cations. *Berichte der Bunsengesellschaft für physikalische Chemie* **1987**, *91*, 59-66.

[24] Benny, S.; High Temperature Water Gas Shift Catalysts: A Computer Modelling Study, in Department of Chemistry. 2010, University College London.

[25] Mariotto, G.; Murphy, S.; Berdunov, N.; Ceballos, S. F.; Shvets, I. V. Influence of Ca and K on the reconstruction of the $Fe_3O_4$(001) surface. *Surface Science* **2004**, *564*, 79-86.

[26] Qian, B.; Liu, C.; Lu, J.; Jian, M.; Hu, X.; Zhou, S.; Hosseini, T.; Etschmann, B.; Zhang, X.; Wang, H.; Zhang, L. Synthesis of in-situ $Al^{3+}$-defected iron oxide nanoflakes from coal ash: A detailed study on the structure, evolution mechanism and application to water remediation. *Journal of Hazardous Materials* **2020**, *395*, 122696.

[27] Choo, T. K.; Song, Y.; Zhang, L.; Selomulya, C.; Zhang, L. Mechanisms Underpinning the Mobilization of Iron and Magnesium Cations from Victorian Brown Coal Fly Ash. *Energy & Fuels* **2014**, *28*, 4051-4061.

[28] Feng, Q.; Zhao, S.; Xu, Q.; Chen, W.; Tian, S.; Wang, Y.; Yan, W.; Luo, J.; Wang, D.; Li, Y. Mesoporous Nitrogen-Doped Carbon-Nanosphere-Supported Isolated Single-Atom Pd Catalyst for Highly Efficient Semihydrogenation of Acetylene. *Advanced Materials* **2019**, *31*, 1901024.

[29] Liu, Q.; Zhang, Z. Platinum single-atom catalysts: a comparative review towards effective characterization. *Catalysis Science & Technology* **2019**, *9*, 4821-4834.

[30] Hao, H.; Sun, D.; Xu, Y.; Liu, P.; Zhang, G.; Sun, Y.; Gao, D. Hematite nanoplates: Controllable synthesis, gas sensing, photocatalytic and magnetic properties. *Journal of Colloid and Interface Science* **2016**, *462*, 315-324.

[31] Mohapatra, M.; Behera, D.; Layek, S.; Anand, S.; Verma, H. C.; Mishra, B. K. Influence of Ca Ions on Surfactant Directed Nucleation and Growth of Nano Structured Iron Oxides and Their Magnetic Properties. *Crystal Growth & Design* **2012**, *12*, 18-28.

[32] Ja'baz, I.; Chen, J.; Etschmann, B.; Ninomiya, Y.; Zhang, L. Effect of silica additive on the high-temperature fireside tube corrosion during the air-firing and oxy-firing of lignite (Xinjiang coal) – Characteristics of bulk and cross-sectional surfaces for the tubes. *Fuel* **2017**, *187*, 68-83.

[33] Jia, C.-J.; Sun, L.-D.; Yan, Z.-G.; You, L.-P.; Luo, F.; Han, X.-D.; Pang, Y.-C.;

Zhang, Z.; Yan, C.-H. Single-Crystalline Iron Oxide Nanotubes. *Angewandte Chemie* **2005**, *117*, 4402-4407.

[34] Nozaki, T.; Pati, S. P.; Shiokawa, Y.; Suzuki, M.; Ina, T.; Mibu, K.; Al-Mahdawi, M.; Ye, S.; Sahashi, M. Identifying valency and occupation sites of Ir dopants in antiferromagnetic α-$Fe_2O_3$ thin films with X-ray absorption fine structure and Mössbauer spectroscopy. *Journal of Applied Physics* **2019**, *125*, 113903.

[35] Martis, V.; Oldman, R.; Anderson, R.; Fowles, M.; Hyde, T.; Smith, R.; Nikitenko, S.; Bras, W.; Sankar, G. Structure and speciation of chromium ions in chromium doped $Fe_2O_3$ catalysts. *Physical Chemistry Chemical Physics* **2013**, *15*, 168-175.

[36] Liu, X.; Liu, J.; Zhang, S.; Nan, Z.; Shi, Q. Structural, Magnetic, and Thermodynamic Evolutions of Zn-Doped $Fe_3O_4$ Nanoparticles Synthesized Using a One-Step Solvothermal Method. *The Journal of Physical Chemistry C* **2016**, *120*, 1328-1341.

[37] Liu, J.; Bin, Y.; Matsuo, M. Magnetic Behavior of Zn-Doped $Fe_3O_4$ Nanoparticles Estimated in Terms of Crystal Domain Size. *The Journal of Physical Chemistry C* **2012**, *116*, 134-143.

[38] Qi, Z.; Joshi, T. P.; Liu, R.; Liu, H.; Qu, J. Synthesis of Ce(III)-doped $Fe_3O_4$ magnetic particles for efficient removal of antimony from aqueous solution. *Journal of Hazardous Materials* **2017**, *329*, 193-204.

[39] Nguyen, X. S.; Zhang, G.; Yang, X. Mesocrystalline Zn-Doped $Fe_3O_4$ Hollow

Submicrospheres: Formation Mechanism and Enhanced Photo-Fenton Catalytic Performance. *ACS Applied Materials & Interfaces* **2017**, *9*, 8900-8909.

[40] Jozwiak, W. K.; Kaczmarek, E.; Maniecki, T. P.; Ignaczak, W.; Maniukiewicz, W. Reduction behavior of iron oxides in hydrogen and carbon monoxide atmospheres. *Applied Catalysis A: General* **2007**, *326*, 17-27.

[41] Spreitzer, D.; Schenk, J. Reduction of Iron Oxides with Hydrogen—A Review. *steel research international* **2019**, *90*, 1900108.

[42] Pan, L.; Zhu, X. -D.; Xie, X. -M.; Liu,Y . -T. Smart Hybridization of $TiO_2$ Nanorods and $Fe_3O_4$ Nanoparticles with Pristine Graphene Nanosheets: Hierarchically Nanoengineered Ternary Heterostructures for High-Rate Lithium Storage. *Advanced Functional Materials* **2015**, *25*, 3341-3350.

[43] Han, F.; Ma, L.; Sun, Q.; Lei, C.; Lu, A. Rationally designed carbon-coated $Fe_3O_4$ coaxial nanotubes with hierarchical porosity as high-rate anodes for lithium ion batteries. *Nano Research* **2014**, *7*, 1706-1717.

[44] Shavorskiy, A.; Müller, K.; Newberg, J. T.; Starr, D. E.; Bluhm, H. Hydroxylation of Ultrathin $Al_2O_3$/NiAl(110) Films at Environmental Humidity. *The Journal of Physical Chemistry C* **2014**, *118*, 29340-29349.

[45] Liu, Q.; Qin, H.; Boscoboinik, J. A.; Zhou, G. Comparative Study of the Oxidation of NiAl(100) by Molecular Oxygen and Water Vapor Using Ambient-Pressure X-ray Photoelectron Spectroscopy. *Langmuir* **2016**, *32*, 11414-11421.

[46] van Bokhoven, J. A.; Sambe, H.; Ramaker, D. E.; Koningsberger, D. C. Al K-

Edge Near-Edge X-ray Absorption Fine Structure (NEXAFS) Study on the Coordination Structure of Aluminum in Minerals and Y Zeolites. *The Journal of Physical Chemistry B* **1999**, *103*, 7557-7564.

[47] Yoshimura, T.; Tamenori, Y.; Iwasaki, N.; Hasegawa, H.; Suzuki, A.; Kawahata, H. Magnesium K-edge XANES spectroscopy of geological standards. *Journal of Synchrotron Radiation* **2013**, *20*, 734-740.

[48] Li, J.; Liang, J.-X.; Lin, J.; Liu, J.; Wang, X.; Zhang, T. Dual metal active sites in an $Ir_1/FeO_x$ single-atom catalyst: a redox mechanism for the water-gas-shift reaction. *Angewandte Chemie International Edition* **2020**, *59*, 2-10.

[49] Fu, X.-P.; Guo, L.-W.; Wang, W.-W.; Ma, C.; Jia, C.-J.; Wu, K.; Si, R.; Sun, L.-D.; Yan, C.-H. Direct Identification of Active Surface Species for the Water–Gas Shift Reaction on a Gold–Ceria Catalyst. *Journal of the American Chemical Society* **2019**, *141*, 4613-4623.

[50] Sun, X.; Lin, J.; Zhou, Y.; Li, L.; Su, Y.; Wang, X.; Zhang, T. $FeO_x$ supported single-atom Pd bifunctional catalyst for water gas shift reaction. *AIChE Journal* **2017**, *63*, 4022-4031.

[51] Chen, Y.; Lin, J.; Li, L.; Qiao, B.; Liu, J.; Su, Y.; Wang, X. Identifying Size Effects of Pt as Single Atoms and Nanoparticles Supported on $FeO_x$ for the Water-Gas Shift Reaction. *ACS Catalysis* **2018**, *8*, 859-868.

[52] Sushil, S.; Batra, V. S. Catalytic applications of red mud, an aluminium industry waste: A review. *Applied Catalysis B: Environmental* **2008**, **81**, 64-77.

[53] Sourav, S.; Wachs, I. E. Cr-Free, Cu Promoted Fe Oxide-Based Catalysts for High-Temperature Water-Gas Shift (HT-WGS) Reaction. *Catalysts* **2020**, *10*, 305.

[54] Silva, C. L. S.; Marchetti, S. G.; Júnior, A. d. C. F.; Silva, T. d. F.; Assaf, J. M.; Rangel, M. C. d. Effect of gadolinium on the catalytic properties of iron oxides for WGSR. *Catalysis Today* **2013**, *213*, 127-134.

[55] Júnior, I. L.; Millet, J.-M. M.; Aouine, M.; Rangel, M. d. C. The role of vanadium on the properties of iron based catalysts for the water gas shift reaction. *Applied Catalysis A: General* **2005**, *283*, 91-98.

[56] Pereira, A. L. C.; Santos, N. A. d.; Ferreira, M. L. O.; Albornoz, A.; Rangel, M. d. C. Effect of cobalt on the activity of iron-based catalysts in water gas shift reaction. *Studies in Surface Science and Catalysis* **2007**, *167*, 225-230.

[57] Costa, J. L. R.; Marchetti, G. S.; Rangel, M. D. C. A thorium-doped catalyst for the high temperature shift reaction. *Catalysis Today* **2002**, *77*, 205-213.

[58] Liu, Q.; Ma, W.; He, R.; Mu, Z. Reaction and characterization studies of an industrial Cr-free iron-based catalyst for high-temperature water gas shift reaction. *Catalysis Today* **2005**, *106*, 52-56.

[59] Yu, J.; Tian, F.-J.; Li, C.-Z. Novel Water-Gas-Shift Reaction Catalyst from Iron-Loaded Victorian Brown Coal. *Energy Fuels* **2007**, *21*, 395-398.

[60] Zhu, M.; Wachs, I. E. Resolving the Reaction Mechanism for $H_2$ Formation from High-Temperature Water−Gas Shift by Chromium−Iron Oxide Catalysts.

*ACS Catalysis* **2016**, *6*, 2827-2830.

[61] Liu, Q.; Ma, W.; He, R.; Mu, Z. Reaction and characterization studies of an industrial Cr-free iron-based catalyst for high-temperature water gas shift reaction. *Catalysis Today* **2005**, *106*, 52-56.

[62] Zhu, M.; Rocha, T. C. R.; Lunkenbein, T.; Knop-Gericke, A.; Schlögl, R.; Wachs, I. E. Promotion Mechanisms of Iron Oxide-Based High Temperature Water−Gas Shift Catalysts by Chromium and Copper. *ACS Catalysis* **2016**, *6*, 4455-4464.

# Chapter 7 Conclusions and future research recommendations

## 7.1 Conclusions

This thesis presented a comprehensive leaching, precipitation and synthesis process of Victorian brown coal fly ash for the preparation of Fe- and Mg-based nanomaterials. Through multi-step temperature-varied leaching process, an integrated Fe and Mg extraction technology has been established. Additionally, the influences of inherent Al and Mg impurities on the structures and performances (including water treatment and WGSR) of synthesized α-$Fe_2O_3$ nanoflakes are also elucidated. Finally, experimental investigations and intensive characterizations, the growth mechanisms of two-dimensional $Mg(OH)_2$ nanosheets are provided, and the resultant facet-engineered MgO nanosheets with Fe(III) is a promising catalyst for the WGSR. The results provide a database for the design and scale-up of industrial low-rank coal ash leaching process and offer more alternatives to the low-cost nano-adsorbents towards water treatment and more options for the green catalysts towards the WGSR.

### 7.1.1 Integrated coal fly ash leaching, precipitation and synthesis process

Two-dimensional α-$Fe_2O_3$ and MgO nanosheets have been synthesized from brown coal fly ash. For the leaching process, the results confirmed a mass yield of around 25% and a purity of 98.23 *wt%* for the final MgO nanosheet and 45% with a purity of 94.34 *wt%* for α-$Fe_2O_3$ nanosheet. The α-$Fe_2O_3$ nanosheet has a hematite structure with an averaged diameter of 200−400 and 50 nm in thickness for the individual round sheet, and the MgO nanosheet possesses a periclase structure with an averaged diameter of

100−200 and 10 nm in thickness for the single hexagonal lamella.

### 7.1.2 Synthesis of Al-defect α-$Fe_2O_3$ nanoflake and its application to water treatment

A unique $Fe_{1.72}Al_{0.28}O_3$ nanoflake has been synthesized from coal fly ash. The product achieved a yield of 32 %, based on the mass of water-washed, dried fly ash. Crystal defects of the nanoflakes were introduced through the in-situ isovalent replacement of $Fe^{3+}$ by $Al^{3+}$ upon hydrothermal treatment. Consequently, a flattened nanoflake-like morphology with a diameter of around 300 nm and 50 nm in thickness was achieved, and a relatively large specific surface area of 80.12 $m^2\ g^{-2}$ was secured. The $Al^{3+}$ dopant distorted the original atomic structure of standard α-$Fe_2O_3$, resulting in reduced lattice parameters (a = 5.005(43) Å, c = 13.727 (44) Å), a smaller first shell (Fe-O bond distance of 1.95(0.21) Å) and a reduced periodic symmetry (Fe coordination number of 4.5(0.3)). The as-synthesized nanoflakes exhibit higher efficiency and enhanced adsorption performance with a maximum adsorption capacity of 68.3, 80.6, 61.1 and 213.8 mg g-1 of Cr(VI), As(V), As(III) and Congo red, respectively.

### 7.1.3 Synthesis of (111) facet-engineered MgO-Fe(III) nanosheets and its application to the High-temperature WGSR.

The synthesis of a facet-engineered MgO(111)-Fe(III) nanosheet as a HT-WGSR catalyst was achieved, which involves an initial growth of a (001)-facet dominant

$Mg(OH)_2$ precursor by an ethanol-mediated hydrothermal process followed by in-situ conversion of $Mg(OH)_2$ to MgO(111) facet during the HT-WGSR. Results reveal that, ethanol resulted in a preferential restriction of the entire crystal growth on [001] direction. Upon the loading of 30 *wt%* $Fe^{3+}$, the (001)-facet enhanced $Mg(OH)_2$ nanosheet undertook a dehydroxylation into MgO(111) after calcination and reduction. During the HT-WGSR, the reduced product is beneficial in promoting the formation of surface formates and the reduction of $Fe^{3+}$ on the oxygen vacancy of the (111) facet, leading to increased CO conversion by a factor of two in comparison to the commercial $Mg(OH)_2$ loaded with the same amount of $Fe^{3+}$, and by nearly seven time compared to the nano-sized hematite reference.

### 7.1.4 Synthesis of Magnetite with a Surrounded Core-Shell Structure from Fly Ash Waste and Its Superior Catalysis Performance for High-Temperature Water-Gas Shift Reaction.

A facile process for the design of magnetite-based, surrounded catalysts with a core-shell structure from coal fly ash, an industrial solid waste was demonstrated, and the application to classic high temperature water-gas shift reaction (WGSR). The feedstock was initially synthesized through a leaching-precipitation-hydrothermal process, leading to the formation of a nanosheet-like hematite precursor consisting of $Fe^{3+}$ as principal element and trace cations including $Al^{3+}$, $Mg^{2+}$ and other cations (*e.g.* $Ca^{2+}$, $Ti^{4+}$ and $Mn^{2+}$). Upon a subsequent thermal reduction, the nanosheet broke into smaller

particles with a core in form of magnetite and a diameter of ~20 nm, whereas the inherent impurity elements were activated to migrate to the outer surface forming a shell with a thickness in a few nanometres. The elemental composition, porosity and thickness of the shell are highly tunable. Upon the addition of ethanol during the hydrothermal stage, a slightly higher content of $Al^{3+}$ (8.92 *wt%*) and $Mg^{2+}$ (2.58 *wt%*) were successfully embedded within the shell of the catalyst, which in turn increased the shell thickness by nearly twice, and created more nanochannels in mesopore scale within the shell. Due to the protection effect of shell, the two catalysts exhibited higher activity, thermal stability and long-term durability for HT-WGSR at 400ºC and 450ºC. In particular, the catalyst synthesized with a thicker shell slightly more impurities exhibited the highest activity at a temperature. Compared to the pure hematite, the best activity increased the CO conversion by nearly four times and decreased the magnitude of the deactivation rate constant by four times too. Additionally, apart from $Al^{3+}$ being a textual promoter enhancing the interfacial area of the catalysts, the trace impurity elements, in particular 2.58 *wt%* $Mg^{2+}$ was confirmed to promote the redox rate of catalysts by promoting the formation of formate, the adsorption rate of CO and the desorption of $CO_2$ molecules on the catalyst surface too. These trace impurities are supposed to atomically disperse within the nano-scale shell, thereby creating extra active sites to interact strongly with the magnetite core. This study opens a new direction on the valorization of solid waste into high-value catalysts, thereby promoting the sustainability of solid waste management, but it also provides an alternative, cost-

effective and scalable approach for the design and fine-tuning of surrounded catalysts.

## 7.2 Recommendations for future work

The research results demonstrated in this thesis have proven the feasibility of low-rank Victorian brown coal fly leaching and synthesis for the Fe- and Mg-based nanomaterials and their applications. A comprehensive synthesis process which integrates leaching, precipitation and hydrothermal treatment has been proposed and the applications to water treatment and WGSR have been conducted. The recommendations for future work are shown as follows:

### 7.2.1 Applicability study of the proposed leaching process for other elements and solid wastes

Studies on the other types of solid wastes such as steel slag and red mud are recommended to examine the applicability of the leaching part in this thesis, especially the precipitation process for the targeted metal elements. This applicability research will enhance the robustness of this PhD project findings and facilitate the worldwide scale-up of low-rank coal fly ash leaching process.

### 7.2.2 Economic evaluation

Preliminary economic cost evaluations on the overall process of fly ash leaching, precipitation and hydrothermal treatment to synthesize Fe- and Mg-based

nanomaterials as compared to direct synthesis from pure Fe and Mg-bearing chemical agents are recommended to conduct. These results will be fundamental for subsequent industry pilot scale research and production.

### 7.2.3 Pilot scale research

The next step is an industrial pilot-scale process about:

(1) The continuous feeding of brown coal fly ash and it will produce the large volume of leachate containing Fe and Mg, which is critical to examine the stability of the whole leaching system. The pilot-scale trial will provide a fundamental insight into the technical feasibility of this technology. Moreover, the potential environmental impacts should be evaluated.

(2) The constant and fast water treatment process using column method. In the practical system, the bottleneck problem of an adsorbent lies in how to achieve a high and stable adsorption capacity. The pilot-scale trial will offer an important guide to the further use this process in practical situations. In addition, the possible environmental threats should be addressed.

(3) The ultralong time testing of Fe-based catalysts. Normally, rapid coke formation and sintering in WGSR will reduce catalytic reactivity at an industrial scale. Therefore, it is of practical significance to evaluate its ultralong-term state. The pilot-scale trial will give a prediction on the performance and lifespan of catalysts in industrial conditions.

### 7.2.3 Other applications of synthesized Fe- and Mg-based materials

Current application researches of the synthesized products are only limited to the water treatment and WGSR. For the subsequent studies, more relevant applications including batteries, sensors, $CO_2$ reduction, CO oxidation, $H_2O$ splitting and ion separation can be tried to further evaluate the potential performances of synthesized nanomaterials, which will bring the value-added utilization of coal fly ash waste into another high level.

# Appendix A
# Chapter 3 in publication form

ACS Sustainable Chemistry & Engineering

Letter

Cite This: ACS Sustainable Chem. Eng. 2018, 6, 15982−15987

pubs.acs.org/journal/ascecg

# Coal Waste to Two-Dimensional Materials: Fabrication of $\alpha$-$Fe_2O_3$ Nanosheets and MgO Nanosheets from Brown Coal Fly Ash

Binbin Qian, Tahereh Hosseini, Xiwang Zhang, Yue Liu, Huanting Wang, and Lian Zhang*

Department of Chemical Engineering, Monash University, Wellington Road, Clayton, Victoria 3800, Australia

Supporting Information

ABSTRACT: High-purity 2-D $\alpha$-$Fe_2O_3$ nanosheets and MgO nanosheets have been successfully fabricated with a high extraction yield of 45 and 25 wt %, respectively, from a brown coal fly ash, an otherwise valueless waste. A two-stage counter-current solid−liquid extraction method was first employed under the mild conditions of 25−60 °C and atmospheric pressure to selectively extract $Fe^{3+}$ and $Mg^{2+}$, which were then precipitated out separately upon gradual addition of NaOH and subsequent hydrothermal treatment. Finally, 2-D nano-sized $\alpha$-$Fe_2O_3$ nanosheet was obtained with a lamellar morphology, while the synthesized $Mg(OH)_2$ precursor undertook an extra multistep calcination to convert into the respective 2-D MgO nanosheet.

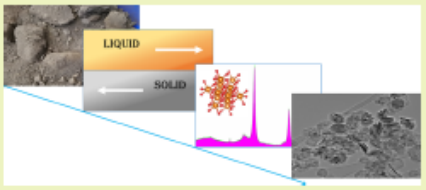


KEYWORDS: Brown coal fly ash, Waste utilization, Multistep acid leaching, Hydrothermal treatment, Nanosheet

Downloaded via MONASH UNIV on December 6, 2018 at 06:50:57 (UTC).
See https://pubs.acs.org/sharingguidelines for options on how to legitimately share published articles.

## INTRODUCTION

Since the synthesis of carbon tubes in 1991,[1] nanometric materials with varying morphologies such as nanoribbons,[2] nanorods,[3] nanowires,[4] nanorings,[5] and nanosheets[6] have been attracting increased attention around the world, owing to their unique properties and potential applications. Among the nanostructured families, nanosized MgO and $Fe_2O_3$, both accessible and versatile metal oxides, have been used widely in a variety of applications, including adsorbent,[7] catalyst,[8] refractory materials,[9] cancer therapy,[10] antibacterial,[11] superconductor,[12] battery,[13] gas sensing,[14] and photoelectrochemical performance.[15]

In the past couple of decades, a variety of synthesis methods have been developed and optimized for the manufacturing of nano-MgO and nano-$Fe_2O_3$, including wet precipitation,[16] CVD,[17] sol−gel,[14,18] solid state reaction,[19] thermal treatment,[20] hydrolysis,[11,21] hydrothermal,[22] anodization,[15] and solvothermal.[23] Although nano-MgO and nano-$Fe_2O_3$ have been successfully synthesized from these methods, the starting materials are mostly pure chemicals such as $Mg(NO_3)_2{\cdot}6H_2O$,[16] $MgCl_2$,[24] $MgSO_4$,[16] $FeCl_3{\cdot}6H_2O$,[23] and $Fe_2(SO_4)_3{\cdot}7H_2O$,[25] only limited studies have taken feedstock into account.[26,27] In this sense, from the process sustainability perspective, the utilization of a low-cost feedstock such as Mg- or Fe-rich industrial waste is critical. To this end, a brown coal fly ash collected from the brown coal-fired power generation station in the state of Victoria in Australia has been tested. To date, over 1,000,000 tonnes of brown coal fly ash has been produced annually in the last 30 years in Victoria, most of which is however simply dumped into ash ponds. This hazardous ash waste poses potential threats to the air, soil, and even underground water while little is being used. Traditionally, fly ash is used widely as an additive into cement,[28] concrete,[29] and agricultural industries.[30] Some fly ashes are also used to synthesize nanomaterials such as nanosilica,[31] zeolite,[32,33] and CNT.[34] However, different from bituminous coal fly ashes, brown coal fly ash in Victoria contains relatively high concentrations of metallic cations, particularly $Fe^{3+}$ and $Mg^{2+}$ (Table 1). It is thus impractical to use the brown coal fly ash in the traditional ways mentioned above. Instead, we hypothesized that the (Fe, Mg)-rich Victorian Brown coal fly

Table 1. XRF Analysis of Yallourn Fly Ash, Final Leaching Residue, $\alpha$-$Fe_2O_3$ Nanosheet, and MgO Nanosheet (wt %)[a]

| | Yallourn fly ash | Leaching residue | $\alpha$-$Fe_2O_3$ nanosheet | MgO nanosheet |
|---|---|---|---|---|
| $SiO_2$ | 4.19 | 11.83 | 0 | 0 |
| $Al_2O_3$ | 3.71 | 6.36 | 1.72 | 0 |
| CaO | 9.49 | 32.11 | 1.82 | 1.19 |
| MgO | 26.74 | 1.29 | 0.38 | 98.23 |
| $Fe_2O_3$ | 49.14 | 2.02 | 94.34 | 0.57 |
| $Na_2O$ | 0.76 | 0 | 0 | 0 |
| $K_2O$ | 0.13 | 0.29 | 0 | 0 |
| $SO_3$ | 3.84 | 45.89 | 0.91 | 0 |
| $P_2O_5$ | 0.12 | 0 | 0 | 0 |
| MnO | 0.83 | 0.05 | 0.27 | 0 |
| $TiO_2$ | 1.05 | 0.16 | 0.56 | 0.01 |

[a]Measurement errors of all elements are between 0.01 and 0.3 wt %.

Received: August 10, 2018
Revised: October 25, 2018
Published: November 14, 2018

 © 2018 American Chemical Society 

DOI: 10.1021/acssuschemeng.8b03952
ACS Sustainable Chem. Eng. 2018, 6, 15982−15987

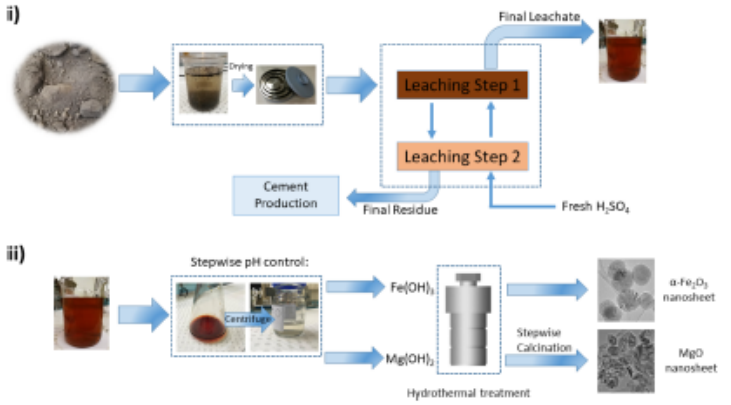


Figure 1. Schematic illustration of (i) the two-step counter-current leaching method for Victorian brown coal fly ash and (ii) $\alpha$-$Fe_2O_3$ nanosheets and MgO nanosheets synthesized from the final leachate in (i).

ash could be a good raw material for the synthesis of $\alpha$-$Fe_2O_3$ nanosheets and MgO nanosheets.

Through a hydrometallurgical leaching process, previous works have extracted Fe or Mg from fly ash while with low extraction yields.[35−37] Based on this special brown coal fly ash, Hosseini et al.[37] found that there is a need for further research to develop an efficient extraction process which breaks the structure of the magnesium ferrite inverse-spinels to release $Fe^{3+}$ and $Mg^{2+}$. The main challenge is that $NH_4Cl$ is too weak to cleave the strong affinity between Mg and Fe within the $MgFe_2O_4$ matrix, which would otherwise still remain in the final residue and has to be returned as a waste to the fly ash pond. This forms our hypothesis in this study for the use of a strong acid such as $H_2SO_4$ as an alternative leaching agent. Therefore, a novel two-step counter-current leaching method using $H_2SO_4$ as the leaching agent, as shown in Figure 1, is further employed to enforce the extraction of $Fe^{3+}$ and $Mg^{2+}$ out of the ferrite inverse-spinels in the brown coal fly ash. It is desirable that the process developed here and the results are applicable to the other brown coal ashes in the world rich in magnesium ferrite, such as ash samples from the pulverized brown coal-fired power plants from Romania and Poland,[38] Mg-rich process tailings and waste rocks,[39] and even acid activation of Mg-abundant clay minerals.[40]

In this paper, we for the first time report the extraction results of $Mg^{2+}$ and $Fe^{3+}$ out of inverse-spinel ferrite-rich brown coal fly ash via a two-stage counter-current solid−liquid leaching method through the use of sulfuric acid. Additionally, efforts were made to synthesize two-dimensional $\alpha$-$Fe_2O_3$ nanosheets and MgO nanosheets based on the resultant leachate. As far as the authors are aware, such an effort has yet to be reported for any fly ash sample across the world. The results achieved are thus expected to shed new insights on the value-added utilization of low-rank coal fly ash samples.

## EXPERIMENTAL SECTION

**Synthesis Methods.** For the leaching experiments, 15% $H_2SO_4$ was used as a leaching agent and the liquid to solid mass ratio was fixed at 2. The mixed slurry was fed into a continuously stirred beaker for the leaching experiments. The first stage leaching was conducted at room temperature, while the second stage was conducted at 60 °C by placing the beaker inside a hot water bath. Figure 1 presents the two-stage counter-current solid−liquid extraction flowsheet. In this process, the fresh ash is leached by the used acid generated from the second stage, whereas residue from the first stage is further leached by the fresh acid. This configuration allows for a larger concentration gradient between the liquid phase and the solid, thus maximizing the extraction yield in each stage.

After leaching, 20 mL of the final leachate was taken for a further experiment. Here, a 1 M NaOH solution was added to the taken leachate to adjust the pH to around 4 to precipitate out the $Fe^{3+}$ cation.[41] The resultant slurry was centrifuged at the speed of 8000 rpm for 8 min to separate out $Fe(OH)_3$. This $Fe(OH)_3$ was further washed by Milli-Q water, and then, a 1 M NaOH solution was added dropwise until its pH reached about 6. After a vigorous stirring for 1 h, the slurry was transferred to a 120 mL autoclave I. Regarding the resultant $Mg^{2+}$-rich leachate, 1 M NaOH solution was added to the leachate dropwise until its pH reached about 11. A white precipitate was obtained, and then, 20 mL of ethanol was added into the solution and stirred continuously for a few minutes. Afterward, the white slurry was entirely transferred to a 120 mL autoclave II. Both of the above-closed autoclaves I and II were then placed inside a preheated hot-air oven maintained at 180 °C for 12 h. After that, they were cooled to room temperature naturally. The obtained precipitates were filtered, washed with Milli-Q water and ethanol sequentially to reduce the agglomeration, and later further dried at 80 °C for 2 h. Finally, the dark red sample from autoclave I was stored in a vacuum drying oven for further analysis, and the white colored material from autoclave II was subjected to calcination in a muffle furnace in air under the program of 280 °C for 2 h, 350 °C for 2 h, and finally 450 °C for 2 h to preserve the morphological features of the $Mg(OH)_2$ nanocrystallines in the final MgO products.[16]

**Chemicals, Experiment, and Instruments.** All details are provided in the Supporting Information.

## RESULTS AND DISCUSSION

As shown in Table 1, most Mg and Fe have been removed from the original fly ash. The final leaching residue possesses a chemical composition that is close to gypsum derived from the desulfurization unit in a coal-fired power plant, which is a potential material to be used in the calcium sulfoaluminate



DOI: 10.1021/acssuschemeng.8b03952
ACS Sustainable Chem. Eng. 2018, 6, 15982−15987

(CSA) cement clinker manufacturing industry. The primary species in a CSA cement clinker include belite ($Ca_2SiO_4$), ye'elimite ($Ca_4Al_6O_{12}(SO_4)$), aluminate ($Ca_3Al_2O_6$), and ferrite ($Ca_4(Al, Fe)_2O_7$), requiring abundance of both Ca and S along with a certain amount of Al.[42,43] The $\alpha$-$Fe_2O_3$ nanosheet with a purity of 94.34 wt % is a promising material which exhibits excellent performance in a $NO_2$ sensor,[14] lithium-ion battery,[13] and photoelectrochemical water splitting.[15] In terms of a high-purity MgO nanosheet with a 98.23 wt % magnesium oxide, such a versatile metal oxide has wide applications in catalysts for selective dehydrogenation,[8] bacteriocide,[11] and adsorbent.[7]

Figure 2 demonstrates the high overall extraction yields of the two major cations, $Mg^{2+}$ and $Fe^{3+}$, from the two-stage leaching procedure. It is obvious that the time-dependent extraction trends are similar for both cations. The leaching fraction of each cation increased exponentially over time, reaching its maximum at around 20 min. With regard to the final leachate discharged from the second stage, its original pH was close to 1 while increased to around 4 upon the addition of NaOH, allowing the precipitation of the nearly entire $Fe^{3+}$ as a hydroxide (Figure 1). Inductively coupled plasma optical emission spectroscopy (ICP-OES) was used to quantify the concentrations of all the remaining cations, including $Mg^{2+}$, $Fe^{3+}$, $Ca^{2+}$, and $Al^{3+}$ cations, in the final leachate after the $Fe^{3+}$ precipitation stage (Figure 2, inset). It is confirmed that $Mg^{2+}$ is the most dominant cation in the final leachate. The concentration of $Mg^{2+}$ in the leachate reaches 31,082 ppm, comprising 97.71% of all the four fly ash-derived cations (excluding $Na^+$). Note that the other cations in the leachate are undetectable by ICP-OES.

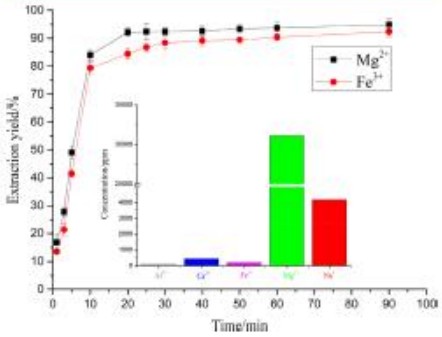


Figure 2. Time-resolved leaching of $Mg^{2+}$ and $Fe^{3+}$ out of fly ash (inset: ICP-OES analysis of final leachate after $Fe^{3+}$ precipitation).

After the hydrothermal treatment of $Fe(OH)_3$ and $Mg(OH)_2$ (followed by a subsequent step calcination), nanosized $\alpha$-$Fe_2O_3$ and MgO were obtained. The purities of the as-synthesized $\alpha$-$Fe_2O_3$ and MgO nanosheets were determined by XRF to be 94.34 and 98.23 wt %, respectively (Table 1), substantiating the fact that most of $Ca^{2+}$ and $Fe^{3+}$ can be precipitated via $H_2SO_4$ leaching and pH control precipitation, respectively. Since the weight percentages of MgO and $Fe_2O_3$ account for 26.74 and 49.41 wt %, respectively, in the original fly ash (Table 1) and 94.88% of MgO and 92.34% of $Fe_2O_3$ were extracted out upon acid leaching (Figure 2), the final MgO nanosheet and $\alpha$-$Fe_2O_3$ nanosheet reach mass yields of around 25% and 45% on the basis of the original fly ash, respectively.

Figure 3(a) shows a typical sample for as-synthesized $\alpha$-$Fe_2O_3$ nanosheets. The XRD pattern in Figure 3(b) depicts the crystal details for $\alpha$-$Fe_2O_3$, indicating that it is the hematite structure (ICSD #22505) in the trigonal system with the lattice constant of a = 5.038 Å and c = 13.772 Å. The surface morphology of the as-synthesized $\alpha$-$Fe_2O_3$ was observed by high-resolution SEM imaging in Figure 3(c). It is confirmed that the as-synthesized $\alpha$-$Fe_2O_3$ nanosheets exhibit a diameter of 200−400 nm, and its nanostructure is different from the previous results using additives. Through using polyethylene

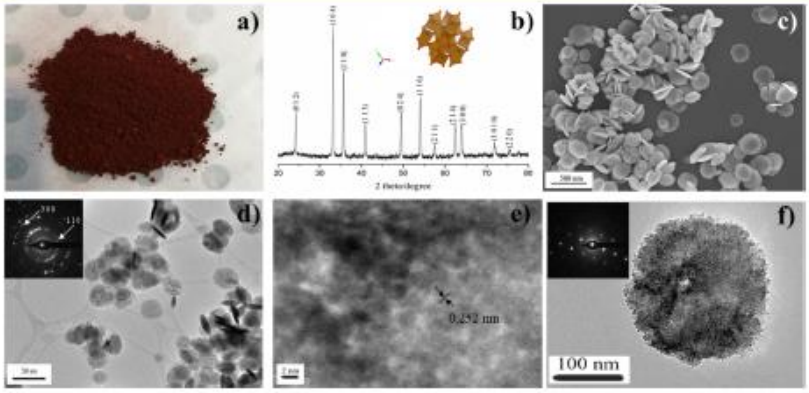


Figure 3. (a) Typically synthesized $\alpha$-$Fe_2O_3$ nanosheet sample. (b) Selected range of XRD pattern for $\alpha$-$Fe_2O_3$ nanosheets (inset: $\alpha$-$Fe_2O_3$ polyhedral model). (c) SEM image of $\alpha$-$Fe_2O_3$ nanosheets. (d) TEM representative nanosheets (inset: SAED pattern from d). (e) HRTEM image of $\alpha$-$Fe_2O_3$ nanosheet. (f) Well-grown single $\alpha$-$Fe_2O_3$ crystal (inset: SAED pattern from f).



DOI: 10.1021/acssuschemeng.8b03952
ACS Sustainable Chem. Eng. 2018, 6, 15982−15987

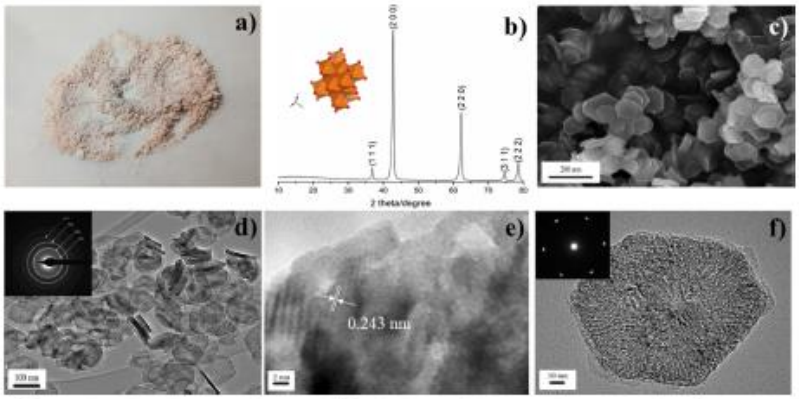


**Figure 4.** (a) Typically synthesized MgO nanosheet sample. (b) Selected range of XRD pattern for MgO nanosheets (inset: MgO polyhedral model). (c) SEM image of MgO nanosheets. (d) TEM representative nanosheets (inset: SAED pattern from d). (e) HRTEM image of MgO nanosheet. (f) Well-grown single MgO crystal (inset: SAED pattern from f).

glycol and sodium acetate, hexagonal nanosheets or quasi-spherical nanoplates of hematite were synthesized,[2,3] and through the use of glycine, cubic-like or spherical hematite nanoparticles can be obtained.[44]

Figure 3(d), (e), and (f) further show the representative high-resolution TEM images of the as-synthesized $\alpha$-$Fe_2O_3$ nanosheet. As shown in Figure 3(d), these products are confirmed to display a round lamellar morphology with an average size of ~300 nm. Some of the $\alpha$-$Fe_2O_3$ particles stand straight on the copper grid, indicating a thickness of approximately 50 nm. The inset is the selected area electron diffraction (SAED) patterns taken from Figure 3(d), exhibiting the inner-outside rings corresponding to (1 1 0) and (3 0 0) planes of $\alpha$-$Fe_2O_3$, and the incomplete diffraction ring spots imply the disordered and unsystematic crystal orientation for nanosized $\alpha$-$Fe_2O_3$. Figure 3(e) illustrates a HRTEM image of an as-synthesized $\alpha$-$Fe_2O_3$ nanosheet, where the lattice fringes separated by the $d$-spacing of 0.252 nm can be indexed to the (1 1 0) plane. Figure 3(f) illustrates a single $\alpha$-$Fe_2O_3$ nanosheet with an obvious round outline. The corresponding SAED pattern (inset) can be indexed to the [0 0 1] zone axis diffraction of $\alpha$-$Fe_2O_3$ nanosheets for {1 1 0} crystal facts.

Figure 4(a) shows the final product of the MgO nanosheets. The crystal structure of the as-synthesized MgO nanosheets was determined by XRD and is shown in Figure 4(b). It is clear that all the diffraction peaks can be indexed to the FCC periclase structure (ICSD #26958) with a lattice constant of $a$ = 4.203 Å. However, one noteworthy exception has been observed here: the diffraction peaks of the synthesized nano-MgO show a slight shift from the periclase standard due to a trace of magnesium iron oxide ($Mg_{1-x}Fe_xO$) formed by a $Fe^{3+}$ impurity (Table 1) being incorporated into MgO during the precipitation process. A low amount of $Fe^{3+}$ can dissolve into the MgO lattice producing a very little distortion that is undetectable by the XRD.[45]

The surface morphology of the as-synthesized MgO was observed by high-resolution SEM imaging in Figure 4(c). It can be seen that the MgO nanosheet has been successfully synthesized. The MgO nanosheets exhibit a diameter of 100–200 nm, which is consistent with the previous results using $NH_3{\cdot}H_2O$ or ethylenediamine as the precipitation agent and chemical-grade $MgSO_4$ as the feedstock.[16] Therefore, the averaged diameter of 100–200 nm synthesized here is applicable and shows a distinctively different property compared to the bulk sample. For the catalyst applications, a minimum diameter of 100 nm is essential for the MgO nanosheet.[46]

Additionally, it is noteworthy that the overall hexagonal morphology of these lamellar-like particles is consistent with the hexagonal crystallographic characteristics of brucite ($Mg(OH)_2$), evidencing that the structure of brucite was well retained in the multistep calcination stage.

Figure 4(d), (e), and (f) further depict the representative high-resolution TEM images of the as-synthesized MgO nanosheet. As shown in Figure 4(d), these products are further confirmed to display a hexagonal lamellar morphology with an average size of ~100 nm. By checking the MgO particles standing straight on the copper grid, it is also referable that these nanosheets have a thickness of approximately 10 nm. Such a thickness is still comparable with those synthesized from using pure chemicals, which can be attributed to the strong dispersion effect of ethanol added to the hydrothermal precipitation stage.[47] The inset is the selected area electron diffraction (SAED) patterns taken from Figure 4(d), exhibiting inner-outside rings corresponding to (1 1 1), (2 0 0), (2 2 0), and (2 2 2) planes of MgO. Figure 4(e) illustrates the HRTEM image of the as-synthesized MgO nanosheet, where the lattice fringes are separated by a distance of 0.243 nm which can be attributed to the (1 1 1) plane of MgO. Figure 4(f) illustrates an individual MgO nanosheet with an obvious hexagonal outline. The 6-fold symmetry of the corresponding SAED pattern (inset) can be indexed to the [1−1 1] or [1−1 −1] zone axis diffraction of MgO nanosheets for {2 2 0} crystal facts.



DOI: 10.1021/acssuschemeng.8b03952
ACS Sustainable Chem. Eng. 2018, 6, 15982−15987

## CONCLUSION

In summary, 2-D $\alpha$-$Fe_2O_3$ and MgO nanosheets have for the first time been successfully synthesized from brown coal fly ash, an otherwise valueless waste. This study differs from the previous researches that focused on the cement additive or the synthesis of alumina and zeolite from fly ash. Instead, it opens a new application for brown coal fly ash that is mostly landfilled or used as a low-value additive in the construction industry. The synthesized two-dimensional nano-$Fe_2O_3$ and nano-MgO can be used in a broad variety of high-value applications. For the Victorian brown coal fly ash used here, the typical results confirmed a mass yield of around 25% and a purity of 98.23 wt % for the final MgO nanosheet and 45% with a purity of 94.34 wt % for $\alpha$-$Fe_2O_3$ nanosheet. The $\alpha$-$Fe_2O_3$ nanosheet has a hematite structure with an averaged diameter of 200−400 and 50 nm in thickness for the individual round sheet, and the MgO nanosheet possesses a periclase structure with an averaged diameter of 100−200 and 10 nm in thickness for the single hexagonal lamella. These two kinds of nanosheets are small enough to have distinct properties when compared to the bulk $Fe_2O_3$ or MgO samples.

## ASSOCIATED CONTENT

### Supporting Information

The Supporting Information is available free of charge on the ACS Publications website at DOI: 10.1021/acssuschemeng.8b03952.

Further information on fly ash properties, pretreatment, and instruments. (PDF)

## AUTHOR INFORMATION


### Corresponding Author

*E-mail: lian.zhang@monash.edu. Tel: +61-3-9905-2592. Fax: +61-3-9905-5686.

### ORCID

Binbin Qian: 0000-0001-7145-2926

Xiwang Zhang: 0000-0002-4319-527X

Huanting Wang: 0000-0002-9887-5555

Lian Zhang: 0000-0002-2761-880X


### Notes

The authors declare no competing financial interest.

## ACKNOWLEDGMENTS

The authors gratefully acknowledge the Australian Research Council (IH170100009) and the China Scholarship Council (CSC) for financial support. The authors also acknowledge the use of facilities within the Monash Centre for Electron Microscopy (MCEM).

## REFERENCES


(1) Iijima, S. Helical microtubules of graphitic carbon. *Nature* **1991**, *354* (6348), 56−58.

(2) Bronner, C.; Durr, R. A.; Rizzo, D. J.; Lee, Y.-L.; Marangoni, T.; Kalayjian, A. M.; Rodriguez, H.; Zhao, W.; Louie, S. G.; Fischer, F. R.; Crommie, M. F. Hierarchical On-Surface Synthesis of Graphene Nanoribbon Heterojunctions. *ACS Nano* **2018**, *12*, 2193−2200.

(3) He, R.; Zhang, A.; Ding, Y.; Kong, T.; Xiao, Q.; Li, H.; Liu, Y.; Zeng, J. Achieving the Widest Range of Syngas Proportions at High Current Density over Cadmium Sulfoselenide Nanorods in $CO_2$ Electroreduction. *Adv. Mater.* **2018**, *30*, 1705872.

(4) Law, M.; Greene, L. E.; Johnson, J. C.; Saykally, R.; Yang, P. Nanowire dye-sensitized solar cells. *Nat. Mater.* **2005**, *4*, 455.

(5) Jia, H.; Gao, Y.; Huang, Q.; Cui, S.; Du, P. Facile three-step synthesis and photophysical properties of [8]-, [9]-, and [12]cyclo-1,4-naphthalene nanorings via platinum-mediated reductive elimination. *Chem. Commun.* **2018**, *54*, 988−991.

(6) Coleman, J. N.; Lotya, M.; O'Neill, A.; Bergin, S. D.; King, P. J.; Khan, U.; Young, K.; Gaucher, A.; De, S.; Smith, R. J.; Shvets, I. V.; Arora, S. K.; Stanton, G.; Kim, H.-Y.; Lee, K.; Kim, G. T.; Duesberg, G. S.; Hallam, T.; Boland, J. J.; Wang, J. J.; Donegan, J. F.; Grunlan, J. C.; Moriarty, G.; Shmeliov, A.; Nicholls, R. J.; Perkins, J. M.; Grieveson, E. M.; Theuwissen, K.; McComb, D. W.; Nellist, P. D.; Nicolosi, V. Two-Dimensional Nanosheets Produced by Liquid Exfoliation of Layered Materials. *Science* **2011**, *331*, 568−571.

(7) Richards, R.; Li, W.; Decker, S.; Davidson, C.; Koper, O.; Zaikovski, V.; Volodin, A.; Rieker, T.; Klabunde, K. J. Consolidation of Metal Oxide Nanocrystals. Reactive Pellets with Controllable Pore Structure That Represent a New Family of Porous, Inorganic Materials. *J. Am. Chem. Soc.* **2000**, *122*, 4921−4925.

(8) Marella, R. K.; Prasad Neeli, C. K.; Rao Kamaraju, S. R.; Burri, D. R. Highly active Cu/MgO catalysts for selective dehydrogenation of benzyl alcohol into benzaldehyde using neither $O_2$ nor $H_2$ acceptor. *Catal. Sci. Technol.* **2012**, *2*, 1833−1838.

(9) Serena, S.; Sainz, M. A.; Caballero, A. The system Clinker−MgO−$CaZrO_3$ and its application to the corrosion behaviour of $CaZrO_3$/MgO refractory matrix by clinker. *J. Eur. Ceram. Soc.* **2009**, *29*, 2199−2209.

(10) Krishnamoorthy, K.; Moon, J. Y.; Hyun, H. B.; Cho, S. K.; Kim, S. J. Mechanistic investigation on the toxicity of MgO nanoparticles toward cancer cells. *J. Mater. Chem.* **2012**, *22*, 24610−24617.

(11) Makhluf, S.; Dror, R.; Nitzan, Y.; Abramovich, Y.; Jelinek, R.; Gedanken, A. Microwave-Assisted Synthesis of Nanocrystalline MgO and Its Use as a Bacteriocide. *Adv. Funct. Mater.* **2005**, *15*, 1708−1715.

(12) Bhargava, A.; Alarco, J. A.; Mackinnon, I. D. R.; Page, D.; Ilyushechkin, A. Synthesis and characterisation of nanoscale magnesium oxide powders and their application in thick films of $Bi_2Sr_2CaCu_2O_8$. *Mater. Lett.* **1998**, *34*, 133−142.

(13) Chen, J.; Xu, L.; Li, W.; Gou, X. $\alpha$-$Fe_2O_3$ Nanotubes in Gas Sensor and Lithium-Ion Battery Applications. *Adv. Mater.* **2005**, *17*, 582−586.

(14) Navale, S. T.; Bandgar, D. K.; Nalage, S. R.; Khuspe, G. D.; Chougule, M. A.; Kolekar, Y. D.; Sen, S.; Patil, V. B. Synthesis of $Fe_2O_3$ nanoparticles for nitrogen dioxide gas sensing applications. *Ceram. Int.* **2013**, *39*, 6453−6460.

(15) Peerakiatkhajohn, P.; Yun, J.; Chen, H.; Lyu, M.; Butburee, T.; Wang, L. Stable Hematite Nanosheet Photoanodes for Enhanced Photoelectrochemical Water Splitting. *Adv. Mater.* **2016**, *28*, 6405−6410.

(16) Ding, Y.; Zhang, G.; Wu, H.; Hai, B.; Wang, L.; Qian, Y. Nanoscale Magnesium Hydroxide and Magnesium Oxide Powders: Control over Size, Shape, and Structure via Hydrothermal Synthesis. *Chem. Mater.* **2001**, *13*, 435−440.

(17) Watari, T.; Nakayoshi, K.; Kato, A. Preparation of submicron magnesium oxide powders by vapor-phase reaction of magnesium and oxygen. *Nippon Kagaku Kaishi* **1984**, *6*, 1075−1076.

(18) Utamapanya, S.; Klabunde, K. J.; Schlup, J. R. Nanoscale metal oxide particles/clusters as chemical reagents. Synthesis and properties of ultrahigh surface area magnesium hydroxide and magnesium oxide. *Chem. Mater.* **1991**, *3*, 175−181.

(19) Guan, H.; Wang, P.; Zhao, B.; Zhu, Y.; Xie, Y. Synthesis of high surface area nanometer magnesia by solid-state chemical reaction. *Front. Chem. China* **2007**, *2* (2), 204−208.

(20) Beruto, D.; Botter, R.; Searcy, A. W. $H_2O$-Catalyzed Sintering of ~2-nm-Cross-Section Particles of MgO. *J. Am. Ceram. Soc.* **1987**, *70*, 155−159.

(21) Ristić, M.; Musić, S.; Godec, M. Properties of $\gamma$-FeOOH, $\alpha$-FeOOH and $\alpha$-$Fe_2O_3$ particles precipitated by hydrolysis of $Fe^{3+}$ ions in perchlorate containing aqueous solutions. *J. Alloys Compd.* **2006**, *417*, 292−299.




DOI: 10.1021/acssuschemeng.8b03952
ACS Sustainable Chem. Eng. 2018, 6, 15982−15987

(22) Liu, J.; Liang, C.; Zhang, H.; Zhang, S.; Tian, Z. Silicon-doped hematite nanosheets with superlattice structure. *Chem. Commun.* **2011**, *47*, 8040−8042.
(23) Hao, H.; Sun, D.; Xu, Y.; Liu, P.; Zhang, G.; Sun, Y.; Gao, D. Hematite nanoplates: Controllable synthesis, gas sensing, photocatalytic and magnetic properties. *J. Colloid Interface Sci.* **2016**, *462*, 315−324.
(24) Henrist, C.; Mathieu, J. P.; Vogels, C.; Rulmont, A.; Cloots, R. Morphological study of magnesium hydroxide nanoparticles precipitated in dilute aqueous solution. *J. Cryst. Growth* **2003**, *249*, 321−330.
(25) Tadic, M.; Panjan, M.; Damnjanovic, V.; Milosevic, I. Magnetic properties of hematite ($\alpha$-$Fe_2O_3$) nanoparticles prepared by hydrothermal synthesis method. *Appl. Surf. Sci.* **2014**, *320*, 183−187.
(26) Ma, X.; Ma, H.; Jiang, X.; Jiang, Z. Preparation of magnesium hydroxide nanoflowers from boron mud via anti-drop precipitation method. *Mater. Res. Bull.* **2014**, *56*, 113−118.
(27) Prasad, B.; Ghosh, C.; Chakraborty, A.; Bandyopadhyay, N.; Ray, R. K. Adsorption of arsenite ($As^{3+}$) on nano-sized $Fe_2O_3$ waste powder from the steel industry. *Desalination* **2011**, *274*, 105−112.
(28) Rajamma, R.; Ball, R. J.; Tarelho, L. A. C.; Allen, G. C.; Labrincha, J. A.; Ferreira, V. M. Characterisation and use of biomass fly ash in cement-based materials. *J. Hazard. Mater.* **2009**, *172*, 1049−1060.
(29) Fraay, A. L. A.; Bijen, J. M.; de Haan, Y. M. The reaction of fly ash in concrete a critical examination. *Cem. Concr. Res.* **1989**, *19*, 235−246.
(30) Ferreira, C.; Ribeiro, A.; Ottosen, L. Possible applications for municipal solid waste fly ash. *J. Hazard. Mater.* **2003**, *96*, 201−216.
(31) Yan, P.; Jiang, J.; Tian, S.; Liu, Z.; Shi, J.; Li, K.; Chen, X.; Xu, Y. A Green and Facile Synthesis of Ordered Mesoporous Nanosilica Using Coal Fly Ash. *ACS Sustainable Chem. Eng.* **2016**, *4*, 4654−4661.
(32) Lee, Y.; Soe, J.; Zhang, S.; Ahn, J.; Park, M.; Ahn, W. Synthesis of nanoporous materials via recycling coal fly ash and other solid wastes: A mini review. *Chem. Eng. J.* **2017**, *317*, 821−843.
(33) Sivalingam, S.; Sen, S. *Appl. Surf. Sci.* **2019**, *463*, 190−196.
(34) DUNENS, O. M.; MACKENZIE, K. J.; HARRIS, A. T. Synthesis of Multiwalled Carbon Nanotubes on Fly Ash Derived Catalysts. *Environ. Sci. Technol.* **2009**, *43*, 7889−7894.
(35) Sahoo, P. K.; Kim, K.; Powell, M. A.; Equeenuddin, S. M. Recovery of metals and other beneficial products from coal fly ash: a sustainable approach for fly ash management. *Int. J. Coal Sci. Technol.* **2016**, *3*, 267−283.
(36) Valeev, D.; Mikhailova, A.; Atmadzhidi, A. Kinetics of Iron Extraction from Coal Fly Ash by Hydrochloric Acid Leaching. *Metals* **2018**, *8* (7), 533.
(37) Hosseini, T.; Selomulya, C.; Haque, N.; Zhang, L. Indirect carbonation of victorian brown coal fly ash for $CO_2$ sequestration: multiple-cycle leaching-carbonation and magnesium leaching kinetic modelling. *Energy Fuels* **2014**, *28*, 6481−6493.
(38) Valentim, B.; Bialecka, B.; Gonçalves, P.; Guedes, A.; Guimarães, R.; Cruceru, M.; Calus-Moszko, J.; Popescu, L.; Predeanu, G.; Santos, A. Undifferentiated Inorganics in Coal Fly Ash and Bottom Ash: Calcispheres, Magnesiacalcispheres, and Magnesiaspheres. *Minerals* **2018**, *8*, 140.
(39) Beaudoin, G.; Nowamooz, A.; Assima, G. P.; Lechat, K.; Gras, A.; Entezari, A.; Kandji, E. H. B.; Awoh, A.-S.; Horswill, M.; Turcotte, S.; Larachi, F.; Dupuis, C.; Molson, J.; Lemieux, J.-M.; Maldague, X.; Plante, B.; Bussière, B.; Constantin, M.; Duchesne, J.; Therrien, R.; Fortier, R. Passive Mineral Carbonation of Mg-rich Mine Wastes by Atmospheric $CO_2$. *Energy Procedia* **2017**, *114*, 6083−6086.
(40) Barrios, M. S.; González, L. V. F.; Rodríguez, M. A. V.; Pozas, J. M. M. Acid activation of a palygorskite with HCl: Development of physico-chemical, textural and surface properties. *Appl. Clay Sci.* **1995**, *10*, 247−258.
(41) Choo, T. K.; Etschmann, B.; Selomulya, C.; Zhang, L. Behavior of $Fe^{2+/3+}$ Cation and Its Interference with the Precipitation of $Mg^{2+}$ Cation upon Mineral Carbonation of Yallourn Fly Ash Leachate under Ambient Conditions. *Energy Fuels* **2016**, *30*, 3269−3280.
(42) Ma, B.; Li, X.; Shen, X.; Mao, Y.; Huang, H. Enhancing the addition of fly ash from thermal power plants in activated high belite sulfoaluminate cement. *Constr. Build. Mater.* **2014**, *52*, 261−266.
(43) Pace, M. L.; Telesca, A.; Marroccoli, M.; Valenti, G. L. Use of Industrial Byproducts as Alumina Sources for the Synthesis of Calcium Sulfoaluminate Cements. *Environ. Sci. Technol.* **2011**, *45*, 6124−6128.
(44) Trpkov, D.; Panjan, M.; Kopanja, L.; Tadic, M. Hydrothermal synthesis, morphology, magnetic properties and self-assembly of hierarchical $\alpha$-$Fe_2O_3$ (hematite) mushroom-, cube- and sphere-like superstructures. *Appl. Surf. Sci.* **2018**, *457*, 427−438.
(45) Marchetti, S. G.; Spretz, R.; Ulla, M. A.; Lombardo, E. A. Identification of the species formed in the Fe/MgO system: A Raman and Mössbauer study. *Hyperfine Interact.* **2000**, *128*, 453−466.
(46) Selvamani, T.; Yagyu, T.; Kawasaki, S.; Mukhopadhyay, I. Easy and effective synthesis of micrometer-sized rectangular MgO sheets with very high catalytic activity. *Catal. Commun.* **2010**, *11*, 537−541.
(47) Kumari, L.; Li, W. Z.; Vannoy, C. H.; Leblanc, R. M.; Wang, D. Z. Synthesis, characterization and optical properties of $Mg(OH)_2$ micro-/nanostructure and its conversion to MgO. *Ceram. Int.* **2009**, *35*, 3355−3364.



DOI: 10.1021/acssuschemeng.8b03952
ACS Sustainable Chem. Eng. 2018, 6, 15982−15987

# Appendix B
# Chapter 4 in publication form

Appendix B

Journal of Hazardous Materials 395 (2020) 122696

Contents lists available at ScienceDirect

Journal of Hazardous Materials

journal homepage: www.elsevier.com/locate/jhazmat

# Synthesis of *in-situ* $Al^{3+}$-defected iron oxide nanoflakes from coal ash: A detailed study on the structure, evolution mechanism and application to water remediation

Binbin Qian[a], Cheng Liu[a], Jun Lu[a], Meipeng Jian[a], Xiaoyi Hu[a], Song Zhou[a], Tara Hosseini[a], Barbara Etschmann[b], Xiwang Zhang[a], Huanting Wang[a], Lian Zhang[a,*]

[a] Department of Chemical Engineering, Monash University, Wellington Road, Clayton, Victoria 3800, Australia
[b] School of Earth, Atmosphere and Environment, Monash University, Clayton, Victoria 3800, Australia

ARTICLE INFO

Editor: Xiaohong Guan
*Keywords:*
Crystal growth
Defect engineering
Nanoflakes
Water chemistry
Waste recovery

ABSTRACT

The recovery of value-added materials from coal ash waste is of highly economic value and sustainable significance. However, researches on the synthesis of defect-engineering nanomaterials from coal ash are still blank. Herein, iron oxide ($Fe_{1.72}Al_{0.28}O_3$, simplified as FAO) nanoflakes were successfully synthesized from a brown coal fly ash (BCFA) waste. The obtained FAO nanoflakes possess a round-shape morphology with a diameter of around 300 nm and 50 nm in thickness. With the progress of hydrothermal treatment, the impure $Al^{3+}$ gradually replaced part of the $Fe^{3+}$ in the $\alpha$-$Fe_2O_3$ crystal. Specifically, $Al^{3+}$ was preferentially adsorbed on the (001) facet, hindering the growth of $Fe^{3+}$ on the [001] direction and thus causing the flattening of the resultant FAO. The introduced $Al^{3+}$ also serves as the disordered defects on the hematite surface, leading to decreased crystal parameters for hematite, the formation of a compact first shell and a reduced periodical symmetry for the central cation $Fe^{3+}$. The defects were also found to significantly improve the adsorption capacity of the resultant FAO for Cr(VI), As(V), As(III) and Congo red in waste water, with the maximum adsorption capacity of 68.3, 80.6, 61.1 and 213.8 mg $g^{-1}$, respectively. Cyclic tests also confirmed a relatively strong stability for the as-synthesised adsorbents.

## 1. Introduction

Reducing the waste volume and even reusing the waste in value-added ways are critical for a sustainable development of the future economy. Over years, the environmental concerns related to the waste management have been receiving increased attention (Schwarzenbach et al., 2006; Colón et al., 2012). Out of the most common industrial wastes, coal fly ash is one largest contributor as a solid waste, due to the fact that coal remains as the single largest solid fuel for power generation in most of the countries. Each year, around 750 million tonnes of coal fly ash is generated in the world (Blissett and Rowson, 2012). In Australia, the annual production of coal fly ash waste is estimated to reach over ten million tonnes, however, most of which is directly dumped into ash ponds, contaminating the soil and groundwater. Therefore, the utilization of this abundant solid waste has been raised as an urgent local and even global issue. Traditionally, coal fly ash is used as a low-value additive into the cement or concrete (Palomo et al., 1999), geotechnology (Rogbeck and Hartlén, 1996) and others (Pandey and Singh, 2010). Recently, for the sake of the environmental sustainability, plenty of efforts have been made to synthesize various nanomaterials from fly ash, such as $Ca_5Si_6Al(OH)O_{16}{\cdot}5H_2O$ nanosheets (Bai et al., 2015), carbon nanotubes (Dunens et al., 2009), $SO_4^{2-}$-$SnO_2$ catalyst (Thirumurthy and Thirunarayanan, 2015), mesoporous nanosilica (Yan et al., 2016), zeolite (Wang et al., 2003; Liu et al., 2013) and others (Khatri and Rani, 2008; Li and Zhang, 2010). However, most of these synthesized nanomaterials are relevant to alumina and/or silica which are the matrix for the coal ashes derived from high-rank coals. For the ash derived from a low-rank coal such as brown coal, it is implausible to synthesize these Al-/Si-rich nano-particles, due to the shortage of these two elements in the respective ashes.

Owing to the unique properties and excellent applications, nanomaterials with lower value in one dimension such as nanosheets, nanoflakes, nanodisks and nanocakes have been widely developed in the nanoparticle research field (Coleman et al., 2011; Alnasser et al., 2019; Zhang et al., 2017). With the use of pure reagent grade chemicals, a variety of new methodologies have been developed for the synthesis of

* Corresponding author.
*E-mail address:* lian.zhang@monash.edu (L. Zhang).

https://doi.org/10.1016/j.jhazmat.2020.122696
Received 30 December 2019; Received in revised form 1 April 2020; Accepted 9 April 2020
0304-3894/ © 2020 Elsevier B.V. All rights reserved.

# Appendix B



these nanomaterials. However, the synthesis of low-dimensional nanomaterials from solid waste including fly ash is rarely reported, which provides an opportunity and challenge for low-cost nanomaterial production (Ruan et al., 2011; Genovese et al., 2015; Gong et al., 2015; Qian et al., 2018). Hereby, considering that the BCFA collected from a local power generation station in the state of Victoria, Australia is rich in Fe (Choo et al., 2014, 2016; Hosseini et al., 2014), we hypothesized that this Fe-rich coal fly ash could be a potential raw material to synthesize Fe-based low-dimensional nanomaterials. If successful, the fly ash-derived Fe-based nanomaterials could be used to replace those derived from pure reagent grade chemicals, such as $\alpha$-$Fe_2O_3$, $\gamma$-$Fe_2O_3$, $Fe_3O_4$ and FeOOH. Consequently, this would greatly improve the diversification of low-rank coal ash utilization and the values of its derivatives. In addition, considering that fly ash is a mixture of a broad variation of different elements, it is unknown how the impure cations such as $Al^{3+}$ would affect the structure and function of the resultant Fe-bearing nanoparticles. Answering such a question is another key research goal of this paper, which is believed to contribute to the fundamental science underpinning the nanoparticle growth.

Herein, for the first time, we report the synthesis of a new *in-situ* $Al^{3+}$-substituted $\alpha$-$Fe_2O_3$ nanoflakes from BCFA waste, through an initial acid leaching-alkaline precipitation process and subsequent hydrothermal treatment. The evolution of morphologies, lattice parameters, crystal structures and atomic environments have been investigated intensively, in order to elaborate the influence of $Al^{3+}$, an impure and inherent cation derived from fly ash that is unlikely fully separated out of fly ash leachate. In addition, to validate the high performance of the as-synthesized nanoflakes, adsorption tests including cyclic trials have been conducted extensively for a variety of typical heavy metal ions and inorganic dyes in waste water, including Cr(VI), As(V), As(III) and Congo red. These contaminants in waste water are highly toxic and carcinogenic (Nordstrom, 2002; Mattagajasingh et al., 2008; Kang et al., 2018; Cramer and Cole, 2017). The Fe-bearing nanostructures are environmentally friendly, non-toxic, and corrosion-resistant, and hence, have been tested widely in this field (Ai et al., 2007; Wei et al., 2013; Pastora et al., 2014; Yang et al., 2014; Wang et al., 2013, 2012). However, compared with the pure chemicals, the presence of impure $Al^{3+}$ within the BCFA is supposed to alter the crystal structure of hematite, thereby resulting in enhanced adsorption performance. To the best of our knowledge, there is still a lack of studies on the influence of impurities on the structure and performance of Fe-bearing nanoflake. Therefore, this work is expected to establish new knowledge and to open a new avenue to synthesize $\alpha$-$Fe_2O_3$ nanoflakes from low-rank coal fly ash, an otherwise valueless solid waste.

## 2. Experimental

### 2.1. Materials

The BCFA waste was collected from the Energy Australia Yallourn power plant located in the Latrobe Valley, Victoria, Australia. Table S1 shows the chemical composition of the fly ash sample. It is clear that iron (Fe) is the most abundant element in this fly ash. The as-received fly ash sample was washed at a liquid to solid (L/S) mass ratio of 10 to remove the unburnt carbon and water-soluble species. Subsequently, the fly ash sample was dried in an oven at 105 °C for 12 h and then ground using a tungsten-carbide vibratory ring pulverizer, producing a particle size of less than 150 $\mu$m prior to use. All the chemicals including NaOH, $FeCl_3{\cdot}6H_2O$, $Al(NO_3)_3{\cdot}9H_2O$, HCl (32 *wt*%), $HNO_3$ (65 *wt*%), $K_2Cr_2O_7$, $Na_2HAsO_4{\cdot}7H_2O$ and Congo red were purchased from Sigma-Aldrich. Milli-Q water was used throughout all the experiments.

### 2.2. Synthesis of FAO nanoflakes

A two-step cross-current leaching method was used to extract $Fe^{3+}$ from the Victorian BCFA, as shown in Fig. S1. Due to the presence of most of the $Fe^{3+}$ in a stable spinel structure such as magnesium ferrite ($MgFe_2O_4$) (Choo et al., 2014), in each step, 32 *wt*% HCl was used as the leaching agent to mix with water-washed fly ash or the leaching residue derived from the previous step, at a L/S mass ratio of around two in a closed 250 mL conical flask. The flask was further put in a thermostatically controlled water bath at 60 °C and stirred for a period of 90 min. The stirring rate was controlled at 300 rpm throughout all the runs. After leaching, the slurry was immediately filtered via a vacuum pump and a filter paper with a cut-off size of 450 µm. As shown in Fig. S2, the resultant leachate is dominated by $Fe^{3+}$ and $Mg^{2+}$ due to the breakage of the spinel. However, a small amount of $Ca^{2+}$ and $Al^{3+}$ is also introduced into the leachate, probably due to their co-existence with $Fe^{3+}$ and $Mg^{2+}$ in the spinel. Subsequently, 1 mol/L NaOH was added dropwise into the leachate until its pH reached 3.6, forming a slurry that was then centrifuged at 10,000 rpm for 10 min to obtain the $Fe(OH)_3$ precipitate. The precipitate was washed three times with Milli-Q water. Afterwards, the precipitate was mixed with 40 mL of Milli-Q water and put into an ultrasonic bath for 1 h. Then 1 mol/L of NaOH solution was further dropped into the resultant slurry to adjust its final pH to 6, resulting in new slurry that was transferred into a number of 150 mL autoclaves and placed inside a preheated hot-air oven maintained at 180 °C. At different time intervals, the autoclaves were taken out and cooled down to room temperature naturally. The obtained precipitates were filtered and immersed in ethanol for 24 h, filtered and washed with distilled water three times to remove NaOH and then with ethanol to reduce the agglomeration, and finally dried at 80 °C for 2 h.

As a control experiment, synthesis of pure standard $\alpha$-$Fe_2O_3$ nanoparticles based on the use of chemical grade $FeCl_3{\cdot}6H_2O$ with and without the doping of $Al^{3+}$ was also conducted. In a typical experiment, around 3.25 g of $FeCl_3{\cdot}6H_2O$ was dissolved in 20 mL Milli-Q water, forming a solution of 0.1625 g/mL $FeCl_3{\cdot}6H_2O$ that is comparable with the leachate derived from fly ash. The following steps for the precipitation of $\alpha$-$Fe_2O_3$ out of this solution are exactly the same as those described above.

### 2.3. Adsorption experiment

Cr(VI) and As(III and V) solutions were made by dissolving $K_2Cr_2O_7$, $NaAsO_2$ and $Na_2HAsO_4{\cdot}7H_2O$ into Milli-Q water, respectively. Adsorption isotherm experiments were conducted in 200 mL beakers containing these heavy metal ion solutions with concentrations from 5–500 mg $L^{-1}$. The pH of the solution was adjusted to 6.0 ± 0.1 with dilute HCl and NaOH. After 0.03 g of adsorbents was added to the 50 mL of each solution in a glass beaker, the whole solution was stirred magnetically at 200 rpm at 25.0 ± 1 °C for 24 h. The solid and liquid were separated by centrifuge to measure the concentrations of the remaining arsenic and chromium in the liquid solutions. To determine the adsorption kinetic, the initial concentrations of these heavy metal ions were fixed at 40 mg $L^{-1}$, and the test lasted 300 min for each run. All the other conditions are the same as the isotherm experiments.

Congo red ($C_{32}H_{22}N_6O_6S_2Na_2$) was selected as a typical organic water pollutant (Pastora et al., 2014). Different amounts of adsorbents were mixed with 50 mL of 100 mg $L^{-1}$ Congo red solutions. After each solution (loaded with adsorbent) was stirred magnetically for 12 h, the adsorbents were separated by centrifuge and the supernatant solutions were analyzed by UV–vis spectroscopy (Shimadzu, Model 2600). The remaining concentration of Congo red was determined by the absorbance bands at $\lambda_{max}$ = 498 nm using a linear calibration curve over 5–80 mg $L^{-1}$. To evaluate the maximum adsorption capacity, the initial concentrations of Congo red was varied from 10 to 500 mg $L^{-1}$ and 0.025 g adsorbent was added into 50 mL (0.5 g $L^{-1}$) of the Congo red solutions in 200 mL beakers. These beakers were further stirred magnetically at 200 rpm at 25.0 ± 1 °C for 12 h. Afterwards, the solid and liquid were separated by centrifuge and UV–vis spectroscopy was employed to measure the remaining Congo red concentrations in the supernatant. To determine the adsorption kinetic, the initial

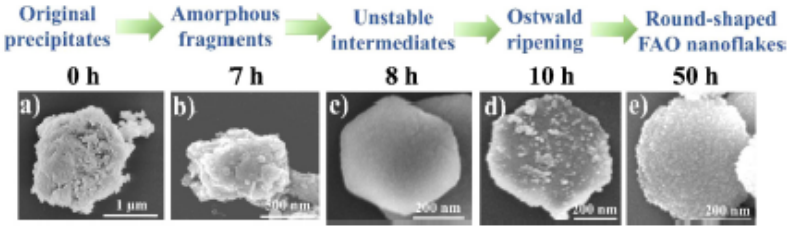


Fig. 1. SEM images and growing process of hydrothermal products synthesized from BCFA at different hydrothermal treatment duration. (a) 0 h, (b) 7 h, (c) 8 h, (d) 10 h, and (e) 50 h.

concentration of these heavy metal ions was fixed at 100 mg $L^{-1}$, and the test lasted 300 min for each run. All the other conditions are the same as the isotherm experiments. Note that cyclic tests were also conducted to test the stability of the synthesized FAO. For the cyclic heavy metal adsorption test, the spent FAO nanoflake was washed by 0.05 mol $L^{-1}$ NaOH solution for 12 h and then Milli-Q water to reach a neutral pH prior to the next cycle. For the cyclic Congo red adsorption test, the spent FAO nanoflake was washed by ethanol under ultrasonication three times, and further washed by Milli-Q water prior to next cycle. The conditions were the same as adsorption kinetic experimental parameters.

### 2.4. Material characterization

X-ray diffraction (XRD) analysis was used for phase identification and the determination of unit cell parameters. The XRD patterns were recorded on a Rigaku SmartLab 3000A diffractometer with Cu Kα radiation (λ = 0.15406 nm). The X-ray tube was operated at 40 kV and 15 mA. The synthesized samples were scanned between 20° and 80° with a D/teX Ultra detector, at a scanning speed of 5°/min. Morphologies and structures of the as-synthesized materials were characterized by scanning electron microscopy (SEM) (FEI Nova NanoSEM 450 FEGSEM) and scanning transmission electron microscopy (STEM) (FEI Tecnai G2 F20 S-TWIN STEM). X-ray photoelectron spectra (XPS) was determined by using an AXIS Ultra spectrometer (Escalab 250Xi, Thermo Fisher Scientific, USA) with an Al Kα anode. Fe K-edge X-ray absorption near-edge spectroscopy (XANES) and extended X-ray absorption fine structure spectroscopy (EXAFS) were conducted at Beamline BL16A1 of NSRRC (National Synchrotron Research Radiation Centre) in Taiwan. Fe K-edge XANES spectra were processed using ATHENA software (a part of DEMETER package) and Fe EXAFS data were fitted using Artemis (part of Demeter) with FEFF version 8.

Inductively coupled plasma optical emission spectroscopy (ICP-OES, Optima 7000 DV, PerkinElmer) was used to quantify the ratio of Al in the as-synthesized FAO nanoflakes and the concentration of Cr and as after adsorption experiments. To determine the atomic composition of the as-synthesized products, about 0.01 g FAO nanoflakes was used and dissolved into 50 mL of 65 wt% $HNO_3$ at room temperature. After 24 h, the solid sample was found completely dissolved, forming a clear yellow solution that is ready for the ICP analysis.

UV–vis spectroscopy (Shimadzu, Model 2600) was used to determine the concentrations of remaining Congo red after adsorption experiments.

## 3. Results and discussion

### 3.1. Synthesis of FAO nanoflakes

Since the BCFA waste contains a significant amount of $Fe_2O_3$ (33.5 wt%, Table S1), and the two-step strong HCl leaching process (Fig. S1) is successful in breaking the spinel structure, approximately 95 % of iron was leached out of fly ash and all of the resultant $Fe^{3+}$ precipitated out upon the increase of the leachate pH up to 3.6. Meanwhile, a small fraction of $Al^{3+}$ was also leached out and partially co-precipitated out with $Fe^{3+}$ due to the overlapped pH precipitation range (Dyer et al., 1998). Effort has been made by fine tuning the leachate pH value to eliminate the precipitation of $Al^{3+}$. However, it was unsuccessful, causing either incomplete precipitation of $Fe^{3+}$, or the precipitation of other cations such as $Ca^{2+}$ and $Mg^{2+}$, which were also leached out and preferentially precipitated at higher pH value. In this sense, the final pH value was optimised at 3.6, causing the presence of around 7.23 wt% $Al^{3+}$ in the form of $Al_2O_3$ and a few trace elements such as CaO and MgO in the final precipitate, as shown in Table S1. However, the yield of the resultant FAO is high, reaching 32 % on the mass basis of water-washed and dried fly ash. To date, such a high yield has yet to be reported for the synthesis of any other nano-sized materials from coal fly ash. More specifically, the as-synthesized precipitate from fly ash was found to bear a BET specific surface area of 80.12 $m^2 g^{-1}$, which is far larger than the pure α-$Fe_2O_3$ nanoparticle (synthesized under the same condition as FAO) with a specific surface area of only 31.73 $m^2 g^{-1}$, as shown in Fig. S3(a). The pore size analysis of the FAO is shown in Fig. S3(b). It is obvious that a sharp pore distribution with an average diameter of 3.7 nm is estimated by the Barrett – Joyner – Halenda (BJH) method. In addition, it is noteworthy that the final leaching residue possesses a chemical composition (Table S1) that is close to silicon adjustment raw material (Palomo et al., 1999), which is a potential material to be used in the Portland cement clinker manufacturing industry.

### 3.2. Micro-structural morphology of as-synthesized FAO nanoflakes

Fig. 1 visualizes the growth dynamic underpinning the crystal precipitation in the hydrothermal treatment stage. For the original precipitate prior to the hydrothermal treatment, the $Fe^{3+}$-bearing particle suspended in the slurry shows an irregular structure with individual seeds agglomerating into clusters of 1 – 2 μm in diameter (Fig. 1(a)). The irregularity remained unchanged in the first five hours for the hydrothermal treatment, as demonstrated in Fig. S4(a)-(c). Starting from the duration of 7 h in Fig. 1(b), the coarse clusters commenced to collapse into smaller fragments with a size less than 1 μm on average. Interestingly, remarkable changes occurred when the hydrothermal time increased to 8 h. The clusters are fully gone and replaced by individual particles with tiny wrinkles on surface. The entire morphology for each single particle also shows a uniformly regular hexagonal structure with a nominal diameter of around 500 nm (Fig. 1(c)). The evolution of the morphology continued when the hydrothermal time was further extended to 10 h. As shown in Fig. 1(d), the surface turned rough again, with numerous debris deposited on the surface of the hexagonal hematite. However, most of the debris disappeared in another 10 h, whilst the hexagonal shape gradually turned into a round shape with a comparatively smooth surface shown in Fig. S4(e). This is mainly due to the Ostwald ripening effect, which can be briefly

described as the growth of larger crystals at the expense of smaller ones deposited on them (Xie et al., 2017; Yu et al., 2018). In our study, a longer hydrothermal process benefits the growth of the unstable crystals and the deposition of smaller debris (crystals) on larger the particles. Eventually, the smaller debris will be embedded within the matrix to form round nanoflakes. With the hydrothermal treatment duration being extended beyond 20 h, the shape transition is almost complete here.

Finally, the product achieved for the longest hydrothermal treatment duration of 50 h, as shown in Fig. 1(e), was found to consist predominantly of round nanoparticles with a diameter of around 300 nm each. These nanoparticles formed here are also rather flat, as demonstrated in Fig. S4(f). For simplification, this final product is termed as FAO nanoflakes hereafter. In addition, a close view of the single particle surface, as shown in Fig. 1(e), still confirmed a non-smooth surface with abundance of tiny seeds, which might be associated with the effect of impure $Al^{3+}$ on the growth process.

To prove this hypothesis, two extra efforts were made to synthesize the $\alpha$-$Fe_2O_3$ nanoparticles based on the use of pure $Fe^{3+}$ solution (made from $FeCl_3{\cdot}6H_2O$) with and without the addition of $Al^{3+}$ at a same concentration to the fly ash leachate, respectively. As demonstrated in Fig. S5, in the case of using pure $FeCl_3$ with the absence of $Al^{3+}$, the final product exhibits a polyhedron structure with an average size of around 100 nm in Fig. S5(a), whereas the addition of extra $Al^{3+}$ induced the flattening of the particle and the formation of a relatively rough surface with plenty of defects in Fig. S5(b). The final morphology in Fig. S5(b) also resembles well with the $Al^{3+}$-substituted $\alpha$-$Fe_2O_3$ nanoflake synthesized from fly ash in Fig. 1(e).

### 3.3. $Al^{3+}$-defect determination and formation mechanism

Fig. 2(a) shows the XRD patterns of the as-synthesized standard $\alpha$-$Fe_2O_3$ nanoparticles and FAO nanoflake in 50 h. The diffraction peaks of FAO nanoflakes match well with those of standard $\alpha$-$Fe_2O_3$ nanoparticles, indicating that the entire crystal structure of FAO nanoflakes is the rhombohedral $\alpha$-$Fe_2O_3$. However, there is a slight shift to higher degree of the 2θ positions for FAO, which is demonstrated in Fig. 2(a) inset. According to the Bragg laws of $2d\sin\theta = n\lambda$, for an identical X-ray wavelength of $\lambda = 0.15406$ nm, the increase in 2θ corresponds to a decrease in the d-spacing, which is an indicator of the reduction on the magnitude of the lattice parameters of hematite. Again, such a decrease in lattice parameters should be mainly attributed to the presence of impure $Al^{3+}$ within the FAO nanoflake. During the hydrothermal treatment step, the impure $Al^{3+}$ would enter into the $\alpha$-$Fe_2O_3$ lattice and replace a portion of $Fe^{3+}$ ion to form an *in-situ* substitutional solid solution of $Fe_{2-x}Al_xO_3$. The ionic radius of 0.053 nm for $Al^{3+}$ is smaller than $Fe^{3+}$ at 0.06 nm, and hence, the substitutional solid solution $Fe_{2-x}Al_xO_3$ meets the Hume-Rothery rules satisfactorily (Laissardière et al., 2005):

$$\%\ difference = \left|\frac{r_1 - r_2}{r_2}\right| \times 100\ \% \leq 15\% \quad (1)$$

Where $r_1$ is the solute ionic radius for $Al^{3+}$ and $r_2$ is the solvent ionic radius for $Fe^{3+}$. The difference of 11.67 % between these two radiuses is smaller than 15 %, favouring the formation of $Fe_{2-x}Al_xO_3$. Regarding the other impure ions such as $Ca^{2+}$, it can be ruled out here because the radius of $Ca^{2+}$ is 0.1 nm and its difference to $Fe^{3+}$ is 66.67 %, which is not favourable to form a stable solid solution.

To further verify the $Al^{3+}$-induced defects in FAO nanoflakes, XPS spectrum of the as-synthesized FAO nanoflakes was recorded to determine the O 1s chemical states, as shown in Fig. 2(b). Only two peaks were observed, 529.3 eV and 531.8 eV, which are attributed to the Fe-O-Fe bond (Yu et al., 2015) and the Al−OH bond (Sun et al., 2017; Fang et al., 2013), respectively. The existence of Al−OH bonds rather than Al-O-Al proved a preferential bonding of impure $Al^{3+}$ with the hydroxyl functional group on the surface. Additionally, XPS spectra for Fe 2p and Al 2p were also conducted (Fig. S6). The two major peaks together with two satellites (sat.) in Fe 2p spectrum are clearly observed, which are located at 711.3 eV ($Fe2p_{3/2}$), 725.0 eV ($Fe2p_{1/2}$), 719.8 eV ($Fe2p_{3/2}$ sat.), and 733.9 eV ($Fe2p_{1/2}$ sat.), respectively. And one peak for Al 2p spectrum is located at 73.9 eV. All these are the features for the co-existence of chemical states of $Fe^{3+}$ and $Al^{3+}$ in the FAO nanoflakes (Yu et al., 2015; Fang et al., 2013). Surface functional groups of the FAO nanoflakes were further characterized by Fourer Transformed Infrared Spectroscopy (FTIR), as shown in Fig. S7. The adsorption bands around 440 and 530 $cm^{-1}$ are attributed to the Fe-O bond vibration from crystalline $\alpha$-$Fe_2O_3$ (Kang et al., 2018). The bonds near 1000 $cm^{-1}$ correspond to residual hydroxyl groups (Ai et al., 2007). In addition, some weak peaks distributed around 3700 $cm^{-1}$ also correspond to the hydroxyl groups (Kang et al., 2018).

TEM imaging analyses of the final FAO nanoflakes synthesized in 50 h hydrothermal treatment are shown in Fig. 3. In Fig. 3(a), one can further verify the formation of a round shape with an averaged diameter of ~300 nm and a thickness of approximately 50 nm. In addition, the inset of Fig. 3(a) for the corresponding selected area electron diffraction (SAED) pattern demonstrates the presence of multiple-ring diffraction spots for the various orientations of the as-synthesized nanoflake. In addition to the {1 1 0} and {3 0 0} equivalent facets (red in inset) from $\alpha$-$Fe_2O_3$, another set of diffraction spots is also detected, which can be indexed to the {0 1 2} and {1 1 3} equivalent facets from $\alpha$-$Al_2O_3$. Fig. 3(b) demonstrates that the building blocks of a single FAO nanoflake are individually around 5 nm in size. Interestingly, these

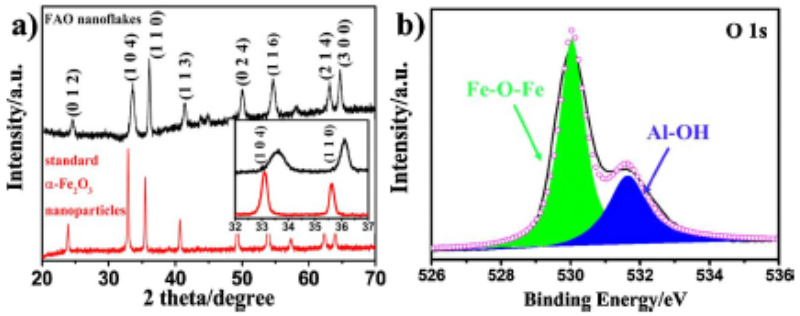


Fig. 2. XRD and XPS analysis of as-synthesized samples. (a) XRD pattern of standard $\alpha$-$Fe_2O_3$ nanoparticles and FAO nanoflakes (Inset: selected 2 theta range from 32-37 degree), (b) The measured (solid line) and corresponding fitting curve (dashed line) of XPS O 1s of FAO nanoflakes.

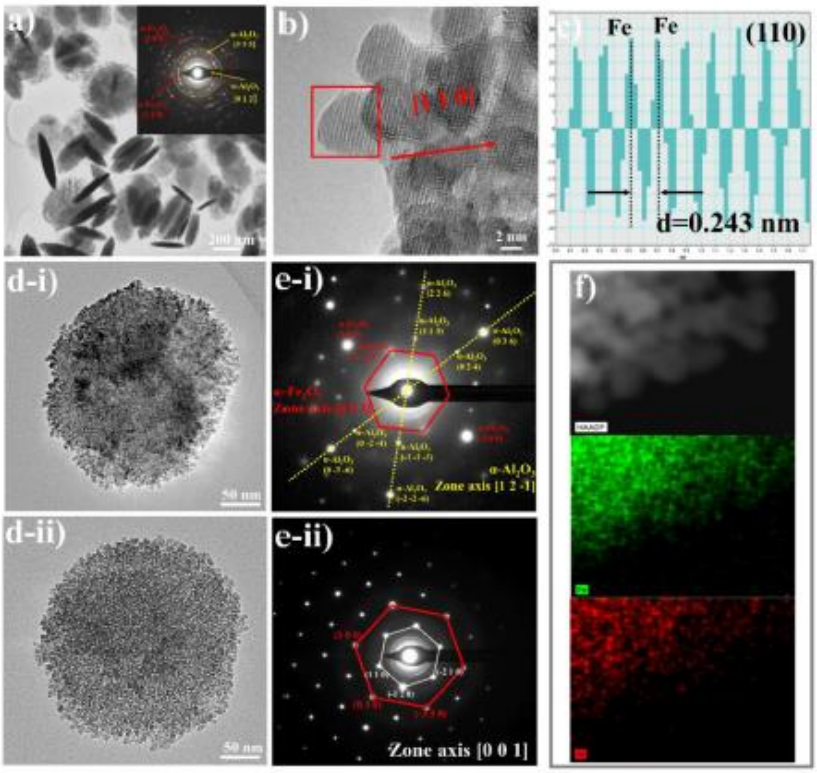


Fig. 3. TEM images of FAO nanoflakes (hydrothermal treatment time of 50 h) synthesized from BCFA. (a) An overall view of round-shaped FAO nanoflakes with various orientations (inset: SAED of (a)), (b) High magnification TEM from (a), (c) The corresponding intensity profiles of the red box from (b), (d-i) and (d-ii) are two crystallized cases of single FAO nanoflake, (e-i) and (e-ii) are SAED of (d-i) and (d-ii), respectively, (f) From top to bottom: HAADF-STEM image of region characterization from (d), element mapping of Fe (green) and Al (red) (For interpretation of the references to colour in this figure legend, the reader is referred to the web version of this article).

nanoparticles seemingly self-orientate together to form an ultimately round nanoflake. The clear fringe d-spacing value in Fig. 3(b) was measured as ~ 0.251 nm that concurs well with the interplanar spacing of (1 1 0) for $\alpha$-$Fe_2O_3$. Clearly, the individual crystals preferentially assembled on this direction for the formation of flat nanoflake observed here. Additionally, owing to the preferential orientation of (1 1 0) facet, the X-ray diffraction intensity for this facet was enhanced remarkably, as evident in Fig. 2(a).

Fig. 3(c) is the corresponding intensity line profile from the red box in Fig. 3(b). It clearly demonstrates a adjacent Fe position value (d-spacing value) of 0.243 nm, which falls right between the $d_{(1\ 1\ 0)}$ of 0.251 nm for $\alpha$-$Fe_2O_3$ and $d_{(1\ 1\ 0)}$ of 0.238 nm for $\alpha$-$Al_2O_3$, indicating that $Al^{3+}$ replaced $Fe^{3+}$ position from the original $\alpha$-$Fe_2O_3$ and caused the reduction on the d-spacing of (1 1 0). The reduced d-spacing is highly consistent with the XRD results of $2\theta_{(1\ 1\ 0)}$ of around 36.15° (Cu K$\alpha$) based on the Bragg laws.

Fig. 3(d–i) and (d-ii) are two typical crystal structures for the single nanoflakes. Intriguingly, the whole single nanoflake exhibits a "single-crystal" feature, as suggested by the respective SAED patterns in Fig. 4 (e-i) and (e-ii), respectively. From Fig. 3(e–i), the SAED pattern is composed of two sets of diffraction spots, corresponding to an electron beam parallel to the zone axis [0 0 1] of $\alpha$-$Fe_2O_3$ and [1 2 -1] of $\alpha$-$Al_2O_3$. From Fig. 3(e-ii), the inter-cross hexagonal diffraction spots can be indexed to the [0 0 1] zone axis for single-crystal structured rhombohedral $\alpha$-$Fe_2O_3$. However, the round-shaped nanoflake still has an incomplete morphology (indented outlines) compared with a perfect hexagonal nanoparticle derived from a single crystal. Thereby, the resultant nanoflake should be deemed as a "pseudo-single-crystal hematite" structure. Clearly, for the lattice distortions, the corresponding SAED (Fig. 3(e-i)) is simply a spatial overlay composed of two sets of diffraction spots from $\alpha$-$Fe_2O_3$ and $\alpha$-$Al_2O_3$ rather than within a periodic superlattice structure. Therefore, this implies that the $Al^{3+}$-induced crystal defects are present in a highly disordered manner within the FAO nanoflake. This is also substantiated by the noticeable difference between the diffraction patterns in Fig. 3(d-ii) and (e-ii)). The similar phenomena have been reported for the doping of tin (Sn) as dopant into $\alpha$-$Fe_2O_3$ (Aoshima et al., 2012).

Finally, Fig. 3(f) is a close-up region from Fig. 3(d–i) in high-angle annular dark-field (HAADF)-STEM. The corresponding elemental mapping images reveal that Fe and Al are homogeneously distributed

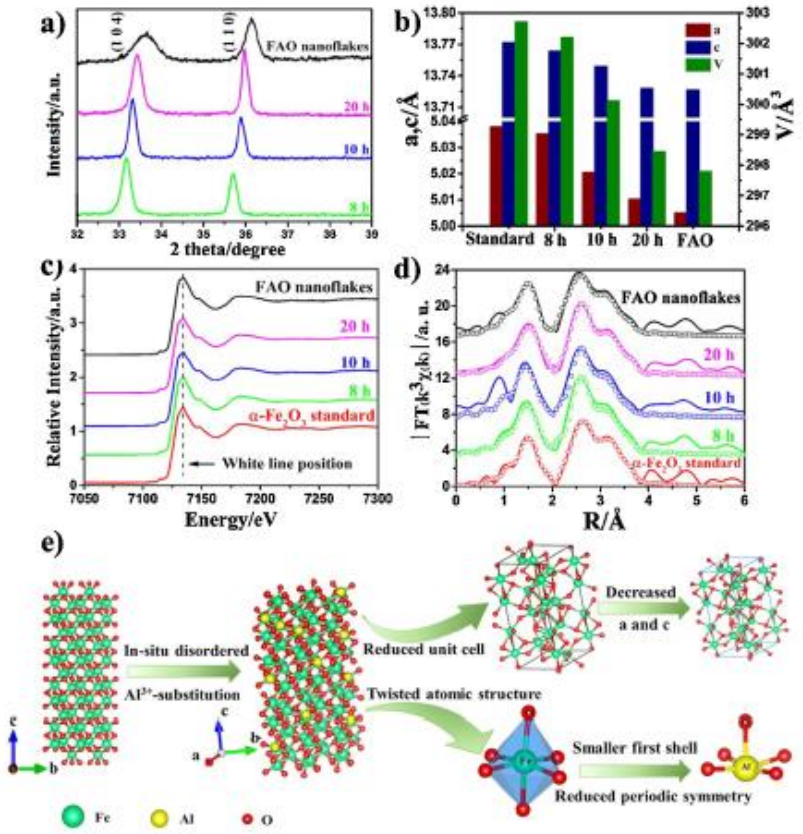


Fig. 4. XRD and XAS analysis of as-synthesized α-$Fe_2O_3$ products synthesized from BCFA. (a) A selected range of XRD patterns of $Fe_2O_3$ at the hydrothermal treatment duration of 8 h, 10 h, 20 h and 50 h (FAO nanoflakes), (b) Lattice parameters of a value, c value and cell volume of $Fe_2O_3$ calculated based on the Rietveld refinement method, (c) Fe K-edge XANES spectra of FAO nanoflakes and α-$Fe_2O_3$ reference, (d) The measured (solid line) and corresponding fitting curve (dashed line) of $k^3$-weighted EXAFS spectra of α-$Fe_2O_3$ products compared with α-$Fe_2O_3$ standard, (e) Schematic illustration of crystal defects formation process.

inside the nanoflake. In other words, $Al^{3+}$ is atomically dispersed within the hematite matrix. In contrast, other impure ions from the leaching of fly ash including $Ca^{2+}$ and $Mg^{2+}$ are undetectable, confirming that they did not enter into hematite crystal structure in the hydrothermal treatment. More specifically, the impure $Al^{3+}$ was adsorbed preferentially on the (001) facet that is rich in hydroxyl groups due to the difference of the surface hydroxy group configuration of the various crystal facets of hematite. The double coordination nature of hydroxyl functions (Jia et al., 2005) in turn hindered the growth of $Fe^{3+}$ on the [001] direction. The presence of hydroxyl group and its preferential bonding with $Al^{3+}$ has been demonstrated in Fig. 2(b). In addition, the as-synthesized $Al^{3+}$-substituted α-$Fe_2O_3$ nanoflake can be deemed to have a nominal chemical formula of $Fe_{2-x}Al_xO_3$. Based on the atomic compositions determined by ICP-OES, the mole ratio of Fe to Al was found to be 8.51. Therefore, the final formula can be regarded as $Fe_{1.72}Al_{0.28}O_3$ with respect to the final as-synthesized FAO nanoflake in 50 h.

### 3.4. Atomic coordination of $Fe^{3+}$ and its time-resolved evolution

Fig. 4(a) shows the XRD patterns of the Fe-bearing precipitates formed in different hydrothermal treatment duration. To reiterate, the products demonstrate a poor crystallinity in the first 7 h. Once the hydrothermal treatment time is increased to 8–10 h, substantial changes are confirmed for all the diffraction peaks. The sample exhibits a high degree of crystallinity and all the diffraction peaks are in conformity with rhombohedral α-$Fe_2O_3$, which is highly consistent with the changes of the morphology from random clusters to regular hexagonal particles in Fig. 1. Extending the hydrothermal time beyond 10 h does not alter the XRD pattern any more. Instead, as discussed above, the 2θ positions of (1 0 4) and (1 1 0) facets gradually shifts right as the hydrothermal treatment time prolongs. The Rietveld refinement method based on the program X'Pert HighScore was used to determine the lattice parameters of the precipitates, and the results are illustrated in Fig. 4(b). It is obvious that with the prolonging of the hydrothermal treatment time, the lattice parameters of a, c and cell volume V

decrease from 5.038(67), 13.772(18) and 302.722(5) Å of standard α-$Fe_2O_3$ nanoparticles (**Table S2**) to 5.005(43), 13.727(44) and 297.853(3) Å at 50 h, respectively. With the increase on the hydrothermal treatment duration, the isovalent *in-situ* substitution of $Fe^{3+}$ by $Al^{3+}$ is enhanced stably, as evident by a continuing reduction on the magnitude of the three lattice parameters summarized in **Table S2**, with all the respective XRD patterns and fitting results illustrated in **Fig. S8-S12**.

Detailed atomic structure of the as-synthesized FAO nanoflake is further verified through Fe K-edge XANES and EXAFS. As depicted in Fig. 4(c), the XANES curves prove that the white line position of all the precipitate samples closely resembles that of standard α-$Fe_2O_3$. However, a close view of the pre-edge position, as depicted **Fig. S13**, reveals a gradual shift of the white-line, which is a qualitative indicator of the change/distortion in the local geometry with increasing hydrothermal annealing time (Chen et al., 2014; Wilke et al., 2001). To quantitatively clarify the effect of Al on the local structure of Fe in atomic level, Fe K-edge EXAFS spectra in Fig. 4(d) were analyzed using Artemis. This analysis is expected to offer the atomic coordination details of $Fe^{3+}$, including bond distance (R), coordination number (N) and Debye-Waller factor ($\sigma^2$) of ligands coordinated to the absorbing element.

Table 1 demonstrates that with the hydrothermal time prolongs, the Fe-O bond distance decreases from the standard α-$Fe_2O_3$ (2.01(0.01) Å) to the final 50 h product (1.95(0.21) Å), which is attributed to the intrusion of the smaller $Al^{3+}$ into the crystal lattice of hematite. The mixed Fe-O and Al-O bonds contribute to the first shell jointly and result in a smaller crystal lattice that has been discussed in the XRD part. In contrast, the second shell for the Fe-Fe bond is rather constant in terms of the bond distance, which is also very close to standard α-$Fe_2O_3$ nanoparticles, indicating that the distortion of $Fe_{2-x}Al_xO_3$ lattice is mainly attributed to intrusion of $Al^{3+}$ into the short-range first shell. With regards the coordination number (N), the refined N value of standard sample is 5.9(0.3) and 3.8(0.6) for Fe-O and Fe-Fe, respectively, which are close to the theoretical values of 6 and 4 (Jia et al., 2005). However, the value of N of the first shell decreases from 5.2(0.7) in 8 h to 4.5(0.3) in 50 h, indicating a gradual and slow intrusion of $Al^{3+}$ into the α-$Fe_2O_3$ lattice. Finally, as a summary, Fig. 4(e) illustrates the evolution of the *in-situ* disorder replacement of $Al^{3+}$ into the hematite structure upon hydrothermal treatment, which results in reduced unit cell and twisted atomic structure for $Fe^{3+}$ that preferentially grows on its (1 1 0) crystal direction.

### 3.5. Adsorption performance

Finally, the adsorption experiments were conducted to evaluate the potential applications of the as-synthesized FAO nanoflakes in water treatment. Fig. 5(a) shows the adsorption isotherms for Cr(VI), As(V) and As(III) of the fresh as-synthesized FAO nanoflakes and standard α-$Fe_2O_3$ nanoparticles prepared from pure $FeCl_3{\cdot}6H_2O$, respectively. The Langmuir adsorption equation was used to model the adsorption data over the concentration range of 5–500 mg $L^{-1}$ and to calculate the maximum adsorption capacity:

**Table 1**
Structural parameters calculated from EXAFS analysis.

| Samples | Shell | N | R/Å | $\delta^2$/Å$^{-2}$ | R factor |
|---|---|---|---|---|---|
| α-$Fe_2O_3$ standard | Fe-O | 5.9(0.3) | 2.01(0.01) | 0.0135 | 0.044 |
| | Fe-Fe | 3.8(0.6) | 2.95(0.83) | 0.0073 | |
| 8 h | Fe-O | 5.2(0.7) | 1.98(0.05) | 0.0117 | 0.028 |
| | Fe-Fe | 3.6(0.2) | 2.98(1.09) | 0.0026 | |
| 10 h | Fe-O | 4.7(0.6) | 1.97(0.09) | 0.0101 | 0.039 |
| | Fe-Fe | 4.8(0.9) | 2.96(0.75) | 0.0048 | |
| 20 h | Fe-O | 4.8(1.5) | 1.97(0.06) | 0.0132 | 0.012 |
| | Fe-Fe | 4.0(1.2) | 2.94(0.39) | 0.0014 | |
| 50 h | Fe-O | 4.5(0.3) | 1.95(0.21) | 0.0130 | 0.036 |
| | Fe-Fe | 4.1(0.9) | 2.95(0.13) | 0.0051 | |

$$q_e = \frac{q_m b c_e}{1 + b c_e} \quad (2)$$

Where $C_e$ (mg $L^{-1}$) is the equilibrium concentration of heavy metal ions, $q_e$ (mg $g^{-1}$) is the amount of heavy-metal ions adsorbed per unit weight of the adsorbent at equilibrium, $q_m$ (mg $g^{-1}$) is the theoretical maximum adsorption capacity, and $b$ is the equilibrium constant. Results show that the Langmuir model fits all the experimental data fit well. Note that the Freundlich model was also used to fit the isotherm adsorption data, as shown in Fig. S14. Clearly, the Langmuir fittings are better than the Freundlich fittings, which are further quantified by the $R^2$ coefficient summarized in Table S3. This indicates that the adsorption proceeds more likely via a monolayer chemical adsorption on the adsorbent surface.

Back to Fig. 5, a large difference is notably observed between the fresh as-synthesized FAO nanoflakes and the standard α-$Fe_2O_3$ nanoparticles. Based on the isotherms, the calculated maximum adsorption capacity, $q_m$ of the fresh FAO nanoflake reaches 68.3 mg $g^{-1}$ for Cr(VI), 80.6 mg $g^{-1}$ for As(V) and 61.1 mg $g^{-1}$ for As(III). These values are significantly higher than the respective $q_m$ of the standard α-$Fe_2O_3$ nanoparticles, which is around 15.7, 22.7 and 10.6 mg $g^{-1}$ for the three respective cations. Furthermore, it is noteworthy that the adsorption capacities of the FAO nanoflakes are comparable and even higher in comparison with the reported nanomaterials, such as α-$Fe_2O_3$ nanostructures (Wei et al., 2013; Cao et al., 2012; Hao et al., 2014; Du et al., 2013; Qiu et al., 2011), $Fe_3O_4$ (Wang et al., 2013), FeOOH (Wang et al., 2012), CuO (Martinson and Reddy, 2009) and $CeO_2$ (Cao et al., 2010), as listed in Table S4. Specifically, although the as-synthesized FAO nanoflake in this study does not possess the largest specific surface area, its maximum removal capacity for the three heave metal cations are larger than all the other samples except the nanowire hematite. This should be due to its unique structure as elaborated before, and also its strong hydrophilicity as evident in Fig. 2(b). In addition, the adsorption kinetics experiments of Cr(VI), As(V) and As(III) ions with an initial concentration of 40 mg $L^{-1}$ were conducted, as shown Fig. 5(b). Obviously, as for the fresh crystal-defect FAO nanoflake, the adsorption reaction moves rapidly in the initial 120 min, achieving the removal percentages of about 80 % for Cr(VI), 82 % for As(V) and 76 % for As (III). In comparison, for the standard α-$Fe_2O_3$ nanoparticles, only 17 % of Cr(VI), 29 % of As(V) and 16 % of As(III) were removed.

To investigate the applicability of the crystal-defect FAO nanoflakes towards water remediation, adsorption experiments using Congo red were also conducted. **Fig. S15** shows the effect of fresh FAO nanoflakes dosage from 0 to 1 g $L^{-1}$ on the removal of Congo red with an initial concentration 100 mg $L^{-1}$ in 12 h. Upon the increase of the dosage to 0.5 g $L^{-1}$, 99.6 % of the Congo red was removed out of water (shown in **Fig. S15** inset). Accordingly, the dosage of 0.5 g $L^{-1}$ was then used to evaluate the maximum adsorption capacity of both FAO nanoflake and standard α-$Fe_2O_3$ nanoparticle. Fig. 5(c) shows the respective adsorption isotherms. Based on the Langmuir adsorption equation, the maximum adsorption capacity for fresh FAO nanoflakes and standard α-$Fe_2O_3$ nanoparticles was found to reach 213.8 mg $g^{-1}$ and 65.9 mg $g^{-1}$, respectively. Here again, the obtained adsorption capacity of our FAO nanoflake is higher than similar materials, such as α-$Fe_2O_3$ nanostructures (Wei et al., 2013; Hao et al., 2014; Jia et al., 2015; Maiti et al., 2017), γ-$Fe_2O_3$ (Fei et al., 2013), FeOOH (Wang et al., 2012), $MnO_2$ (Fei et al., 2008), γ-$Al_2O_3$ (Cai et al., 2010) and boehmite (Cai et al., 2009), as listed in Table S5. Similarly, it should be partially due to the unique structure and strong hydrophilicity of our nanoflake. To evaluate the adsorption rate of FAO nanoflakes, the adsorption kinetics experiments of Congo red with an initial concentration of 100 mg $L^{-1}$ were also conducted, as shown Fig. 5(d). As for the defected FAO nanoflake, the adsorption reaction occurred rapidly in the initial 120 min, achieving a removal percentage of about 97 % for Congo red. This is much higher than the standard α-$Fe_2O_3$ nanoparticles for the removal of only 26 % Congo red in the same duration.

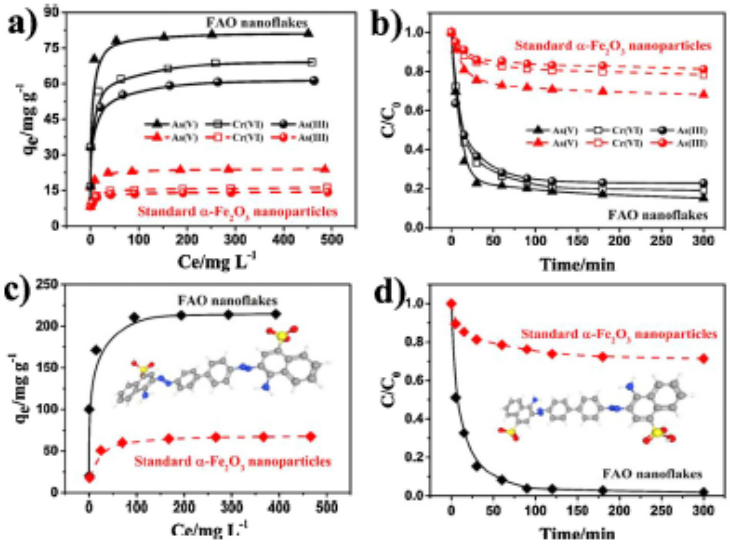


**Fig. 5.** Adsorption properties of the fresh as-synthesized FAO nanoflakes. (a) Langmuir adsorption isotherms of Cr (VI), As(V), As(III), (b) Adsorption rate curves of Cr(VI), As(V), As(III), (c) Langmuir adsorption isotherm of Congo red, (d) Adsorption rate curves of Congo red. (In all the four figures, solid lines are for the FAO nanoflakes and dashed lines are for the standard $\alpha$-$Fe_2O_3$ nanoparticles. In (c) and (d), inset is the molecule structure for Congo red with C (grey), H (white), N (blue), O (red) and S (yellow)) (For interpretation of the references to colour in this figure legend, the reader is referred to the web version of this article).

Regarding the spent FAO nanoflakes, the morphology remains unchanged, as indicated in Fig. S16. This is an indicator of its strong stability. Additionally, the cyclic test results in Fig. S17 and Fig. S18 further confirmed a strong adsorption performance of the spent FAO nanoflake. The gradual loss of the FAO nanoflake capacity from the third cycle is mainly attributed to the batch-scale (i.e., non-continuous) refluxing approach used for the regeneration of the spent adsorbent here, which lacks a way to avoid the re-adsorption of these cations back on the regenerated surface. Therefore, a portion of the surface-active sites is saturated and lost in the next cycle, as has been observed for the other adsorbents elsewhere (Wei et al., 2013; Hao et al., 2014; Maiti et al., 2017; Lee et al., 2013). Nevertheless, even after four cycles, the regenerated FAO nanoflake still bears a much larger removal capacity than the fresh standard $\alpha$-$Fe_2O_3$ nanoparticles.

### 3.6. Implications

Herein, a nanoflake structured hematite has been successful synthesized from a local coal fly ash waste. Its larger adsorption capacity than the literature was also confirmed by testing various traces metals and Congo red in aqueous solution. Such an effort is clearly beneficial in valorizing this local waste, and hence, this study is expected to cast a profound impact from the practical perspective. Moreover, through the intensive characterization, detailed knowledge for the structure of the $Al^{3+}$-substituted hematite has been established, which is expected to extend and cast a broad implication on the use of this structure or similar ones in the other areas such as catalysis. As a key catalyst precursor, hematite is usually doped with $Al^{3+}$ or other cations with an ionic radius close to $Fe^{3+}$ to promote its textural parameter, and consequently its catalytic performance (Pal et al., 2018). However, as far as the authors are aware, no study has yet to be made to elaborate the fundamentals underpinning the structural role of $Al^{3+}$ and the time-resolved evolution and optimization of the structure. Clearly, the results here have the potential to assist in fine-tuning the structure of the $Al^{3+}$-doped hematite such as through a hydrothermal annealing to improve its catalytic performance, which is underway by us.

## 4. Conclusions

A unique $Fe_{1.72}Al_{0.28}O_3$ (FAO) nanoflake has for the first time been successfully synthesized from BCFA waste, an otherwise valueless industry by-product. The product achieved a yield of 32 %, based on the mass of water-washed, dried fly ash. Crystal defects of the FAO nanoflakes were introduced through the *in-situ* isovalent replacement of $Fe^{3+}$ by $Al^{3+}$ upon hydrothermal treatment. Consequently, a flattened nanoflake-like morphology with a diameter of around 300 nm and 50 nm in thickness was achieved, and a relatively large specific surface area of 80.12 $m^2\ g^{-2}$ was secured. Detailed structure characterization indicates that, the $Al^{3+}$ dopant distorted the original atomic structure of standard $\alpha$-$Fe_2O_3$, resulting in reduced lattice parameters (a = 5.005(43) Å, c = 13.727 (44) Å), a smaller first shell (Fe-O bond distance of 1.95(0.21) Å) and a reduced periodic symmetry (Fe coordination number of 4.5(0.3)). Compared with the standard nanosized $\alpha$-$Fe_2O_3$ and even those reported in the literature, the as-synthesized FAO nanoflakes exhibit higher efficiency and enhanced adsorption performance with a maximum adsorption capacity of 68.3, 80.6, 61.1 and 213.8 mg $g^{-1}$ of Cr(VI), As(V), As(III) and Congo red, respectively. These values are around 3-5 times larger than the standard $\alpha$-$Fe_2O_3$ nanoparticles that is free in $Al^{3+}$. This work demonstrates the viability of converting the low-rank coal ash waste into value-added materials that are highly efficient for wastewater remediation.

### Credit author statement

Binbin Qian: Paper writing; Adsorbent synthesis and analysis and data interpretation.

Cheng Liu and Jun Lu: Adsorption test, result discussion and proofreading.

Meiping Jian and Xiaoyu Hu: Help on the TEM analysis and data interpretation.

Tara Hosseini: Help with fly ash leaching process optimization.

Barbara Etschmann: Help with XAS data processing and interpretation.

Xiwang Zhang and Huanting Wang: Co-supervision of Binbin Qian

# Appendix B



for the research direction, results discussion and paper polishing.

Lian Zhang: Co-supervision of first two authors for the research direction, results discussion and paper polishing.

## Declaration of Competing Interest

The authors declare that they have no known competing financial interests or personal relationships that could have appeared to influence the work reported in this paper.

## Acknowledgements

The authors gratefully acknowledge the Australian Research Council (IH170100009) and Binbin Qian acknowledges the China Scholarship Council (CSC NO. 201708610139) for financial support. The authors also acknowledge the use of facilities within the Monash Centre for Electron Microscopy (MCEM). Dr Ting-Shan Chan at the beamline BL16A1of Taiwan National Synchrotron Radiation Research Center (NSRRC) is also acknowledged for the synchrotron XANES analysis.

## Appendix A. Supplementary data

Supplementary material related to this article can be found, in the online version, at doihttps://doi.org/10.1016/j.jhazmat.2020.122696.

## References

Ai, Z.H., Lu, L.R., Li, J.P., Zhang, L.Z., Qiu, J.R., Wu, M.H., 2007. Fe@$Fe_2O_3$ core–shell nanowires as the iron reagent. 2. An efficient and reusable sono-fenton system working at neutral pH. J. Phys. Chem. C 111, 7430–7436.

Alnasser, F., Castagnola, V., Bonelli, L., Esquivel-Gaon, M., Elloqbi, E., McIntyre, J., Byrne, H.J., Dawson, K.A., 2019. Graphene nanoflake uptake mediated by scavenger receptors. Nano Lett. 19, 1260–1268.

Arakima, M., Onuki, M., Satoh, A., 2012. Structural analysis of self-assembled lattice structures composed of cubic hematite particles. J. Phys. Chem. C 116, 17863–17871.

Bai, J., Li, Y., Ren, L., Mao, M., Zeng, M., Zhao, X., 2015. Thermal insulation monolith of aluminum tobermorite nanosheets prepared from fly ash. ACS Sustain. Chem. Eng. 3, 2866–2873.

Blissett, R.S., Rowson, N.A., 2012. A review of the multi-component utilisation of coal fly ash. Fuel 97, 1–23.

Cai, W., Yu, J., Cheng, B., Su, B.L., Jaroniec, M., 2009. Synthesis of boehmite hollow core/shell and hollow microspheres via sodium tartrate-mediated phase transformation and their enhanced adsorption performance in water treatment. J. Phys. Chem. C 113, 14739–14746.

Cai, W., Yu, J., Jaroniec, M., 2010. Template-free synthesis of hierarchical spindle-like γ-$Al_2O_3$ materials and their adsorption affinity towards organic and inorganic pollutants in water. J. Mater. Chem. 20, 4587–4594.

Cao, C.Y., Cai, Z.M., Chen, C.Q., Song, W.G., Cai, W., 2010. Ceria hollow nanospheres produced by a template-free microwave-assisted hydrothermal method for heavy metal ion removal and catalysis. J. Phys. Chem. C 114, 9865–9870.

Cao, C.Y., Qu, J., Yan, W.S., Zhu, J.F., Wu, Z.Y., Song, W.G., 2012. Low-cost synthesis of flowerlike α-$Fe_2O_3$ nanostructures for heavy metal ion removal: adsorption property and mechanism. Langmuir 28, 4573–4579.

Chen, L., Zhang, X., Shelby, M., 2014. Recent advances on ultrafast X-ray spectroscopy in the chemical sciences. Chem. Sci. 5, 4136–4152.

Choo, T.K., Song, Y., Zhang, L., Selomulya, C., Zhang, L., 2014. Mechanisms underpinning the mobilization of iron and magnesium cations from victorian brown coal fly ash. Energy Fuels 28, 4051–4061.

Choo, T.K., Cashion, J., Selomulya, C., Zhang, L., 2016. Reductive leaching of iron and magnesium out of magnesioferrite from victorian brown coal fly ash. Energy Fuels 30, 1162–1170.

Coleman, J.N., Lotya, M., O'Neill, A., Bergin, S.D., King, P.J., Khan, U., Young, K., Gaucher, A., De, S., Smith, R.J., Shvets, I.V., Arora, S.K., Stanton, G., Kim, H.Y., Lee, K., Kim, G.T., Duesberg, G.S., Hallam, T., Boland, J.J., Wang, J.J., Donegan, J.F., Grunlan, J.C., Moriarty, G., Shmeliov, A., Nicholls, R.J., Perkins, J.M., Grieveson, E.M., Theuwissen, K., McComb, D.W., Nellist, P.D., Nicolosi, V., 2011. Two-dimensional nanosheets produced by liquid exfoliation of layered materials. Science 331, 568–571.

Colón, J., Cadena, E., Pognani, M., Barrena, R., Sánchez, A., Font, X., Artola, A., 2012. Determination of the energy and environmental burdens associated with the biological treatment of source-separated municipal solid wastes. Energy Environ. Sci. 5, 5731–5741.

Cramer, A.J., Cole, J.M., 2017. Removal or storage of environmental pollutants and alternative fuel sources with inorganic adsorbents via host–guest encapsulation. J. Mater. Chem. A 5, 10746–10771.

Du, Y., Fan, H., Wang, L., Wang, J., Wu, J., Dai, H., 2013. α-$Fe_2O_3$ nanowires deposited diatomite: highly efficient absorbents for the removal of arsenic. J. Mater. Chem. A 1, 7729–7737.

Dunens, O.M., MacKenzie, K.J., Harris, A.T., 2009. Synthesis of multiwalled carbon nanotubes on fly ash derived catalysts. Environ. Sci. Technol. 43, 7889–7894.

Dyer, J.A., Scrivner, N.C., Dentel, S.K., 1998. A practical guide for determining the solubility of metal hydroxides and oxides in water. Environ. Prog. Sustain. Energy 17, 1–8.

Fang, R.C., Sun, Q.Q., Zhou, P., Yang, W., Wang, P.F., Zhang, D.W., 2013. High-performance bilayer flexible resistive random access memory based on low-temperature thermal atomic layer deposition. Nanoscale Res. Lett. 8, 92.

Fei, J.B., Cui, Y., Yan, X.H., Qi, W., Yang, Y., Wang, K.W., He, Q., Li, J.B., 2008. Controlled preparation of $MnO_2$ hierarchical hollow nanostructures and their application in water treatment. Adv. Mater. 20, 452–456.

Fei, J., Zhao, J., Du, C., Ma, H., Zhang, H., Li, J., 2013. The facile 3D self-assembly of porous iron hydroxide and oxide hierarchical nanostructures for removing dyes from wastewater. J. Mater. Chem. A 1, 10300–10305.

Genovese, M., Jiang, J., Lian, K., Holm, N., 2015. High capacitive performance of exfoliated biochar nanosheets from biomass waste corn cob. J. Mater. Chem. A 3, 2903–2913.

Gong, J., Liu, J., Chen, X., Jiang, Z., Wen, X., Mijowska, E., Tang, T., 2015. Converting real-world mixed waste plastics into porous carbon nanosheets with excellent performance in the adsorption of an organic dye from wastewater. J. Mater. Chem. A 3, 341–351.

Hao, T., Yang, C., Rao, X., Wang, J., Niu, C., Su, X., 2014. Facile additive-free synthesis of iron oxide nanoparticles for efficient adsorptive removal of Congo red and Cr(VI). Appl. Surf. Sci. 292, 174–180.

Hosseini, T., Selomulya, C., Haque, N., Zhang, L., 2014. Indirect carbonation of victorian brown coal fly ash for $CO_2$ sequestration: multiple-cycle leaching-carbonation and magnesium leaching kinetic modelling. Energy Fuels 28, 6481–6493.

Jia, C.J., Sun, L.D., Yan, Z.G., You, L.P., Luo, F., Han, X.D., Pang, Y.C., Zhang, Z., Yan, C.H., 2005. Single-crystalline iron oxide nanotubes. Angew. Chem. 117, 4402–4407.

Jia, Z., Liu, J., Wang, Q., Li, S., Qi, Q., Zhu, R., 2015. Synthesis of 3D hierarchical porous iron oxides for adsorption of Congo red from dye wastewater. J. Alloys. Compd. 622, 587–595.

Kang, D.J., Hu, C.Q., Zhu, Q.S., 2018. Morphology controlled synthesis of hierarchical structured $Fe_2O_3$ from natural ilmenite and its high performance for dyes adsorption. Appl. Surf. Sci. 459, 327–335.

Khatri, C., Rani, A., 2008. Synthesis of a nano-crystalline solid acid catalyst from fly ash and its catalytic performance. Fuel 87, 2886–2892.

Lalasardibrea, G.T., Manh, D.N., Mayouc, D., 2005. Electronic structure of complex Hume-Rothery phases and quasicrystals in transition metal aluminides. Prog. Mater. Sci. 50, 679–788.

Lee, H.U., Lee, S.C., Lee, Y.C., Vetrik, S., Kim, C., Lee, S.G., Lee, Y.B., Nam, B., Lee, J.W., Park, S.Y., Lee, S.M., Lee, J., 2013. Sea-urchin-like iron oxide nanostructures for water treatment. J. Hazard. Mater. 262, 130–136.

Li, Y., Zhang, F.S., 2010. Catalytic oxidation of methyl orange by an amorphous FeOOH catalyst developed from a high iron-containing fly ash. Chem. Eng. J. 158, 148–153.

Liu, M., Xi, B., Hou, L., Yu, S., 2013. Magnetic multi-functional nano-fly ash-derived zeolite composites for environmental applications. J. Mater. Chem. A 1, 12617–12626.

Maiti, D., Mukhopadhyay, S., Devi, P.S., 2017. Evaluation of mechanism on selective, rapid, and superior adsorption of congo red by reusable mesoporous α-$Fe_2O_3$ nanorods. ACS Sustain. Chem. Eng. 5, 11258–11267.

Martinson, C.A., Reddy, K.J., 2009. Adsorption of arsenic(III) and arsenic(V) by cupric oxide nanoparticles. J. Colloid Interface Sci. 336, 406–411.

Mattagajasingh, S.N., Misra, B.R., Misra, H.P., 2008. Carcinogenic chromium(VI)-induced protein oxidation and lipid peroxidation: implications in DNA–protein crosslinking. J. Appl. Toxicol. 28, 987–997.

Nordstrom, D.K., 2002. Worldwide occurrences of arsenic in ground water. Science 296, 2143–2145.

Pal, D.B., Chand, R., Upadhyay, S.N., Mishra, P.K., 2018. Performance of water gas shift reaction catalysts: a review. Renewable Sustainable Energy Rev. 93, 549–565.

Palomo, A., Grutzeck, M.W., Blanco, M.T., 1999. Alkali-activated fly ashes: a cement for the future. Cem. Concr. Res. 29, 1323–1329.

Pandey, V.C., Singh, N., 2010. Impact of fly ash incorporation in soil systems. Agric. Ecosyst. Environ. 136, 16–27.

Pastora, J.G., Bringas, E., Ortiz, I., 2014. Recent progress and future challenges on the use of high performance magnetic nano-adsorbents in environmental applications. Chem. Eng. J. 256, 187–204.

Qian, B., Hosseini, T., Zhang, X., Liu, Y., Wang, H., Zhang, L., 2018. Coal waste to two-dimensional materials: fabrication of α-$Fe_2O_3$ nanosheets and MgO Nanosheets from brown coal fly ash. ACS Sustain. Chem. Eng. 6, 15982–15987.

Qiu, G., Huang, H., Genuino, H., Opembe, N., Stafford, L., Dharmarathna, S., Suib, S.L., 2011. Microwave-assisted hydrothermal synthesis of nanosized α-$Fe_2O_3$ for catalysts and adsorbents. J. Phys. Chem. C 115, 19526–19531.

Rogbeck, J., Hartlén, J., 1996. Ash gravel — a material for recycling. Waste Manage. 16, 109–112.

Ruan, G., Sun, Z., Peng, Z., Tour, J.M., 2011. Growth of graphene from food, insects, and waste. ACS Nano 5, 7601–7607.

Schwarzenbach, R.P., Escher, B.I., Fenner, K., Hofstetter, T.B., Johnson, C.A., Von Gunten, U., Wehrli, B., 2006. The challenge of micropollutants in aquatic systems. Science 313, 1072–1077.

Sun, C., Zeng, R., Zhang, J., Qiu, Z.J., Wu, D., 2017. Effects of UV-Ozone treatment on sensing behaviours of EGFETs with $Al_2O_3$ Sensing Film. Mater. 10, 1432.

Thirumurthy, K., Thirumaryanan, G., 2015. A facilely designed, highly efficient green synthetic strategy of a peony flower-like $SO_4^{2-}$-$SnO_2$-fly ash nano-catalyst for the

Appendix B



three component synthesis of a serendipitous product with dimedone in water. RSC Adv. 5, 33595–33606.
Wang, D.J., Zhang, Y.H., Dong, A.G., Tang, Y., Wang, Y.J., Xia, J.C., Ren, N., 2003. Conversion of fly ash cenosphere to hollow microspheres with mullite/mullite composite shells. Adv. Funct. Mater. 13, 563–567.
Wang, B., Wu, H., Yu, L., Xu, R., Lim, T.T., Lou, X.W., 2012. Template-free Formation of uniform urchin-like α-FeOOH hollow spheres with superior capability for water treatment. Adv. Mater. 24, 1111–1116.
Wang, T., Zhang, L., Wang, H., Yang, W., Fu, Y., Zhou, W., Yu, W., Xiang, K., Su, Z., Dai, S., Chai, L., 2013. Controllable synthesis of hierarchical porous $Fe_3O_4$ particles mediated by Poly(diallyldimethylammonium chloride) and their application in arsenic removal. ACS Appl. Mater. Interfaces 5, 12449–12459.
Wei, Z., Xing, R., Zhang, X., Liu, S., Yu, H., Li, P., 2013. Facile template-free fabrication of hollow nestlike α-$Fe_2O_3$ nanostructures for water treatment. ACS Appl. Mater. Interfaces 5, 598–604.
Wilke, M., Farges, F., Petit, P.E., Brown, G.E., Martin, F., 2001. Oxidation state and coordination of Fe in minerals: an Fe K-XANES spectroscopic study. Am. Mineral. 86, 714–730.
Xie, J., Zhang, X., Zhang, H., Zhang, J., Li, S., Wang, R., Pan, B., Xie, Y., 2017. Intralayered ostwald ripening to ultrathin nanomesh catalyst with robust oxygen-evolving performance. Adv. Mater. 29, 1604765.
Yan, F., Jiang, J., Tian, S., Liu, Z., Shi, J., Li, K., Chen, X., Xu, Y., 2016. A green and facile synthesis of ordered mesoporous nanosilica using coal fly ash. ACS Sustain. Chem. Eng. 4, 4654–4661.
Yang, J., Zhang, H., Yu, M., Emmanuelawati, I., Zou, J., Yuan, Z., Yu, C., 2014. High-content, well-dispersed $\gamma$-$Fe_2O_3$ nanoparticles encapsulated in macroporous silica with superior arsenic removal performance. Adv. Funct. Mater. 24, 1354–1363.
Yu, Q., Meng, X., Wang, T., Li, P., Ye, J., 2015. Hematite films decorated with nanostructured ferric oxyhydroxide as photoanodes for efficient and stable photoelectrochemical water splitting. Adv. Funct. Mater. 25, 2686–2692.
Yu, L., Han, R., Sang, X., Liu, J., Thorsen, M.P., Hudak, B.M., Patel, A., Page, K., Guiton, B.S., 2018. Shell-induced ostwald ripening: simultaneous structure, composition, and morphology transformations during the creation of hollow iron oxide nanocapsules. ACS Nano 12, 9051–9059.
Zhang, X., Cheng, H., Zhang, H., 2017. Recent progress in the preparation, assembly, transformation, and applications of layer-structured nanodisks beyond graphene. Adv. Mater. 29, 1701704.

# Appendix C
# Chapter 5 in publication form

Applied Catalysis A, General 618 (2021) 118132

Contents lists available at ScienceDirect

Applied Catalysis A, General

journal homepage: www.elsevier.com/locate/apcata

# Synthesis of (111) facet-engineered MgO nanosheet from coal fly ash and its superior catalytic performance for high-temperature water gas shift reaction

Binbin Qian [a], Jianghao Zhang [b,c], Song Zhou [a], Jun Lu [a], Yue Liu [a], Baiqian Dai [a], Cheng Liu [a], Yong Wang [c], Huanting Wang [a], Lian Zhang [a,*]

[a] Department of Chemical Engineering, Monash University, Wellington Road, Clayton, Victoria, 3800, Australia
[b] State Key Joint Laboratory of Environment Simulation and Pollution Control, Research Center for Eco-Environmental Sciences, Chinese Academy of Sciences, 100085, Beijing, PR China
[c] The Gene and Linda Voiland School of Chemical Engineering and Bioengineering, Washington State University, Pullman, WA, 99164, USA

ARTICLE INFO

*Keywords:*
Coal fly ash
Facet engineering
MgO nanosheet
Waste treatment
Water gas shift reaction

ABSTRACT

Synthesis of high-value products from coal ash, an otherwise valueless waste is crucial to both sustainable waste treatment and low-cost material fabrication. However, research in this area is still sparse, with majority of the researches being conducted on the synthesis of alumina/silica-based nanomaterials such as zeolite from fly ash. Herein, we report a facile synthesis of high-purity, magnesium hydroxide ($Mg(OH)_2$) nanosheet from a brown coal fly ash (BCFA) waste via leaching, precipitation and ethanol-mediated hydrothermal processing in sequence. The resultant nanosheet from fly ash bears a specific surface area of around 100 $m^2/g$, and an averaged aspect ratio of 11.8, as opposed to only 1.5 for the commercial $Mg(OH)_2$ and the one synthesed without the mediation of ethanol during hydrothermal processing. The fly ash derived $Mg(OH)_2$ nanosheet was subsequently loaded with 30 wt% $Fe^{3+}$ (as $Fe_2O_3$) via incipient wetness impregnation and calcined into a (111) facet-rich MgO, which was proved for a superior catalysis performance for high-temperature water gas shift reaction (HT-WGSR). At the reaction temperatures of 400–450 °C, the CO conversion was increased by a factor of two compared to a reference catalyst consisting of identical Fe loading on the $Mg(OH)_2$ support synthesized without ethanol, and by a factor of seven compared to a nano-sized hematite catalyst synthesized from same hydrothermal process without ethanol addition. This is mainly due to the abundant oxygen vacancy on the (111) facet of the MgO nanosheet support, which improved the reducibility of $Fe^{3+}$ as well as facilitated the formation and decomposition of intermediate formates that in turn promoted the forward reaction. This study is expected to open a new direction for the valorisation of fly ash and any Mg-bearing solid wastes into high-value materials such as catalyst or catalyst support for a broad range of catalytic applications.

## 1. Introduction

Due to the continuous use of coal as the single largest solid fuel for the power generation in most countries, coal fly ash is one of the largest solid wastes with an annual yield of approximate 750 million tons, among which 10 million tons is discharged in Australia [1,2]. Conventionally, coal fly ash is used as a low-value additive into cement-based construction materials [3], road base [4] and agriculture [5]. With the increased awareness of the superiority of nanoparticles, various nanomaterials have been synthesised from fly ash, such as silicon nanorods [6], carbon nanofibers [7], geopolymer [8], mesoporous nanosilica [9], zeolite [10] and ordered mesoporous molecular sieves [11]. Despite of these findings, most of the reported nanomaterials are limited to alumina ($Al_2O_3$) and/or silica ($SiO_2$), which are abundant in the coal ashes produced from high-rank coals. For the ash produced from a low-rank coal such as brown coal, it is implausible to synthesise these Al-/Si-based nanomaterials as they are generally lean in the low-rank coal ashes.

As a continuation of our effort on the synthesis of hematite ($\alpha$-$Fe_2O_3$) nanoflake from a Mg-rich local coal ash, namely BCFA [12], in this work,

* Corresponding author.
*E-mail address:* lian.zhang@monash.edu (L. Zhang).

https://doi.org/10.1016/j.apcata.2021.118132
Received 9 February 2021; Received in revised form 14 March 2021; Accepted 30 March 2021
Available online 3 April 2021
0926-860X/© 2021 Elsevier B.V. All rights reserved.

we further report the synthesis of high-purity, magnesium hydroxide ($Mg(OH)_2$) nanosheet from the same fly ash, and a successful demonstration of its high-value application for the use as catalyst promoting the hydrogen production from HT-WGSR. The principal motivation for such an effort is to utilise the Mg-rich fly ash as a substitute for natural dolomite or chrysotile for the production of high-purity brucite ($Mg(OH)_2$) and magnesia (MgO). On the one hand, as a by-product derived from high-temperature coal combustion, fly ash bears negligible fibrous asbestiform crystal habitus that is however present in natural dolomite and serpentine. Therefore, the use of fly ash is expected to cause less/-negligible risk to the development of malignant mesothelioma and lung cancers induced by the environmental exposure to asbestos [13]. On the other hand, the presence of alkali and alkaline earth metals including $Mg^{2+}$ in fly ash hinders its use as an additive to cement, which would otherwise lead to the breakage of the road and bridge [14].

From the scientific perspective, this research aims to synthesise a facet-rich nanosheet structure for $Mg(OH)_2$ and MgO from fly ash, based on the rational that the crystal materials with a controlled facet at nanoscale level is crucial for boosting their performance in catalysis [15–18]. For the target oxide MgO, its (111) is composed exclusively of alternating polar monolayers of $O^{2-}$ and $Mg^{2+}$, and hence, a strong electrostatic field perpendicular to the (111) facet is created, which has abundant Lewis basicity $O^{2-}$ sites (oxygen vacancy). This in turn makes the (111) facet ideal for the storage of hydrogen [19], carbon capture [20] and catalysis [21]. To date, most of the proposed synthesis procedures are complex and/or energy-intensive, including the deposition of MgO on a facet-rich substrate such as Si(100), Ag(111) or GaAs(001) [22], mechanical polishing followed by acid etching [23], ion bombardment [24], electron beam annealing (1000 °C) in an ultrahigh vacuum (UHV) [25], benzyl alcohol-assisted supercritical synthesis [26] and multistep MgO-$Mg(OH)_2$-MgO transformation upon heating under dynamic vacuum [27]. For the catalysis performance evaluation, the HT-WGSR was chosen here. This is because this reaction has been remaining as the most practical reaction for hydrogen production, contributing to over 95 % of hydrogen produced by steam methane reforming of hydrocarbon fuels followed by WGSR [28]. For the hydrogen production from renewable biogas reforming, the WGSR is also one of the three principal steps [29]. In addition, although plenty of catalysts have been developed for the HT-WGSR, the development of non-toxic substitutes for the commercial Cr-laden hematite is still ongoing and the reaction mechanism is also in dispute [30]. There is also a lack of application of the facet-dependent nanocrystal catalysts to the HT-WGSR [15].

In this study, we demonstrate a novel synthesis of high-purity, (111) facet-dominant MgO from BCFA, as per a facile leaching-precipitation-hydrothermal scheme in Fig. 1. In brief, upon an initial crushing and water-washing, the BCFA powders are treated by leaching, precipitation and ethanol-mediated hydrothermal treatment sequentially, leading to the production of $Mg(OH)_2$ nanosheet with a high purity, high yield and high selectivity. Afterwards, it was impregnated with 30 wt% $Fe^{3+}$ and calcined successfully into an (111)-facet rich MgO-supported catalyst. Extensive characterisations based on XRD, TEM, XPS and synchrotron X-ray adsorption spectroscopy (XAS) have been conducted to elucidate the properties of the resultant products. For HT-WGSR catalysis performance evaluation, apart from CO conversion and time-on-stream testing, *in-situ* DRIFTS, CO-TPR and $H_2$-TPR were also conducted to elucidate the unique reducibility of $Fe^{3+}$ and reaction mechanism on the (111)-facet directional MgO. The results reported hereby are expected to cast a broad impact on the sustainable utilisation of solid wastes and low-cost synthesis of facet-engineered catalysts in the clean energy research area.

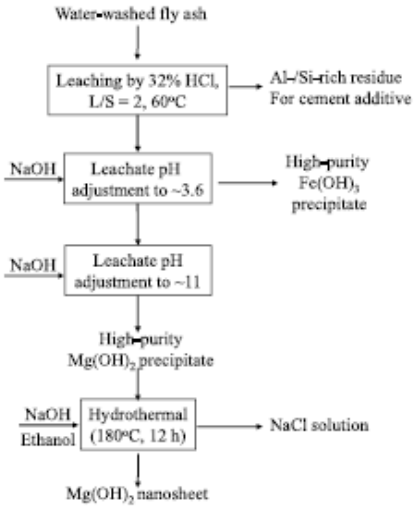


**Fig. 1.** Scheme of synthesis of high-purity $Mg(OH)_2$ nanosheet from BCFA. Note that all the three products including Al-/Si-rich residue, high-purity Fe $(OH)_3$ and $Mg(OH)_2$ nanosheet can be used rather than landfilled, enabling a full recovery and reuse of this special fly ash.

## 2. Experimental

### 2.1. Materials

The BCFA waste was collected from the Energy Australia Yallourn power plant located in the Latrobe Valley, Victoria, Australia. Table 1

**Table 1**
Mass yield, elemental compositions, specific surface area and aspect ratio of raw fly ash and as-synthesized $Mg(OH)_2$ nanoparticles (wt%).

| | Percent (%) | | |
|---|---|---|---|
| | Raw fly ash | $Mg(OH)_2$ nanosheet synthesised with the use of ethanol | $Mg(OH)_2$ nanoparticles synthesised without the use of ethanol |
| Mass yield, wt% on unit fly ash mass | – | 19.9 | |
| | | Elemental composition, wt% | |
| $SiO_2$ | 12.45 | N.D.[a] | N.D. |
| $Al_2O_3$ | 7.47 | N.D. | N.D. |
| $Fe_2O_3$ | 33.35 | 0.45 | 0.29 |
| CaO | 5.22 | 0.49 | 0.57 |
| MgO | 14.51 | 68.39 | 69.21 |
| $K_2O$ | 0.06 | N.D. | N.D. |
| $SO_3$ | 1.42 | N.D. | N.D. |
| MnO | 0.41 | N.D. | N.D. |
| $TiO_2$ | 0.79 | N.D. | N.D. |
| Loss of Ignition[c] | 24.32 | 30.67 | 29.93 |
| | | Physical properties | |
| Aspect ratio, [-] | – | 11.8 | 1.5 |
| Specific surface area ($m^2\ g^{-1}$) | – | 103.7<br>340.7 (Calcined)<br>104.5 (FEMN5)[b] | 78.2<br>321.7 (Calcined)<br>100.8 (NMN5)[b] |

[a] N.D.: Not detectable by XRF.
[b] after the loading with 30 wt% $Fe^{3+}$ and further calcination at 400 °C for 4 h.
[c] LOI was measured by heating a sample up to 800 °C in air in TGA. The LOI for a commercial $Mg(OH)_2$ was found to be around 31 wt%.

shows the elemental composition of the BCFA sample. It is clear that both Fe and Mg are abundant in this fly ash, whereas Al and Si are rather lean. The as-received fly ash sample was washed at a liquid to solid (L/S) mass ratio of 10 to remove the unburnt carbon and water-soluble species (e.g. alkali metals). Subsequently, it was dried in an oven at 105 °C for 12 h and ground using a tungsten-carbide vibratory ring pulveriser, producing a particle size of < 150 μm prior to use.

All the other chemicals including HCl (32 *wt*%), NaOH, MgO, ethanol, silicon carbide (SiC), $FeCl_3{\cdot}6H_2O$ and $Fe(NO_3)_3{\cdot}9H_2O$ were purchased from Sigma-Aldrich. Milli-Q water was used throughout all the experiments. Note that SiC was sieved to a narrow size of 105–165 μm, pre-ultrasonicated and dried prior to the HT-WGSR experiments.

### 2.2. Synthesis of $Mg(OH)_2$ nanosheets and Fe-Mg-O catalysts

The leaching process was consistent with our previous research [12]. To be specific, a two-step cross-current leaching method was used to extract $Mg^{2+}$ from the BCFA, as shown in Fig. S1 in the Supporting Information (SI). In each step, 32 *wt*% HCl was used as the leaching agent to mix with water-washed fly ash or the leaching residue derived from the previous step, at a L/S mass ratio of around two in a closed 250 mL conical flask. The flask was further placed in a thermostatically controlled water bath at 60 °C and stirred for a period of 90 min. The stirring rate was controlled at 300 rpm throughout all the runs. Afterwards, the slurry was filtered via a vacuum pump and a filter paper with a cut-off size of 450 μm. As shown in Fig. S2, the resultant leachate is dominated by $Fe^{3+}$ and $Mg^{2+}$, accompanied by a small amount for $Ca^{2+}$ and $Al^{3+}$. Subsequently, 1 mol/L NaOH was added dropwise into the leachate until its pH reached ~3.6, forming a slurry that was then centrifuged at 10,000 rpm for 10 min to remove the $Fe(OH)_3$ precipitate. For the resultant $Mg^{2+}$-rich leachate, 1 M NaOH solution was added dropwise into it until its pH reached ~11. Consequently, a white slurry was obtained, and centrifuged at 8000 rpm for 10 min to obtain the $Mg(OH)_2$ precipitate. The $Mg(OH)_2$ precipitate was further suspended into Milli-Q water and ultrasonicated for approximately 1 h. Subsequently, 1 mol/L of NaOH solution was dropped into the slurry via a peristaltic pump at a discharge rate of 9.6 mL/min. The resultant suspending solution was placed at room temperature and stirred continuously at 100 rpm. Its pH was closely monitored every 2 min in the first 20 min and then every 30 s. Once the pH reached 11, approximately 10 mL of ethanol was added into the suspension to prevent the agglomeration of the particles and to tune the growth of $Mg(OH)_2$ as an organic additive [31]. For each condition, three repeats were conducted to secure a high accuracy and sufficient sample. The resultant suspending solutions were combined and transferred into a 120 mL autoclave. The closed autoclave was finally placed inside a preheated hot-air oven maintained at 180 °C for 12 h, followed by a natural cooling down to room temperature. The obtained precipitate was filtered, washed with distilled water to remove the excessive NaOH and then with ethanol to reduce the agglomeration, and finally dried at 80 °C for 2 h.

Three reference materials were synthesised and tested, including $Mg(OH)_2$ nanoparticles that were synthesised from the same BCFA, and by exactly the same procedure without the addition of ethanol in the hydrothermal step; commercial MgO purchased from Sigma-Aldrich, and hematite ($Fe_2O_3$) nanoparticles synthesised from using pure $FeCl_3$ solution as the precursor, as per a similar hydrothermal procedure detailed in our previous research [12].

An impregnation method was used to load $Fe^{3+}$ on a MgO support. Specifically, the as-synthesised $Mg(OH)_2$ was first mixed with $Fe(NO_3)_3{\cdot}9H_2O$ at a mass percentage of 30 *wt*% for $Fe_2O_3$ (Hereafter, the loading amount of iron is described as 30 *wt*% $Fe^{3+}$). A very small amount of water (i.e. 1–2 ml per unit gram of $Mg(OH)_2$) was then gradually added into the mixture which was also continuously stirred until it turned pulpy. The resultant pulp was then dried at 80 °C overnight, and calcined in air at 400 °C for 4 h. The $Fe^{3+}$-MgO catalysts with ethanol treatment (facet-engineered), without ethanol treatment and from commercial purchase are denoted as FEMNS, NMNS and CMP, respectively. Notably, before the XRD analysis of the reduced FEMNS, NMNs and CMP, they were dispersed in ethanol and the resultant suspensions were dropped onto a clean glass substrate with subsequent drying at room temperature for one day and subsequent heating in the muffle furnace at 350 °C for 2 h, which is expected to make the (111) facet perpendicular to the diffraction vector *s* (the vector that bisects the angle between the incident and diffracted beam) to produce more collectible scattered beams [32]. It is also noteworthy that, only 30 *wt*% of $Fe^{3+}$ was tested in this study, aiming to demonstrate the superiority of the fly ash-derived MgO nanosheet over its counterparts. Regarding the optimisation of the mass fraction of $Fe^{3+}$ as well as other conditions such as those for the HT-WGSR, it is out of the scope.

### 2.3. HT-WGSR testing

Catalytic performance was evaluated in a continuous-flow fixed bed reactor at 400–450 °C and under the atmospheric pressure. For each run, 50–170 mg of a synthesised catalyst was blended and co-loaded with ten times the amount of pre-cleaned SiC, and then heated to 400 °C under the protection of $N_2$ at a heating rate of 10 °C/min, which simultaneously removed the surface contaminants. Afterwards, the dry CO gas at a concentration of ~ 4.5 vol% was fed into the system at a flow rate of 200 mL/min for 1–2 h, until the $CO_2$ signal was negligible (< 0.1 %) in the outlet gas. Note that the dry CO gas functioned as a reducing agent for an *in-situ* reduction of $Fe^{3+}$ into ferrous $Fe^{2+}$, which is expected to be the active site [33,34]. Catalysts were reduced at both 400 and 450 °C and it was found that the CO conversion for catalysts reduced at 400 °C is higher, as shown in Fig. S3. Therefore, the reduction temperature was set at 400 °C for all the runs. After catalyst reduction, CO and steam were introduced at a concentration of ~ 4.5–5 vol% each to commission the HT-WGSR for ~60 min for most of the cases. For two typical catalysts, time-on-stream testing in 10 h was also conducted. The overall gas flow rate remained at 200 mL/min, resulting in a space velocity of 0.23–0.89 $m^3\ g_{Fe2O3}^{-1}\ h^{-1}$.

The outlet gas stream was on-line monitored by an MKS Multigas™ 2030 Fourier-transform infrared spectroscopy (FTIR) continuous gas analyser for CO, $CO_2$, $H_2O$ and $CH_4$. It was also periodically sampled for the quantification of $H_2$, CO, $CO_2$ and $CH_4$ by an Agilent gas chromatography (GC) coupled with a TCD detector. The analysis showed a good consistence between the two analytic instruments. A closed mass balance for carbon was also confirmed. For the catalyst performance evaluation, the CO conversion based on the difference of inlet and outlet CO concentrations was used primarily.

### 2.4. Catalyst characterisation

A number of advanced facilities, including X-ray diffraction (XRD), scanning electron microscopy (SEM), transmission electron microscopy (TEM), small area electron diffraction (SAED), X-ray photoelectron spectroscopy (XPS) and synchrotron soft X-ray near-edge X-ray absorption fine structure (NEXAFS) have been employed to characterize the solid samples. Details for each analysis procedure can be found in the SI. Note that the (NEXAFS analysis was conducted on the total electron yield (TEY) mode that is highly surface intensive [35].

For the catalysis mechanistic study, *In-situ* diffuse reflectance infrared Fourier transform spectroscopy (DRIFTS), CO-Temperature Programmed Reduction (TPR) and $H_2$-TPR were performed, with the detail for each analysis procedure given in the SI.

## 3. Results and discussion

### 3.1. Synthesis and properties of BCFA derived $Mg(OH)_2$ and Fe-Mg-O catalysts

As demonstrated in Table 1, the $Mg(OH)_2$ precipitate from fly ash has

a mass yield of around 19.9 % on the basis of water-washed fly ash. This is due to a successful extraction of the majority of the inherent $Mg^{2+}$ out of fly ash matrix, leaving MgO with a content of around 1.3 wt% in the leaching residue [36]. In addition, Table 1 indicates a high purity for the two nano-$Mg(OH)_2$ derived from the hydrothermal step, with a MgO content of around 69 wt% and an LOI content of around 31 wt% that is very close to the commercial $Mg(OH)_2$. Interestingly, the impurities such as $Fe^{3+}$ and $Ca^{2+}$ are controlled at a negligible level, whist the other elements are indeed negligible. This further demonstrates a high selectivity for the extraction of $Mg^{2+}$ from fly ash. Regarding the physical properties of the two $Mg(OH)_2$ products, the one formed upon the addition of ethanol has a BET specific surface area of around 103.7 $m^2/g$, which is slightly higher than the one without ethanol. Nevertheless, these BET values are comparable and even superior to the nano $Mg(OH)_2$ synthesised from pure chemicals elsewhere [37,38]. After calcination at 400 °C, The BET surface area for the resultant MgO was further improved to 340.7 $m^3/g$ and 321.7 $m^2/g$ for the $Mg(OH)_2$ synthesis with and without ethanol, respectively. These values are comparable and also superior to previous findings [39–41]. The loading of 30 wt% $Fe^{3+}$ clearly occupied some of the pores, and hence, reverted the surface area to around 100 $m^2/g$.

XRD patterns for $Mg(OH)_2$ nanosheets prepared with and without ethanol treatment are shown in Fig. 2(a). All diffraction peaks can be indexed to the hexagonal brucite structure of $Mg(OH)_2$ (ICSD 34401) with lattice constants of a = 3.148 Å and c = 4.787 Å. The fact that no peaks associated other phases were observed further confirmed the high-purity of the $Mg(OH)_2$ nanosheets synthesised. Moreover, the addition of ethanol in the hydrothermal stage led to an enhanced intensity of the (0 0 1) peak. More specifically, the intensity ratio of peak (0 0 1) to (1 0 1) reaches 1.32 after the addition of ethanol, relative to merely 0.71 in the absence of ethanol and 0.79 in the standard file ICSD #34401. This is a clear evidence of the preferential orientation of $Mg(OH)_2$ on the (0 0 1) facet. Such a phenomenon is associated with the change of the surface energy upon the adsorption of organic molecules during hydrothermal modification [42,43]. The ethanol used here should work both as a dispersant and an anionic surfactant that was apparently adsorbed more readily on the (0 0 1) facet to reduce the high potential energy of the system, hindering the growth of nanoparticle in the [0 0 1] direction while promoting the edgewise growth normal to c-axis. Note that the trace impurities including $Ca^{2+}$ and $Fe^{3+}$ from fly ash leachate can be ruled out here, as the use of pure $MgCl_2$ solution lead to exactly the same structure for $Mg(OH)_2$, as demonstrated in Fig. S4.

The SEM images of the $Mg(OH)_2$ samples are shown in Fig. 2(b) and (c), respectively. Fig. 2(c) confirms a regular hexagonal structure for Mg $(OH)_2$ synthesised without the presence of ethanol. The averaged diameter reaches 113 nm and the mean thickness is 76 nm (Figs. S5–S6). These thickened sheets clearly tended to grow at a comparable rate in both c- and a- directions, thereby culminating in the shape of roughly equiaxed particles. In contrast, upon the addition of ethanol in the hydrothermal stage, Fig. 2(b) shows the abundance of well-grown thinner nanosheet with an averaged diameter of 212 nm and a mean thickness of 18 nm (Figs. S5–S6). Consequently, the aspect ratio of diameter to thickness for $Mg(OH)_2$ has been increased dramatically, reaching 11.8 for the use of ethanol versus merely 1.5 without ethanol, as shown in Table 1.

In the temperature window of 400–450 °C employed for calcination, reduction and HT-WGSR in this study, the as-synthesised $Mg(OH)_2$ is supposed to dehydroxylate into MgO crystal and a vapor-phase $H_2O$. For the resultant MgO, its (111) facet was found equivalent to facet (001) in the original $Mg(OH)_2$ in terms of orientation [44]. In other words, the (001) facet in $Mg(OH)_2$ can contribute to the exposure of unstable (111) facet for MgO, as depicted in Fig. 3(a).

Fig. 3(b) for the XRD patterns of the reduced Fe-Mg-O catalysts confirmed the hypothetical transformation route in Fig. 3(a). All the diffraction peaks can be indexed to the standard FCC periclase (MgO) structure (ICSD #26958) with a lattice constant of a = 4.203 Å. More interestingly, the calcined FEMNS based on the (001) facet-rich Mg $(OH)_2$ nanosheet bears a stronger crystallinity degree (manifested as peak sharpness) and intensity for the (111) and (222) diffraction peaks than its counterpart, calcined NMNS without the use of ethanol. This confirms the transformation route in Fig. 3(a). The HRTEM image in Fig. 3(c1) attests the abundance of irregular nanoparticles derived from the reduction of NMNS crystals. In contrast, the calcined FEMNS in Fig. 3 (c2) displays a well-defined, intact hexagonal lamellar morphology with an average diameter of ~100 nm. These nanosheets also feature a thickness of approximately 10 nm that is comparable with its (001) facet-rich $Mg(OH)_2$ precursor. More specifically, the HRTEM image in Fig. 3(c3) of the standing nanosheet (blue region in (c2)), and its

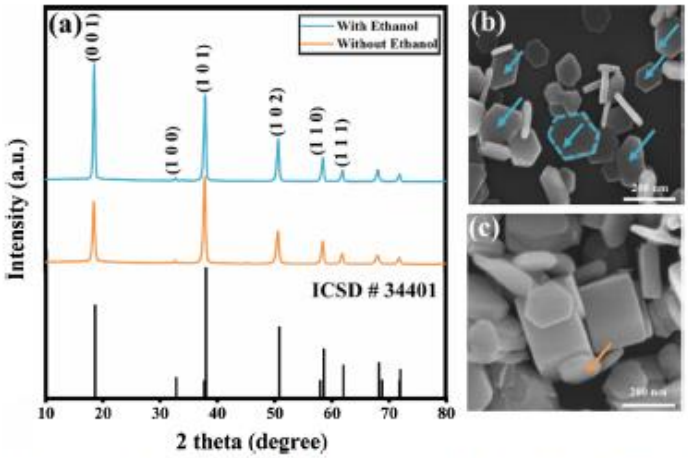


Fig. 2. (a) XRD patterns for $Mg(OH)_2$ nanosheets with and without ethanol treatment. (b) and (c) are SEM images for $Mg(OH)_2$ nanosheets with and without ethanol, respectively.

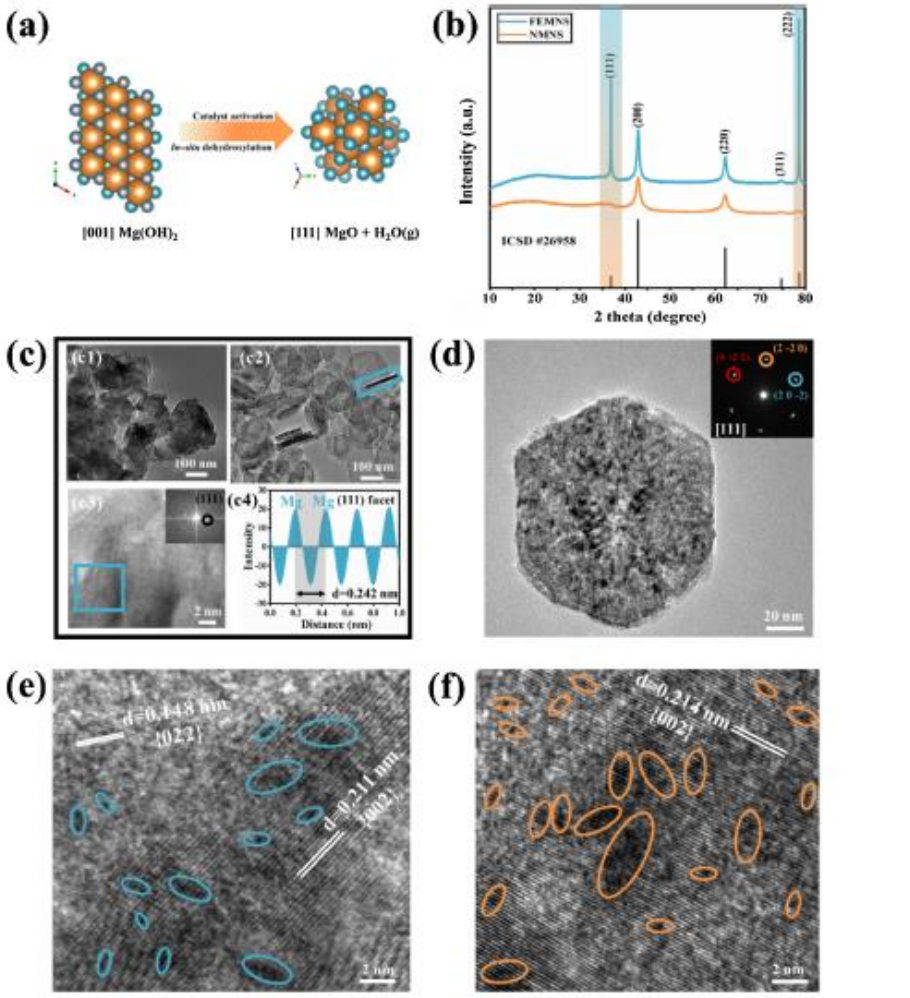


Fig. 3. (a) Equivalent orientations from [001] of $Mg(OH)_2$ to [111] of MgO during *in-situ* dehydroxylation. (b) XRD patterns for FEMNS and NMNS. (c) HRTEM images of catalysts: (c1) NMNS nanoparticles, (c2) FEMNS nanosheets, (c3) high-magnification TEM image from the blue region in (c2) (Inset is the corresponding FFT pattern for blue region) and (c4) line intensity profile from the blue region in (c3). (d) A typical FEMNS single crystal (inset: SAED pattern). (e) and (f) are bright field HRTEM images of FEMNS and NMNS, respectively. The yellow, blue and white spheres represent Mg, O and H, respectively.

corresponding FFT pattern and line intensity profile in Fig. 3(c4) exhibit the characteristic lattice fringes with a distance of 0.242 nm, which is in good agreement with the (111) lattice spacings in MgO [26]. Furthermore, the structure of a single calcined FEMNS single particle is amplified in Fig. 3(d), which exhibits an obvious hexagonal outline and a 6-fold symmetry of the corresponding SAED pattern that can be indexed to the [111] zone axis diffraction for the {2 -2 0} crystal facts. More intriguingly, regardless of the MgO precursor, the diffraction spot from the loaded $Fe^{3+}$ is undetectable by XRD, indicating that $Fe^{3+}$ is highly dispersed rather than forming any crystalline such as magnetite ($Fe_3O_4$) or magnesium ferrite ($MgFe_2O_4$) that has been reported as the active site for HT-WGSR [34,45]. Probably, it is present as a solid solution such as $Fe_xMg_{1-x}O$ with a non-stoichiometric formula. Fig. 3(e) and (f) shows the bright field HRTEM for the Fe-laden FEMNS and NMNS, respectively. The bright areas in Fig. 3(e) for FEMNS represent the MgO crystals with a lattice d-spacing of 0.148 nm and 0.211 nm for the {022} and {002} facets, respectively. The darker areas (blue ovals) are the contrast from Fe species, which again are confirmed with a high dispersion as nano and even sub-nano clusters, without any crystal structure. Similar observation was confirmed for the Fe-laden NMNS in

Fig. 3(f). However, no obvious discrepancy was discerned for the size and dispersion of Fe-clusters between the two supports.

### 3.2. HT-WGSR performance of Fe-Mg-O catalysts

Fig. 4 displays the CO conversion data on different catalysts. At the reaction temperature of 400 °C, as show in Fig. 4(a), it is evident that the stabilised CO conversion only reached 5% for pure hematite, which is less than the value of 20 % reported elsewhere [46]. This should be due to the harsh HT-WGSR conditions (*i.e.* lower CO/steam partial pressure and higher space velocity) employed here. The HT-WGSR rate is also kinetically controlled by the partial pressures of CO and steam [32,47, 48]. Nevertheless, the discrepancy between the three MgO-supporting catalysts is more interesting. The NMNS catalyst clearly bears a comparable activity with the CMP ($Fe^{3+}$ loaded on commercial MgO), both improving the CO conversion to around 10 % at 400 °C. This substantiates a structural similarity of these two catalysts, as well as the insignificance of trace $Ca^{2+}$ within the fly ash derivates. However, the CO conversion reached ~22 % for the FEMNS at 400 °C. It is further demonstrated in Fig. 4(b) that increasing the reaction temperature to 450 °C improved the CO conversion for all the catalysts, while the discrepancy among different catalysts is still remarkable. In particular, the use of FEMNS resulted in a CO conversion of ~35 % that is around eight-fold higher than the pure hematite and two-fold higher than the NMNS. The NMNS was also slightly more active than the commercial MgO, which should be due to the abundance of nano-size and thus, a larger specific surface area (Table S1) of the NMNS catalyst. More specifically, Table S1 quantitatively compared the mass-based specific reaction rates for all the catalysts tested. The value for FEMNS reached $832.14 \times 10^{-4}$ and $1682.68 \times 10^{-4}$ $mol_{co}\ g^{-1}_{Fe2O3}\ h^{-1}$ at 400 °C and 450 °C, respectively. Both are nearly one order of magnitude higher than pure hematite. In addition, the superior performance of FEMNS is merely attributed to its facet-engineered feature, rather than the specific surface area. As shown in Table 1, the BET specific surface area of FEMNS is very close to that of NMNS and even the commercial MgO-supported catalyst. This means that the preferential orientation of (001) facet was achieved at an expense of the other facets for $Mg(OH)_2$. Fig. 4(c) displays the CO conversion of FEMNS and NMNS at 450 °C over a 10 -h time-on-stream (TOS), which obviously substantiates a stronger stability of FEMNS than its counterpart over a long period.

The CO conversion profiles versus space velocity over the FEMNS and NMNS catalysts are presented in Fig. S7. Due to a shortened residence time, a lower CO conversion is expected at a higher space velocity. Nevertheless, even at the highest space velocity of 0.89 $m^3\ g^{-1}_{Fe2O3}\ h^{-1}$ studied, the CO conversion of FEMNS at 450 °C still reached 10.3 % that is considerably higher than NMNS at 7.4 %.

### 3.3. Mechanistic study

#### 3.3.1. In-situ DRIFTS

Identification of the HT-WGSR reaction pathway and surface intermediates on the catalysts was conducted via *in-situ* DRIFTS at 400 °C. Fig. 5(a) and (b) depict a time-dependent change of the surface upon a continuous injection of 5% CO through the catalyst. Clearly, in terms of peak areas (see Table S2), nearly all the peak areas on the FEMNS catalyst are higher than the respective ones on its counterpart, which should be derived from the abundant oxygen vacancies on MgO (111) facet produced from dehydration of the $Mg(OH)_2$ (001) facet or from the reduction stage. This strongly indicates the abundance of active site on the former catalyst with a nanosheet structure. Specifically, the intensity of the two strongest doublet bands at 2190 and 2114 $cm^{-1}$ increased stably with the progress of the CO injection. These two peaks are the characteristic gas-phase CO [49,50]. Moreover, the peak at 2848 $cm^{-1}$is attributed to CH— stretching of bidentate formats [51], while those at 1610 and 1370 $cm^{-1}$ are attributed to the asymmetric and symmetric OCO stretching vibration of bidentate β-formate [51,52]. Inferably, the dosing of CO onto the reduced Fe-MgO catalysts produced formate species as a surface intermediate. Especially, CO is more sensitive to basic $O^{2-}$ sites, which are abundant on the (111) facet from FEMNS. In addition, another two strong doublet peaks at 2354 and 2310 $cm^{-1}$ appeared, signaling the formation of surface $CO_2$ that is likely derived from the decomposition of the surface formate [52,53]. Additionally, there is a shoulder band at 1263 $cm^{-1}$ for FEMNS, which can be attributed to the vibration of the stable bidentate formate that starts to decompose into $CO_2$ and $H_2$ when the temperature is increased above 450 °C [54]. Nevertheless, the preferential adsorption of CO on these vacancies stabilised the (111) facet, which was in turn detectable by *ex-situ* XRD and TEM in Fig. 3. This phenomenon has also been reported for the carbon adsorption on MgO elsewhere [20,27].

After the injection of CO was ceased, 5% steam was introduced on the catalyst surface system and the resultant DRIFTS spectra were also collected. For both catalysts in Fig. 5(b), it is clear that the bands at 2190 and 2114 $cm^{-1}$ corresponding to gaseous CO disappeared completely. Simultaneously, the intensity of the bands at 1610 and 1370 $cm^{-1}$ also decreased rapidly, indicative of a continuous decomposition of the surface OCO formate into $H_2$ and $CO_2$. To clearly demonstrate the decomposition of the OCO formate, peak areas were calculated and shown in Fig. 5(c) and (d). Fig. 5(c) quantitatively displays the areas of asymmetric OCO formate as a function of reaction time. It is obvious that the initial decomposition for FEMNS (25.24 % for the peak area reduction in 1 min) is much faster than NMNS (11.31 %). Likewise, for the symmetric OCO formate in Fig. 5(d), the initial decomposition for FEMNS (42.05 %) is also faster than NMNS (19.98 %). In addition, as the hierarchy of hydroxylated surface energy for low-index MgO facets follows an ascending order of (111) < (100) < (110) [55], the adsorbed water molecule should be most easily adsorbed on the (111) facet, reacting with the adsorbed CO to form formic acid. This further explains

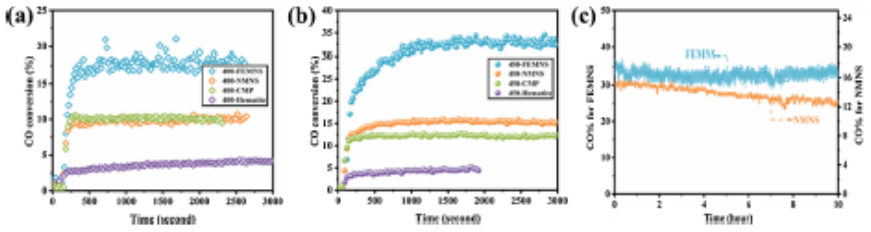


Fig. 4. (a) and (b) are Short-term CO conversion as a function of time-on-stream over FEMNS, NMNS, CMP and hematite at 400 and 450 °C, respectively. (c) Long-term CO conversion as a function of time-on-stream over FEMNS and NMNS at 450 °C The space velocity is 0.23 $m^3\ g^{-1}_{Fe2O3}\ h^{-1}$. 4.5 % CO and 4.5 % $H_2O$ balanced with He.

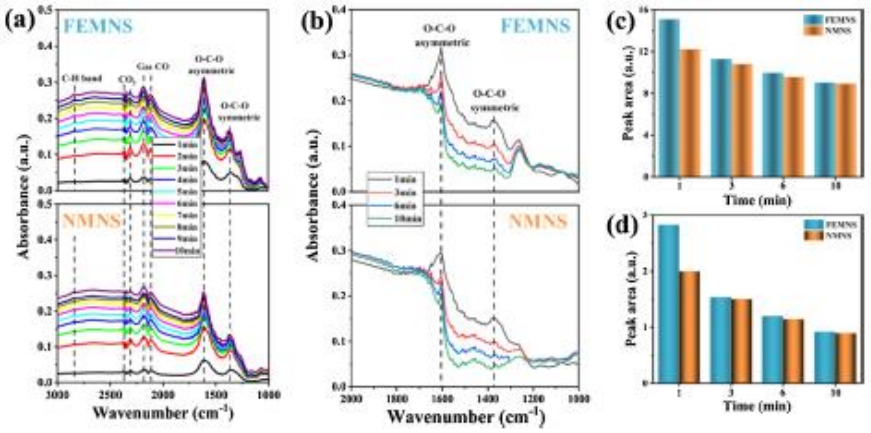


Fig. 5. (a) *In-situ* DRIFTS of CO adsorption for FEMNS (upper) and NMNS (lower), (b) *in-situ* DRIFTS of $H_2O$ adsorption for FEMNS (upper) and NMNS (lower), (c) and (d) are peak areas of asymmetric and symmetric OCO formate, respectively.

an intensified peak for the surface formate on FEMNS.

### 3.3.2. $H_2$-TPR and CO-TPR

The above results suggest that the remarkable performance of FEMNS towards HT-WGSR is due to the formation of abundant formates, which can be attributed to the oxygen vacancies from ferrous $Fe^{2+}$ and/or the high-energy MgO(111) facet, or even from the interface formed between $Fe^{2+}$ and the support MgO [56,57]. To confirm this hypothesis, the reducibility of both catalysts was studied by the $H_2$-TPR and CO-TPR. As shown in Fig. 6(a), the pure hematite $H_2$-TPR profile consists

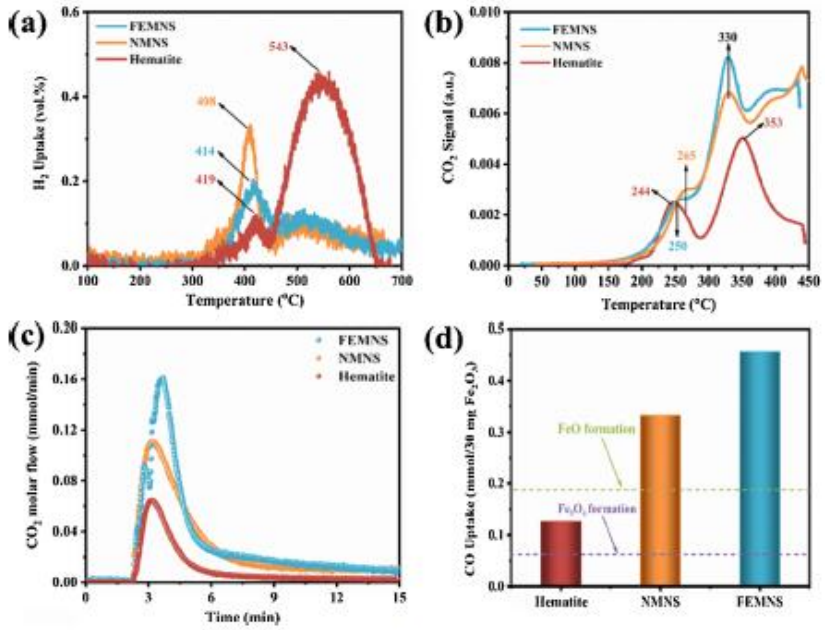


Fig. 6. (a) $H_2$-TPR profiles of FEMNS, NMNS and hematite, (b) CO-TPR profiles of FEMNS, NMNS and hematite, (c) Isothermal CO reduction at 400 °C of FEMNS, NMNS and hematite, (d) CO uptake amount for FEMNS, NMNS and hematite.

of fairly separated peaks, with a smaller peak at ~419 °C for the reduction of hematite to magnetite ($Fe_3O_4$), and a much larger one of ~543 °C for a further reduction to metallic iron ($Fe^0$) [58]. In contract, for both MgO-supposed catalysts, the former peak for the reduction into magnetite at the similar temperature is predominant, whereas the second one is much weaker and also displays a long tail for a very slow reduction of magnetite. In particular, the FEMNS bears a larger and broader peak after 400 °C. This suggests a stabilisation of $Fe^{2+}$ by MgO into a solid solution such as $Fe_xMg_{1-x}O$, which can lead to a high dispersion of very finely divided $Fe^{2+}$ to promote the HT-WGSR. The CO-TPR in Fig. 6(b) further confirmed the highest reducibility of $Fe^{3+}$ within FEMNS and the stabilisation of the reduced $Fe^{2+}$. Both of FEMNS and NMNS also exhibit a larger shoulder peak at 250–265 °C temperatures than pure hematite, which should be due to the high dispersion of $Fe^{3+}$ on the support. The majority of the $Fe^{3+}$ on the supported catalysts is also reduced at 330 °C that falls in the overlap between the two reduction zones, $Fe_2O_3$ to $Fe_3O_4$ and $Fe_3O_4$ to FeO/Fe. This reflects a mixing of different oxidation states for Fe and even the presence of structural impurities/defects for the two catalysts. Moreover, the first peak for the FEMNS catalyst is located at 250 °C, which is slightly lower than NMNS at 265 °C. Regarding the second sharp peak located at 330 °C, the FEMNS catalyst clearly presents a much stronger intensity than its counterpart. Such a feature provides another strong evidence of the abundance of MgO(111) facet within the FEMNS catalyst, as a similar $CO_2$ desorption temperature of ~352 °C has been confirmed from the MgO(111) nanosheet synthesized elsewhere [26], due to the abundance of oxygen vacancy, $O^{2-}$, that functioned as the medium basic sites on MgO(111) [59,60].

The isothermal CO reduction at 400 °C in Fig. 6(c) confirmed a quick and easy reduction of $Fe^{3+}$ on FEMNS. The $Fe^{3+}$ on FEMNS exhibits an early shoulder peak at around 2.8 min, which is accompanied by a larger peak at around 3.5 min. The shoulder peak should be assigned as $Fe^{3+}$ on the facets other than (111) of MgO, as it overlaps with the $Fe^{3+}$ on pure hematite and NMNS. In contrast, the principal peak at 3.5 min should be mostly assigned as $Fe^{3+}$ on the MgO(111) facet, where a strong interfacial interaction should exist, leading to a long tail for a slow secondary reduction of $Fe^{2+}$. Furthermore, based on the peak areas in Fig. 6(c), a quantitative determination of the CO uptake amount for each catalyst was calculated, with the results displayed in Fig. 6(d). It is evident that all the catalysts were reduced to a non-stoichiometric oxidation state for Fe. However, the reduction extent of each catalyst is very different. For pure hematite, its CO uptake amount falls in between the two theoretical values (e.g. 0.0625 mmol-CO and 0.1875 mmol-CO per 30 mg-$Fe_2O_3$ based on Equation S(2) and S(3) for the conversion of hematite to $Fe_3O_4$ and FeO, respectively), indicating the accompanient of $Fe^{3+}$ to $Fe^{2+}$ within it. However, for the other two catalysts, their CO uptake amounts are even above the theoretical value for $Fe^{2+}O$ formation. This is not a sign of the formation of metallic $Fe^0$, as the feastuing peak of 1889 $cm^{-1}$ for the chemisorbed CO [57] on a metal is indiscernable in Fig. 5. The Fe-2p XPS spectra (shown in Fig. 7(a–b)) also failed to find any metallic $Fe^0$ that has a feature binding energy at 706.7 eV. Alternatively, it should be assigned as the loss of the lattice oxygen from the MgO support. Consequently, the $O^{2-}$ from the reduced $Fe^{2+}$ site should be scavenged by the oxygen vacancy, leading to the formation of $Fe_xMg_{1-x}O$ with a non-stoichiometric ratio that is stable enough to inhibit the further reduction of $Fe^{2+}$. As this solid solution carries a non-stoichiometric formula, it was also failed to be detected by the XRD and even TEM. Here again, compared to the other facets in MgO, the (111) one is clearly prone to lossing its lattice oxygen, which in turn favors the reduction of the highly dispersed Fe on its surface. This observation is consistent with the CO-TPR results in Fig. 6(b).

### 3.3.3. *XPS and NEXAFS surface analysis of spent catalysts*

Fig. S8 shows the XPS survey spectra of the spent FEMNS and NMNS catalysts. It further demonstrates a negligible signal from Ca and Al on the surface. Fig. 7(a) shows the high-resolution XPS spectra of Fe 2p region, which can be attributed to two spin-orbit doublet peaks at 710.8 eV and 724.5 eV corresponding to the Fe $2p_{3/2}$ and Fe $2p_{1/2}$, respectively. The doublet is a characteristic of the peaks for $Fe^{2+}$ and $Fe^{3+}$ [61,62]. The quantitative analysis in Fig. 7(b) confirms a molar percentage of 61.2 % for $Fe^{2+}$ from surface Fe on the FEMNS catalyst, relative to 49.1 % $Fe^{2+}$ on the surface of the NMNS counterpart, whereas the metallic $Fe^0$ was not found. This verifies a stronger reducibility for $Fe^{2+}$ and its subsequent stabilisation by the oxygen vacancy on the MgO(111)

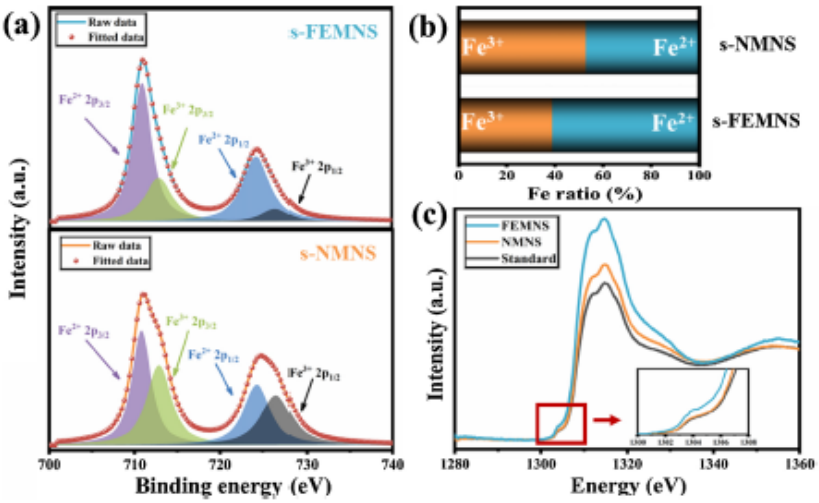


**Fig. 7.** (a) High-resolution XPS spectra of Fe 2p for spent FEMNS (s-FEMNS) and spent NMNS (s-NMNS), (b) Atomic ratio of $Fe^{2+}$ and $Fe^{3+}$ of s-FEMNS and s-NMNS, (c) Mg K-edge XANES spectra of FEMNS, NMNS and MgO reference (inset: the red area highlights the pre-edge absorption region).

facet, which is mainly attributed to the effect of the oxygen vacancy (basic $O^{2-}$ sites) that was produced by CO reduction. To be specific, CO should be preferentially adsorbed on the oxygen vacancy sites, grabbing the lattice oxygen by nucleophilic attack of basic $O^{2-}$ [27] and thus lowering the valence state of Fe. Moreover, such an observation agrees with previous findings that the catalytic activity of $Fe^{2+}$-$Fe^{3+}$ pairs is enhanced upon an increase on the $Fe^{2+}/Fe^{3+}$ ratio [34,63]. As both catalysts have a rather similar dispersion of Fe (as shown in Fig. 3(e) and (f)), the MgO(111) support is clearly the principal factor promoting the reducibility for Fe. It should be mainly due to the presence of abundant oxygen vacancy in the (111) facet, as has been confirmed by the theoretical calculation elsewhere [64]. In addition, Fig. 7(c) depicts the Mg K-edge NEXAFS spectra for both spent catalysts. The entire spectrum pattern as well as their white line positions closely resemble standard MgO, verifying the dominance of MgO rather than $MgFe_2O_4$ on these two catalysts. Moreover, the abundance of oxygen vacancy on FEMNS can be verified by its stronger intensity than the counterpart. This is in line with the previous experimental and theoretical works that have identified that the introduction of oxygen vacancy can affect the relative intensity of the spectral feature, especially the pre-edge region of the Mg K-edge spectra [65,66]. In particular, an enhanced pre-edge at ~1304 eV is confirmed for the FEMNS catalyst, which is a strong indicator of the presence of oxygen vacancy for the central Mg atom site that is highly non-centrosymmetric on the FEMNS catalyst surface.

## 4. Conclusions

The facile synthesis of a facet-engineered MgO(111)-Fe(III) nanosheet from BCFA waste as a HT-WGSR catalyst was successfully demonstrated in this study, which involves an initial leaching, precipitation and growth of a (001)-facet dominant $Mg(OH)_2$ precursor by an ethanol-mediated hydrothermal process followed by conversion of Mg $(OH)_2$(001) to MgO(111) facet during the HT-WGSR. The resultant products bear a high-purity of >98 %, and comparable specific surface area with those synthesised from pure chemical precursors. More intriguingly, upon the loading of 30 wt% $Fe^{3+}$, the thermally unstable (001)-facet enhanced $Mg(OH)_2$ nanosheet undertook a dehydroxylation into well-defined MgO(111) after calcination and reduction, which remained as nanosheets with the abundance of oxygen vacancy (Lewis basicity $O^{2-}$ sites). During the HT-WGSR, the reduced FEMNS is beneficial in promoting the formation and decomposition of surface formates owing to the enhanced CO and $H_2O$ adsorption as well as the reduction of $Fe^{3+}$ on the oxygen vacancy of the (111) facet, leading to increased CO conversion by a factor of two in comparison to the commercial Mg $(OH)_2$ loaded with the same amount of $Fe^{3+}$, and by nearly seven time compared to the nano-sized hematite reference. This study successfully broadens the application of fly ash derivatives in clean energy catalysis areas.

## Author contribution statement

Binbin Qian did experiment of catalysts synthesis, XRD analysis, XANES data work and manuscript writing.

Jianghao Zhang did experiment of DRIFTS and CO-TPR data analysis.

Song Zhou did NEXAFS and XPS analysis.

Jun Lu did SEM analysis and BET work.

Yue Liu did TEM and data analysis.

Baiqian Dai helped to revise manuscript.

Cheng Liu did part of synthetic work and catalytic experiments.

Yong Wang analyzed data of DRIFTS and CO-TPR and revised these parts in the paper.

Huanting Wang gave original ideas of how to synthesize nanosized catalysts and its application in catalysis.

Lian Zhang is the main leader of this work, he provided labs, funds and allowance for Binbin Qian and gave comments and suggestions of this work.

## Declaration of Competing Interest

The authors report no declarations of interest.

## Acknowledgements

The authors gratefully acknowledge the Australian Research Council (IH170100009) and Binbin Qian acknowledges the China Scholarship Council (CSC NO. 201708610139) for financial support. Jianghao Zhang and Yong Wang would like to thank the financial support by the U.S. Department of Energy (DOE), Office of Science, Basic Energy Sciences (BES) and Division of Chemical Sciences, Biosciences and Geosciences (grant DE-FG02-05ER15712) for characterization work including *in situ* DRIFTS. The authors acknowledge the use of instruments and scientific and technical assistance at the Monash Centre for Electron Microscopy, a Node of Microscopy Australia, Monash X-ray Platform and Australian Synchrotron Soft X-ray spectroscopy beamline (Project No. 16167) for the NEXAFS analysis.

## Appendix A. Supplementary data

Supplementary material related to this article can be found, in the online version, at doi:https://doi.org/10.1016/j.apcata.2021.118132.

## References

[1] Z.T. Yao, X.S. Ji, P.K. Sarker, J.H. Tang, L.Q. Ge, M.S. Xia, Y.Q. Xi, Earth-Sci. Rev. 141 (2015) 105–121.
[2] R.S. Blissett, N.A. Rowson, Fuel 97 (2012) 1–23.
[3] B. Ma, X. Li, X. Shen, Y. Mao, H. Huang, Constr. Build. Mater. 52 (2014) 261–266.
[4] R. Fortena, M. Far, C. Segui, V. Cerdá, Waste Manage. 24 (2004) 899–909.
[5] V.C. Pandey, N. Singh, Agr. Ecosyst. Environ. 136 (2010) 16–27.
[6] Y. Jiang, Y. Zhang, X. Yan, M. Tian, W. Xiao, H. Tang, Chem. Eng. J. 330 (2017) 1052–1059.
[7] N. Hintsho, A. Shaikjee, H. Masenda, D. Naidoo, D. Billing, P. Franklyn, S. Durbach, Nanoscale Res. Lett. 9 (2014) 387.
[8] M.I.M. Alzeer, K.J.D. MacKenzie, ACS Sustain. Chem. Eng. 6 (2018) 5273–5282.
[9] F. Yan, J. Jiang, S. Tian, Z. Liu, J. Shi, K. Li, X. Chen, Y. Xu, ACS Sustain. Chem. Eng. 4 (2016) 4654–4661.
[10] W. Feng, Z. Wan, J. Daniels, Z. Li, G. Xiao, J. Yu, D. Xu, H. Guo, D. Zhang, E.F. May, G. Li, J. Clean. Prod. 202 (2018) 390–400.
[11] K.S. Hui, C.Y.H. Chao, J. Hazard. Mater. B 137 (2006) 1135–1148.
[12] B. Qian, C. Liu, J. Lu, M. Jian, X. Hu, S. Zhou, T. Hosseini, B. Etschmann, X. Zhang, H. Wang, L. Zhang, J. Hazard. Mater. 395 (2020) 122696.
[13] A. Bloise, C. Ricchiuti, E. Giorno, I. Fuoco, P. Zumpano, D. Miriello, C. Apollaro, A. Crispini, R. Rosa, R. Punturo, Fibers 7 (2019).
[14] G. Wang, The Utilization of Slag in Civil Infrastructure Construction, Publisher: Elsevier, 2016.
[15] Z. Zhang, S.-S. Wang, R. Song, T. Cao, L. Luo, X. Chen, Y. Gao, J. Lu, W.-X. Li, W. Huang, Nat. Commun. 8 (2017) 488.
[16] S. Rej, C.-F. Hsia, T.-Y. Chen, F.-C. Lin, J.-S. Huang, M.H. Huang, Angew. Chem. Int. Ed. 55 (2016) 7222–7226.
[17] Q. Zhang, H. Wang, ACS Catal. 4 (2014) 4027–4033.
[18] K. Zhou, Y. Li, Angew. Chem. Int. Ed. 51 (2012) 602–613.
[19] V.K. Lazarov, R. Plass, H.C. Poon, D.K. Saldin, M. Weinert, S.A. Chambers, M. Gajdardziska-Josifovska, Phys. Rev. B 71 (2005) 115434.
[20] G.A. Mutch, S. Shulda, A.J. McCue, M.J. Menart, C.V. Ciobanu, C. Ngo, J. A. Anderson, R.M. Richards, D. Vega-Maza, J. Am. Chem. Soc. 140 (2018) 4736–4742.
[21] S. Wu, Y. Peng, T. Chen, J. Mo, A. Large, I. McPherson, H. Chou, I. Wilkinson, F. Venturini, D. Grinter, P. Escoribuela, G. Held, S. Tsang, ACS Catal. 10 (2020) 5614–5622.
[22] R. Arita, Y. Tanida, S. Entani, M. Kiguchi, K. Saiki, H. Aoki, Phys. Rev. B 69 (2004) 235423.
[23] S. Shinozaki, H. Sato, J. Appl. Phys. 43 (1972) 701–706.
[24] V.E. Henrich, Surf. Sci. 57 (1976) 385–392.
[25] V.K. Lazarov, S.A. Chambers, M. Gajdardziska-Josifovska, Phys. Rev. Lett. 90 (2003) 216108.
[26] K. Zhu, J. Hu, C. Kübel, R. Richards, Angew. Chem. Int. Ed. 118 (2006) 7435–7439.
[27] P. Liu, P. Abdala, G. Goubert, M. Willinger, C. Copéret, Angew. Chem. Int. Ed. 60 (2021) 3254–3260.
[28] R.M. Navarro, M.A. Peña, J.L.G. Fierro, Chem. Rev. 107 (2007) 3952–3991.
[29] D. Minh, T. Siang, D. Vo, T. Phan, C. Ridart, A. Nzihou, D. Grouset, Chapter 4 - hydrogen production from biogas reforming: an overview of steam reforming, dry

# Appendix C



reforming, dual reforming, and tri-reforming of methane. Hydrogen Supply Chains, 2018, pp. 111–166.
[30] L. Huang, B. Han, Q. Zhang, M. Pan, H. Cheng, J. Phys. Chem. C 119 (2015) 28934–28945.
[31] P. Wang, C. Li, H. Gong, H. Wang, J. Liu, Ceram. Int. 37 (2011) 3365–3370.
[32] M. Tang, Y. Ren, Y. Hu, L. Ye, B. Yue, H. He, Chin. Chem. Lett. 29 (2018) 935–938.
[33] C.J. Keturakis, M. Zhu, E.K. Gibson, M. Daturi, F. Tao, A.I. Frenkel, I.E. Wachs, ACS Catal. 6 (2016) 4786–4798.
[34] M. Zhu, I.E. Wachs, ACS Catal. 6 (2016) 722–732.
[35] Q. Feng, S. Zhao, Q. Xu, W. Chen, S. Tian, Y. Wang, W. Yan, J. Luo, D. Wang, Y. Li, Adv. Mater. 31 (2019) 1901024.
[36] B. Qian, T. Hosseini, X. Zhang, Y. Liu, H. Wang, L. Zhang, ACS Sustain. Chem. Eng. 6 (2018) 15982–15987.
[37] M. Liu, Y. Wang, L. Chen, Y. Zhang, Z. Lin, ACS Appl. Mater. Interfaces 7 (2015) 7961–7969.
[38] X. Pan, Z. Xu, Y. Zheng, T. Huang, L. Li, Z. Chen, W. Rao, S. Chen, X. Hong, X. Guan, Roy. Soc. Open Sci. 4 (2017) 170883.
[39] Y. Ding, G. Zhang, H. Wu, B. Hai, L. Wang, Y. Qian, Chem. Mater. 13 (2001) 435–440.
[40] N. Selvam, R. Kumar, L. Kennedy, J. Vijaya, J. Alloys Compd. 509 (2011) 9809–9815.
[41] P. Tian, X. Han, G. Ning, H. Fang, J. Ye, W. Gong, Y. Lin, ACS Appl. Mater. Interfaces 5 (2013) 12411–12418.
[42] S.-M. Lee, S.-N. Cho, J. Cheon, Adv. Mater. 15 (2003) 441–444.
[43] Y. Sui, W. Fu, H. Yang, Y. Zeng, Y. Zhang, Q. Zhao, Y. Li, X. Zhou, Y. Leng, M. Li, G. Zou, Cryst. Growth Des. 10 (2010) 99–108.
[44] M.J. McKelvy, R. Sharma, A.V.G. Chizmeshya, R.W. Carpenter, K. Streib, Chem. Mater. 13 (2001) 921–926.
[45] A. Boudjemaa, A. Auroux, S. Boumaza, M. Trari, O. Cherifi, R. Bouarab, React. Kinet. Catal. Lett. 98 (2009) 319–325.
[46] S. Natesakhawat, X. Wang, L. Zhang, U.S. Ozkan, J. Mol. Catal. A Chem. 260 (2006) 82–94.
[47] S. Yao, X. Zhang, W. Zhou, R. Gao, W. Xu, Y. Ye, L. Lin, X. Wen, P. Liu, B. Chen, E. Crumlin, J. Guo, Z. Zuo, W. Li, J. Xie, L. Lu, C.J. Kiely, L. Gu, C. Shi, J. A. Rodriguez, D. Ma, Science 357 (2017) 389–393.
[48] J. Zhang, W. Yan, Z. An, H. Song, J. He, ACS Sustain. Chem. Eng. 6 (2018) 7313–7324.
[49] X.-P. Fu, L.-W. Guo, W.-W. Wang, C. Ma, C.-J. Jia, K. Wu, R. Si, L.-D. Sun, C.-H. Yan, J. Am. Chem. Soc. 141 (2019) 4613–4623.
[50] X. Sun, J. Lin, Y. Zhou, L. Li, Y. Su, X. Wang, T. Zhang, AIChE J. 63 (2017) 4022–4031.
[51] Y. Chen, J. Lin, L. Li, B. Qiao, J. Liu, Y. Su, X. Wang, ACS Catal. 8 (2018) 859–868.
[52] J. Li, J.-X. Liang, J. Lin, J. Liu, X. Wang, T. Zhang, Angew. Chem. Int. Ed. 59 (2020) 2–10.
[53] M.C. Ribeiro, G. Jacobs, L. Linganiso, K.G. Azzam, U.M. Graham, B.H. Davis, ACS Catal. 1 (2011) 1375–1383.
[54] E.T. Saw, U. Oemar, X.R. Tan, Y. Du, A. Borgna, K. Hidajat, S. Kawi, J. Catal. 314 (2014) 32–46.
[55] P. Geysermans, F. Finocchi, J. Goniakowski, R. Hacquart, J. Jupille, Phys. Chem. Chem. Phys. 11 (2009) 2228–2233.
[56] A. Puigdollers, P. SchlexerOrcid, S. TosoniOrcid, G. PacchioniOrcid, ACS Catal. 7 (2017) 6493–6513.
[57] G. Bond, K. Molloy, F. Stone, Solid State Ion. 101-103 (1997) 697–705.
[58] W. Jozwiak, E. Kaczmarek, T. Maniecki, W. Ignaczak, W. Maniukiewicz, Appl. Catal. A Gen. 326 (2007) 17–27.
[59] Z. Liu, J.A. Cortés-Concepción, M. Mustian, M.D. Amiridis, Appl. Catal. A Gen. 302 (2006) 232–236.
[60] B.M. Choudary, M.L. Kantam, K.V.S. Ranganath, K. Mahendar, B. Sreedhar, J. Am. Chem. Soc. 126 (2004) 3396–3397.
[61] F. Han, L. Ma, Q. Sun, C. Lei, A. Lu, Nano Res. 7 (2014) 1706–1717.
[62] L. Pan, X.-D. Zhu, X.-M. Xie, Y.-T. Liu, Adv. Funct. Mater. 25 (2015) 3341–3350.
[63] Z. Cherkezova-Zheleva, I. Mitov, J. Phys.: Conference Ser. 217 (2010) 012044.
[64] C. Tusche, H.L. Meyerheim, N. Jedrecy, G. Renaud, A. Ernst, J. Henk, P. Bruno, J. Kirschner, Phys. Rev. Lett. 95 (2005) 176101.
[65] J. Wan, W. Chen, C. Jia, L. Zheng, J. Dong, X. Zheng, Y. Wang, W. Yan, C. Chen, Q. Peng, D. Wang, Y. Li, Adv. Mater. 30 (2018) 1705369.
[66] A. Kuzmin, J. Chaboy, IUCrJ 1 (2014) 571–589.